The Siglec-sialic acid axis is a target for innate immunotherapy of glioblastoma

Inauguraldissertation

zur

Erlangung der Würde eines Doktors der Philosophie

vorgelegt der

Philosophisch-Naturwissenschaftlichen Fakultät

der Universität Basel

von

Philip Daniel Schmassmann

Basel, 2022

Genehmigt von der Philosophisch-Naturwissenschaftlichen Fakultät auf Antrag von

Prof. Dr. Gregor Hutter, Prof. Dr. Fiona Doetsch und Prof. Dr. Rainer Glass

Basel, den 15. November 2022

Prof. Dr. Marcel Mayor, Dekan

Für meine Ehefrau, Lara

Summary

In spite of the paradigm shift in cancer therapy that came with the discovery of immune checkpoint inhibitors, current treatment modalities which are predominantly T cell centric, fail to evoke durable tumor rejection in glioblastoma (GBM) patients. Leaving aside the fundamental role innate immune cells play in the tumor microenvironment (TME), especially in less immunogenic tumors such as GBM.

Upregulation of sialic acid-containing glycans on the cell surface and in the tumor microenvironment (hypersialylation) is a key change in malignant tissue and capable of impacting tumorigenesis by promoting cell invasion and metastatic potential. By engaging immunomodulatory sialic acid-binding immunoglobulin-like lectins (Siglecs), tumor hypersialylation can trigger tolerogenic programs in different immune cell types and contributes to the establishment of the immunosuppressive TME.

By targeting inhibitory Siglec-E receptor on GBM-associated microglia (MG) and monocyte-derived cells (MdCs), we show increased tumor cell phagocytosis and improved subsequent T cell activation. Using a poorly immunogenic GBM preclinical model, we further demonstrate the synergistic potential of Siglec-E blockade in combined immunotherapies against GBM. Finally, we showcase the translational relevance of Siglec disruption on patient-derived samples.

To explore other tolerogenic programs within the GBM immune TME on a single-cell level, we performed single-cell RNA sequencing (scRNA-seq) on paired biopsies from the tumor center, peripheral infiltration zone and blood of five primary GBM patients. We revealed a regionally distinct transcription profile of microglia (MG) and monocyte-derived macrophages (MdMs) and an impaired activation signature in the tumor-peripheral cytotoxic-cell compartment. Comparing tumor-infiltrating $CD8^+$ T cells with circulating cells identified $CX3CR1^{high}$ and $CX3CR1^{int}$ $CD8^+$ T cells with effector and memory phenotype, respectively, enriched in blood but absent in the TME.

Based on our data, we propose Siglec-E as innate immune checkpoint in GBM-associated MG and MdCs and underscore the value of Siglec blockade in liberating innate immune responses to potentiate anti-tumor immunity. Further, our scRNA-seq analysis provides a regionally-resolved mapping of transcriptional states in GBM-associated leukocytes, serving as an additional asset to the research community in their effort to uncover novel therapeutic strategies to combat this fatal disease.

Table of contents

1 General Introduction

1.1 Glioblastoma multiforme (GBM) WHO grade IV

The recently updated World Health Organization (WHO) Classification of Tumors of the Central Nervous System introduced molecular parameters in addition to histology to define the different tumor entities. Thus, revolutionizing the century-old principle of diagnosis based largely of light microscopic features [1]. This shift to a combined classification based on both phenotype and genotype expresses itself particularly in the most prevalent group of brain tumors, the gliomas. Gliomas are tumors of neuroepithelial origin and account for more than 70% of all malignant brain tumors [2]. In the new classification, diffusely infiltrating gliomas like WHO grade II and grade III astrocytic tumors and oligodendrogliomas, as well as the grade IV glioblastoma are distinguished from tumors with a more circumscribed growth pattern like the WHO grade I pilocytic astrocytoma, which occurs mainly in childhood and is usually surgically cured [1]. Beside the similar growth pattern and behavior, most of the diffuse gliomas share the genetic driver mutations in the *IDH1* and *IDH2* genes*,* which encode for isocitrate dehydrogenase 1 and 2, enzymes participating in the citric acid (Krebs) cycle [3, 4].

However, for GBM, the most frequent and malignant histologic type within the group of diffuse gliomas and all malignant brain tumors, the vast majority are *IDH*-wildtype (about 90% of cases), which corresponds with the clinically defined primary or de novo GBM. Only around 10% of GBM cases show a positive *IDH*-mutation status and correspond closely to so-called secondary GBM. Despite a similar histologic appearance, primary and secondary GBMs are distinct tumor entities, with primary GBM developing rapidly in patients over 55 years and without evidence of a less malignant precursor lesion. In contrast, secondary GBM progresses from lower grade diffuse gliomas, manifest in younger patients and has a significantly better prognosis than primary GBM [4]. From this prognostic point of view the new combined pheno- and genotypic classification groups tumors that share similar prognostic markers like the *IDH* status but also predictive factors like the methylation status of the methyl-guanine methyl transferase *(MGMT)* promotor, which guides the use of therapies [5].

Despite the advancing molecular characterization of diffuse gliomas and new neurosurgical methods including the use of 5-aminolevulinic Acid (5-ALA) for intra-

operative visualization of malignant tissue for better tumor resection [6], GBM remains a fatal disease without effective long-term treatment options [7]. The current standard of care consists of tumor resection followed by adjuvant chemoradiotherapy resulting in a median overall survival of only 14 months [5, 8].

The ongoing discovery of genetic alterations including whole transcriptome analysis revealing different sub clusters of GBM [9] made further contribution to the understanding of the molecular pathways involved in oncogenesis. This highlights though, the significant inter- and intra-tumor heterogeneity in GBM. So that instead of targeting directly the deregulated tumor cells, modulation of tumor-associated nonmalignant cells in the tumor microenvironment (TME) has become a new approach for GBM therapy.

1.2 Tumor microenvironment (TME) of GBM

The GBM induced neovascularization not only nourishes glioma cells, but also provides a specialized niche for tumor-associated parenchymal cells such as monocyte-derived cells (MdCs), microglia (MG) as the brain-resident macrophages (together referred to as glioma-associated macrophages/microglia, GAMs), peripheral adaptive immune cells and other myeloid and stromal cells. The immune TME (iTME) acts paradoxically in an immunosuppressive manner and seems to promote tumor progression [10, 11]. Of note, tumor-associated microglia can contribute up to 30-50% of the total brain tumor mass and represent therefore an interesting cell population for tumor-targeted modulation [12, 13]. The origin of GAMs, infiltration of peripherally derived macrophages across the blood-brain-barrier (BBB) or recruitment of tissue-resident microglia to the tumor site, as well as their contribution to gliomagenesis are studied intensively to better understand the complex interactions of GBM cells with its microenvironment and vice versa [10, 11, 14].

1.2.1 Origin of GAMs

Using chimeric mice generated by bone-marrow transplantation following irradiation, researchers concluded that, even under homeostatic conditions, microglia are constantly replaced by the active recruitment of bone-marrow derived microglia progenitor cells [15-17]. This changed only until chimeric animals were generated by parabiosis, which does not compromise the BBB integrity and no recruitment of microglia progenitor cells from the blood circulation was found in two models of microglia

activation (axotomy and neurodegeneration). Suggesting that maintenance and local expansion of microglia are solely dependent on limited self-renewal [18]. Although, with a very low turn-over under normal conditions, microglia reside as a permanent population in the brain [12]. In addition, in an experimental mouse model of multiple sclerosis, circulating monocytes were found to efficiently enter the CNS and give rise to mature macrophages, indicating that in certain neuropathological conditions, the BBB is impaired, resulting in bone-marrow derived peripheral monocytes infiltrating the CNS. However, this is a transient event and following disease remission, recruited monocytes vanish, and therefore do not contribute to the resident microglial pool [19]. Moreover, a recent fate mapping analysis revealed that microglia arise from extra-embryonic immature yolk sac progenitors and invade the brain early in development. [20]. Identifying microglia as distinct and ontogenically different population compared to peripheral bone-marrow derived macrophages, which colonize the brain only transiently under pathological conditions [11].

1.2.2 GAM recruitment

Despite their different origin, the accumulation of GAMs in and around GBM has raised the question as to whether these cells are only bystanders or whether they actively influence GBM progression and thus, in the latter case, to what extent it may be possible to exploit these interactions of GAMs with GBM cells.

There are many factors identified which promote microglia and macrophage chemoattraction. However, it remains unclear whether there exist distinct factors that recruit resident microglia or peripheral circulating macrophages to the tumor site [14].

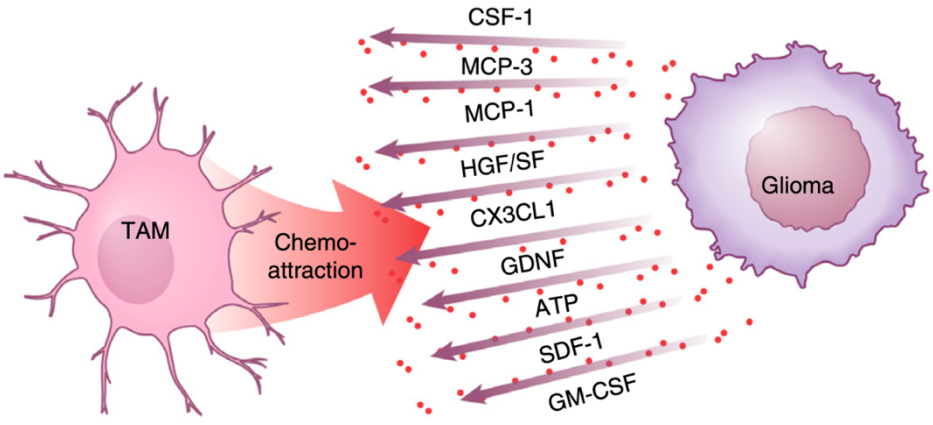

Figure 1 GAM recruitment in GBM.
Glioma cells release several factors, which attract GAMs to the tumor tissue. Figure adapted from [14].

In the healthy brain, the receptor for the cytokine CX3CL1 (fractalkine), CX3CR1, is mostly expressed by microglial cells, where it has been established as a reliable marker for microglia imaging [14]. Notably, an identified polymorphism in the *CX3CR1* gene was shown to be associated with reduced tumor infiltration by microglia which led to an increased survival in GBM patients [21]. However, others reported seemingly contradictory findings regarding the importance of the CX3CL1/CX3CR1 axis in tumor-directed microglia migration [22, 23], thus no definitive conclusion can be drawn.

Colony-stimulating factor 1 (CSF-1), also known as macrophage colony-stimulating factor (M-CSF), is a potent GAM recruiting cytokine and macrophage survival signal [24]. After its blockade, the density of GAMs was reduced and GBM invasion attenuated *in vivo* [24, 25]. Similar results could be achieved by a knockdown of its close relative, ganulocyte-macrophage colony-stimulating factor (GM-CSF), which resulted in reduced microglia-dependent invasion in organotypical brain slices and growth of intracranial gliomas and extended animal survival [26]. Figure 1 gives an overview over the factors important in the recruitment of GAMs.

1.2.3 Activation of GAMs

Microglia accumulated within the GBM iTME, typically undergo a morphological transformation from a ramified, resting cell, to a more activated, amoeboid morphology. However, their functional phenotype remains anti-inflammatory and does not reflect the one described in inflammation [12]. For macrophages, different types of activation have been defined, following *in vitro* stimulation. The pro-inflammatory M1 phenotype is typically acquired after stimulation with Interferon-γ (IFN-γ), alone or in concert with microbial products [e.g. lipopolysaccharide (LPS)]. Whereas anti-inflammatory molecules, such as IL-4, IL-10 and IL-13, are inhibitors of macrophage activation and induce the alternative M2 phenotype [27, 28]. These polarized macrophage subpopulations differ in terms of receptor expression, effector function and cytokine and chemokine production [28]. Given that these definitions of the different activation states are based on *in vitro* conditions, and the M1 and M2 phenotype represent two extremes of a more complex continuum of functional states, they are only to some extent translatable to the *in vivo* setting.

Nevertheless, several studies have analyzed the expression of M1 and M2 markers among GBM associated GAMs and concluded that, similar to solid tumors of other organs, glioma associated macrophages and microglia, exhibit predominantly an alternative M2 polarization with an anti-inflammatory phenotype and reduced phagocytic activity [11, 29-32]. It is believed that glioma-derived molecules such as M-CSF (Figure 1) induce the shift of microglia and macrophages toward the M2 phenotype and thus create a favorable microenvironment for GBM growth [31]. This “educating” effect of GBM on GAMs will be discussed in more detail in the next chapter.

In addition, GAM expression of CD163 and CD204, both of which are considered M2 macrophage markers [33], was significantly higher in grade IV GBM when compared to low grade glioma, indicating that polarization of GBM associated microglia and macrophages toward the M2 phenotype correlates with a more malignant histological grade [34]. Accordingly, others identified the expression of CD74 by human GAMs, a M1 polarization marker, to be positively correlated with increased patient survival [35].

Together with the altered polarization and transcriptional re-programming, effector function of GAMs in the iTME changes as well. As it was shown that supernatants from glioma stem cells inhibited the phagocytosis activity of GAMs and induce the secretion of anti-inflammatory cytokines like interleukin-10 and TGF-β [36].

1.2.4 GAM regulation of GBM growth and invasion

The abundance of microglia and macrophages in the iTME of gliomas has raised the question as to whether these mononuclear cells only act as bystanders or are pathogenetically associated with the disease. Early co-culture studies noted that, the motility of murine glioma cells was increased in the presence of microglial cells, and this glioma promoting effect could be further aggregated by microglia activating substances like GM-CSF [37]. As described above, GM-CSF (CSF-2) and its close relative M-CSF (CSF-1) are constitutively released by the tumor cells and act as chemoattractant for microglia and, at the same time, converts macrophages and microglia into a pro-tumorigenic phenotype [24]. Interfering with this CSF-1 signaling by the blockade of the CSF-1 receptor led to a decreased expression of M2 markers in GAMs, which is consistent with impaired tumor-promoting functions, ultimately resulting in increased survival and regression of established tumors in a mouse GBM model [24].

To shortly summarize the above, so once microglia and macrophages are recruited to the tumor site and re-educated to a pro-tumorigenic phenotype by the tumor, this glioma promoting effect of GAMs is likewise mediated by the release of soluble factors. These factors are synthesized and released by microglia and macrophages and act on glioma growth and invasion, as similar effects on glioma cells could be shown by using GAM-conditioned medium instead of co-cultures [37]. One of these identified factors is the epidermal growth factor (EGF), which is released by microglia and stimulates GBM cell migration and invasion via the upregulated EGF receptor on glioma cells [25]. Several other factors including anti-inflammatory (TGF-β, IL-10) and pro-inflammatory molecules (TNF-α, IL-1β, IL-6) as well as pro-angiogenic factors like VEGF have been reported to play a role in the crosstalk between pro-tumorigenic rendered GAMs and glioma (Figure 2). Transforming growth factor β (TGF-β) promotes directly the migration of glioma cells via processes that likely involve the upregulation of integrin expression and function [38]. Furthermore, TGF-β induces the release of matrix metalloprotease-2 in an inactive pro-from (pro-MMP2) that gets activated upon cleavage by the membrane bound metalloprotease MT1-MMP (membrane type 1 metalloprotease) [38, 39]. GBM-associated microglia upregulate MT1-MMP and thereby facilitate the invasion of glioma cells into the brain parenchyma by metalloprotease-mediated degradation of the extracellular matrix [39]. Deletion of microglial MT1-MMP impairs glioma invasion in organotypic brain slices and may serve as a more feasible target in GAM modulation, since systemic inhibition of the upstream TGF-β results in acute inflammation and disruption of immune system homeostasis [39, 40].

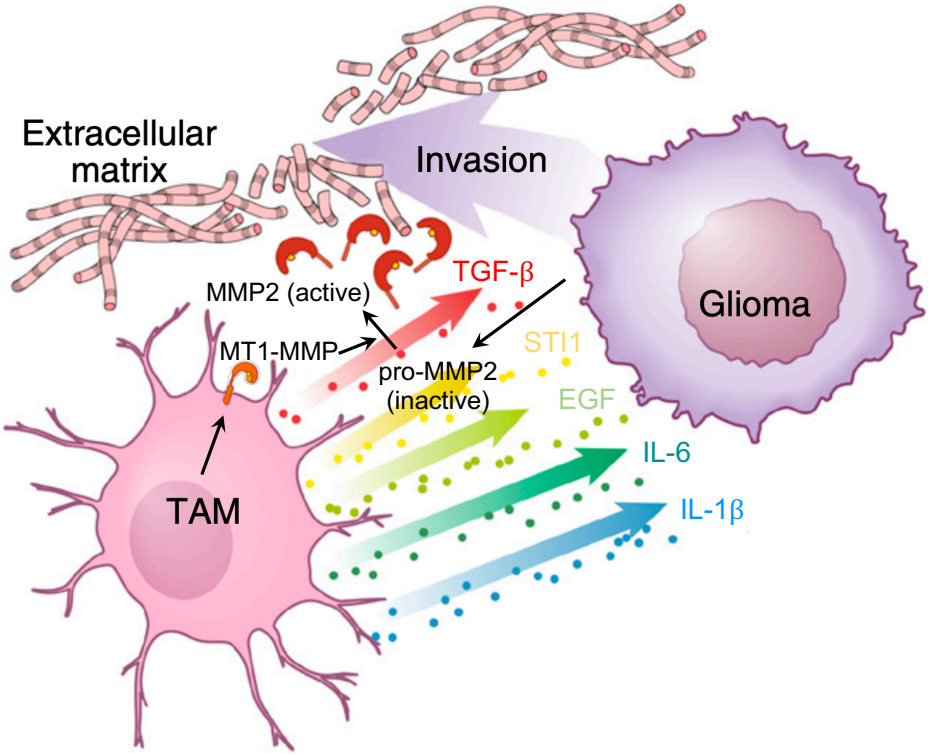

Figure 2 GAM glioma crosstalk.
Pro-tumorigenic rendered microglia release several immunosuppressive and tumor-promoting factors. TGF-β triggers the release of pro-MMP2 from glioma cells, which is then cleaved into active MMP2 by microglia-expressed MT1-MMP. Figure modified from [14].

Along with these soluble factors-mediated glioma-promoting effects, GAMs enable GBM invasion and engraftment more directly as well, by failing to efficiently phagocytose and eliminate the disrupted cancer cells. Their role as phagocytic innate immune cells is perturbed by glioma cells rendering microglia and macrophages to an anti-inflammatory, anti-phagocytic M2 phenotype [36]. Moreover, upregulation of so called “don’t eat me” signals on the surface of glioma cells [41], and masking of antigenic sites by overexpressing sialic acid-rich glycoproteins [42, 43], are both effective strategies to inhibit phagocytosis and to evade innate immune surveillance. These two mechanisms will be discussed in more detail later.

1.2.5 Identification of GAMs

In the healthy brain the majority of the mononuclear population consists of resident microglia. However, the diseased brain presents a different picture. In many neuropathological conditions the integrity of the blood brain barrier is impaired, resulting in an infiltration of monocytic cells from the periphery. Understanding the differences

between these two cell types is critical, as they represent ontogenetically distinct populations with different behavior in various types of CNS injuries [19].

Traditionally, approaches to distinguish these two cell populations in mice have relied on their expression of the hematopoietic marker CD45, with yolk-sac derived microglia being $CD45^{low}$ and infiltrating macrophages of hematopoietic origin $CD45^{high}$ [44]. This paradigm was recently challenged by a study using irradiated chimeras with head protection which impedes the massive unspecific influx of monocytes due to a disrupted blood-brain barrier [45]. The authors could thereby show, that microglia are able to upregulate CD45 and represent an inherent part of the $CD45^{high}$ population in the tumor context [45].

As described above, in the healthy brain, the fractalkine receptor, CX3CR1, is mostly expressed by microglia and the generation of knock-in *Cx3cr1*^{GFP} and *Cx3cr1*^{CreERT} mice advanced the specificity of microglia research significantly [46-48]. However, infiltrating monocytes, differentiating into macrophages express CX3CR1 as well, implying that CX3CR1 does not represent a microglia-specific marker, especially in the context of glioma [22]. Of note, new emerging insights identified perivascular, meningeal and choroid plexus macrophages as non-parenchymal brain macrophages that mediate immune responses at brain boundaries and like microglia, they express CX3CR1 in the healthy brain as well [49]. Therefore, better targets are needed to accurately distinguish resident microglia from infiltrating inflammatory monocytes and residing non-parenchymal brain macrophages to better understand their contribution in glioma formation, maintenance and progression.

In a traumatic brain injury model, *in vivo* time-lapse two-photon imaging of microglia revealed their rapid and targeted migration and process extension to the site of injury, establishing a barrier between the healthy and injured tissue. This rapid chemotactic response is mediated by the release of nucleotides following CNS injuries [50]. Microglia express several purinergic receptors, including G protein-coupled $P2Y_{12}$ receptor (P2RY12) which was implied to be a primary site at which nucleotides act to induce microglial chemotaxis. P2RY12 is also expressed on platelets and there required for normal platelet aggregation and blood coagulation [51]. In the brain parenchyma its expression is limited to microglia and has established itself as very useful marker to specifically identify this cell population [52].

Recent advances in RNA sequencing and other cell profiling technologies have enabled the discovery of cell-type-specific signature genes. Among these, transmembrane protein 119 (TMEM119) of unknown function is exclusively expressed in microglia in the brains of mice and humans [53]. Hence, TMEM119-specific antibodies are widely used in immunohistochemical and flow cytometric applications and very recently knock-in *Tmem119*^{EGFP} reporter mice as well as *Tmem119*^{CreERT2} mice for microglia specific inducible knock-down experiments were introduced [54].

Gene expression profiling not only identified microglia specific surface proteins but also microglial signature genes like *Sall1*, which encodes a transcriptional regulator [55]. Accordingly, the introduction of *Sall1*^{GFP} [56] and *Sall1*^{CreERT2} [57] knock-in mouse lines represent an additional model for microglia specific tracking and genetic modulation *in vivo*.

The ongoing large scale transcriptional profiling of microglial cells will further identify novel cell lineage specific genes like *Hexb*, which is highly expressed in microglia and encodes a subunit of the lysosomal enzyme β-hexosaminidase, that catalyzes the degradation of gangliosides [58]. These novel instruments for cell-specific tracking and genetic modulation will advance the specificity and sophistication with which to study microglial function, in the glioma setting, as well as to further decipher the distinct roles of the different mononuclear populations in the glioma TME.

1.2.6 GAM modulation in glioma therapy

As microglial cells are attracted toward glioma in large numbers—glioma tissue consists of as much as 30% microglial cells—and as outlined above, microglia density in gliomas positively correlates with malignancy, invasiveness, and tumor grading, therefore these tumor-associated microglia and macrophages represent an interesting target for modulation and anti-tumor innate immunotherapy.

Most of the strategies used aim at impairing GAM recruitment to the tumor site and thereby prevent their glioma promoting effects. Interesting targets for attenuating this tumor infiltration of GAMs include receptor blockade of the recruiting cytokine CSF-1 [24], disrupting periostin which is secreted by GBM stem cells and recruits GAMs through integrin $\alpha_v\beta_3$ signaling [59] and inhibition of the CXCR4 chemotactic pathway. The latter was mainly implicated in macrophage mobilization through increased stromal cell-derived factor-1 (SDF-1) expression after radiation therapy [60]. As

combination of radiotherapy and a small molecule inhibitor of SDF-1/CXCR4 interactions prevented GAM infiltration and tumor recurrence [61].

A different approach in modulating glioma associated microglia aims at reversing their tumor-promoting effects and re-educate them into an anti-tumor phenotype, rather than just preventing their infiltration. One study could show that by using activated natural killer (NK) cells combined with an antibody directed against the proteoglycan Neuroglial-2 (NG2) on GBM cells, this anti-tumor rendering of GAMs is feasible [62].

In this thesis, reversing of the pro-tumorigenic phenotype of glioma associated microglia, especially regarding their role in the phagocytic innate immune surveillance is studied by targeting the CD47-SIRPα pathway and the sialic acid-Siglec axis. The following two chapters provide the rationale behind choosing these targets and shortly summarize their potential in anti-tumor innate immunotherapy.

1.3 The CD47-SIRPα pathway

CD47 is a widely expressed transmembrane protein with numerous functions, among which the inhibition of phagocytosis is the most noted one [63]. Upon binding and activating its receptor, signal regulatory protein-α (SIRPα), an inhibitory protein expressed on the surface of mononuclear cells, CD47 inhibits the phagocytic activity of macrophages and serves as an anti-phagocytic or “don’t eat me” signal [64]. The signal is transmitted by phospho-activating SIRPα’s immunoreceptor tyrosine-based inhibiting motif (ITIM) present on the cytoplasmic tail of SIRPα. Subsequent binding and activation of SHP-1 and SHP-2 [src homology-2 (SH2)-domain containing protein tyrosine phosphatases] blocks phagocytosis, potentially by preventing the accumulation of myosin-IIA at the phagocytic synapse [65]. CD47 expression is best-characterized in its role in the homeostasis of hematopoietic cells, in particular red blood cells and platelets. CD47 expression is required to protect these cells from rapid elimination by splenic macrophages, thus CD47 was identified as a marker of self [64]. During diseases, inflammation-mediated mobilized hematopoietic stem cells protect themselves from phagocytosis by upregulating CD47 on their surface [66]. This CD47 overexpression is co-opt by tumor cells and represents a common feature of hematologic and solid tumors, allowing them to evade innate immune surveillance [41, 66-68].

Establishing CD47 as a critical regulator of phagocytic innate immune surveillance and elimination.

1.3.1 CD47-SIRPα anti-phagocytic axis in GBM

As CD47 has been identified as primary “don’t eat me” signal and its expression is highly upregulated on the surface of nearly all human solid tumor cells, including GBM [41], disrupting the CD47-SIRPα anti-phagocytic pathway promises to be capable of re-educating GAMs from a tumor-promoting role to an anti-tumor one by inducing GAMs to phagocytose tumor cells. Transcriptional analysis of glioma patients revealed that high CD47 mRNA expression levels were associated with a decreased probability of progression-free and overall survival, suggesting that CD47 expression levels may serve as a clinically relevant prognostic factor in low and high grade gliomas [41].

Willingham et al. first described the re-educating effect of anti-CD47 blockade in models of GBM. Using targeted monoclonal antibodies against CD47 enabled macrophage dependent phagocytosis of patient-derived glioblastoma neurospheres *in vitro*. Furthermore, administration of anti-CD47 antibodies inhibited tumor growth in orthotopic immunodeficient mouse xenotransplantation models established with patient GBM cells and increased the survival of the mice over time [41]. Validating CD47 as a potential target in GBM therapy.

Follow-up studies could show that anti-CD47 treatment re-polarized GAMs *in vivo* to a M1 phenotype and both M1- and M2-polarized macrophages displayed a higher GBM cell phagocytosis rate under anti-CD47 treatment, indicating that M2 GAMs are rendered phagocytic again [69]. Moreover, the therapeutic efficacy of anti-CD47 treatment was also demonstrated *in vitro* and *in vivo* in patient-derived orthotopic xenograft models of five aggressive and etiologically distinct pediatric brain tumors (medulloblastoma, atypical teratoid rhabdoid tumor, primitive neuroectodermal tumor, pediatric glioblastoma, and diffuse intrinsic pontine glioma) [70]. The safety and efficacy of targeting CD47 was further tested and validated in an immunocompetent syngeneic host, using an orthotopic mouse high-grade glioma model [70].

More recently, Gregor Hutter and colleagues could distinguish the different responses of brain resident microglia and infiltrating peripheral macrophages upon anti-CD47 treatment within the microenvironment of GBM. By using a mouse model with genetically color-coded macrophages (*Ccr2*^{RFP}) and microglia (*Cx3cr1*^{GFP}), they

showed that even in mice lacking Ccr2-mediated macrophage recruitment to the brain (*Ccr2*$^{RFP/RFP}$ *Cx3cr1*$^{GFP/+}$), microglia-mediated GBM phagocytosis was sufficient to reduce tumor burden and prolong survival upon anti-CD47 treatment. Identifying microglia as effector cells of GBM cell phagocytosis in response to anti-CD47 blockade [71].

1.4 The sialic acid-Siglec pathway

The observation that essentially all tumor cells are characterized by changes in carbohydrate composition and density was already made several decades ago [72] with its exact function in tumor biology remaining elusive for many years after its initial discovery. Until a growing body of evidence supported crucial roles for glycans at various pathophysiological steps of tumor progression, with glycans regulating tumor proliferation, invasion, metastasis and angiogenesis [73, 74]. The aberrant glycosylation of cancer cells represents therefore a key feature of malignant transformation. Although the process of glycan biosynthesis is not template bound, unlike protein biosynthesis, it is not random either [75]. It is dependent on the coordinated action of processing enzymes, like glycosyltransferases and glycosidases [76], substrate availability, cellular environment and the underlying protein structure [77].

The carbohydrate portion of a glycoconjugate, such as a glycoprotein or glycolipid is often terminated by negatively charged sialic acids. Sialic acids are *N*- or *O*-substituted derivates of neuraminic acid. The predominant sialic acid found in mammalian cells, including humans, bears at its amino site an acetyl group and is therefore termed N-acetyl-neuraminic acid (Neu5Ac). The addition of sialic acids is mediated by sialyltransferases, a family of glycosyltransferases [78]. Hypersialylation, meaning the upregulation of sialic acid containing glycans (sialoglycan) on the cell surface through altered sialyltransferase expression and the increased introduction of the non-human sialic acids like *N*-glycolyl-neuraminic acid (Neu5Gc) originating from food sources (xenosialylation - since humans lack the enzyme which hydroxylates Neu5Ac into Neu5Gc [79]) are, together with the altered glycosylation itself, key changes of malignant tissue and important for cancer progression [80].

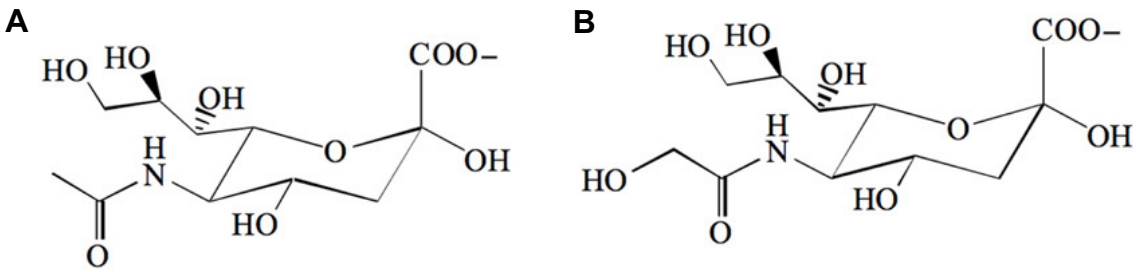

Figure 3 The two major sialic acids found on cancer cells.
(A) N-acetyl-neuraminic acid (Neu5Ac) and, (B) N-glycolyl-neuraminic acid (Neu5Gc) [81].

The importance of hypersialylation in cancer was observed early on, when tumor cells pretreated with neuraminidase (sialidase), which enzymatically removes sialic acids from glycans, were implanted in dogs and growth inhibition of tumors was observed [82]. Functionally, cancer-associated hypersialylation impacts directly tumor cell interaction with the microenvironment and promotes tumorigenesis: Increased expression of sialoglycans promotes cell detachment from the tumor mass through electrostatic repulsion of negative charges, which physically inhibits and disrupts cell–cell adhesion [73, 74]. Moreover, sialic acid residues on tumor cell glycoproteins stimulate migration and invasion by enhancing cell adhesion to collagen I, facilitate tumor cell extravasation through interaction with E-selectin on activated endothelial cells and disable apoptosis induction in cancer cells by hypersialylation of the Fas receptor [42, 83]. Along with these direct pro-tumorigenic effects, sialic acids can modulate immune cells in the tumor microenvironment through engagement of sialic acid-binding immunoglobulin-like lectins (Siglecs). Siglecs are expressed on most cells of the immune system and can transmit immunosuppressive signals upon binding to sialic acids. Hypersialylation of cancer cells can thus contribute to tumor immune evasion [42].

Siglecs belong to the immunoglobulin (Ig) superfamily and are cell-surface transmembrane receptors with immune-modulatory function, that are comprised of an extracellular portion characterized by a V-set immunoglobulin-like domain, containing the carbohydrate recognition domain (CRD), and one or more C2-set immunoglobulin-like domains. The majority of Siglecs are inhibitory immune receptors that possess – similar to the inhibitory SIRPα receptor – ITIMs in their intracellular domain that signal negatively via the recruitment of tyrosine phosphatases SHP1 and SHP2 [84].

To date, 14 Siglecs have been identified in humans and nine in mice. The family can further be subdivided into two groups: those that are conserved across mammalian species, which include Siglec-1 (sialoadhesin), Siglec-2 (CD22), Siglec-4 (myelin-associated glycoprotein, MAG) and Siglec-15. And a group of CD33-related Siglecs that are variable across mammals. The CD33-related Siglecs are thought to have all derived from one another via gene duplication and include in human Siglec-3 (CD33), Siglec-5, Siglec-6, Siglec-7, Siglec-8, Siglec-9, Siglec-10, Siglec-11, Siglec-14 and Siglec-16 [85, 86].

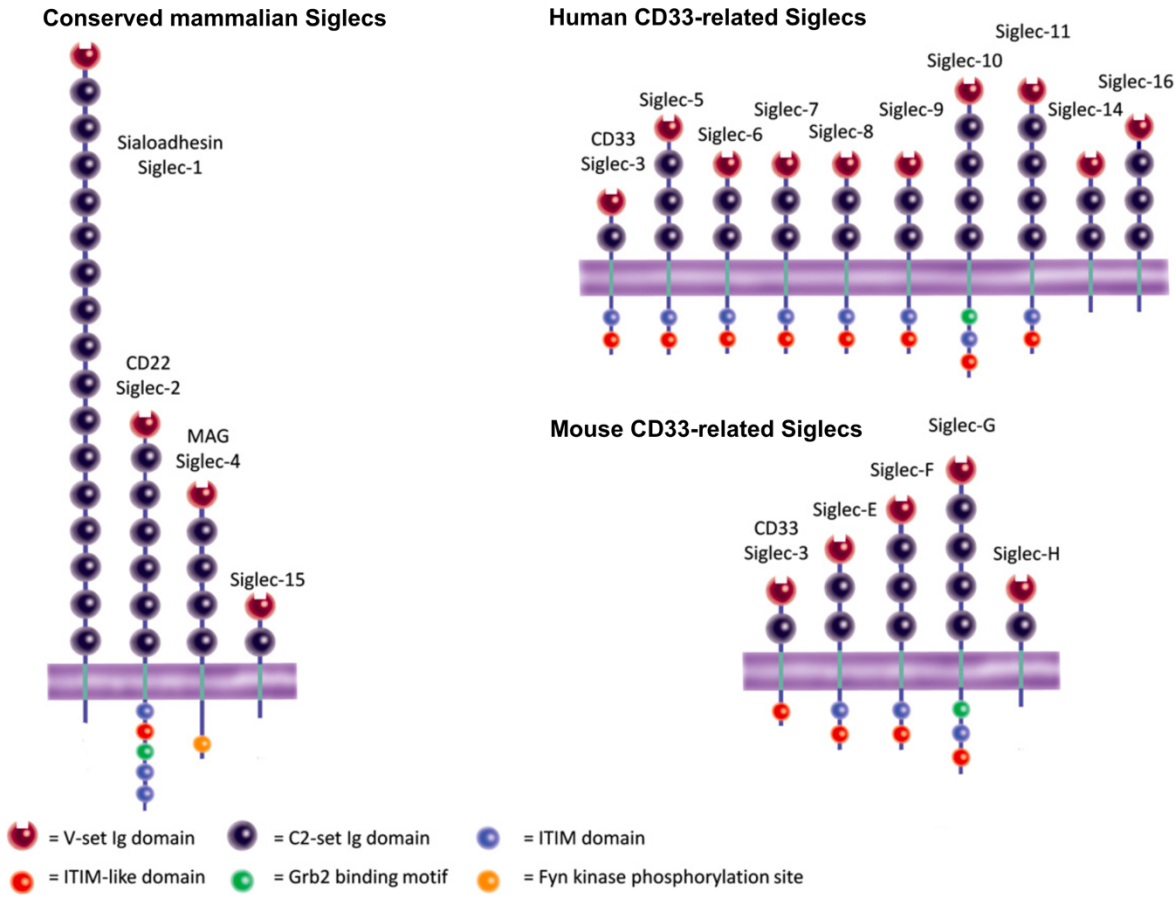

Figure 4 Nomenclature and structure of Siglecs in humans and mice.
Siglecs are single-pass transmembrane proteins that comprise a single sialic acid-binding V-set domain, variable numbers of C2 Ig-like domains, a transmembrane region and a cytosolic tail. The evolutionarily conserved Siglec subgroup is shown on the left; the rapidly evolving CD33-related subgroup is depicted on the right (human CD33-related Siglecs on the top, murine on the bottom). Siglec-12 has lost its lectin activity in humans and its name has therefore been changed to Siglec-XII (not shown). SIGLEC-13 gene is deleted in humans. See key for symbols representing extracellular and intracellular domains. Abbreviations: C, constant; GRB2, growth factor receptor-bound protein 2; Ig, immunoglobulin; ITIM, immunoreceptor tyrosine-based inhibitory motif; MAG, myelin-associated glycoprotein; V, variable. Figure adapted from [87].

The CD33-related Siglecs underwent rapid evolutionary diversification through gene duplications, deletions and exon shuffling as well as single-nucleotide changes resulting in amino-acid substitution within the CRD, which alters sialic acid recognition and ligand specificity, furthering diversification of the CD33-related Siglecs [88]. This rapid evolution led as well to marked inter-species differences, mirrored by the fact that human Siglecs are numbered in the order of discovery, while mouse CD33-related Siglecs were given alphabetical designations [89] (Figure 4). Based on sequence similarity, map position and gene structure, orthologous correspondence may be tentatively assigned amongst some of the CD33-related Siglecs between species. Putative orthologous pairs for human and murine CD33-related Siglecs have been described for: human CD33/Siglec-3 and mouse CD33/Siglec-3; human Siglec-6 and mouse Siglec-F; human Siglec-9 and mouse Siglec-E and human Siglec-10 and mouse Siglec-G. However, the validity of such “orthologous correspondence” assignment may be limited, as different parts of a gene may have different evolutionary history, and only a part of gene X in one species may be orthologous to gene X’ in another species [89].

Functionally, the relatively high density of sialoglycans on mammalian cells serves a similar purpose as described for CD47, and can be considered as self-associated molecular patterns (SAMPs), which limits immune responses against self [90]. In this regard, broadly binding CD33-related Siglecs, like Siglec-9, can be considered as pattern recognition receptors (PRR) for sialoglycan-SAMPs, as Siglec-9 shows a quite broad binding spectrum, while the CRDs of most Siglecs are more specified towards certain ligands [77, 91].

Of note, a few Siglecs – such as Siglec-14, Siglec-15 and Siglec-16 - lack intracellular ITIMs and associate instead with the immunoreceptor tyrosine-based activation motif (ITAM) adaptor DAP12 and are predicted to be activating receptors. Interestingly, these activating CD33-related Siglecs have a paired inhibitory receptor. For example, activating Siglec-14 pairs with inhibitory Siglec-5 and activating Siglec-16 pairs with inhibitory Siglec-11 [85]. The evolution of these activating receptors may have been driven to counterbalance the pathogen exploitation of inhibitory Siglecs, providing the host with additional activatory pathways to combat these pathogens [85, 86].

1.4.1 Tumor immune evasion through Siglecs

The physiological role of Siglecs to counter-regulate overshooting immune reactions and limit tissue damage during inflammation can be exploited by pathogens to evade immune surveillance. Several clinically relevant pathogens are sialylated and bind to Siglecs as a molecular mimicry of the sialoglycan-SAMP structures, including *group B streptococcus* [92], *Escherichia coli* , *Haemophilus influenza* and HIV [93]. These pathogen-host interactions are believed to be one of the major drivers of the high polymorphism found in CD33-related Siglecs including the evolution of activating Siglecs as discussed above.

Analogous to pathogens mimicking self via Siglec engagement, it is believed that the hypersialylation of tumor cells is an attempt to render the tumor microenvironment anti-inflammatory and to evade immune surveillance [42]. In line with this hypothesis, Carolyn Bertozzi and colleagues showed that the increased density of sialylated glycans on cancer cells inhibits human natural killer (NK) cell activation and cytotoxicity through engagement of Siglec-7 [94]. An *in vivo* model of immunodeficient mice with transferred human NK cells and human cancer cell lines underlined the inhibitory effect of tumor associated sialoglycan on NK cells through recruitment of Siglec-7 and Siglec-9 [95].

Siglec functions were described as well for myeloid innate immune cells in the tumor context. Using a genetic model, engagement of murine Siglec-E inhibited tumoricidal neutrophil activity, whereas upon Siglec-E depletion metastasis formation was markedly reduced *in vivo* and tumor killing by neutrophils enhanced [96]. Similarly, the cancer-associated heavily glycosylated protein LGALS3BP was shown to inhibit neutrophil activation in a sialic acid dependent manner through Siglec-9 and Siglec-5 signaling [97]. More recently, Siglec-9 engagement on tumor associated macrophages by the sialylated cancer-specific MUC1 glycoform could potentiate a pro-tumorigenic M2 phenotype *in vitro* [98].

There is experimental evidence that inhibitory Siglecs can influence the adaptive anti-tumor immunity as well. For example, it has been shown that Siglec-G inhibits dendritic cell (DC) cross-presentation by impairing MHC class I–peptide complex formation, which attenuated cytotoxic T lymphocyte (CTL) responses. Accordingly, Siglec-G deficient mice generated more antigen-specific CTLs to inhibit tumor growth [99]. In another approach one study demonstrated that desialylated human DCs loaded with

tumor-antigens showed enhanced ability to induce an anti-tumor T cell activity [100]. Highlighting, the relevance of the inhibitory effect mediated by *cis* binding of Siglec ligands on the immune cell itself [85]. Furthermore, it has been stated that tumor hypersialylation substantially influences tumor growth by facilitating the presence of regulatory T cells (Tregs) [101] and that tumor-infiltrating lymphocytes (TILs) upregulate Siglecs, including Siglec-9, which correlated with reduced survival in cancer patients [102].

The growing body of evidence that cancer cells exploit the sialic acid-Siglec pathway to re-educate the tumor microenvironment and evade anti-tumor immunity together with the highly aberrant glycosylation and sialylation associated with brain malignancies, make the sialic acid-Siglec interactions attractive targets for immunotherapy against GBM [43].

1.4.2 Sialic acid-Siglec pathway in GBM and as potential “don’t eat me” signal

Initially, immunoinhibitory Siglecs in brain pathologies were primarily associated with CD33/Siglec-3 as a genetic risk factor for Alzheimer’s disease (AD) [103-105]. Subsequent functional studies showed that CD33/Siglec-3 inhibits microglial uptake of amyloid beta plaques in diseased brains [106]. More recently, CD22/Siglec-2 was as well identified as a negative regulator of phagocytosis that is upregulated on aged microglia and inhibition of CD22 promoted the clearance of myelin debris, amyloid-β oligomers and α-synuclein fibrils in a *in vivo* AD-model [107]. Other studies identified important roles of Siglecs in neuroinflammatory diseases, where immunoinhibitory Siglecs convey neuroprotective functions by alleviating especially microglial neurotoxicity [108, 109]. This neuroprotective effect of Siglecs in microglia was shown for Siglec-11 and Siglec-E, the mouse orthologue of human Siglec-9. Engagement of these receptors prevented the production of superoxide radicals and inhibited microglial phagocytosis of neural debris [108, 109]. Further implicating the sialoglycan-Siglec axis in impairing the phagocytic function of microglia, though not (yet) in the tumor context.

With the paradigm shift in cancer therapy that came with the discovery of immune checkpoint inhibitors, the sialoglycan-Siglec pathway attracted very recently great attention as a novel target in immunotherapy, not least also in brain malignancies. Especially since phase II and phase III clinical trials of classical immune checkpoint inhibitors (ICI) like PD-1/PD-L1 inhibitors showed no significant improvement in median overall survival of glioblastoma patients [110, 111].

Correlative single-cell transcriptomic analysis including data from The Cancer Genome Atlas (TCGA) showed that most members of the Siglec family are differentially expressed in glioma [112]. Interestingly, the inhibitory Siglecs-5, -7 and -9 showed higher expression levels on immune cells – mainly on macrophages and GAMs - with increasing malignancy [112]. Cell surface staining by flow cytometry and immunohistochemistry confirmed the high expression of Siglec-5, -7 and -9 on glioma-infiltrating myeloid cells and, to a lesser extent, as well on MDSCs (myeloid-derived suppressor cell), which represent a more immature myeloid cell population. Additionally, the authors stained for Siglec ligands by using recombinant human Siglec-Fc chimeras and found that freshly isolated human glioma cells predominantly express sialic acid ligands for Siglec-7 and -9, indicating possible sialic acid-Siglec interactions between glioma cells and myeloid populations in the TME [113].

In a more translational approach, others investigated the role of immunomodulatory Siglecs in the treatment with glucocorticosteroids, including dexamethasone, which is frequently used to control tumor-induced edema in brain tumor patients. They found in response to dexamethasone treatment alterations in cell surface sialylation and Siglec recognition [114]. Specifically, Siglec-E was significantly upregulated on microglia together with the induction of an anti-inflammatory cytokine profile and increased Siglec-E ligand expression on glioma cells [115]. Other immune cells possibly involved in anti-glioma immunity are studied as well. One group could show that GBM-derived extracellular vesicles (EVs) highly express ligands for Siglec-9 and by modifying the EV glycan surface, including desialylation, EV internalization by monocyte-derived DCs was significantly increased. This may represent a way to potentiate pulsing of DCs in anti-cancer vaccination therapy [116].

First experimental evidence that linked Siglecs with whole tumor cell phagocytosis in glioma dates back to 2013, where Siglec-H, which serves as a microglia-specific marker [117, 118], was suggested to be a phagocytic receptor for glioma cells [119]. Until very recently, new insights into the sialic acid-Siglec anti-phagocytic axis have emerged. In particular, Siglec-10 was identified as the receptor of CD24, respectively its particular glycoform, delivering a “don’t eat me” signal. Tumor-expressed CD24 promoted innate immune evasion through its interaction with Siglec-10 expressed on GAMs [120]. Another study focused on Siglec-15 as an immune suppressor and potential target for cancer immunotherapy. Interestingly, Siglec-15 lacks the

intracellular ITIM and, in contrast to the inhibitory Siglec family members, signals via the ITAM-containing adapter protein DAP12 [121]. Using a genetic mouse model and intracranial injection of murine glioma cell line GL261, the authors found significantly slower tumor growth associated with more macrophages and CD8+ T cells in the TME upon genetic ablation of Siglec-15. Together with ex vivo re-stimulation assays, their data support a role for Siglec-15 in macrophage-mediated suppression of tumor immunity [122].

The mounting evidence of Siglec engagement by cancer cells to evade anti-tumor immune response, especially innate immune response, make sialic acid-Siglec interactions very attractive candidates for potentiating anti-tumor immunity in the innate TME of GBM.

2 Aim of the thesis

A growing body of evidence highlights the fundamental role of innate immune cells in orchestrating cancer immunity. This is particularly the case for the innate driven GBM iTME, mainly consisting of microglia (MG) and monocyte-derived cells (MdCs). Given the poor prognosis of GBM patients with a median survival of about 14 months with standard of care and the rather disappointing outcomes of classical immunotherapeutic agents, novel treatment approaches are urgently needed.

Recent work suggests hypersialylation within the TME as a key change in malignant tissues, capable of promoting tumorigenesis by a plethora of mechanisms. Whether targeting the Siglec-sialic acid-axis might be beneficial to overcome tolerogenic programs in the innate iTME of GBM merits in-depth investigation.

In my MD-PhD thesis, I focus on:

- The in-depth characterization of Siglec-E depletion in MG and MdCs in a pre-clinical GBM mouse model
- The region-dependent transcriptional profiles of GBM-associated immune cells from tumor center, periphery and peripheral blood of the same patient using single-cell RNA-sequencing
- Providing an overview of the current literature in the field of GBM innate immunotherapy, focusing on MG-centered approaches

3 Results

3.1 The Siglec-sialic acid-axis is a target for innate immunotherapy of glioblastoma

Philip Schmassmann[1]*, Julien Roux[2,3], Alicia Buck[4], Nazanin Tatari[1], Sabrina Hogan[1], Jinyu Wang[5], Sohyon Lee[6], Berend Snijder[6], Tomás A. Martins[1], Marie-Françoise Ritz[1], Tala Shekarian[1], Deniz Kaymak[1], Marta McDaid[1], Michael Weller[4], Tobias Weiss[4], Heinz Läubli[5,7#] and Gregor Hutter[1,8*#]

[1]Brain Tumor Immunotherapy Lab, Department of Biomedicine, University Hospital and University of Basel, Switzerland.

[2]Bioinformatics Core Facility, Department of Biomedicine, University Hospital and University of Basel, Switzerland.

[3]Swiss Institute of Bioinformatics, Basel, Switzerland.

[4]Department of Neurology, Clinical Neuroscience Center, University Hospital and University of Zurich, Switzerland.

[5]Cancer Immunotherapy Lab, Department of Biomedicine, University Hospital and University of Basel, Switzerland.

[6]Institute of Molecular Systems Biology, ETH Zurich, Switzerland

[7]Division of Oncology, Department of Theragnostics, University Hospital Basel, Switzerland.

[8]Department of Neurosurgery, University Hospital Basel, Switzerland.

[#]These authors contributed equally to this work as co-senior authors.

- submitted -

3.1.1 Abstract

Glioblastoma (GBM) is the most aggressive form of primary brain tumor, for which effective therapies are urgently needed. Cancer cells are capable of evading clearance by phagocytes such as microglia and monocyte-derived cells through engaging tolerogenic programs. Here, we found that high level of Siglec-9 expression correlates with reduced survival in GBM patients. Using conditional knockouts of Siglec-E, the murine functional homologue of Siglec-9, together with single-cell RNA sequencing, we demonstrated significant pro-phagocytosis effects in microglia and monocyte-derived cells in the absence of Siglec-E. Loss of Siglec-E on monocyte-derived cells enhances antigen cross-presentation and production of pro-inflammatory cytokines, resulting in more efficient T cell priming. This bridging of innate and adaptive responses delays tumor growth and results in prolonged survival. Further, we showed synergistic activity of Siglec-E blockade in combinatorial immunotherapies and demonstrate its translational potential against GBM.

3.1.2 Introduction

Glioblastoma (GBM) is a fatal disease without effective long-term treatment options. The current standard of care consists of tumor resection followed by adjuvant chemoradiotherapy resulting in a median overall survival of only 14 months [123]. Cancer immunotherapy using immune checkpoint inhibitors (ICI), has improved the outcomes of different cancer patients [124], but clinical trials of systemic T cell ICI showed only disappointing results in GBM [125-127]. This was attributed in part to the highly immunosuppressive immune tumor microenvironment (iTME) of GBM, which mainly consists of yolk sac-derived microglia (MG) and monocyte-derived cells (MdCs) [128, 129], together termed glioma-associated microglia/macrophages (GAMs). Recent work identified GBM associated MG and MdCs as effector cells of tumor cell phagocytosis in response to blockade of the ‘don’t eat me’-signal CD47 [69-71]. However, variability in the magnitude and durability of this response suggests the presence of additional, yet unknown such signals.

Upregulation of sialic acid-containing glycans on tumor cell surface and in the tumor microenvironment (hypersialylation) is a key change in malignant tissue and capable of impacting tumorigenesis by promoting cell invasion and metastatic potential [43, 74, 80, 83]. By engaging immunomodulatory sialic acid-binding immunoglobulin-like lectins (Siglecs), tumor hypersialylation can trigger tolerogenic programs in

different immune cell types and contributes to the establishment of the immunosuppressive iTME [130]. Recent work has shown that inhibitory CD33-related Siglecs, including human Siglec-7, Siglec-9 and Siglec-10, promote tumor progression in various models of pancreatic, breast and ovarian cancer by inducing a regulatory M2-like phenotype in tumor-associated macrophages (TAMs) [96, 98, 120, 130]. Similarly, increased density of sialylated glycans on cancer cells inhibits human NK cell activation and cytotoxicity [94] and facilitates induction of regulatory T cells (Tregs) through engagement of Siglec-7/-9 [101, 131]. However, little is known on the induction of tolerogenic programs via Siglec receptors on MG and MdCs in the GBM iTME.

Here, we aimed to define the role of inhibitory Siglecs in innate-centered GBM immunotherapy. We found high *SIGLEC9* expression to be associated with worse clinical outcome in glioma patients, and identified Siglec-E, the murine functional homologue of Siglec-9 [96], as an anti-phagocytic signal in a preclinical GBM model. Further we showed synergistic activity of Siglec-E blockade in combinatorial immunotherapies and demonstrated its translational potential against GBM.

3.1.3 Results

3.1.3.1 Expression of inhibitory Siglec receptors is associated with reduced survival in glioma patients.

Stratification of glioma patients (combined GBM and low-grade glioma (LGG), The Cancer Genome Atlas, TCGA [132]) by *SIGLEC9* expression (measured with RNA-sequencing) revealed a marked overall survival advantage for patients with lower *SIGLEC9* expression (Fig. 1a). Focusing on all human Siglec receptors in GBM patients alone revealed a significant correlation between high expression and reduced overall survival only for *SIGLEC9* (Supplementary Data Fig. 1a). In contrast, in LGG, expression of 8 out of 15 Siglec receptors correlated significantly with reduced patient survival (Supplementary Data Fig. 1b) [132]. We investigated *SIGLEC9* expression at the single cell level in our single-cell RNA sequencing (scRNA-seq) dataset consisting of five primary GBM patients [133], where we found *SIGLEC9* to be predominantly expressed by GAMs (Fig. 1b). This was also the case for other Siglec receptors showing a negative correlation with overall survival in GBM patients by trend (*SIGLEC1, CD22, SIGLEC7* and *SIGLEC10*) (Supplementary Data Fig. 1a, c). Beside GAMs, we observed expression of *CD22* and *SIGLEC10* in B cells, and of *SIGLEC7* in NK cells,

as previously reported by others (Supplementary Data Fig. 1c) [94, 134, 135]. Expression of UDP-GlcNAc 2-epimerase/ManNAc kinase (*GNE*), a rate-limiting enzyme in the sialic acid biosynthesis pathway [136], was mainly expressed by GBM cells (Fig. 1b); suggesting that there could be interactions between Siglec-9 in GAMs and sialic acid in GBM cells. Flow cytometry (FC) analysis of primary human GBM- and glioma-associated mouse MG revealed high expression of Siglec-9 and Siglec-E protein, respectively (Fig. 1c, d, Supplementary Data Fig. 1d, e). A significant upregulation of Siglec-E was observed on mouse MG in the orthotopic tumor context (Fig. 1d). Staining of primary human GBM cells with recombinant Siglec-9 Fc chimeras to determine their sialic acid composition revealed a highly sialylated cell surface (Fig. 1e), which was at similar levels to the mouse malignant astrocytoma cell line CT-2A [137], but not GL261 or the retrovirally induced primary mouse glioma cell line PDGF^{+}*Trp53*$^{-}$ [138] (Fig. 1f).

3.1.3.2 Inhibitory Siglec receptors on microglia reduce tumor cell phagocytosis.

To investigate the role of Siglec-sialic acid signaling in regulating the MG-mediated anti-tumor immune response, we employed an orthotopic GBM mouse model with MG specific spatio-temporal deletion of *Siglece* by crossing *Siglece*$^{fl/fl}$ mice [139] with *Sall1*^{CreERT2} mice [57] (*Siglece*$^{fl/fl}$ x *Sall1*^{CreERT2}). *Sall1*^{CreERT2} mice harbor a tamoxifen-inducible *Cre* activity under transcriptional control of the *Sall1* promotor. *Sall1* represents a MG signature gene, not expressed by peripheral MdCs [55]. We induced *Siglece* deletion by intraperitoneal (i.p.) tamoxifen injections beginning 7 days post inoculation of Luc2-tdTomato labelled tumor cells and after confirmation of tumor engraftment by bioluminescence imaging (BLI) (Fig. 1g). We did not observe survival differences in CT-2A or GL261 tumor bearing mice (Fig. 1h), despite efficient deletion of Siglec-E in MG (Fig. 1i, j, Supplementary Data Fig. 1f). Nevertheless, FC analysis of the iTME unveiled high MG proliferation upon Siglec-E knockout (Fig. 1k), accompanied by an enhanced MG GBM-cell uptake measured as the percentage of tdTomato^{+} MG (Fig. 1l-n). The Siglec-E deletion-mediated pro-phagocytic effect in MG was more prominent in CT-2A tumor bearing animals than in GL261-grafted mice (Fig. 1m, n), probably due to the higher Siglec-E ligand expression on CT-2A than in GL261 cells (Fig. 1f). Intracellular uptake of tumor-derived tdTomato fluorescence by MG was microscopically confirmed using imaging flow cytometry (Fig. 1o, Supplementary Data Fig. 1g). Together, these results indicated that inhibitory Siglec-E receptor plays a role in regulating MG-mediated tumor cell phagocytosis. However, perturbing Siglec-E

signaling in MG was not sufficient to improve survival, leading us to comprehensively investigate differences between iTME in *Siglece*$^{fl/fl}$ and *Siglece*$^{fl/fl}$ x *Sall1*^{CreERT2}.

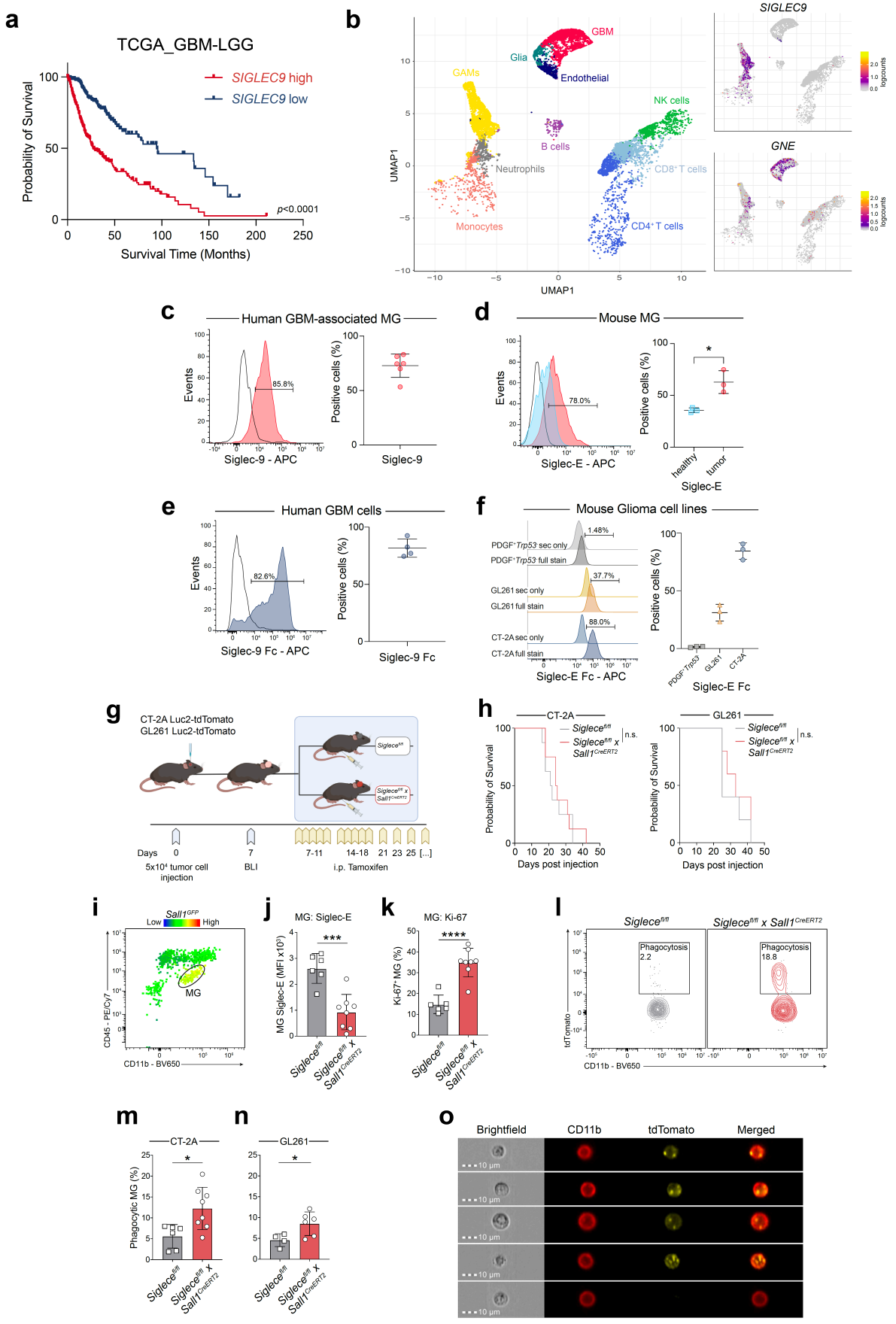

Fig. 1 High *SIGLEC9* expression is associated with reduced survival in glioma patients, and its mouse homologue Siglec-E inhibits MG tumor cell phagocytosis.
a, Kaplan-Meier survival curve of glioma patients (combined GBM and low-grade glioma (LGG)), based on their *SIGLEC9* expression level using the RNA-seq dataset from The Cancer Genome Atlas (TCGA) [132]. The median mRNA expression value was selected as cutoff for high and low expression groups. **b**, Uniform Manifold Approximation and Projection (UMAP) plot showing scRNA-seq cell type annotation in five primary human glioblastoma [133] (left) and UMAP showing expression of *SIGLEC9* and *GNE* in the respective clusters (right). Expression is shown as normalized log_2 counts. **c, d** Representative histograms and quantification of FC analysis of Siglec-9 expression by human GBM-associated MG (n = 6 donors) (**c**) and Siglec-E expression by mouse MG from healthy and tumor-bearing mice (n = 3 mice per group) (**d**) **e**, **f**, Representative histograms and quantification of FC analysis of Siglec-9 ligand expression by human $CD45^{neg}$ GBM cells (n = 4 donors) (**e**) and Siglec-E ligand expression by mouse glioma cell lines derived from $PDGF^{+}$ $Trp53^{-}$ murine gliomas (grey), or cultured GL261 (yellow) and CT-2A (blue) cell lines (n = 3 independent experimental replicates) (**f**). **g**, Schematic of experimental design **h**, Survival CT-2A (left) and GL261 (right) tumor-bearing animals after MG-conditional Siglec-E deletion (n = 5-8 mice per group). **i**, Gating strategy to identify $CD11b^{+}CD45^{low}$ glioma-associated MG in mouse brain tumor single cell suspensions. Gating strategy was confirmed in *Sall1^{GFP} reporter* mice. **j-n**, FC analysis of Siglec-E (**j**) and Ki-67 (**k**) expression in MG. Representative contour plots showing MG CT-2A tumor cell phagocytosis (**l**) and quantification of FC-based MG CT-2A (**m**) and GL261 (**n**) tumor cell phagocytosis measured as percentage of $tdTomato^{+}$ MG (n = 4-8 mice per group). Results shown are from one experiment, representative of two independent experiments **o**, Imaging cytometry showing mouse glioma-associated MG engulfing tdTomato expressing CT-2A tumor cells. Experiment was performed once. Statistics: Data are presented as mean ± SD, log-rank Mantel-Cox test (**a**, **h**), unpaired two-tailed Student's t test (**d**, **j**, **k**, **m**, **n**). $*p \leq 0.05$, $***p \leq 0.001$, $****p \leq 0.0001$.

3.1.3.3 MG activation through Siglec-E deletion induces a counteracting, compensatory MdC response.

Co-expression patterns of CD163 and CD86 in infiltrating MdCs (Fig. 2a) revealed a 'M2-like' protumorigenic polarization in *Siglece$^{fl/fl}$* x *Sall1^{CreERT2}* mice (Fig. 2b, c). Furthermore, we observed a counteracting upregulation of Siglec-E in the total MdC population upon MG-specific Siglec-E deletion (Fig. 2d), particularly prevalent in the more abundant $CD163^{high}CD86^{low}$ 'M2-like' MdCs (Fig. 2b). Of note, this compensatory upregulation on MdCs was only observed for Siglec-E, whereas we did not measure expression changes in other Siglec receptors (Supplementary Data Fig. 2a).

Using scRNA-seq, we profiled the iTME from *Siglece$^{fl/fl}$* and *Siglece$^{fl/fl}$* x *Sall1^{CreERT2}* CT-2A tumor-bearing mice (Fig. 2e), identifying 23 distinct cell clusters, including seven GAM clusters, ten lymphoid clusters, one NK cell cluster, three dendritic cell (DC) and one B cell cluster (Fig. 2f, Supplementary Data Fig. 2b-d). Focusing on GAM clusters (Fig. 2g), two MG clusters were identified (MG_1 and MG_2). A differential

expression analysis between cells from *Siglece*$^{fl/fl}$ and *Siglece*$^{fl/fl}$ x *Sall1*^{CreERT2} CT-2A tumor-bearing mice for these MG clusters revealed a partial reversal of a disease-associated MG (DAM)-phenotype upon Siglec-E deletion (Supplementary Data Fig. 2e). DAMs were initially described in a genetic mouse model of Alzheimer's disease [140], but have been reported in other models of neurodegeneration and neuroinflammation [141, 142], where excessive activation of MG proinflammatory functions may be detrimental and accelerate the disease [143]. Upon Siglec-E deletion, we observed downregulation of DAM-signature genes [143], including tetraspanins (*Cd9*), chemokines (*Cxcl13*), molecules involved in Trem2-signaling (*Lgals3*) and tissue remodeling (*Spp1, Gpnmb*). In contrast, genes involved in phagocytosis (*Axl*, *Arg1*) and cellular activation (*Trpm2*) were upregulated (Supplementary Data Fig. 2e). Along the same line, gene set enrichment analysis (GSEA) on the differentially expressed genes using the MSigDB Hallmark collection [144] identified TNF-α signaling via NF-κB to be upregulated in Siglec-E depleted MG (Supplementary Data Fig. 2f).

Focusing on MdCs, we identified two phenotypically distinct monocyte-derived cell (MdC) clusters (MdC_Ly6c^{low}CD11c^{+} and MdC_Ly6c^{low}CD11c^{-}), probably representing intermediate stages of differentiation towards monocyte-derived DCs and monocyte-derived macrophages, respectively [145, 146]. Among MdCs clusters, differential expression analysis attributed the highest number of differentially expressed genes (DEGs) to the MdC_Ly6c^{low}CD11c^{+} cluster (57 DEGs in MdC_Ly6c^{low}CD11c^{+}; 12 DEGs in Monocytes, 10 DEGs in MdC_Ly6c^{low}CD11c^{-}, 12 DEGs in TAMs and 10 DEGs in MdC_Proliferating, at a 5% FDR). GSEA on the differentially expressed genes ascribed a highly immunosuppressive phenotype to these MdC_Ly6c^{low}CD11c^{+} cells upon MG-specific Siglec-E deletion, with downregulation of genes modulating type I and type II interferon responses and TNF-α signaling (Fig. 2h).

In addition, differential abundance analysis revealed significant increases in CD8^{+} T cell clusters 9 and 11 (CD8^{+} T cells_Effector/pre-exhausted and CD8^{+} T cells_Exhausted) in *Siglece*$^{fl/fl}$ x *Sall1*^{CreERT2} mice (Supplementary Data Fig. 2g). This corroborates the hypothesis that the infiltrating MdCs render the iTME pro-tumorigenic. Although we focused our analysis on immune cells, we still captured transcripts originating from CD45^{neg} cells (Fig. 2i), which acquired a progressive phenotype with upregulation of genes involved in epithelial-mesenchymal transition (EMT), KRAS signaling and increased TGFβ signaling after MG-specific Siglec-E deletion (Fig. 2j), which might

facilitate the immunosuppressive shift of the MdC subcluster. Together, these data identified a population of early phase MdCs as a main driver of the counteracting immunosuppressive response upon Siglec-E deletion induced MG activation.

To test our hypothesis of early phase MdCs as main counteracting force to the anti-tumor MG response, we combined MG-specific Siglec-E deletion with C-C chemokine ligand 2 (Ccl2) neutralization (Fig. 2k). This inhibits recruitment of Ccr2-expressing inflammatory monocytes (Supplementary Data Fig. 2c) to the tumor by retaining them in the bone marrow [147]. Indeed, anti-Ccl2 treatment led to less excessive infiltration of MdCs to the tumor site and converted their ‘M2-like’ polarization state upon concomitant MG-specific Siglec-E deletion. However, both phenotypes ameliorated only to control level (Fig. 2l, m), indicating that recruitment of MdCs to the GBM iTME is a highly redundant mechanism which cannot be perturbed by antagonizing the action of a single tumor-attracting chemokine. Accordingly, the combination of MG-specific Siglec E deletion and anti-Ccl2 treatment did not improve survival (Fig. 2n). These results showcase that MG-specific Siglec-E deletion promotes tumor cell phagocytosis, which is subsequently counteracted by infiltrating MdCs that acquire an immunosuppressive phenotype in the perturbed iTME.

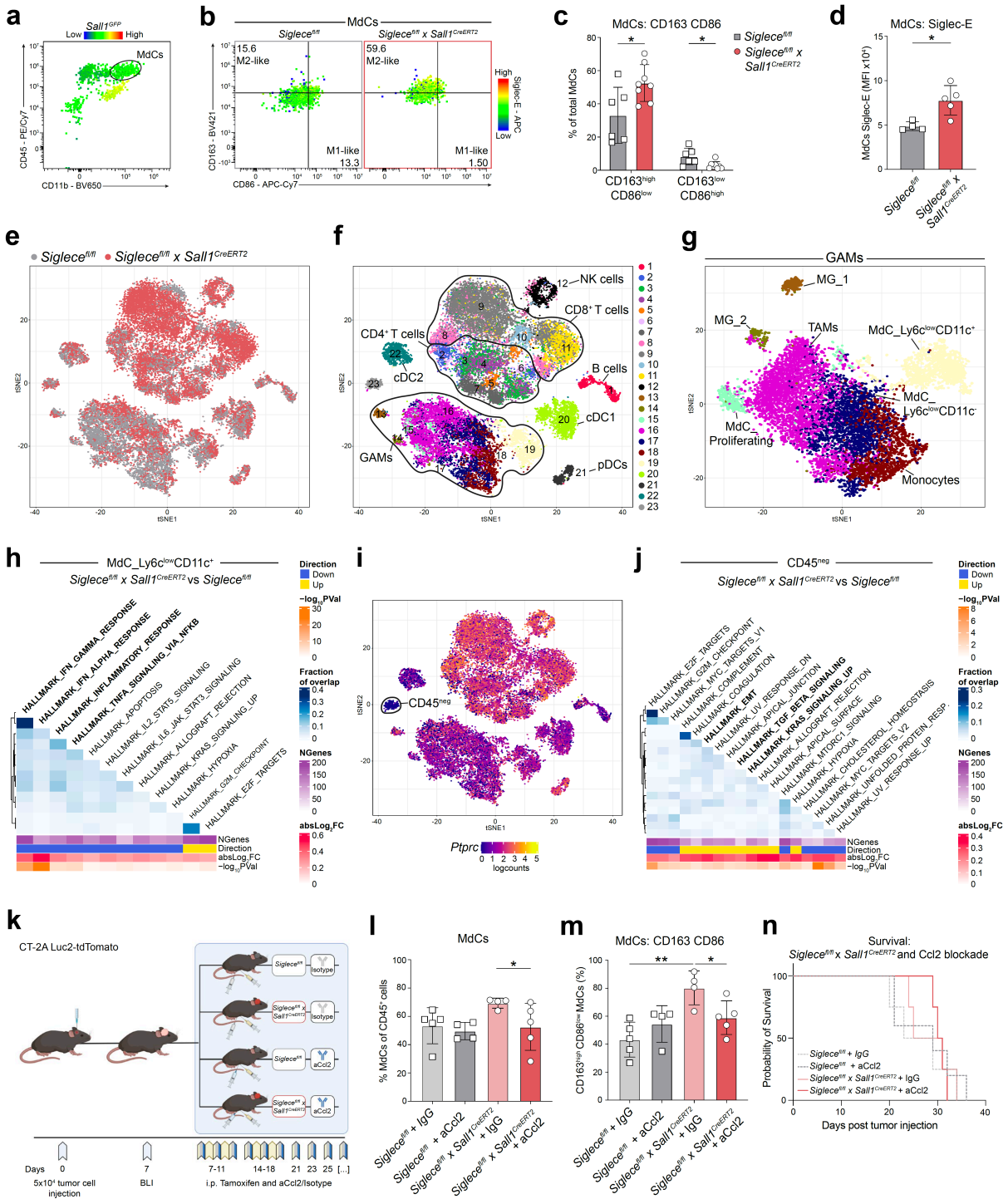

Fig. 2 MG activation via MG-specific Siglec-E deletion induces counteracting MdC responses.

a-d, FC analysis of CD86 and CD163 expression on tumor infiltrating MdCs, identified as CD11b^{+}CD45^{high} events. Gating strategy was confirmed in *Sall1*^{GFP} reporter mice (**a**), shown as representative dot plots, overlayed with Siglec-E expression (**b**) and quantification of CD163^{high}CD86^{low}, CD163^{low}CD86^{high} co-expression (n = 6-9 mice per group) (**c**) and Siglec-E expression of MdCs (n = 4-5 mice per group) (**d**). Results shown are from one experiment, representative of two independent experiments **e**, t-distributed stochastic neighbor embedding (tSNE) plot from scRNA-seq analysis showing the distribution of sorted immune cells from *Siglece*$^{fl/fl}$ (grey) and *Siglece*$^{fl/fl}$ x *Sall1*^{CreERT2} (red) tumors. **f**, tSNE plot showing the annotated

cell populations. **g**, tSNE plot of scRNA-seq analysis showing the subset of GAMs and their annotation. **h**, Heatmap representation of Gene Set Enrichment Analysis (GSEA) results between MdC_Ly6c^{low}CD11c^{+} cells from *Siglece*$^{fl/fl}$ x *Sall1*^{CreERT2} and *Siglece*$^{fl/fl}$ tumors using the MSigDB Hallmark collection. The colors on the heatmap represent the fraction of overlap (Jaccard coefficient) between genes annotated to the significant gene sets. NGenes represents the size of the gene sets, and absLog$_2$FC represents the average absolute log$_2$ fold-change of genes in the gene sets. **i**, tSNE plot showing *Ptprc* (Cd45) expression across cells. Expression is shown as normalized log$_2$ counts. **j**, Heatmap representation of GSEA results between CD45^{neg} cells from *Siglece*$^{fl/fl}$ x *Sall1*^{CreERT2} and *Siglece*$^{fl/fl}$ tumors similar to panel (**h**). **k**, Schematic of experimental design. **l-n**, FC analysis of tumor infiltrating MdCs from *Siglece*$^{fl/fl}$ and *Siglece*$^{fl/fl}$ x *Sall1*^{CreERT2} CT-2A tumor-bearing mice treated with anti-Ccl2 or isotype control. Percentage of MdCs (**l**), percentage of CD163^{high}CD86^{low} co-expressing MdCs (**m**) and survival (**n**) in treatment groups (n = 4-5 mice per group). Experiment was performed once. Statistics: Data are presented as mean ± SD, multiple unpaired Student's t test with Holm-Sidak's corrected multiple comparison test (**c**), unpaired two-tailed Student's t test (**d**), one-way ANOVA with Sidak's corrected multiple comparison test (**l**, **m**). For statistical analysis of scRNA-seq data, please refer to Methods section. *$p \leq 0.05$, **$p \leq 0.01$.

3.1.3.4 Siglec-E deficiency in whole GAM population improves innate anti-tumor immunity

To test the role of inhibitory Siglec receptors on all GAMs, we used *Cx3cr1*^{CreERT2} mice [148], which harbor tamoxifen-inducible *Cre* activity under transcriptional control of the C-X3-C motif chemokine receptor 1 (*Cx3cr1*) promoter. This allowed us to target both GAM populations in the GBM iTME (MG, as well as *Cx3cr1*-expressing MdCs) (Fig. 3a). CT-2A engrafted mice in the *Siglece*$^{fl/fl}$ x *Cx3cr1*^{CreERT2} group showed a delayed tumor growth measured by in vivo BLI (Fig. 3b, c, Supplementary Data Fig. 3a) resulting in prolonged survival compared to *Siglece*$^{fl/fl}$ control mice (Fig. 3d). FC based immune profiling revealed increased MG- and MdC-mediated tumor cell phagocytosis by dual MG/MdC-specific Siglec-E deletion (Fig. 3e, f), accompanied by increased production of effector cytokine TNF-α (Fig. 3f). Additionally, MG displayed accentuated antigen presentation capacity with increased surface MHC-II and costimulatory CD86 expression upon *Cx3cr1*-specific Siglec-E deletion. The MdC compartment showed CD86 increase only by trend, and no difference in MHC-II expression (Fig. 3f). The proportion of intratumoral MdCs was comparable between cohorts at endpoint, indicating that recruitment of these cells to the tumor site remained intact in *Cx3cr1*-specific Siglec-E deleted mice (Supplementary Data Fig. 3b). In fact, MdCs were the dominant CD45^{+} cell population at endpoint (Supplementary Data Fig. 3b), highlighting the potent myeloid influx during CT-2A tumor progression.

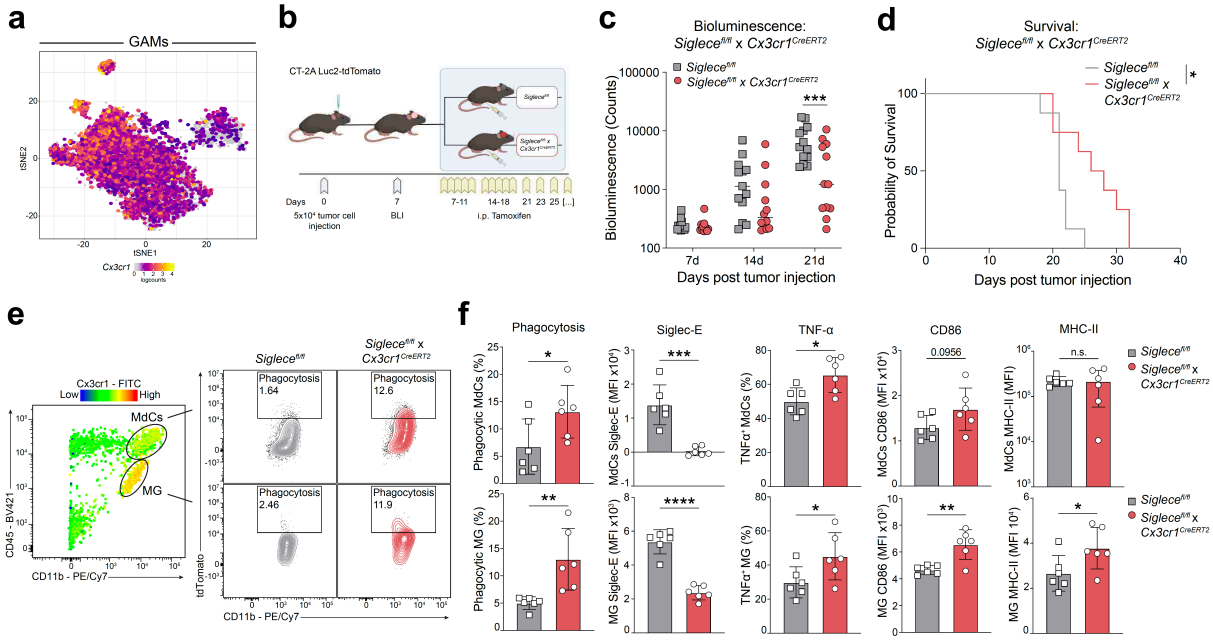

Fig. 3 GAM-specific Siglec-E deletion boosts innate anti-tumor immunity.
a, tSNE plot of scRNA-seq analysis showing *Cx3cr1* expression in the GAM clusters subset. Expression is shown as normalized $\log_2$ counts. **b**, Schematic of experimental design. **c**, **d**, Surrogate tumor growth assessed by BLI (n = 12-13 mice per group) (**c**) and survival (n = 8 mice per group) (**d**). Results were pooled from two independent experiments. **e**, **f**, FC analysis of MdCs (top row) and MG (bottom row) from *Siglece*$^{fl/fl}$ and *Siglece*$^{fl/fl}$ x *Cx3cr1*^{CreERT2} CT-2A tumor bearing mice. Representative contour plots showing tumor cell phagocytosis assessed by td Tomato$^+$ MdCs and MG (**e**) and bar graphs showing quantified phagocytosis as well as expression of Siglec-E, TNF-α, CD86 and MHC-II within MdCs (top row) and MG (bottom row) upon GAM-specific Siglec-E deletion and respective Cre-negative littermate controls (**f**) (n = 6 mice per group). Results shown are from one experiment, representative of two independent experiments. Statistics: Data are presented as median (**c**) and mean ± SD (**f**), two-way ANOVA with Sidak's corrected multiple comparison test (**c**), log-rank Mantel-Cox test (**d**), unpaired two-tailed Student's t test (**f**). *$p \leq 0.05$, **$p \leq 0.01$, ***$p \leq 0.001$, ****$p \leq 0.0001$.

3.1.3.5 Siglec-E deficient MdCs show increased antigen cross-presentation and T cell cross-priming capacity

Within tumor-infiltrating lymphocytes, we observed mainly a CD8$^+$ T cell driven response upon GAM-specific Siglec-E deletion with increased activation signature (CD69$^+$Ki-67$^+$ co-expression) and effector cytokine interferon-γ (IFN-γ) production (Fig. 4a, b). Together with the absent MHC-II response in MdCs after increased tumor cell phagocytosis, we hypothesized that loss of Siglec-E on MdCs could enhance antigen cross-presentation and cross-priming of CD8$^+$ T cells. Therefore, we pulsed the CD11b$^+$ GAM fraction on day 15 post tumor-inoculation with ovalbumin protein (Fig. 4c) and evaluated the presence of MHC-I bound ovalbumin-derived peptide SIINFEKL.

Indeed, we noted a significant increase in antigen cross-presentation by MdCs, but not MG, upon Siglec-E deletion (Fig. 4d). Co-culture of ovalbumin-pulsed CD11b$^+$ GAMs with naive CD8$^+$ T cells from OT-I transgenic mice expressing ovalbumin-specific T cell receptors, resulted in increased OT-1 T cell activation in an antigen-specific manner by GAMs from *Siglece*$^{fl/fl}$ x *Cx3cr1*^{CreERT2} mice compared to *Siglece*$^{fl/fl}$ control (Fig. 4e-g). In vivo depletion of CD8$^+$ T cells using an anti-CD8 antibody diminished the anti-tumor effect of GAM Siglec-E deletion (Fig. 4h, i). Of note, we observed a delayed tumor growth in the CD8$^+$ T cell depleted *Siglece*$^{fl/fl}$ x *Cx3cr1*^{CreERT2} mice compared to *Siglece*$^{fl/fl}$ until day 14 post tumor injection (Fig. 4h), confirming increased level of innate immune tumor control of Siglec-E deletion during early tumor growth. However, Siglec-E deletion-driven tumor cell phagocytosis seems insufficient to induce a lasting anti-tumor immune response which ultimately relies on the generation of adaptive immunity mediated by cytotoxic CD8$^+$ T cells.

Efficient priming of CD8$^+$ T cells and promoting their effector functions requires both antigen cross-presentation and secretion of pro-inflammatory cytokines by MdCs [149]. An unbiased proteomic analysis of tumor-associated MdCs revealed overrepresentation of the IL-17 signaling pathway in Siglec-E deleted compared to wildtype MdCs, using the KEGG Pathway database (Supplementary Data Fig. 4b) [150]. IL-17 is known to trigger activation of the canonical nuclear factor κB (NF-κB) cascade, and subsequently upregulates expression of various pro-inflammatory genes [151]. To test this, we profiled signature genes within the NF-κB signaling pathway in tumor-associated MdCs 15 days post tumor engraftment by quantitative real-time PCR (qPCR). This revealed increased expression of pro-inflammatory genes (*Il1b, Ccl5* and *Tnf, Il1a* by trend) and genes associated with the activator protein 1 transcription-complex (AP-1) (*Fos* and *Jun* by trend) in MdCs from *Siglece*$^{fl/fl}$ x *Cx3cr1*^{CreERT2} mice versus *Siglece*$^{fl/fl}$ animals (Fig. 4j, Supplementary Data Fig. 4c). Increased NF-κB signaling induced also negative feedback circuits by increased expression of *Nfkbia* which is one of the earliest genes induced following NF-κB activation leading to termination of NF-κB signaling [152]. Collectively, these findings indicate that GAM-specific Siglec-E deletion promotes tumor cell phagocytosis by MG and MdCs, enhances intratumoral CD8$^+$ T cell responses by antigen cross-presentation and increases production of pro-inflammatory cytokines by MdCs, potentially mediated by NF-κB signaling axis.

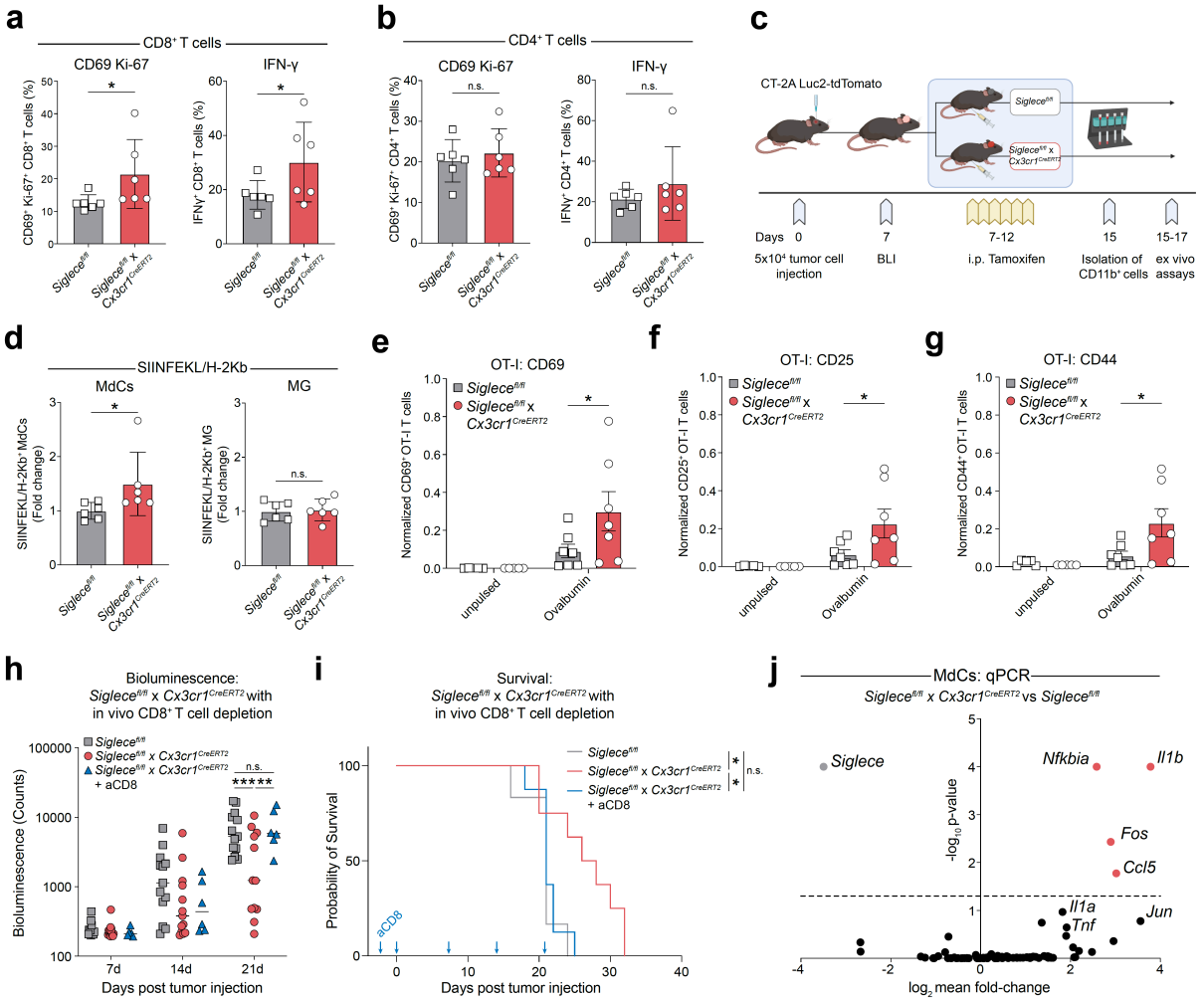

Fig. 4 Intratumoral Siglec-E-deleted MdCs show increased antigen cross-presentation and T cell cross-priming capacity ex vivo.

a, **b**, FC analysis of CD69 and Ki-67 co-expression (left panels) and intracellular IFN-γ production (right panels) in tumor-infiltrating CD8⁺ (**a**) and CD4⁺ T cells (**b**) from *Siglece*$^{fl/fl}$ and *Siglece*$^{fl/fl}$ x *Cx3cr1*^{CreERT2} CT-2A tumor-bearing animals (n = 6 mice per group). Results shown are from one experiment, representative of two independent experiments. **c**, Schematic of experimental design. **d**, FC analysis of SIINFEKL peptide bound to H-2Kb on MdCs (left) and MG (right) (n = 6 mice per group). Results were pooled from two independent experiments. **e**-**g**, FC analysis of CD69 (**e**), CD25 (**f**) and CD44 (**g**) on SIINFEKL peptide-specific OT-I T cells, after co-culture with unpulsed or ovalbumin-pulsed CD11b⁺ GAMs (n = 7 mice per group). Results were pooled from two independent experiments. **h**, **i**, BLI as surrogate for tumor growth (n = 6-13 mice per group) (**h**) and survival (n = 6-8 mice per group) (**i**) of in vivo CD8⁺ T cell depleted *Siglece*$^{fl/fl}$ x *Cx3cr1*^{CreERT2} CT-2A tumor-bearing animals, compared to animals from Fig. 3c and 3d. Blue arrows in Fig. 4i indicate anti-mouse CD8a i.p. administrations (days -2, 0, 7, 14 and 21). Results shown are from one experiment, representative of two independent experiments. **j**, qPCR analysis of NF-κB target genes in MdCs sorted from *Siglece*$^{fl/fl}$ and *Siglece*$^{fl/fl}$ x *Cx3cr1*^{CreERT2} CT-2A tumor-bearing mice on day 15 after tumor cell injection, and 8 days after induction of GAM-specific Siglec-E deletion (n = 9-10 mice per group). Results were pooled from three independent experiments, with n = 3-4 mice pooled per genotype each. qPCR analysis of *Siglece* was done separately, n = 4 mice per genotype. Statistics: Data are presented as mean ± SD (**a, b, d**), mean ± SEM (**e-g**) and median (**h**), unpaired Student's t test (**a**, **b**), two-tailed Mann-Whitney test (**d**), one-way ANOVA with Sidak's corrected multiple

comparison test (**e**-**g**), two-way ANOVA with Sidak's corrected multiple comparison test (**h**), log-rank Mantel-Cox test (**i**), two-way ANOVA for NF-κB target genes and unpaired two-tailed Student's t test for *Siglece* (**j**). *$p \leq 0.05$, **$p \leq 0.01$, ***$p \leq 0.001$.

3.1.3.6 Genetic targeting of sialic acid on CT-2A cells recapitulates main findings of GAM-specific Siglec-E deletion in vivo

To complement the effect of immune evasion mediated by Siglec-E receptor, we targeted its sialic acid ligands on CT-2A cells by knocking out the GNE enzyme (CT-2A$^{\Delta GNE}$) (Fig 5a, Supplementary Data Fig. 5a). CT-2A$^{\Delta GNE}$ cells showed no differences with regard to their in vitro proliferation and viability compared to wildtype control (CT-2A^{WT}) (Supplementary Data Fig. 5b). Orthotopic transplantation of CT-2A$^{\Delta GNE}$ cells into C57BL/6 mice (Fig. 5b) resulted in increased tumor cell phagocytosis, TNF-α production and a MG-restricted MHC-II response (Fig. 5c), recapitulating the main findings from the GAM Siglec-E deletion in both innate immune populations. Although we observed a favorable CD4$^+$ T cell response with less CD25$^+$Foxp3$^+$ Tregs and more Cxcr3$^+$T-bet$^+$ Th1 CD4$^+$ T cells in CT-2A$^{\Delta GNE}$ tumor bearing animals at endpoint (Supplementary Data Fig. 5c), the main driver of the adaptive immune response after innate immune activation were CD8$^+$ T cells. This was exemplified by less abundant PD-1$^+$, TIM-3$^+$, LAG-3$^+$ and CTLA-4$^+$ co-expressing CD8$^+$ T cells, greater degranulation capacity and increased IFN-γ production in CT-2A$^{\Delta GNE}$ tumor bearing animals (Fig. 5d, e), ultimately improving survival (Supplementary Data Fig. 5d). Together, targeting Siglec receptor ligands in the tumor recapitulates the main findings of GAM-specific Siglec-E deletion in the host.

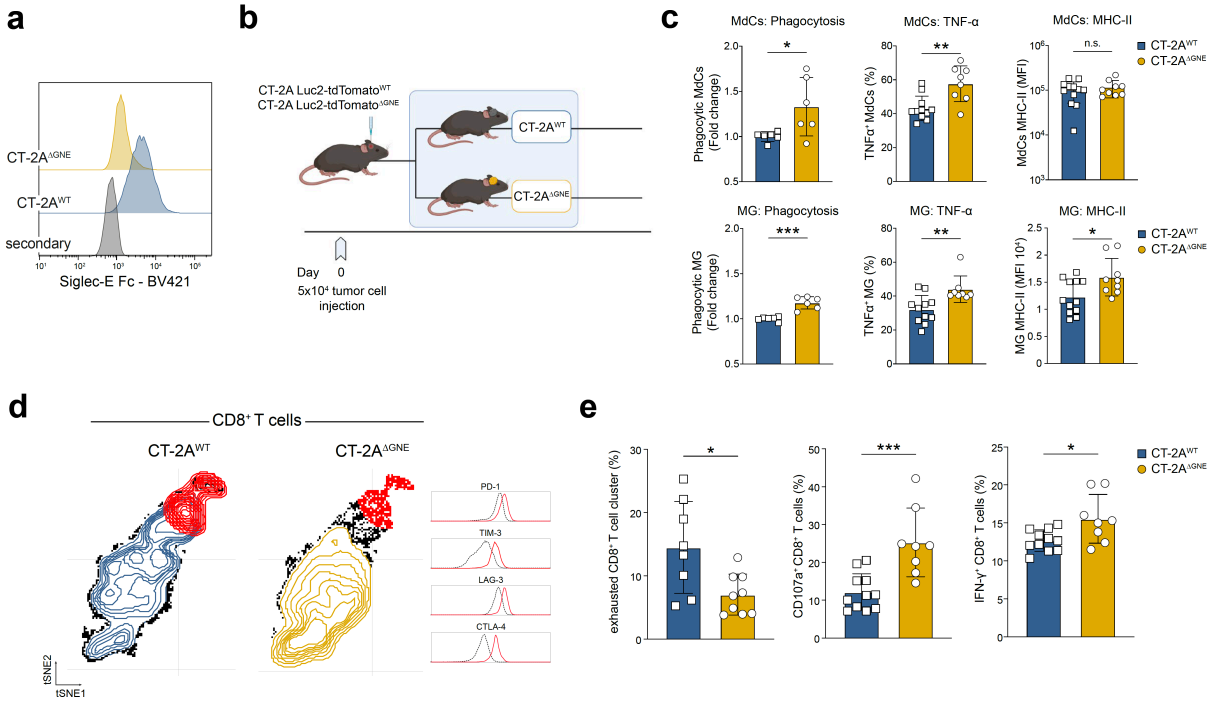

Fig. 5 Genetic targeting of sialic acid on CT-2A cells recapitulates main findings of Siglec-E deletion in the host.

a, Representative histogram of Siglec-E Fc staining on CT-2A^{WT} and CT-2A$^{\Delta GNE}$ cells. **b,** Schematic of experimental design. **c**, FC analysis of phagocytosis, and TNF-α and MHC-II expression on MdCs (top row) and MG (bottom row) from CT-2A^{WT} and CT-2A$^{\Delta GNE}$ injected C57BL/6 wildtype mice (n = 6 mice per group for phagocytosis, n = 8-11 mice per group for other analyses). Results were pooled from two independent experiments. **d**, FC analysis of inhibitory T cell receptors on intratumoral CD8$^+$ T cells visualized on tSNE map (tSNE maps show concatenated CD8$^+$ T cells from n = 8 mice per group). Red cluster marks exhausted CD8$^+$ T cells identified by high co-expression of inhibitory receptors (PD-1, TIM-3, LAG-3 and CTLA-4), indicated by histograms. Red histogram marks median marker expression in red cluster (exhausted CD8$^+$ T cell cluster) and black dotted histogram indicates median marker expression in the remaining cells. **e**, Quantification of FC analysis, showing percentage of exhausted CD8$^+$ T cells (PD-1^{high}, TIM-3^{high}, LAG-3^{high} and CTLA-4^{high}) (left), CD107a$^+$ (middle) and IFN-γ$^+$ (right) intratumoral CD8$^+$ T cells between CT-2A^{WT} and CT-2A$^{\Delta GNE}$ injected C57BL/6 wildtype mice (n = 8-11 mice per group). Results were pooled from two independent experiments. Statistics: Data are presented as mean ± SD, unpaired two-tailed Student's t test. *$p \leq 0.05$, **$p \leq 0.01$, ***$p \leq 0.001$.

3.1.3.7 GAM-specific Siglec-E deletion improves combinatorial immunotherapy in GBM

To harness and further elucidate the therapeutic potential of GAM-specific Siglec-E deletion (*Siglece$^{fl/fl}$* x *Cx3cr1^{CreERT2}*), we initiated combination treatments with CD47 blockade (Fig.6a), an established innate immunotherapeutic agent [69-71]. It has been previously shown that CD47 blockade enhances tumor cell phagocytosis and

T cell cross-priming as well [153]. We observed a significant reduction of tumor growth and improved overall survival in the combinatorial condition with 11% (1/9) of animals showing tumor rejection (Fig. 6b, c). In *Siglece*$^{fl/fl}$ x *Cx3cr1*^{CreERT2} tumors collected at endpoint, tumor-infiltrating CD8^{+} T cells demonstrated high level of PD-1 expression, while PD-L1 was significantly upregulated on CD45^{neg} and CD45^{pos} cells (Fig. 6d, e). This compensatory T cell checkpoint upregulation could be caused by increased CD8^{+} T cell activation and IFN-γ production after GAM-specific Siglec-E deletion (Fig. 4a) [154]. To overcome this potential resistance mechanism, we additionally treated tumor bearing *Siglece*$^{fl/fl}$ x *Cx3cr1*^{CreERT2} mice with both CD47 and PD-1 blocking antibodies (Fig. 6f). These triple-therapy treated animals exhibited a sustained survival benefit, with 23% (3/13) of animals having tumor rejection (Fig. 6g, h). Contra-lateral hemisphere tumor-rechallenging of surviving animals in this treatment cohort led to tumor rejection, whereas GAM-Siglec-E deleted/anti-CD47 treated mice succumbed to tumor progression after rechallenge (Fig. 6i). This data suggests that development of a lasting immunological memory and tumor control in GBM can only be achieved by targeting both innate and adaptive immune checkpoints to tackle the manifold immune tolerance mechanisms occurring during tumor progression.

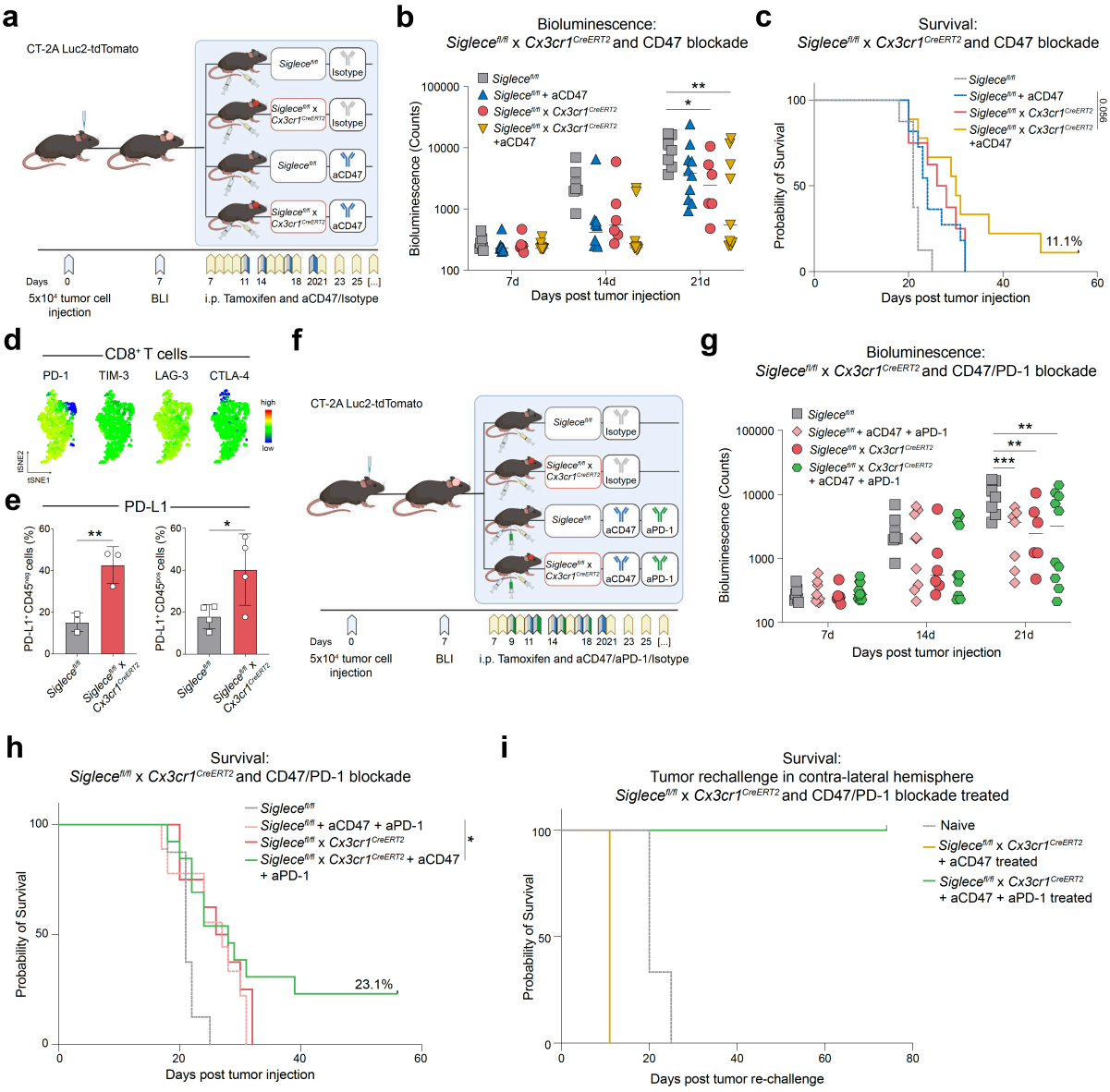

Fig. 6 Siglec-E deletion boosts GBM immunotherapy.

a, Schematic of experimental design. **b**, **c**, Surrogate tumor growth assessed by BLI (n = 6-10 mice per group) (**b**) and survival (n = 8-11 mice per group) (**c**) of *Siglece*$^{fl/fl}$ and *Siglece*$^{fl/fl}$ x *Cx3cr1*^{CreERT2} CT-2A tumor-bearing animals treated with anti-CD47 or isotype control. Results were pooled from two independent experiments. **d**, FC analysis of inhibitory T cell receptors on intratumoral CD8^{+} T cells shown on tSNE map (tSNE maps shows concatenated CD8^{+} T cells from n = 6 mice per group) **e**, FC analysis of PD-L1 expression on CD45^{neg} (left) and CD45^{pos} cells (right) from of *Siglece*$^{fl/fl}$ and *Siglece*$^{fl/fl}$ x *Cx3cr1*^{CreERT2} mice (n = 3-4 mice per group). **f**, Schematic of experimental design. **g**, **h**, Surrogate tumor growth assessed by BLI (n = 6-10 mice per group) (**g**) and survival (n = 8-13 mice per group) (**h**) of *Siglece*$^{fl/fl}$ and *Siglece*$^{fl/fl}$ x *Cx3cr1*^{CreERT2} CT-2A tumor-bearing animals treated with anti-CD47 and anti-PD1 or isotype control. Results were pooled from two independent experiments. **i**, Rechallenge of the tumor-free mice from Fig. 5c and 5h and tumor-naive control mice with intracranial injection of 5 x 10^{4} CT-2A tumor cells into the contra-lateral hemisphere (n = 1 for *Siglece*$^{fl/fl}$ x *Cx3cr1*^{CreERT2} + aCD47 treated, n = 3 mice per group for other two groups). Statistics: Data are presented as median (**b, g**) and mean ± SD (**e**), two-way ANOVA with Sidak's corrected multiple comparison

test (**b**, **g**), unpaired two-tailed Student's t test (**e**), restricted mean survival time (RMST) comparison (**c, h**). *$p \leq 0.05$, **$p \leq 0.01$, ***$p \leq 0.001$, ****$p \leq 0.0001$.

3.1.3.8 Siglec-9 blockade induces immune response and anti-tumor activity in human GBM explants

To determine the translational potential of Siglec-9 blockade, we prospectively collected GBM specimens from four primary and one recurrent GBM patient undergoing neurosurgical resection. All samples were neuropathologically diagnosed as GBM grade 4, *Isocitrate Dehydrogenase 1/2* (*IDH*) wild type (Supplementary Table 1). Intact tumor fragments (explants) were subsequently cultured in 3D perfusion bioreactors for five days in the presence or absence of Siglec-9 blocking antibody (Fig. 7a). As previously reported by us, this culture system provides flow of the media through the tissue, enabling culturing intact tissue of greater thickness and thereby better preserving the GBM iTME compared to static conditions (Fig. 7b) [155].

Analysis of secreted soluble proteins by highly sensitive proximity extension assay (PEA) technology after 5 d in culture identified three out of five patients (60%) as responders to Siglec-9 blockade, as indicated by a signature of induced TNF-α, IFN-γ and Granzyme B (GZMB) expression (Fig. 7c). Notably, one of the non-responders was the patient with recurrent GBM (BTB 700R). Within the responders, the observed increase was significant for IFN-γ and Granzyme B and by trend for TNF-α ($p = 0.06$) (Supplementary Data Fig. 6a).

Next, we assessed the anti-tumor activity of Siglec-9 blockade-induced immune activation on a single cell level. Single cell suspensions from nine additional newly diagnosed glioma patients (eight GBM, grade 4, *IDH* wildtype and one LGG; Supplementary Table 1), were exposed to Siglec-9 blocking antibody or control for 48 h (Fig. 7d). Using an automated image-based screening platform [156] to read-out $S100B^+CD45^-$ or $NESTIN^+CD45^-$ glioma cell counts (Fig. 7e), Siglec-9 disruption efficiently reduced the number of glioma cells despite interpatient heterogeneity (Fig. 7f, Supplementary Data Fig. 6b).

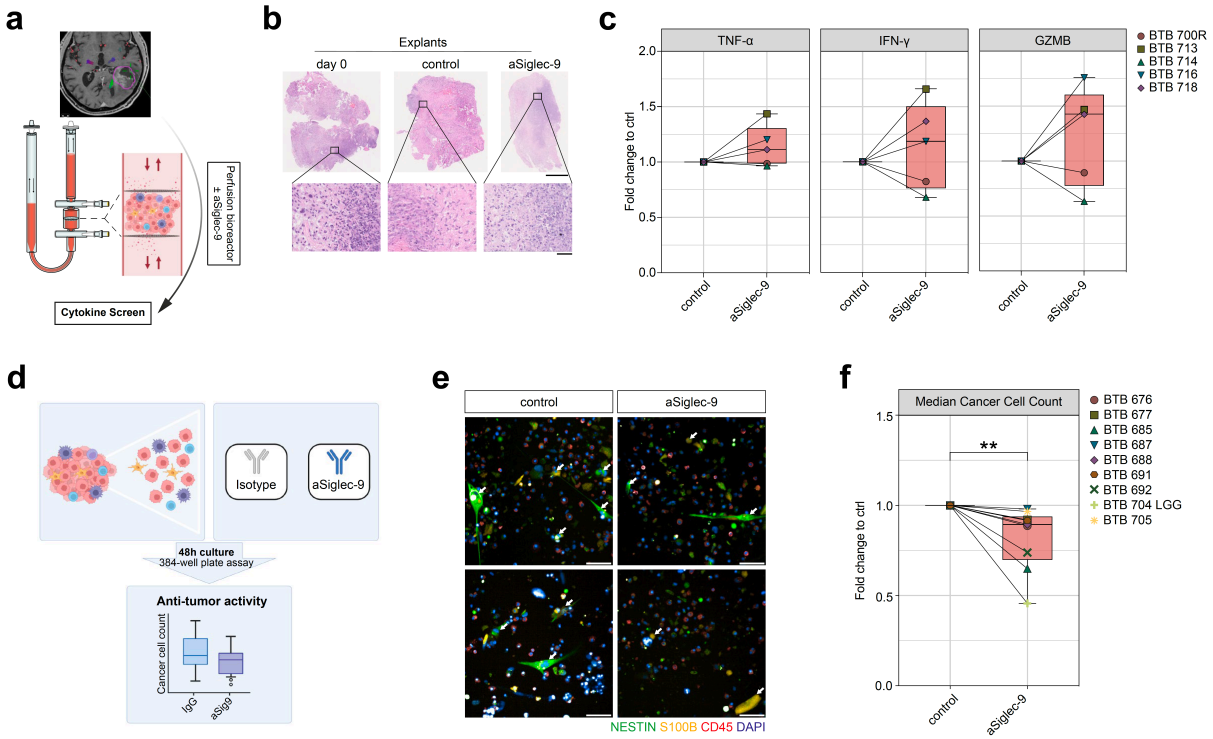

Fig. 7 Siglec-9 blockade induces immune response and anti-tumor activity in human GBM explants.

a, Schematic of experimental design. Fresh tumor biopsies were taken and directly transferred into 3D perfusion bioreactors. Explants were cultured for 5 days in the presence or absence of anti-Siglec-9 blocking antibody. Soluble proteins from bioreactor media were measured by PEA to assess response per patient sample. **b**, Representative H&E-stained images of formalin-fixed paraffin-embedded explants on the day of tumor resection (day 0) and after 5 days of culture in perfusion bioreactors. Scale bars, 1000 µm (overview) and 50 µm (close-up). **c**, Fold change in TNF-α, IFN-γ and GZMB secretion measured in the media of anti-Siglec-9 treated versus control bioreactors, for each individual patient. **d**, Schematic of experimental design. Glioma samples (n = 9) were dissociated and cultured for 48 hours in the presence of Siglec-9 blocking antibody or isotype control. **e**, Representative immunofluorescence images of one patient sample (BTB 688) treated with isotype (left) or anti-Siglec-9 (right). White arrows denote cancer cells. Scale bar, 50 µm**. f**, Fold change in median cancer cell count in anti-Siglec-9 treated versus control. Per patient, 6 technical replicates for control and 3 technical replicates for anti-Siglec-9 samples (Supplementary Data Fig 6b). Median of technical replicates is used and plotted as fold change. Statistics: unpaired two-tailed Student's t test (**f**). **p ≤ 0.01.

3.1.4 Discussion

Here, we identified the Siglec-sialic acid-axis as innate immune inhibitory pathway in GBM mediating a strongly immunosuppressive TME. We demonstrate that the deletion of Siglec receptors on MG and MdCs or reduction of Siglec ligands on tumor cells can reverse this immune suppression allowing successful combinatorial immunotherapy in preclinical models. As the main mechanism, we show that Siglec-E deletion leads to increased tumor cell phagocytosis by MG and MdC and elevated expression of NF-κB target genes in MdCs. This mediates cross-priming of $CD8^+$ T cells and ultimately synergizes with cancer immunotherapy to convey a substantial survival benefit in a highly aggressive and poorly immunogenic CT-2A GBM preclinical model [157].

Previous preclinical studies have shown similar anti-phagocytic [107, 120, 158, 159] and macrophage differentiating properties [98, 122, 130] for Siglec receptors in cancer and other diseases. Our study expands this knowledge on the interactions of Siglec receptors with sialoglycans by dissecting the complex interplay between the two main innate immune populations in the GBM iTME. We found a counteracting MdC response upon Siglec-E deletion-driven MG activation and proliferation. Yeo and colleagues recently reported similar changes in their study investigating longitudinal changes in the immune cell composition throughout tumor progression in a genetic mouse GBM model. [160] Specifically, they identified a highly proliferating population of GBM-associated MG, for which the authors discussed a decisive role in activating emergency myelopoiesis in GBM and recruiting bone marrow-derived immunosuppressive myeloid cells to the GBM iTME [160]. This paralleled our observation of a Siglec-E deletion induced activation and proliferation of MG cells, and the counteracting ingress of immunosuppressive MdCs which could only be reverted to control level by Ccl2 inhibition. Even though, the tumor cells were not the primary focus of our scRNA-seq analysis after MG Siglec-E disruption, we found profound changes in the CT-2A transcriptome as well, particularly concerning EMT pathways. This might unveil further tumor-cell intrinsic plasticity and resistance mechanisms upon perturbance of iTME components, e.g. MG, and highlights potential paracrine and intercellular reactions between neoplastic cells and MG induced by highly selective deletion of Siglec-E.

By extending the cell type specific Siglec-E deletion to the MdC compartment, we observed increased anti-tumor immunity and upregulation of NF-κB target genes.

Others similarly attributed a role as a negative modulator of NF-κB activity to Siglec-9 [158, 161]. In our RNA validation data, *Ccl5* was among the highest upregulated NF-κB target genes upon MdC-specific Siglec-E deletion. Several studies showed positive correlations between expression of inflammatory chemokine Ccl5 and immune cell recruitment to the tumor [162-164]. However, some controversy arose regarding the role of Ccl5 in cancer, as other studies suggested that Ccl5 has potential tumor-promoting effects, either by directly affecting tumor growth by expanding cancer stem cells [165] or promoting immune escape by stabilizing PD-L1 [166]. Unlike IFN-γ, which enhances PD-L1 expression at the transcriptional level [154], Ccl5 has been shown to modulate deubiquitination and stability of PD-L1 [166]. This might contribute to the adaptive resistance after Siglec-E deletion, and illustrate the complex relationship between innate and adaptive immune responses to build an effective and persistent antitumor immunity.

Our data highlight the Siglec-sialic acid axis as an attractive therapeutic target in GBM patients. Together with recent findings, our study further underlines the importance of combining innate and adaptive immunotherapies, especially in less immunogenic and ICI-resistant tumors such as GBM [153]. Targeting sialic acids as ligands for Siglec receptors on tumor cells represents an alternative approach to therapeutically disrupt the Siglec-sialic acid pathway, as demonstrated by genetically targeting sialic acid biosynthesis in CT-2A cells. By applying this strategy, concerns regarding functional redundancy and potential compensatory mechanisms after blockade of one Siglec receptor would be mitigated. In line with this, recent work showcased high efficacy of direct targeting of tumor sialylation [120, 159, 167-169]. However, systemic administration of chemical inhibitors of sialic acid biosynthesis was associated with fatal toxicity [170]. Therefore, more sophisticated approaches using for example antibody-sialidase conjugates, restricting the enzymatic desialylation to tumor-antigens seem promising [167, 169]. Hence, this would require a tumor-antigen as target for therapeutic desialylation. In GBM, the epidermal growth factor receptor variant III (EGFRvIII) could serve as a tumor-antigen, as it is expressed in roughly 20-30% of all patients [171]. Yet, even this targeted desialylation would most likely cause severe adverse events, given that the highest concentration of sialic acid prevails in the brain where it participates as an integral part of ganglioside structure in synaptogenesis and neural transmission [172]. Additional work will be needed to identify GBM cell-specific sialylation patterns which would make a cancer cell targeted desialylation therapy

amenable to the constrained conditions of the human brain. This would open new avenues for combinatorial therapies targeting both sialic acid and Siglec receptors.

To showcase the translational relevance of Siglec-9/E disruption within GBM, we first assessed Siglec-9 blocking antibody on cultured, perfused 3D tumor explants (as recently described by us [155]) and observed increased anti-tumoral cytokine production in 60% of patients. Second, we took advantage of an image-based ex-vivo drug screening platform, which demonstrated that Siglec-9 disruption efficiently reduced the number of glioma cells despite interpatient heterogeneity. Notably, we observed the biggest decrease in tumor cell count after Siglec-9 blockade in the LGG patient and considering the TCGA survival data, further studies on the role of Siglec receptors in LGG are needed.

Taken together, we show that loss of inhibitory Siglec receptors promotes glioma-associated MG and MdCs to phagocytize GBM cells and improve cross-presentation and subsequent T cell activation. Using a poorly immunogenic GBM preclinical model, we demonstrated the synergistic therapeutic potential of combined Siglec-E blockade with ICI against GBM to facilitate innate and adaptive anti-tumor immune responses. Furthermore, we demonstrated the translational potential of Siglec-9 blockade-induced immune activation in patient-derived explant cultures, paving the way to local therapy regimens. These results build on growing interest in designing combination immunotherapies with innate and adaptive ICI, and underscore the value of Siglec blockade in liberating innate immune responses to potentiate anti-tumor immunity.

3.1.5 Methods

Human samples

Human adult GBM tissue samples were obtained from the Neurosurgical Clinic of the University Hospital of Basel, Switzerland in accordance with the Swiss Human Research Act and institutional ethics commission (EKNZ 02019-02358). All patients gave written informed consent for tumor biopsy collection and signed a declaration permitting the use of their biopsy specimens in scientific research, including storage in our brain tumor biobank (Req-2019- 00553). All patient identifying information was removed and tissue was coded for identification. Patient characteristics from all participating patients are listed in Supplementary Table 1.

Human GBM tissue dissociation

Resected GBM tissue samples were immediately placed on ice and transferred to the laboratory for single cell dissociation within 2-3 h after resection. Human brain tissue was manually minced using razor blades and enzymatically dissociated at 37°C for 30 minutes with 1 mg mL^{-1} collagenase-4 (#LS004188, Worthington Biochemical Corporation, USA) and 250 U mL^{-1} DNAse1 (#10104159001, Roche, Switzerland) in a buffer containing Hank's Balanced Salt Solution (HBSS) with Ca^{2+}/Mg^{2+}, 1% MEM non-essential amino acids (Gibco), 1 mM sodium pyruvate (Gibco), 44 mM sodium bi-carbonate (Gibco), 25 mM HEPES (Gibco), 1% GlutaMAX (Gibco) and 1% antibiotic-antimycotic (Sigma-Aldrich). Cells were filtered and separated from dead cells, debris and myelin by a 0.9 M sucrose (#84100, Simga Aldrich, USA) density gradient centrifugation. Upon ACK-lysis for removal of erythrocytes (Gibco) the single-cell suspension was used for flow cytometry.

Mice

All animal handling, surveillance, and experimentation were performed according to the guidelines and legislation of the Swiss Federal Veterinary Office (SFVO) and the Cantonal Veterinary Office, Basel-Stadt, Switzerland, under license # 2929. *Siglece*$^{fl/fl}$ [29] mice were crossed to *Sall1*^{CreERT2} [30], kindly provided by Prof. Nishinakamura (Kumamoto University, Kumamoto, Japan) or to *Cx3cr1*^{CreERT2} [40] mice, received from Prof. Niess (University Hospital Basel, Basel, Switzerland) generating offspring mice harboring a tamoxifen-inducible Siglec-E conditional knockout in MG or GAM population, respectively. For both *Cre* lines *Siglece*$^{fl/fl}$ mice were used as controls.

Rag2/OT-I (*Rag2*^{tm1Fwa}Tg(TcraTcrb)1100Mjb) mice were kindly provided by Prof. Alfred Zippelius (University Hospital Basel, Basel, Switzerland) and originally obtained from Taconic (USA). C57BL/6 mice were obtained from Janvier Labs (France) and bred in-house at the Department of Biomedicine, University Hospital Basel, Basel, Switzerland. Mice of both sexes were used throughout the study; sex-matched and age-matched controls were used in individual experiments. All animals were euthanized before reaching humane endpoint, including loss of locomotor activity, weight loss (up to 20%) and central nervous system symptoms. The survival time was measured from the day of tumor cell implantation to the day of euthanasia. Mice of different treatment groups were co-housed in the same cage to blind experimenter in determining humane endpoint.

Mouse Genotyping

The following primers were used: *Sall1*^{CreERT2} (1): AGC TAA AGC TGC CAG AGT GC; *Sall1*^{CreERT2} (2): CAA CTT GCG ATT GCC ATA AA; *Sall1*^{CreERT2} (3): GCG TTG GCT ACC CGT GAT AT. *Cx3cr1*^{CreERT2} (1): AAG ACT CAG GTG GAC CTG CT; *Cx3cr1*^{CreERT2} (2): CGG TTA TTC AAC TTG CAC CA; *Cx3cr1*^{CreERT2} (3): AGG ATG TTG ACT TCC GAG TTG. *Siglece*$^{fl/fl}$ (1): CAG CCC ATC TTT GGC AGA TCC TTG T; *Siglece*$^{fl/fl}$ (2): AGT CAA AAC AAA CAC AGC ACA AGC C. PCR amplification was done using GoTaq G2 Green Master Mix (#M7823, Promega, USA).

Cell lines

The mouse malignant glioma cell line GL-261 was purchased from the DSMZ-German Collection of Microorganisms and Cell Cultures GmbH, Leibniz-Institute (Braunschweig, Germany). The mouse malignant astrocytoma cell line CT-2A was a kind gift from Prof. Seyfried (Boston College, Chestnut Hill, USA). The murine cell lines were cultured in Dulbecco's modified Eagle medium (DMEM), high glucose, no glutamine (Gibco) supplemented with 10% fetal bovine serum (FBS) (PAN-Biotech), 1% GlutaMAX (Gibco) and 1% Penicillin-Streptomycin (Sigma-Aldrich). All tumor cell lines were cultured as adherent monolayers, maintained at 37°C, 5% CO_2 and regularly split when reached around 80% confluence. All cell lines were regularly tested for mycoplasma contamination using a biochemical test kit (#LT07-318, Lonza, Switzerland) and were free of mycoplasma contamination.

Transduction of mouse GBM cell lines

For in vivo tumor monitoring by bioluminescence imaging (BLI) and fluorescent labelling of tumor cells in FC-based phagocytosis assay, GL261 and CT-2A cells were lentivirally transduced to express luciferase 2 (Luc2) and fluorescent reporter protein tdTomato (GL261 Luc2-tdTomato, CT-2A Luc2-tdTomato). The lentiviral Luc2-tdTomato construct was a gift from Prof. Bentires (University of Basel, Basel, Switzerland). For lentiviral transduction, tumor cells were plated at 5 x 10^4 cells per well of a 24-well plate 16h prior to transduction. Media was replaced with 0.5 mL antibiotic-free media containing 8 ug mL^{-1} Polybrene (Sigma-Aldrich). 5 μL of lentivirus suspension was added to the cells and incubated for 6 h at 37°C. Afterwards, transduction medium was replaced with normal growth medium and cells were expanded for 4 d and positively sorted for tdTomato expression. Luciferase expression was checked by using in vitro bioluminescence imaging by adding 100 μL of 15 mg mL^{-1} D-luciferin solution (#LUCNA-1G, Goldbio, USA) to the cells and imaged after 2 min using a Fusion FX system (Vilber, France).

Stereotactic tumor cell injection

Intracranial tumor engraftment was performed at age 8–12 weeks. Mice were being anesthetized with 2.5% isoflurane in an induction chamber. Anesthesia was maintained at 1.5% isoflurane delivered through a nose adaptor on the stereotactic frame. A midline incision was made and a burr hole was drilled at 1 mm posterior to the Bregma, and 2 mm lateral from the midline to the right. Stereotactic injection of tumor cells was done using a Hamilton 10 µL syringe (#80300, 701N, 26s/2”/2, Hamilton) at a depth of 3mm below the dura surface. A microinjection pump was used to inject 5 x 10^4 tumor cells in 3 µL PBS + 2% FBS total volume at 1 µL/min injection speed. One minute after injection ended, the needle was slowly retracted to avoid reflux of the cell suspension. The scalp wound was closed with sutures (5-0, Polypropylene suture, #8661H, Ethicon, USA).

In vivo bioluminescent imaging (BLI)

Mice were images by BLI starting at 7 d post tumor injection. Isoflurane-anesthetized mice were injected intraperitoneally (i.p.) with 150 mg kg^{-1} D-luciferin (#LUCNA-1G, Goldbio, USA) and imaged after 5 min using a Newton 7.0 BLI system (Vilber, France). A region of interest (ROI) was drawn around the head and quantitated

on mean luminescence (photon count per pixel area). Mice were imaged weekly and checked for neurological symptoms and weighed daily from day 21 onwards.

In vivo treatments

Tamoxifen (#T5648-5G, Sigma-Aldrich, USA) was dissolved in corn oil (#C8267, Sigma-Aldrich, USA) and 2.5 mg were administered i.p. per mouse and injection, starting from d 7 post tumor injection daily until d 21 and from d 21 onwards, every other day throughout the duration of the experiment. Cre^+ and Cre^- mice were treated with Tamoxifen.

Anti-mouse Ccl2 (clone 2H5, BioXcell) and isotype control (Armenian hamster IgG, BioXcell) were administered at 1 mg kg^{-1} i.p. 3 times per week, starting 7 d after tumor cell injection throughout the duration of the experiment.

Anti-mouse CD47 (clone MIAP410, BioXcell) and isotype control (mouse IgG1, clone MOPC-21, BioXcell) were administered at 4 mg kg^{-1} i.p. on d 11 post tumor injection and at 8 mg kg^{-1} i.p. on d 14, 17 and 20 post tumor injection.

Anti-mouse PD-1 (clone RMP1-14, BioXcell) and isotype control (rat IgG2a, clone 2A3, BioXcell) were administered at 10 mg kg^{-1} i.p. on d 9, 12, 15 and 18 post tumor injection.

Anti-mouse CD8a (clone 53-6.7, BioXcell) for in vivo depletion of $CD8^+$ T cells, was administered at 10 mg kg^{-1} i.p. on d -2 and 0 relative to the time of tumor cell injection and depletion was maintained by weekly treatments throughout the duration of the experiment.

Mouse tumor dissociation

Mice were euthanized by CO_2-suffocation at endpoint or indicated time points and tumor-bearing cerebral hemisphere without cerebellum was harvested into ice-cold HBSS. On ice, brain tissue was manually minced using razor blades and enzymatically dissociated at 37°C for 30 minutes using the same dissociation buffer as described above. The suspension was filtered through a 70 µm strainer and subjected to a density gradient centrifugation using debris removal solution (#130-109-398, Miltenyi Biotec, Germany) according to manufacturer's protocol to remove myelin and cell debris. Following ACK-lysis, the remaining myelin- and erythrocytes-depleted tumor cell suspension was used in downstream applications.

Flow cytometry

Primary mouse and human cells were isolated as described above and stained with Zombie fixable viability dye for 20 min at room temperature (#423102, BioLegend, USA) and pre-incubated with anti-mouse Fc block at 10 μg mL^{-1} (#101320, BioLegend, USA) or anti-human Fc block (#422302, BioLegend, USA). Surface markers were stained with appropriate antibodies for 20 min at 4°C. For intracellular staining, cells were fixed and permeabilized using Cyto-Fast Fix/Perm Buffer Set (#426803, BioLegend, USA), prior to staining for 20 min at room temperature in the dark. For transcription factor staining, cells were fixed, permeabilized and washed using True-Nuclear Transcription Factor Buffer Set (#424401, BioLegend, USA) according to the manufacturer's protocol. Followed by staining with intracellular antibodies for 30 min at room temperature in the dark. After respective staining protocol, cells were washed twice and resuspended in FACS buffer. For FC, either a Fortessa LSR II (BD Bioscience) or Cytoflex S (Beckman Coulter) flow cytometer were used for cell acquisition and FlowJo software (v.10.8.1, TreeStar) for data analyzation. Cell sorting was performed using a BD FACSAria III or BD FACSMelody (BD Bioscience). We performed compensation using Ultracomp ebeads Compensation Beads (#01-2222-42, Invitrogen, USA), which were stained with appropriate antibody and analyzed on the same voltage and settings. Gates were drawn by using Fluorescent Minus One (FMO) controls. The antibodies used in flow cytometry and cell sorting can be found in Supplementary Tables 2 and 3. Gating strategies are shown within the figures or summarized in Supplementary Data Fig. 1d, e. Either percentage of cell population of interest or Median Fluorescent Intensity (MFI) are reported.

Imaging flow cytometry

Tumor cell suspensions from *Siglece*$^{fl/fl}$ and *Siglece*$^{fl/fl}$ x *Sall1*^{CreERT2} mice were generated, Fc-receptor blocked and stained with anti-mouse CD11b (clone M1/70, BV650, BioLegend) and anti-mouse CD45 (clone 30-F11, FITC, BioLegend) as described above to identify MG as CD45^{low}CD11b^{+} and MdCs as CD45^{high}CD11b^{+}. DAPI staining was used to exclude dead cells. Imaging flow cytometry was performed on Amnis ImageStreamX Mark II (Merck Millipore). Phagocytosis was analyzed using the IDEAS software onboard internalization-identification algorithm (Amnis), which identifies tdTomato signal within MG events. Pictures were taken at 40X magnification at

low speed, high sensitivity mode. Full gating strategy is shown in Supplementary Data Figure 1h.

scRNA-seq analysis of immune cells

Tumors from *Siglece*$^{fl/fl}$ and *Siglece*$^{fl/fl}$ x *Sall1*^{CreERT2} mice were dissociated as described above and cells were stained with Zombie fixable viability dye, Fc-receptor blocked and stained with CD45 and CD11b. Live, CD45^{+} and/or CD11b^{+} immune cells were sorted into ice-cold PBS with 0.4% BSA. Cells were kept on ice and brought to the Genomics Facility Basel at the Department of Biosystems Science and Engineering of the ETH Zurich, Basel. Single cell capture and cDNA and library preparation were performed with Chromium Next GEM Single Cell 5' Reagent Kits v2 (10x Genomics, CA, USA) following manufacturer's protocol with the goal of loading 10,000 cells per sample. After library preparation, libraries were sequenced using the NovaSeq 6000 systems (Illumina, CA, USA) to produce paired-end 91nt R2 reads with a targeted minimum sequencing depth of 20,000 genes per cell.

The dataset was analyzed by the Bioinformatics Core Facility, Department of Biomedicine, University of Basel. Read quality was assessed with the FastQC tool (version 0.11.5). Sequencing files were processed with STARsolo (STAR version 2.7.10a) [67] to perform sample and cell demultiplexing, and alignment of reads to the mouse genome (mm10; supplemented with the Cre, tdTomato eGFP construct sequences) and UMI counting on gene models from Ensembl 102. The options "*--outFilterType=BySJout --outFilterMultimapNmax=10 --outSAMmultNmax=1 --outFilterScoreMin=30 --soloCBmatchWLtype=1MM_multi_Nbase_pseudocounts --soloUMIlen=10 --soloUMIfiltering=MultiGeneUMI_CR --soloUMIdedup=1MM_CR --soloCellFilter=None --clipAdapterType=False --soloType=CB_UMI_Simple –soloStrand=Reverse –soloMultiMappers=EM*" were used for STARsolo.

For each sample, empty droplets were detected and removed using the *emptyDrops()* function from the Bioconductor DropletUtils package (version 1.14.2; using 5000 iterations, the option *test.ambient=TRUE*, a lower threshold of 100 UMIs and an FDR threshold of 0.1%) [68]. Processing of the UMI counts matrix was performed using the Bioconductor packages scran (version 1.24.0) [69, 70] and scatter (version 1.24.0) [71], following mostly the steps illustrated in the OSCA book (http://bioconductor.org/books/3.15/OSCA/) [70, 72]. A first step of filtering for low-quality cells was done based on library size (at least 600 UMI counts per cell), the number of detected genes

(at least 400 genes detected) and the percentage of reads mapping to mitochondrial genes (larger than 0% and lower than 20%), based on the distribution observed across cells. The presence of doublet cells was investigated with the scDblFinder package (version 1.10.0), and suspicious cells were filtered out (score > 0.9). UMI counts were normalized with size factors estimated from pools of cells created with the scran package *quickCluster()* function [69, 73]. To distinguish between genuine biological variability and technical noise, we modeled the variance of the log-expression across genes using a Poisson-based mean-variance trend. The scran package *denoisePCA()* function was used to denoise log-expression data by removing principal components corresponding to technical noise. Cell cycle phase was inferred using the markers provided in the package Seurat (version 4.1.1) and the *CellCycleScoring()* function. Systematic differences between samples were removed using the *fastMNN()* function (d=50, k=20) of the batchelor package (version 1.12.3) [74], run on the most hypervariable genes across cells (excluding MT genes and ribosomal protein genes, as well as genes at high level in ambient RNA).

Clustering of cells was performed with hierarchical clustering on the Euclidean distances between cells (with Ward's criterion to minimize the total variance within each cluster [75]; package cluster version 2.1.3). The number of clusters used for following analyses was identified by applying a dynamic tree cut (package dynamicTreeCut, version 1.63-1) [76], and the clustering resolution was adapted using the argument deepSplit (default 1). The *scoreMarkers()* function of the scran package was used to find the best markers across clusters. Based on their high levels of MT reads, low number of detected genes and lack of specific cell-type markers, some clusters were deemed composed of low-quality cells and filtered out.

The best markers across clusters and a list of known cell type-specific genes were used for cell type annotation. In addition, the Bioconductor package SingleR (version 1.10.0) was used for unbiased cell-type annotation of the cells [77] using as reference datasets (i) sorted bulk microarray and RNA-seq samples from the ImmGen project [78], (ii) a collection of mouse RNA-seq samples annotated to 28 cell types, available through the celldex Bioconductor package; (iii) a collection of scRNA-seq datasets from virus-specific CD8 T cells, tumor-infiltrating T cells, and virus-specific CD4 T cells available at https://spica.unil.ch/refs [79, 80]. A microglia and a macrophage signature scores were defined by taking to 1-to-1 orthologs in mouse (Using

Ensembl Compara [81]) of genes from the lists obtained in [82], and averaging their center and scaled expression levels. To improve the annotation of the T cells and monocytes/macrophages/microglia clusters, a reclustering was performed based on the set of most hypervariable genes within cells of each of these subsets. Finally, the SingleR high-quality assignments (pruned scores) and the signature scores were used to manually derive a consensus cell type annotation for each cluster.

After quality filtering, the resulting dataset consisted of UMI counts for 28,644 cells, ranging from 1,410 to 5,856 cells per sample. A two-dimensional t-distributed stochastic neighbour embedding (tSNE) used for visualization of cells was calculated using the batch-corrected matrix of low-dimensional coordinates for each cell (perplexity of 30).

Differential abundance analysis across cell types between *Siglece*$^{fl/fl}$ x *Sall1*^{CreERT2} and *Siglece*$^{fl/fl}$ conditions was performed using the *limma-voom* method [83, 84]. Differential abundance of cell types was considered to be significant at a false discovery rate (FDR) lower than 5 %.

Differential expression between conditions, stratified by annotated cell type, was performed using a pseudo-bulk approach, summing the UMI counts of cells from each cell type in each sample when at least 20 cells could be aggregated. The aggregated samples were then treated as bulk RNA-seq samples [85] and for each pairwise comparison genes were filtered to keep genes detected in at least 5% of the cells aggregated. Because the number of cells in the microglia clusters was too low, we pooled both clusters ('MG_1' and 'MG_2') together for the pseudo-bulk analysis. The package edgeR (version 3.38.4) [86] was used to perform TMM normalization [87] and to test for differential expression with the Generalized Linear Model (GLM) framework. Genes with a false discovery rate (FDR) lower than 5% were considered differentially expressed. Gene set enrichment analysis was performed with the function camera [88] on gene sets from the Molecular Signature Database (MSigDB, version 7.5.1) [36, 89]. We retained only sets containing more than 5 genes, and gene sets with a FDR lower than 5% were considered as significant.

Antigen cross-presentation assay

5 x 10^4 CT-2A Luc2-tdTomato cells were intracranially injected into *Siglece*$^{fl/fl}$ and *Siglece*$^{fl/fl}$ x *Cx3cr1*^{CreERT2} mice and tamoxifen i.p. injected on days 7 to 12 after

tumor injection. On d 15, tumor-bearing hemispheres without cerebellum were harvested and dissociated as described above. $CD11b^+$ cells were then isolated using the CD11b+ microbeads (#130-093-636, Miltenyi) according to the manufacturer's instructions on an AutoMACS (Miltenyi). Isolated cells were plated at 5 x 10^4 cells per well of a tissue-culture treated 96-well flat-bottom plate (Costar) in 100 μL IMDM medium (Gibco) with 10% FBS. Full-length ovalbumin protein (#vac-pova, InvivoGen, USA) was added at 100 μg mL^{-1} to the cells and incubated for 20 h at 37°C. Cells were collected with TrypLE (Gibco), Fc-receptor blocked and stained with anti-mouse CD11b (clone M1/70, FITC, BioLegend), anti-mouse CD45 (clone 30-F11, BV605, BioLegend) and APC-labeled anti-SIINFEKL/H-2Kb (#17-5743-80, eBioscience, USA), which specifically detects ovalbumin-derived SIINFEKL peptide bound to H-2Kb. DAPI nuclear stain was used to exclude dead cells. Antigen cross-presentation was assessed using a Cytoflex S flow cytometer (Beckman Coulter) and was measured as the percentage of APC^+ cells within $CD45^{high}CD11b^+$ MdCs and $CD45^{low}CD11b^+$ MG. Differences in antigen cross-presentation were reported as fold change between cells derived from *Siglece*$^{fl/fl}$ x *Cx3cr1*^{CreERT2} and *Siglece*$^{fl/fl}$ mice.

OT-I $CD8^+$ T cell isolation

Spleens from Rag2/OT-I transgenic mice were carefully removed and washed with PBS containing 2% FBS under sterile conditions. Tissue was mechanically dissociated by crushing it with a syringe piston in a 10 cm dish. Cell suspension was passed through a 70 μm strainer and washed. $CD8^+$ T cell isolation was performed using EasySep Mouse $CD8^+$ T cell Isolation Kit (#19853, STEMCELL Technologies, USA) according to manufacturer's protocol.

T cell cross-priming assay

$CD11b^+$ cells were isolated, plated and treated as described in antigen cross-presentation assay. After 20 h incubation of the $CD11b^+$ cells, naive OT-I $CD8^+$ T cells were isolated and added to the $CD11b^+$ cells at 2 x 10^5 cells per well and incubated for an additional 24 h. For T cell activation analysis, cells were collected and stained with CD8a (clone 53-6.7, FITC), CD25 (clone PC61, APC), CD69 (clone H1.2F3, PerCP/Cy5.5) and CD44 (clone IM7, PE) (all from BioLegend) and acquired using a Cytoflex S flow cytometer (Beckman Coulter). Of note, at two weeks post tumor injection (timepoint for $CD11b^+$ cells isolation), we observed a reduced proportion of infiltrating MdCs among $CD11b^+$ cells in *Siglece*$^{fl/fl}$ x *Cx3cr1*^{CreERT2} mice compared to

Siglece$^{fl/fl}$ control, probably due to the delayed tumor growth, since the proportion of MdCs among CD11b$^+$ cells showed a high level of correlation with the BLI count (Supplementary Data Fig. 4a). Therefore, to account for the reduced proportion of the cross-presenting MdCs among the isolated CD11b$^+$ cells in the *Siglece*$^{fl/fl}$ x *Cx3cr1*^{CreERT2} group, T cell activation marker expression was normalized to the mean bioluminescence count.

Proteomics analysis of MdCs

1.5 x 10^5 MdCs per tumor-bearing mouse brain were sorted and thoroughly washed using protein-free PBS, pelleted by centrifugation and the cell pellet was snap frozen on dry ice and kept in -80°C. For mass spectrometry-based proteomics, frozen cell pellets were brought to the Proteomics Core Facility of the University of Basel. There, cells were lysed with 50 µL of lysis buffer (1% Sodium deoxycholate (SDC), 10 mM Tris(2-carboxyethyl)phosphine (TCEP), 100 mM Tris, pH=8.5) using 10 cycles of sonication (30 s on, 30 s off per cycle) on a Bioruptor (Dianode). Following sonication, proteins were reduced by TCEP at 95° C for 10 min. Proteins were alkylated using 15 mM chloroacetamide at 37° C for 30 min and further digested using sequencing-grade modified trypsin (1/50 w/w, ratio trypsin/protein; Promega, USA) at 37° C for 12 hours. After digestion, the samples were acidified using TFA (final 1%). Peptide desalting was performed using iST cartridges (PreOmics, Germany) following the manufacturer's instructions. After drying the samples under vacuum, peptides were stored at -20° C

Dried peptides were resuspended in 0.1% aqueous formic acid and subjected to LC–MS/MS analysis using an Orbitrap Eclipse Tribrid Mass Spectrometer fitted with Ultimate 3000 nano system and a FAIMS Pro interface (all Thermo Fisher Scientific) and a custom-made column heater set to 60°C. Peptides were resolved using a RP-HPLC column (75µm × 30cm) packed in-house with C18 resin (ReproSil-Pur C18–AQ, 1.9 µm resin; Dr. Maisch GmbH) at a flow rate of 0.3 µL/min. The following gradient was used for peptide separation: from 2% B to 12% B over 5 min to 30% B over 70 min to 50% B over 15 min to 95% B over 2 min followed by 18 min at 95% B then back to 2% B over 2 min followed by 8 min at 2% B. Buffer A was 0.1% formic acid in water and buffer B was 80% acetonitrile, 0.1% formic acid in water.

The mass spectrometer was operated in DDA mode with a cycle time of 3 seconds between master scans. Throughout each acquisition, the FAIMS Pro interface switched between CVs of −40 V and −70 V with cycle times of 1.5 s and 1.5 s,

respectively. MS1 spectra were acquired in the Orbitrap at a resolution of 120,000 and a scan range of 375 to 1500 m z^{-1}, AGC target set to 10^6 and maximum injection time set to 50 ms. Precursors were filtered with precursor selection range set to 375–1500 m z^{-1}, monoisotopic peak determination set to “Peptide”, charge state set to 2 to 5, a dynamic exclusion of 30 s.

Precursors selected for MS2 analysis were isolated in the quadrupole with a 1.4 m z^{-1} window and collected for a maximum injection time of 35 ms with AGC target set to “Standard”. Fragmentation was performed with a CID collision energy of 30% and MS2 spectra were acquired in the IT at scan rate “Turbo”.

The raw files were using FragPipe v17.1 software with standard LFQ settings. In brief, the spectra were searched against a mouse protein database (retrieved from Uniprot on 21.04.2022) and commonly observed contaminants by the MSFragger v3.4 search engine [90] using the following criteria: full tryptic specificity was required, 2 missed cleavages were allowed, carbamidomethylation (C) was set as fixed modification, oxidation (M) and acetylation (Protein N-term) were applied as variable modification, minimum and maximum peptide lengths were set to 7 and 50 respectively. LFQ quantification was performed with IonQuant [91] with match between runs (MBR) algorithm was enabled. The database search results were filtered to a false discovery rate (FDR) of 1 %. Differential quantitative analysis was performed using MSstats package (v4.0.1) [92]. The KEGG pathway over-representation analysis was performed using the ClusterProfiler package in R. The genes of interest were selected according to log2 fold change, we selected genes with values between -1 and 1 (n=104) the universe comprised all the genes from the dataset, minGSSize = 3, maxGSSize = 800, pAdjustMethod = "fdr", pvalueCutoff = 1 and qvalueCutoff = 1.

RNA extraction and quantitative real-time PCR (qPCR)

Total RNA was isolated form FACS-sorted MdCs using the Direct-zol RNA MiniPrep plus kit (#R2072, Zymo Research, USA). mRNA was transcribed with iScript cDNA Synthesis Kit (#1708891, Bio-Rad, USA) and qPCR was performed on a CFX96 Real-Time System (Bio-Rad) using SYBR Green qPCR Mastermix (#330500, Qiagen, Germany). For NF-κB target gene analysis, primer array of the RT^2 Profiler PCR Array (#PAMM-025ZD, Qiagen, Germany) was used according to manufacturer’s protocol. Additionally, QuantiTect Primer Assay for *Siglece* (#QT00135597, Qiagen, Germany) was used. *Actb, B2m, Gapdh, Gusb* and *Hsp90ab1* were used to normalize signal

expression. Fold regulation comparison were performed between control and treatment samples using the $2^{-\Delta\Delta Ct}$ method [93].

Staining for Siglec-9 and Siglec-E ligands on tumor cells

For flow cytometric-based analysis of Siglec ligands, single cell suspensions of tumor cells were blocked, live/dead stained and incubated with recombinant human Siglec-9 Fc chimera (#1139-SL-050) or recombinant mouse Siglec-E Fc chimera (#5806-SL-050) both from R&D systems, USA for 20 min on ice. For detection, anti-human IgG (clone HP6017, APC) or anti-mouse IgG2a (clone RMG2a-62, APC or BV421) both from BioLegend, were incubated for 20 min on ice. Samples were acquired on a CytoFLEX S flow cytometer (Beckman Coulter).

Generation of CT-2A$^{\Delta GNE}$ tumor cells

Knockout of *Gne* in CT-2A tumor cells was performed using CRISPR/Cas9 mediated gene editing. The plasmid containing the guide RNAs were kindly provided by Dr. Stanczak (University Hospital Basel, Basel, Switzerland) [94]. Tumor cells were transiently transfected with the plasmid using FuGENE HD transfection reagent (#E2311, Promega, USA) according to manufacturer's protocol and GFP^+ cells were sorted. After their recovery and expansion, cell surface sialylation was analyzed by flow cytometry using recombinant Siglec-E Fc chimera as described above. For enzymatic desialylation control, cells were pre-incubated with 20 mU ml^{-1} Vibrio cholerae-derived neuraminidase (sialidase) (#11080725001, Roche, Switzerland) for 1 h at 37°C on a cell shaker. The wildtype parental cell line, as well as transfected and sorted cells showing normal cell surface sialylation were used as controls. CT-2A$^{\Delta GNE}$ cells were compared to CT-2A^{WT} with regard to their in vitro viability and proliferation, as well as their in vivo tumorigenicity in wildtype C57BL/6 mice. Proliferation was assessed by a MTT assay (#M2128, Sigma-Aldrich, USA) and viability of cells was measured by DAPI-stain exclusion.

Ex vivo perfusion bioreactor

Bioreactor cultures under perfusion were performed according to the manufacturer's instructions (Cellec Biotek AG, Basel, Switzerland) and as previously described [47]. In brief, fresh, intact GBM tissue explants were placed into ice-cold Neurobasal-A medium (#21103049, Life Technologies, USA) and immediately taken to the laboratory (less than 30 min). Tumor tissue was cut into ~20 to 30 mm^3 fragments. Silicone

adaptors and ethylene-tetrafluoroethylene copolymer mesh grids were arranged on the top and bottom of the tissue, and placed into U-CUP perfusion chambers (Cellec Biotek AG). The perfusion media consisted of a 50:50 mix of Neurobasal-A medium (#21103049, Life Technologies, USA) and Dulbecco's modified Eagle's medium/F12 medium (#21331020, Gibco, USA) supplemented with non-essential amino acids (1×; #M7145, Sigma-Aldrich, USA), 1 mM sodium pyruvate (#S8636, Sigma-Aldrich, USA), 44 mM sodium bicarbonate (#25080060, Gibco, USA), 25 mM Hepes (#156301, Gibco, USA), 4 mM l-alanyl-l-glutamine (#25-015-CI, Corning, USA), antibiotic-antimycotic (1×; #15240062, Gibco, USA), human recombinant epidermal growth factor (20 ng/ml; #236-EG-01M, R&D systems, USA), human recombinant fibroblast growth factor (20 ng/ml; #100-18B, PeproTech, UK), heparin sulfate (10 ng/ml; 100-18B, STEMCELL Technologies, USA), and 5% human serum (#H4522-100ML, Sigma- Aldrich, USA). The perfusion flow rate was set at 0.47 ml/min, resulting in a superficial flow velocity of 100 μm/s. Starting from day 0, bioreactor media were either left untreated or supplemented with anti–Siglec-9 antibody (5 μg mL^{-1}; clone 191240, #MAB1139-500, R&D systems, USA). On day 5, culture media were frozen at −80°C and tissues were fixed in 10% neutral buffered formalin (#HT501128, Sigma-Aldrich, USA) for 24 h, afterwards transferred to 70% ethanol and embedded in paraffin.

Multiplexed secreted protein analysis in explant culture media

After five days of culture, we measured soluble proteins including cytokines and chemokines in the media of each bioreactor using the proximity extension assay (PEA) technology developed by Olink Proteomics. Bioreactor media were centrifuged to remove cell debris, and 92 secreted proteins, including cytokines, chemokines, and soluble cell membrane proteins, were measured externally by PEA technology using the Olink Target 96 Immuno-Oncology panel (Olink, Sweden). Differences in normalized protein expression (NPX), Olink's arbitrary unit on a $\log_2$ scale, were reported as fold change to the respective control.

Pharmacoscopy

Tumor dissociation was performed as described above and dissociated single cells were resuspended in DMEM media supplemented with 10% FBS, 25 mM HEPES and 1% Pen/Strep and were seeded at 10^4 cells/well (in 50 μl/well) into clear-bottom, tissue-culture treated, CellCarrier-384 Ultra Microplates (Perkin Elmer, Waltham, Massachusetts, USA). Anti–Siglec-9 antibody (5 μg mL^{-1}; clone 191240, #MAB1139-500,

R&D systems, USA) or human IgG isotype control (#31154, Thermo Fisher Scientific) was added to the single cell suspensions and cultured at 37°C, 5% CO_2 for 48 h. Per patient there were three technical replicate wells for the anti-Siglec-9 treatment and six technical replicate wells for the IgG control. Subsequently, cells were fixed with 4% PFA (Sigma-Aldrich), blocked with PBS containing 5% FBS, 0.1% TritonX and DAPI (4 ug/mL, #422801, Biolegend) for one hour at RT and stained with the following antibodies: Alexa Fluor 488 anti-NESTIN (#656812, Biolegend), Alexa Fluor 555 anti-S100B (#ab274881, Abcam), Alexa Fluor 647 anti-CD45 (#368538, Biolegend) overnight at 4°C. Imaging of the 384 well plates was performed with an Opera Phenix automated spinning-disk confocal microscope at 20x magnification (Perkin Elmer). Single cells were segmented based on their nuclei (DAPI channel) using CellProfiler 2.2.0. Downstream image analysis was performed with MATLAB R2021b. Marker positive cell counts for each condition were derived based on a linear threshold of the histograms of each channel, were averaged across each well and compared between aSiglec-9 treatment and the IgG control group.

Statistical analysis

scRNA-seq and proteomic statistical analysis was completed as described above. All other statistical analyses were performed using GraphPad Prism (GraphPad Software v.9.4.0). Numbers of experimental replicates, numbers of independent experiments and statistical tests used are given in the figure legends. In general, when two groups were compared, significance was determined using an unpaired two-tailed Student's t test. For comparing more than two groups, one-way ANOVA was applied and for comparing a quantitative variable between two groups, two-way ANOVA was used. Survival data were analyzed using the log-rank Mantel-Cox test or restricted mean survival time (RMST). RMST analysis was used to account for the presence of censoring. The calculations were performed in R using the survRM2 package. We used max τ (largest observed time in each of the two groups) and the differences in RMST between subgroups were calculated as 95% CIs with P values. *P* values < 0.05 were considered as statistically significant. No statistical methods were used to predetermine sample size. Data collection and analysis were not performed blind to the conditions of the experiments. Outliers were removed using GraphPad Outlier Calculator (https://www.graphpad.com/quickcalcs/Grubbs1.cfm).

Graphical illustrations

All graphical illustrations were created with BioRender.com

3.1.6 Data availability

The scRNA-seq dataset is available on GEO under accession number GSE212616.

3.1.7 Autor contributions

G.H., H.L. and P.S., conceived and planned the project. P.S. designed, performed and analyzed most experiments and wrote the manuscript. J.R. and S.H. provided bioinformatical support and performed computational analysis. A.B., N.T., J.W., S.L., B.S., T.A.M., M.-F.R., T.S., D.K. and M.M performed and analyzed experiments. M.W., T.W. supervised and coordinated experiments. G.H. and H.L. supervised and coordinated the study and critically revised the manuscript. All authors reviewed the paper and approved its final version.

3.1.8 Acknowledgments

We are grateful to the patients and their families for their consent to donate tissue to our brain tumor biobank. Calculations were performed at sciCORE (http://scicore.unibas.ch/) scientific computing center at the University of Basel. This work was supported by a Swiss Cancer Research MD-PhD Grant (MD-PhD-4818-06-2019) to P.S. as well an Alumni Medizin Basel grant to P.S.; Swiss National Science Foundation Professorial Fellowship (PP00P3_176974); the ProPatient Forschungsstiftung, University Hospital Basel (Annemarie Karrasch Award 2019); Swiss Cancer Research Grant (KFS- 4382-02-2018) to G.H.; the Department of Surgery, University Hospital Basel, to G.H. and P.S.; and by The Brain Tumour Charity Foundation, London, UK (GN- 000562) to G.H. We thank Prof. Alfred Zippelius, Prof. Jan Niess and Prof. Ryuichi Nishinakamura for providing genetic mouse lines; Dr. Manuele Muraro for technical help with the perfusion bioreactors; Dr. Claudio Giachino and Dr. Elena Parmigiani from Prof. Verdon Taylor lab for providing the PDGF^{+}*Trp53*$^{-}$ mouse glioma cell line; Dr. Michal Stanczak for providing the GNE-KO plasmid; Dr. Anne Bärenwaldt and Dr. Natalia Rodrigues Mantuano for discussions and advice; and the genomics, proteomics, flow cytometry and animal core facilities of the University of Basel, Switzerland for technical and logistical support.

3.1.9 Competing interests

G.H. has equity in, and is a cofounder of Incephalo Inc. H.L. is member of the Scientific Advisory Board of GlycoEra, and InterVenn. and has received research support from Palleon Pharmaceuticals and consulting fees from Alector.

3.1.10 Supplementary Data

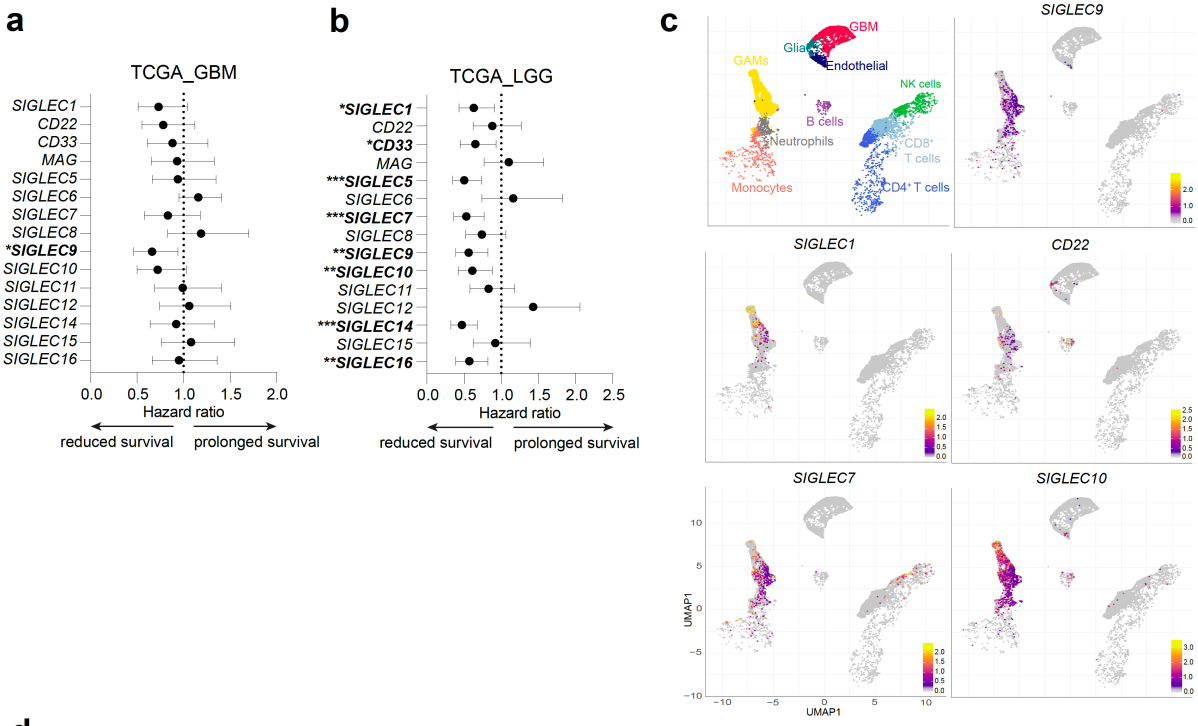

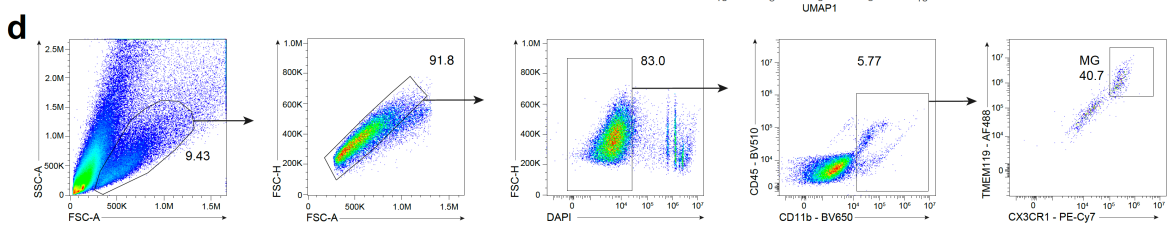

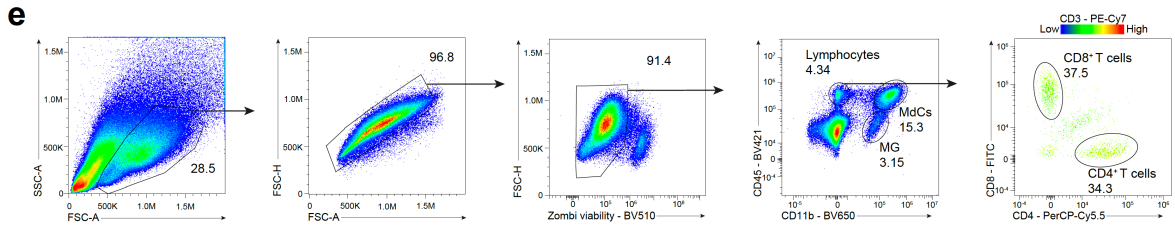

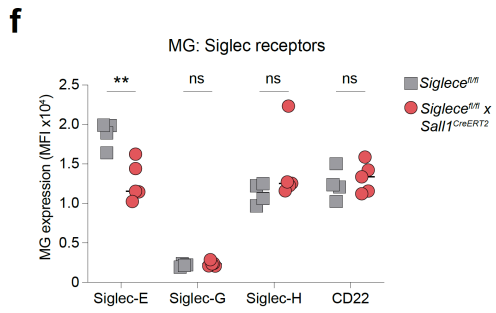

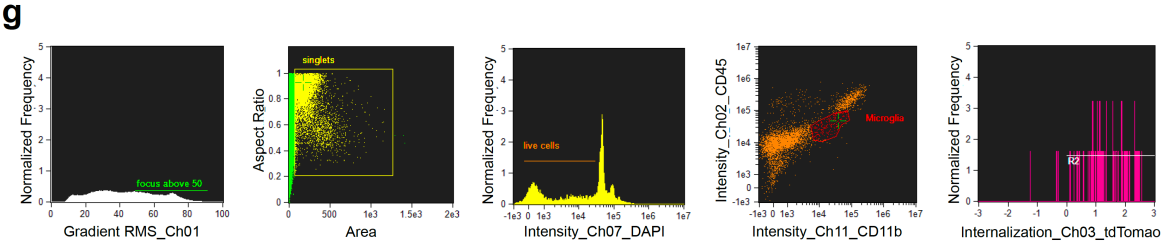

Supplementary Data Fig. 1 High *SIGLEC9* expression significantly correlates with reduced survival in GBM patients and represents a novel immunotherapeutic target.
a, **b**, Forest plots showing hazard ratios for overall survival associated with high expression of human Siglecs using The Cancer Genome Atlas (TCGA) RNA-seq dataset of human GBM (**a**) and low-grade glioma (LGG) (**b**) patients. The median mRNA expression value was selected as cutoff for high and low expression groups. A Cox proportional hazard analysis was performed using the GlioVis data portal [22] and hazard ratios with 95% confidence intervals are shown. **c**, Annotated UMAP plot showing scRNA-seq analysis of five primary human GBM tumors [23] (upper left) and UMAP plots showing expression pattern of selected Siglecs which exhibit a hazard ratio for overall survival of < 0.85 in GBM patients, as shown in Supplementary Data Fig. 1a. **d**, Gating strategy to identify human GBM-associated MG. **e**, Gating strategy to identify mouse glioma-associated immune cells. **f**, Flow cytometry analysis of selected mouse Siglecs on MG from *Siglece*$^{fl/fl}$ and *Siglece*$^{fl/fl}$ x *Sall1*^{CreERT2} mice bearing CT-2A tumors (n = 4-5 mice per group). Experiment was performed once. **g**, Gating strategy for imaging flow cytometry to identify MG tumor cell phagocytosis using the IDEAS software onboard internalization-identification algorithm. Statistics: Data are shown as median (**f**), two-way ANOVA with Sidak's corrected multiple comparison test (**f**). *$p \leq 0.05$, **$p \leq 0.01$, ***$p \leq 0.001$.

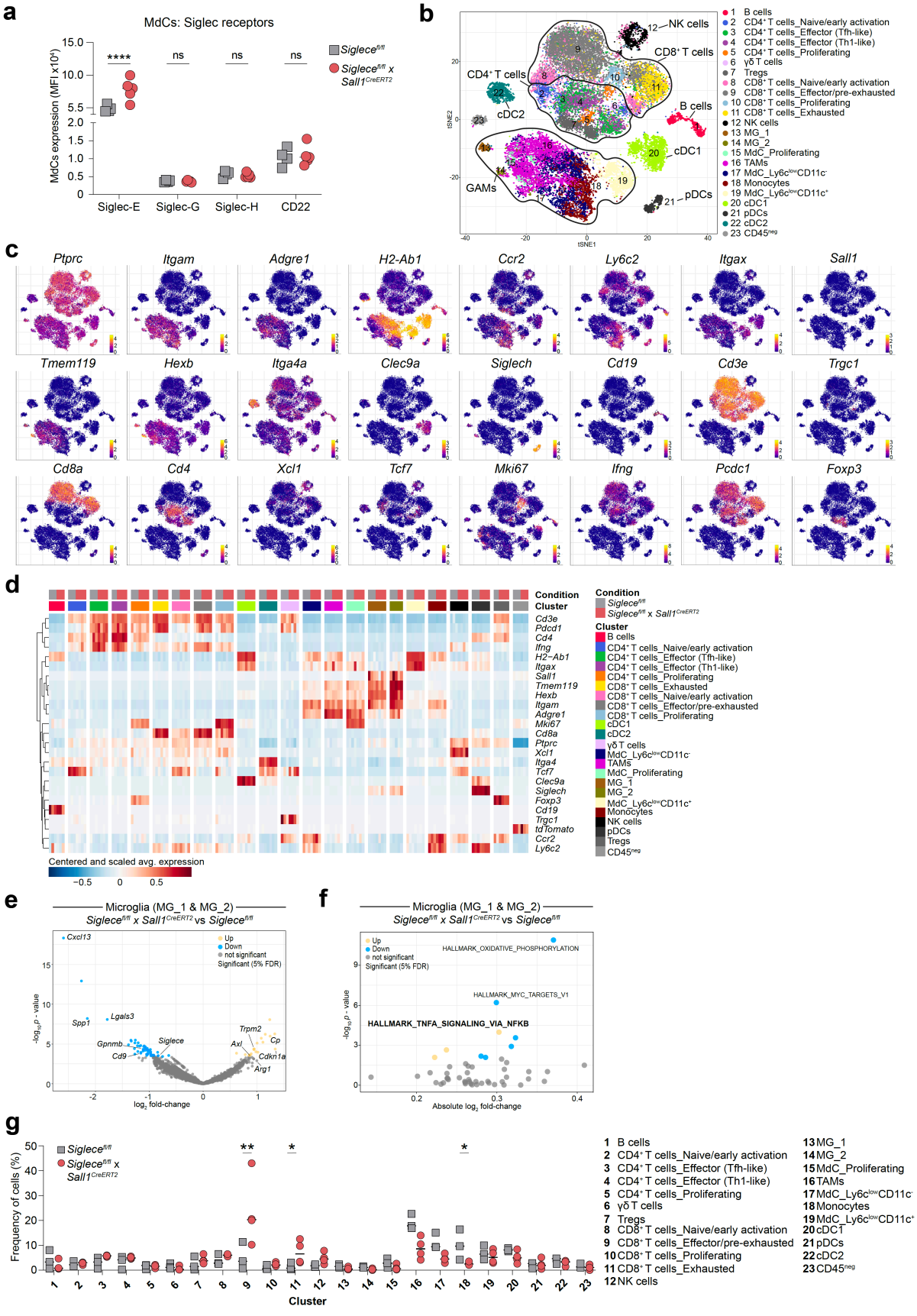

Supplementary Data Fig. 2 scRNA-seq analysis of immune cells from *Siglece*$^{fl/fl}$ and *Siglece*$^{fl/fl}$ x *Sall1*^{CreERT2} mice.

a, Flow cytometry analysis of selected mouse Siglecs on MdCs from *Siglece*$^{fl/fl}$ and *Siglece*$^{fl/fl}$ x *Sall1*^{CreERT2} mice bearing CT-2A tumors (n = 4-5 mice per group). Experiment was performed once. **b**, tSNE plot showing the clustering and annotation of cells from *Siglece*$^{fl/fl}$ and *Siglece*$^{fl/fl}$ x *Sall1*^{CreERT2} mice bearing CT-2A tumors. **c**, tSNE plots showing the expression of selected cell-type specific markers. Expression is shown as normalized $\log_2$ counts **d**, Heatmap displaying log-normalized expression of selected marker genes, averaged across cells of each cluster and sample, and centered and scaled by row. **e**, Volcano plot showing the differential expression analysis results between *Siglece*$^{fl/fl}$ x *Sall1*^{CreERT2} and *Siglece*$^{fl/fl}$ for microglia from the MG_1 & MG_2 clusters. **f**, Scatter plot showing the results of the corresponding GSEA performed on the MSigDB Hallmark collection. **g**, Relative frequencies of *Siglece*$^{fl/fl}$ (gray) and *Siglece*$^{fl/fl}$ x Sall1^{CreERT2} (red) cells in each cluster. Symbols represent biological replicates. Statistics: Data are shown as median (**a**, **g**), two-way ANOVA with Sidak's corrected multiple comparison test (**a**), *limma-voom* method with FDR<5% (**g**). *$p \leq 0.05$, **$p \leq 0.01$, ****$p \leq 0.0001$.

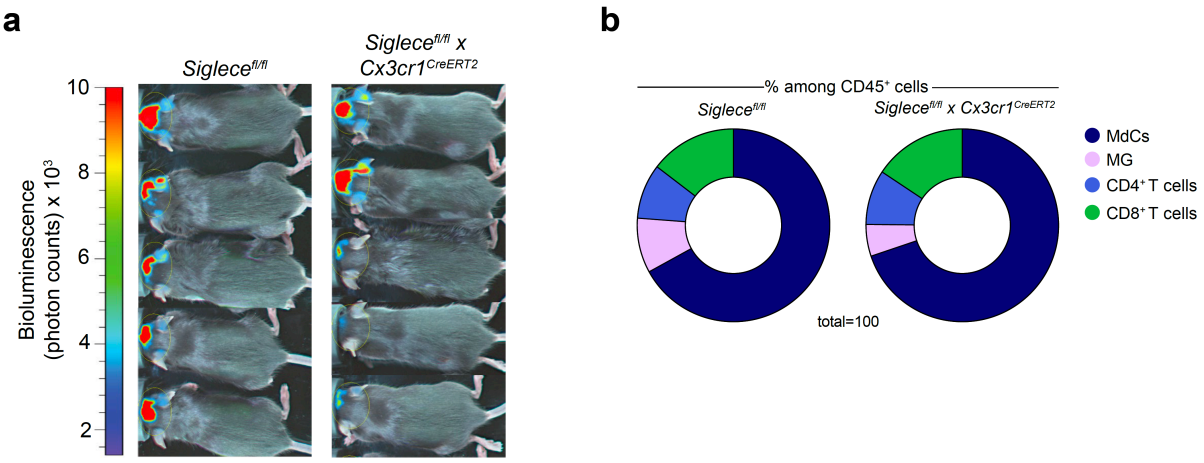

Supplementary Data Fig. 3 *Siglece*$^{fl/fl}$ x *Cx3cr1*^{CreERT2} glioma mouse model.
a, Representative bioluminescence images of day 21 post tumor injection in *Siglece*$^{fl/fl}$ and *Siglece*$^{fl/fl}$ x *Cx3cr1*^{CreERT2} mice engrafted with CT-2A Luc2-tdTomato tumors. Image representative of two independent experiments. **b**, Pie charts represent relative frequencies for main immune cell clusters identified among CD45$^+$ cells within *Siglece*$^{fl/fl}$ and *Siglece*$^{fl/fl}$ x *Cx3cr1*^{CreERT2} mice (n = 6 mice per group). Results shown are from one experiment, representative of two independent experiments.

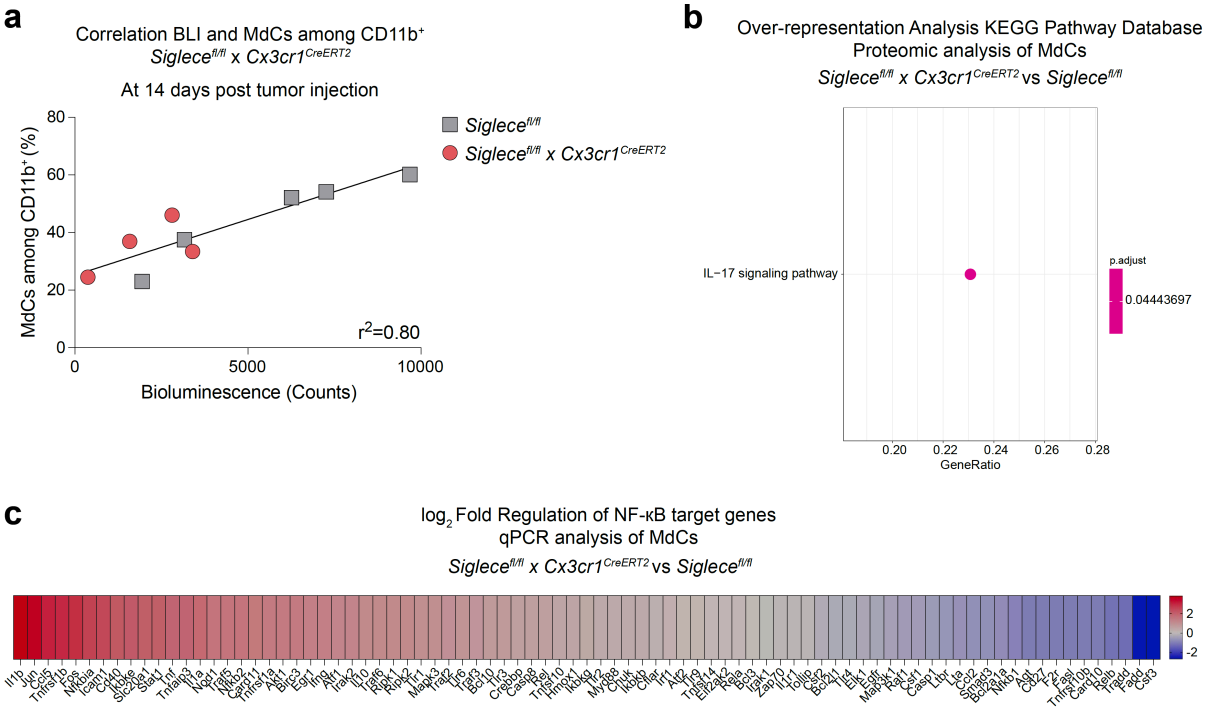

Supplementary Data Fig. 4 Siglec-E deficient MdCs show increased activity.
a, Correlation between MdC influx among CD11b$^+$ cells and tumor size (measured as bioluminescence count) at day 14 post tumor injection in *Siglece*$^{fl/fl}$ and *Siglece*$^{fl/fl}$ x *Cx3cr1*^{CreERT2} mice (n = 4-5 mice per group). **b**, Over-representation analysis (KEGG Pathway Database) of the proteomic analysis of MdCs sorted from *Siglece*$^{fl/fl}$ and *Siglece*$^{fl/fl}$ x *Cx3cr1*^{CreERT2} mice. **c**, Heat map displaying $\log_2$ Fold Regulation of NF-κB target genes between MdCs from *Siglece*$^{fl/fl}$ and *Siglece*$^{fl/fl}$ x *Cx3cr1*^{CreERT2} mice. Statistics: Simple linear regression analysis was done to compute r^2 (**a**), for detailed proteomic statistical analysis, please refer to Methods section.

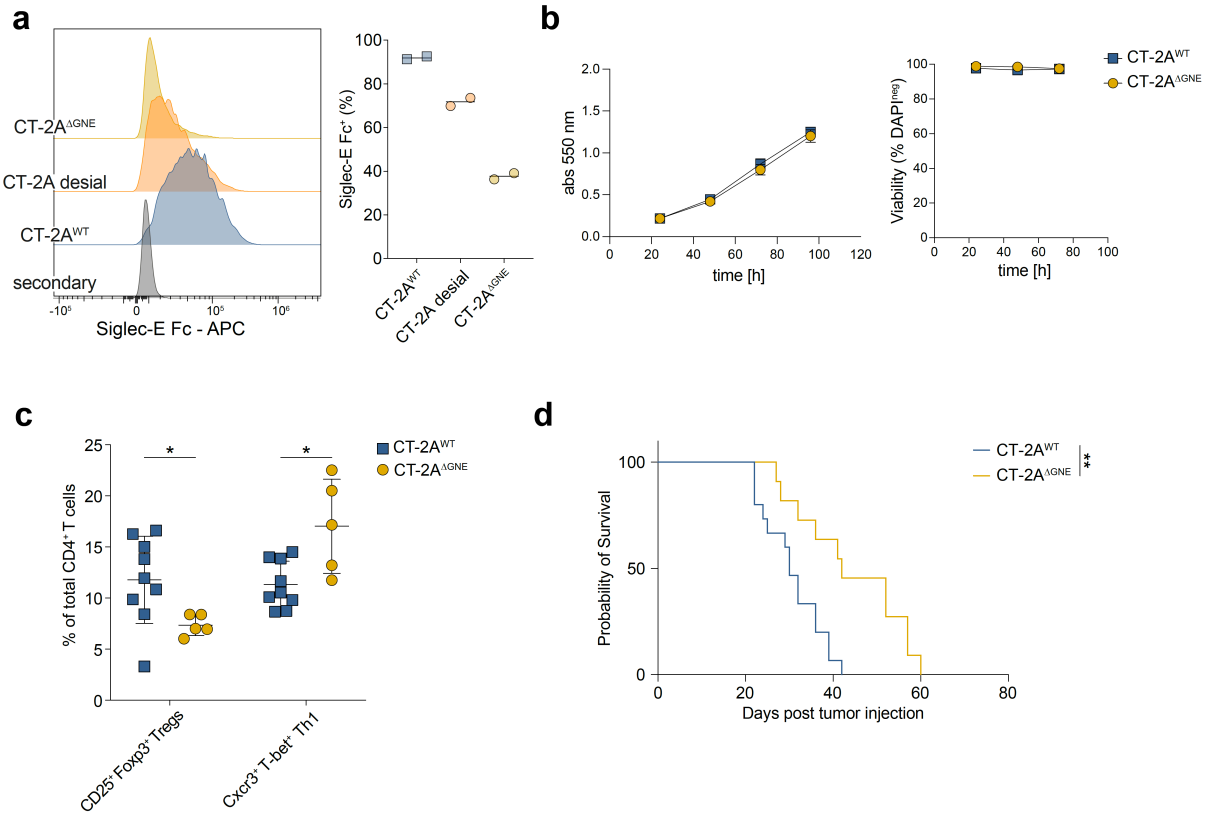

Supplementary Data Fig. 5 Generation of genetically desialylated CT-2A$^{\Delta GNE}$ cells. **a**, Representative histograms (left) and quantification (right) of binding of Siglec-E Fc to CT-2A^{WT}, enzymatically desialylated CT-2A cells (CT-2A desial) and GNE-deficient CT-2A cells (CT-2A$^{\Delta GNE}$) (n = two independent experimental replicates). **b**, In vitro proliferation (left) and cell viability (right) of CT-2A$^{\Delta GNE}$ and CT-2A^{WT} cells (n = two independent experimental replicates). **c**, Flow cytometry analysis showing percentage of CD25^{+} Foxp3^{+} Tregs and Cxcr3^{+} T-bet^{+} Th1 of total CD4^{+} T cells between CT-2A^{WT} and CT-2A$^{\Delta GNE}$ injected C57BL/6 wildtype mice (n =5-9 mice per group). Results were pooled from two independent experiments. **d**, Survival of CT-2A^{WT} and CT-2A$^{\Delta GNE}$ injected C57BL/6 wildtype mice (n =11-15 mice per group). Results were pooled from two independent experiments. Statistics: Data are presented as median (**a**) and mean ± SD (**b**, **c**), two-way ANOVA with Holm-Sidak's corrected multiple comparison test (**c**), log-rank Mantel-Cox test (**d**). *p ≤ 0.05, **p ≤ 0.01.

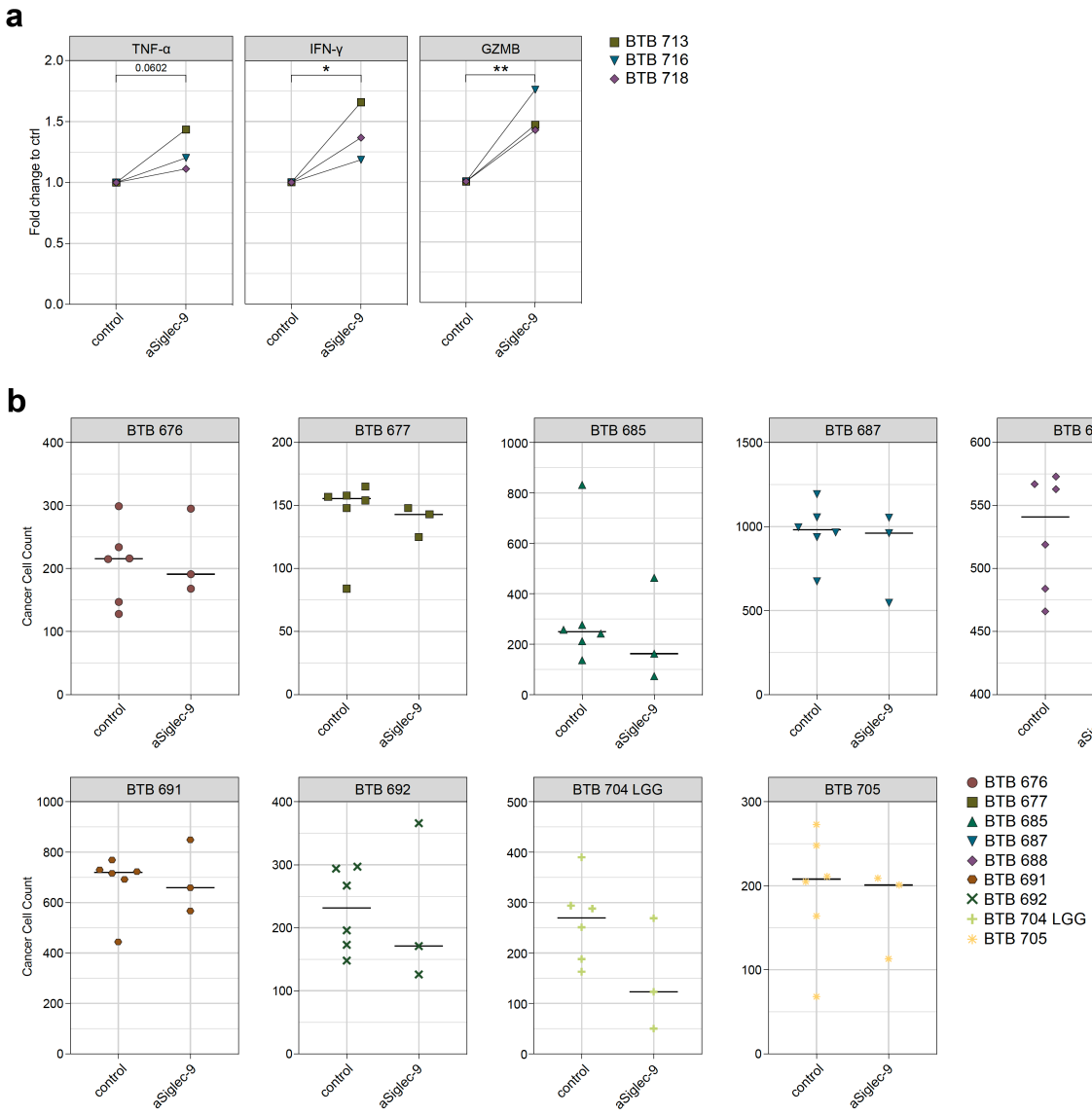

Supplementary Data Fig. 6 Siglec-9 blockade induces immune response and anti-tumor activity in human GBM explants.

a, Fold change of TNF-α, IFN-γ and GZMB secretion measured in anti-Siglec-9 treated versus control bioreactor media in responding patients (response defined as fold change > 1 in all three comparisons). **b**, Number of glioma cells in the different treatment conditions for each patient obtained on a single-cell resolution from the image analyses. Individual symbols represent technical replicates within the treatment conditions. Statistics: Data are presented as median (**b**), unpaired two-tailed Student's t test (**a**). *p ≤ 0.05, **p ≤ 0.01.

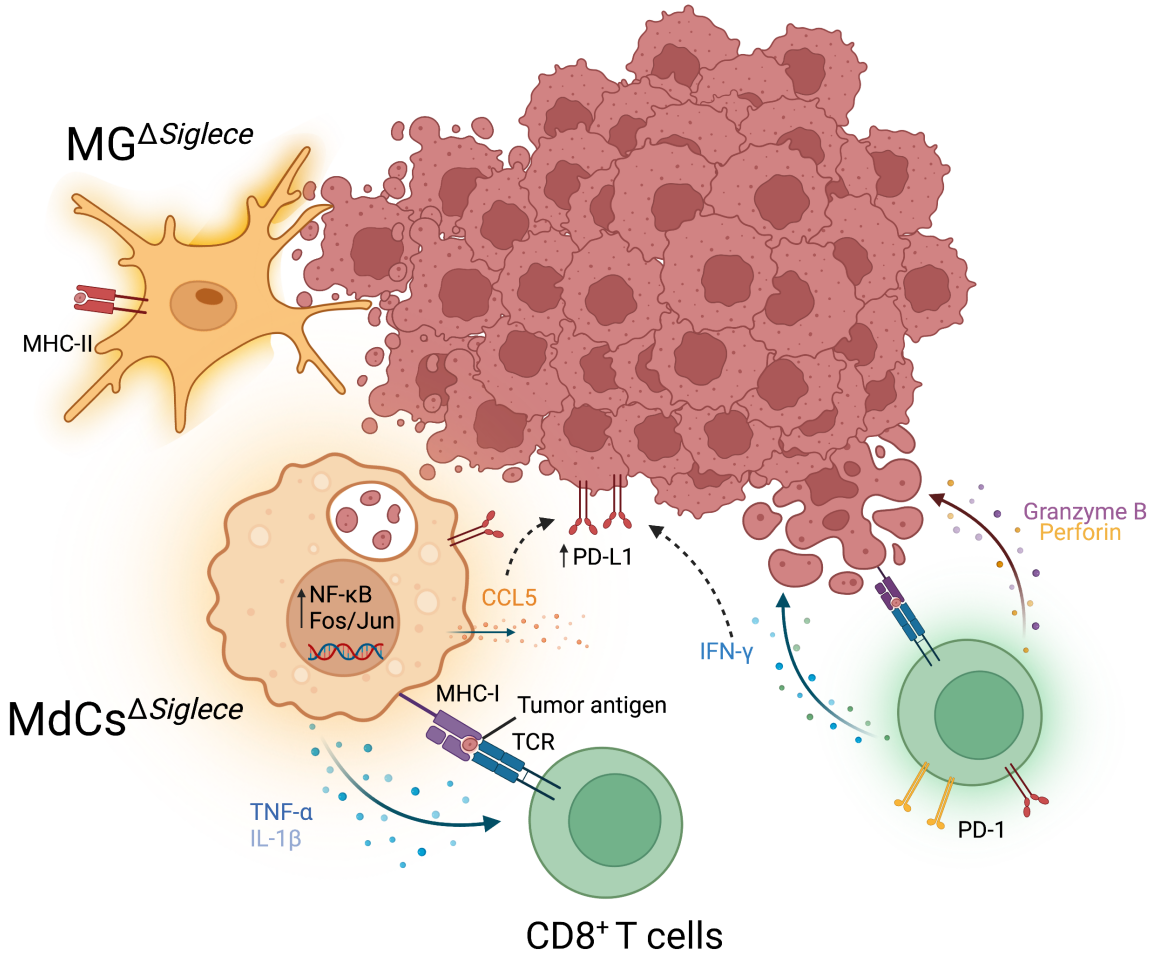

Supplementary Data Fig. 7 Graphical abstract.
Proposed mechanism of bridging of innate and adaptive immune responses upon Siglec-E deletion in microglia (MG) and monocyte-derived cells (MdCs). Created with BioRender.com.

Supplementary Data Table 1 Patient characteristics

ID	Sex	Age	Histo	Grade	Status	IDH	MGMT pro-motor	EGFR	Sub-class	Study
BTB 700R	M	51	GBM	IV	recur-rent	WT	meth-ylated	ampli-fied	classi-cal	Biore-actor
BTB 713	F	47	GBM	IV	primary	WT	meth-ylated	not ampli-fied	mesen-chymal	Biore-actor
BTB 714	M	61	GBM	IV	primary	WT	un-methyl ated	not ampli-fied	pro-neural	Biore-actor
BTB 716	M	72	GBM	IV	primary	WT	un-methyl ated	not ampli-fied	pro-neural	Biore-actor
BTB 718	M	59	GBM	IV	primary	WT	meth-ylated	ampli-fied	classi-cal	Biore-actor
BTB 676	M	71	GBM	IV	primary	WT	meth-ylated	ampli-fied	classi-cal	Phar-ma-cos
BTB 677	M	58	GBM	IV	primary	WT	un-methyl ated	not ampli-fied	classi-cal	Phar-ma-cos
BTB 685	M	63	GBM	IV	primary	WT	un-methyl ated	not ampli-fied	pro-neural	Phar-ma-cos
BTB 687	F	54	GBM	IV	primary	WT	meth-ylated	ampli-fied	pro-neural	Phar-ma-cos
BTB 688	F	72	GBM	IV	primary	WT	meth-ylated	not ampli-fied	mesen-chymal	Phar-ma-cos

BTB 691	M	63	GBM	IV	primary	WT	un-methylated	not amplified	pro-neural	Pharmacos
BTB 692	M	70	GBM	IV	primary	WT	methylated	amplified	classical	Pharmacos
BTB 704	M	62	LGG	I-II	primary	WT	un-methylated	not amplified	LGG	Pharmacos
BTB 705	F	78	GBM	IV	primary	WT	methylated	amplified	classical	Pharmacos

Supplementary Data Table 2 Anti-mouse Flow Cytometry Antibodies

Specificity	Clone	Fluorochrome	Manufacturer	Catalog #
CD45	30-F11	FITC	BioLegend	103107
CD45	30-F11	BV605	BioLegend	103140
CD45	30-F11	BV421	BioLegend	103134
CD45	30-F11	PE	BioLegend	103106
CD45.1	A20	PE-Cy7	BioLegend	110730
CD11b	M1/70	BV650	BioLegend	101259
CD11b	M1/70	APC-Cy7	BioLegend	101226
Cx3cr1	SA011F11	FITC	BioLegend	149020
Siglec-E	M1304A01	APC	BioLegend	677106
Siglec-E	M1304A01	PE	BioLegend	677104
Siglec-E	M1304A01	PerCP-Cy5.5	BioLegend	677114
CD163	S15049I	BV421	BioLegend	155309
CD163	S15049I	PE-Cy7	BioLegend	155320
CD86	GL-1	APC-Cy7	BioLegend	105030
CD80	16-10A1	PE-Cy7	BioLegend	104734
CD80	16-10A1	BV650	BioLegend	104732
I-A/I-E (MHC class II)	M5/114.15.2	PerCP-Cy5.5	BioLegend	107626
NK-1.1	PK136	PE-Cy5	BioLegend	108715
Ly-6G/Ly-6C (Gr-1)	RB6-8C5	AF647	BioLegend	108418
CD3e	145-2C11	PE-Cy7	BioLegend	100319
CD3e	145-2C11	APC-Cy7	BioLegend	100330
CD4	RM4-5	PerCP-Cy5.5	BioLegend	100540
CD8a	53-6.7	FITC	BioLegend	100706
CD8a	53-6.7	PE-Cy7	BioLegend	100722
CD8a	53-6.7	PerCP-Cy5.5	BioLegend	100734
PD-1	29F.1A12	APC-Cy7	BioLegend	135224
TIM-3	RMT3-23	APC	BioLegend	119705
LAG-3	C9B7W	BV421	BioLegend	125221
CTLA-4	UC10-4B9	PE	BioLegend	106306
PD-L1	10F.9G2	BV650	BioLegend	124336
IFN-γ	XMG 1.2	FITC	BioLegend	505806

IFN-γ	XMG 1.2	APC-Cy7	BioLegend	505850
IFN-γ	XMG 1.2	PE	BioLegend	505808
TNF-α	MP6-XT22	APC	BioLegend	506308
Ki-67	16A8	APC	BioLegend	652406
Ki-67	16A8	PE-Cy7	BioLegend	652426
CD25	PC61	APC	BioLegend	102012
CD69	H1.2F3	BV650	BioLegend	104541
CD69	H1.2F3	PerCP-Cy5.5	BioLegend	104522
CD44	IM7	PE	BioLegend	103008
CD107a	1D4B	PE-Cy7	BioLegend	121620
Cxcr3	CXCR3-173	BV650	BioLegend	126531
Foxp3	MF-14	AF488	BioLegend	126406
Foxp3	MF-14	PE	BioLegend	126404
T-bet	4B10	PE-Cy7	BioLegend	644824
Siglec-H	551	PerCP-Cy5.5	BioLegend	129614
CD22	OX-97	FITC	BioLegend	126106
Siglec-G	SH2.1	APC	eBioscience	17-5833-82
H-2Kb	AF6-88.5	APC	BioLegend	116518
H-2Kb-SIINFEKL	25-D1.16	APC	eBioscience	17-5743-82
IgG2a	RMG2a-62	APC	BioLegend	407110
IgG2a	RMG2a-62	BV421	BioLegend	407117
IgG	Polyclonal	AF488	Invitrogen	A32723

Supplementary Data Table 3 Anti-human Flow Cytometry Antibodies

Specificity	Clone	Fluorochrome	Manufacturer	Catalog #
CD45	2D1	BV510	BioLegend	368526
CD11b	ICRF44	BV650	BioLegend	301336
CX3CR1	2A9-1	PE-Cy7	BioLegend	341612
TMEM119	A16075D	-	BioLegend	853302
Siglec-1	7-239	AF647	BioLegend	346006
CD22	HIB22	AF647	BioLegend	302518
CD33	HIM3-4	FITC	BioLegend	303304
Siglec-5	1A5	PE	BioLegend	352004
Siglec-7	6-434	PE	BioLegend	339204
Siglec-8	7C9	APC	BioLegend	347106
Siglec-9	K8	APC	BioLegend	351506
Siglec-10	5G6	PE	BioLegend	347603

3.2 Single-cell characterization of human GBM reveals regional differences in tumor-infiltrating leukocyte activation

Philip Schmassmann[1], Julien Roux[2,3], Steffen Dettling[4], Sabrina Hogan[1], Tala Shekarian[1], Tomás A. Martins[1], Marie-Françoise Ritz[1], Sylvia Herter[5], Marina Bacac[5], and Gregor Hutter[1,6,*]

[1]Brain Tumor Immunotherapy Lab, Department of Biomedicine, University of Basel, Basel, Switzerland

[2]Bioinformatics Core Facility, Department of Biomedicine, University of Basel, Basel, Switzerland

[3]Swiss Institute of Bioinformatics, Basel, Switzerland

[4]Roche Pharmaceutical Research and Early Development, Roche Innovation Center Munich, Penzberg, Germany

[5]Roche Pharmaceutical Research and Early Development, Roche Innovation Center Zürich, Schlieren, Switzerland

[6]Department of Neurosurgery, University Hospital Basel, Basel, Switzerland

- submitted to eLife -

currently under peer-review

bioRxiv pre-print: https://doi.org/10.1101/2022.06.17.496574

3.2.1 Abstract

Glioblastoma (GBM) harbors a highly immunosuppressive tumor microenvironment (TME) which influences glioma growth. Major efforts have been undertaken to describe the TME on a single-cell level. However, human data on regional differences within the TME remain scarce. Here, we performed high-depth single-cell RNA sequencing (scRNAseq) on paired biopsies from the tumor center, peripheral infiltration zone and blood of five primary GBM patients. Through analysis of > 45'000 cells, we revealed a regionally distinct transcription profile of microglia (MG) and monocyte-derived macrophages (MdMs) and an impaired activation signature in the tumor-peripheral cytotoxic-cell compartment. Comparing tumor-infiltrating $CD8^+$ T cells with circulating cells identified $CX3CR1^{high}$ and $CX3CR1^{int}$ $CD8^+$ T cells with effector and memory phenotype, respectively, enriched in blood but absent in the TME. Tumor $CD8^+$ T cells displayed a tissue-resident memory phenotype with dysfunctional features. Our analysis provides a regionally-resolved mapping of transcriptional states in GBM-associated leukocytes, serving as an additional asset to the research community in their effort to uncover novel therapeutic strategies to combat this fatal disease.

3.2.2 Introduction

Glioblastoma (GBM) is a fatal disease without effective long-term treatment options. The current standard of care consists of tumor resection followed by adjuvant chemoradiotherapy resulting in a median overall survival of only 14 months [8]. One of the hallmarks in GBM progression is the high rate of neovascularization. The GBM-induced aberrant vessels not only nourish glioma cells, but also provide a specialized niche for tumor-associated stromal and immune cells such as monocyte-derived macrophages (MdMs), yolk sac-derived microglia (MG) (together termed glioma-associated macrophages/microglia, GAMs), and peripheral adaptive immune cells. This immune tumor microenvironment (iTME) paradoxically acts in an immunosuppressive manner and promotes tumor progression [10]. For example, clinical trials of systemic T cell checkpoint blockade showed only disappointing results [110, 111], which was attributed in part to the immunosuppressive components of the GBM iTME. The origin of GAMs, infiltration of peripherally derived macrophages across the blood-brain-barrier (BBB) or recruitment of tissue-resident MG to the tumor site, as well as their contribution to gliomagenesis are studied intensively [10, 128, 129, 173]. Hence, major efforts have been undertaken to describe the GBM iTME on a single cell level [128,

129, 174]. Or dissect the composition and changes upon disease stages, recurrence and immunotherapy specifically within the GAM compartment [175-177]. However, human data on the composition of the iTME in different tumor regions (contrast enhancing tumor center versus peripheral infiltration zone) remain scarce [178, 179].

To study the region-dependent cellular diversity within individual GBMs, we performed single-cell RNA sequencing (scRNA-seq) on patient-matched biopsies from the tumor center and the peripheral infiltration zone of five primary GBM patients. Additionally, peripheral blood mononuclear cells (PBMC) of the same patients were included to explore the transcriptional changes occurring during tumor infiltration of circulating immune cells.

Our analysis revealed a regionally distinct transcription profile of MG and MdMs and an impaired activation signature in the tumor-peripheral cytotoxic-cell compartment. Comparing tumor-infiltrating $CD8^+$ T cells with PBMC-derived, identified $CX3CR1^{high}$ and $CX3CR1^{int}$ $CD8^+$ T cells with effector and memory phenotype, respectively, enriched in blood but absent in the iTME. Tumor $CD8^+$ T cells displayed features of tissue-resident memory T cells and were characterized by an exhaustion phenotype. This work provides a regionally-resolved map of transcriptional states in glioma-associated cell types complemented by patient-matched PBMCs, revealing an abundance of information about the composition and molecular diversity of the iTME in GBM.

3.2.3 Results

3.2.3.1 scRNA-seq analysis of paired tumor center, periphery and PBMC samples

Fresh, neurosurgically resected tissue from five primary, treatment-naive GBM patients were harvested (Figure 1A, Appendix 1 - table 1). According to the 2021 WHO Classification of Tumors of the Central Nervous System [180], in which the term glioblastoma designates only IDH-wildtype grade 4 tumors, we will hence use the term grade 4 glioma, as we included as well IDH-mutant grade 4 tumors (Appendix 1 - table 1). The tumor center was defined as contrast enhancing, whereas the tumor periphery was defined as T2 hyperintense by magnetic resonance imaging (MRI)-guided, navigated surgical resection (Figure 1B). Increased cellular density of the center vs. periphery samples was confirmed by nuclear DAPI staining on matched histological micrographs of the resected tissue specimens used for scRNA-seq (Figure 1C). As outlined in Figure 1A, we separately processed patient tumor and blood samples and

enriched them for immune cells by fluorescence-activated cell sorting (FACS) (Figure 1 – figure supplement 1A and 1B). The three samples per patient (center, periphery and PBMC) were loaded on different wells of a 10x Genomics Chromium system for a targeted recovery of 10,000 cells. Due to technical issues cells from the center sample of patient BTB 609 could not be collected.

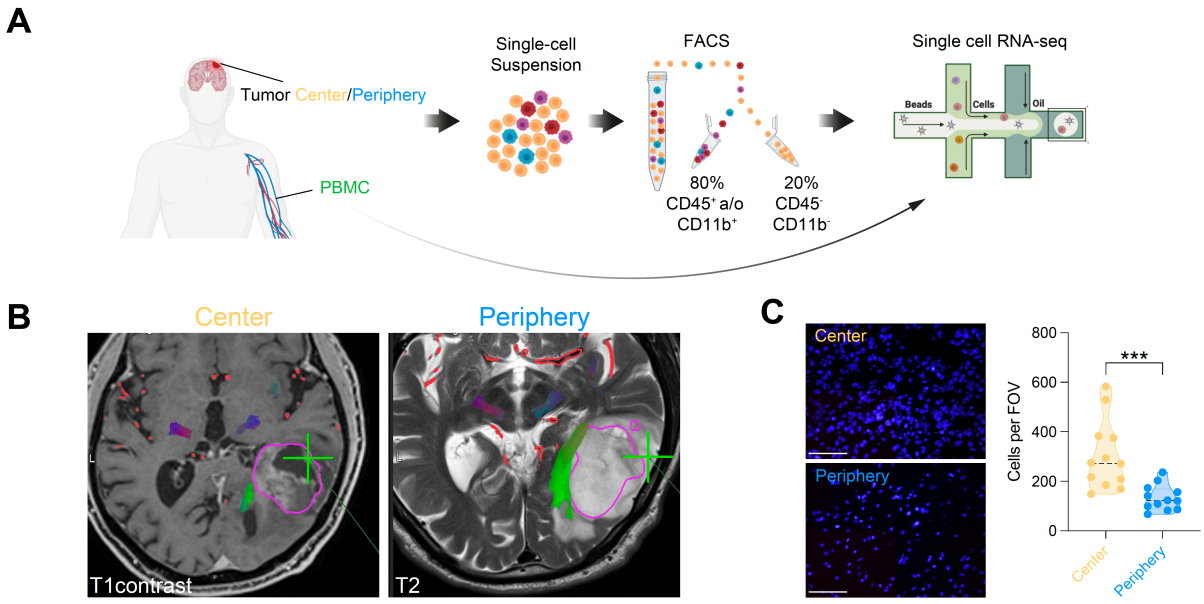

Figure 1 Single-cell RNA-seq of cells from tumor center, periphery and blood.
(A) Experimental workflow for single-cell analysis of cells isolated from tumor center, periphery and peripheral blood mononuclear cells (PBMC), including fluorescent-activated cell sorting and 3'-scRNA-seq. (**B)** Axial T1 with contrast (left) and T2 (right) MRI brain in a patient with a left temporal GBM. Fresh tumor biopsies were taken according to neuronavigation (green cross). The tumor center was defined as contrast enhancing, whereas the tumor periphery was defined as T2 hyperintense. (**C)** Nuclear DAPI staining of resected tissue specimens. 40x magnification (scale bar = 20 μm). n = 3 patients, 4 field of view (FOV) per patient. Statistics: ****p* < 0.001, two-tailed Mann Whitney U test.

In total we analyzed 45,466 cells that passed initial quality control and filtering, comprising 8,254 cells from tumor center, 5,954 cells from tumor periphery and 31,258 PBMCs, with 6,354 to 10,957 cells per patient (Figure 1 – figure supplement 1C-1F). All cells were projected onto a two dimensions *t*-distributed stochastic neighbor embedding (tSNE) [181]. As we observed a good overlap of cells across patients, we chose not to perform any correction for patient-specific effects (Figure 1 – figure supplement 1G). Using hierarchical clustering, the cells were partitioned into clusters (Figure 2 – figure supplement 1A) which were then annotated into eight distinct cell types for the immune subset and five cell types for the CD45 negative subset (Figure 2A; Figure 2 – figure supplement 1B, 1C). Notably: the annotation of most of the immune

cell types was performed by whole-transcriptome comparison of our cells to a reference dataset of bulk RNA-seq samples of sorted immune cell types from human PBMC (Figure 2 – figure supplement 1D) [182]; the annotation of MdMs and microglia was performed by whole-transcriptome comparison to a dataset of bulk RNA-seq samples of sorted immune cell types from the tumor microenvironment of human gliomas (Figure 2 – figure supplement 1E) [128] and using signature scores defined from scRNA-seq of GAMs (Figure 2 – figure supplement 1F-1G) [173]; finally, CD45 negative cells were annotated by whole-transcriptome comparison to a scRNA-seq dataset of *IDH1*^{wt} GBM (Figure 2 – figure supplement 1H, 1I) [183]. The expression of known marker genes across cell types is shown in Figure 2B, and genes whose expression is most specific to each cell type are shown in Figure 2 – figure supplement 2.

To perform a differential expression analysis between tumor sites, we stratified the analysis by annotated cell type and aggregated cells from each patient (see Methods). A principal component analysis (PCA) on the aggregated transcriptome data confirmed that the major source of variation was the cell type lineage (Figure 2C), with notable differences between lymphoid, MG/myeloid cells, and CD45^{-} cells (PCs 1 and 2). Although, there was no clear association between patient *IDH1* status and these or deeper components. Our study was neither designed nor powered to find regional signatures within the iTME depending on *IDH1* status, but rather to identify common transcriptional differences within the iTME between tumor center, periphery and PBMC of *IDH1*^{wt} and *IDH1*^{mut} grade 4 glioma.

Differential abundance analysis between tumor center and periphery only revealed significant changes within the MdM cluster. Where the proportion of MdM cells among leukocytes decreased substantially in the glioma periphery (Figure 2D).

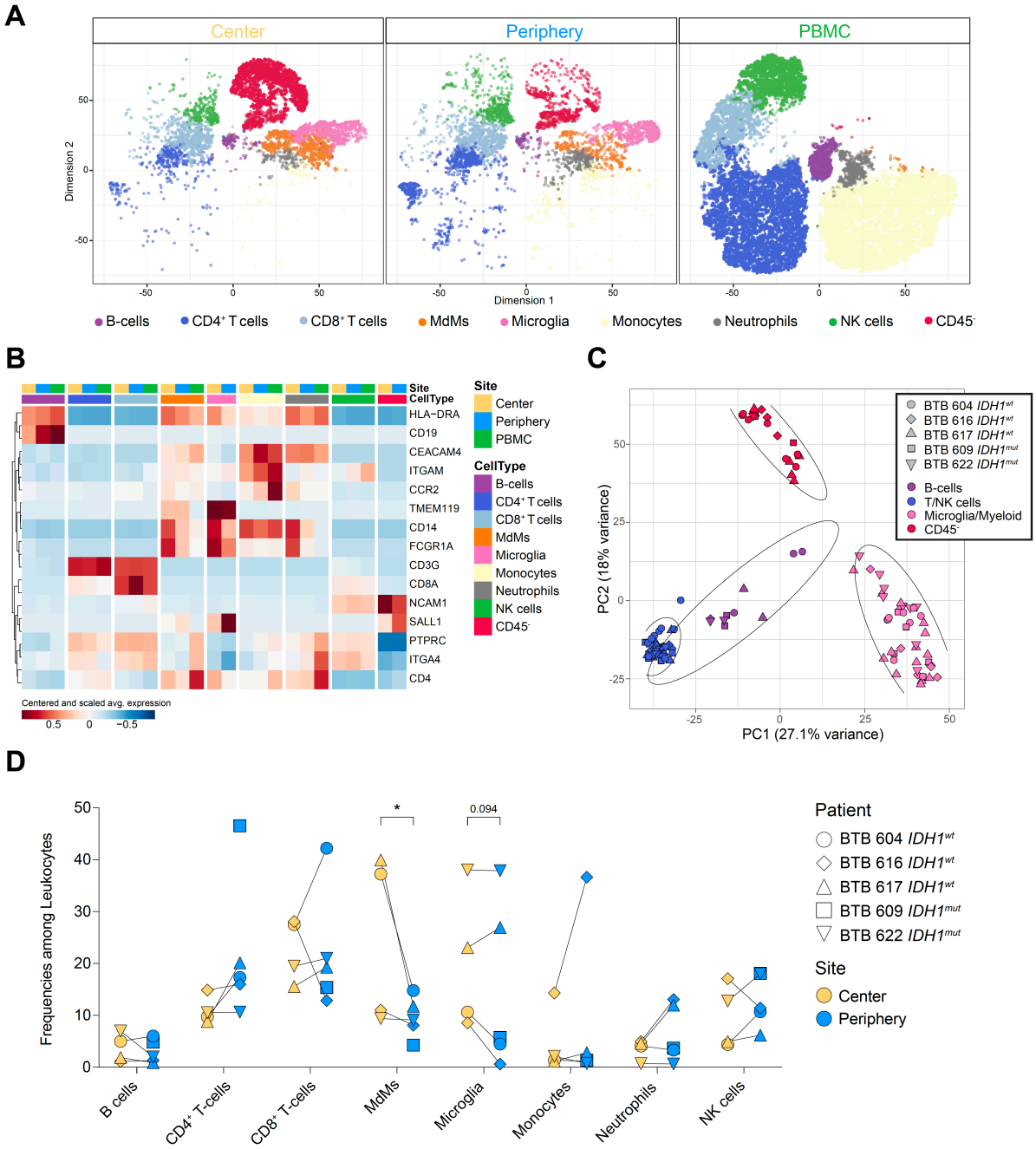

Figure 2 Single-cell RNA-seq analysis identifies main immune cell populations.
(A) Dimensionally reduced tSNE projection of the scRNAseq data showing the identified main cell clusters. (**B)** Heatmap displaying centered and scaled normalized average expression values of characteristic cell-type specific genes used to annotate clusters in (**A**). Columns are ordered by site and cell type, and rows show centered and scaled expression values, hierarchically clustered. (**C)** Principal component (PC) biplot of pseudo-bulk scRNAseq samples aggregated by patient and cell type. Symbols represent individual patients and cell lineage is displayed by different colors. (**D)** Relative frequencies of immune populations among leukocytes between tumor center and periphery. Symbols represent individual patients and paired samples are indicated by connecting lines. Statistics: *FDR<5%, *diffcyt-DA-voom* method.

3.2.3.2 MG and MdMs display regionally distinct transcription profiles

Differential expression analysis between MG from tumor center and periphery revealed a highly significant downregulation of inflammatory genes in the peripheral MG. This included scavenger receptors (*CD36* and *MARCO*), chemokines (*CXCL3* and *CCL20*) and immune receptors (*IL7R [184]* and *CD109*, a negative regulator of TGF-β signaling [185]) as well as genes involved in cell growth (*CSRP1*) and cell metabolism (*SMPDL3A [186]* and *SDS*) (Figure 3A).

Interestingly, we found upregulation of Inhibitor of DNA-Binding 1, also known as Inhibitor of Differentiation 1 (*ID1*) in the peripheral MG, which is well described in GBM progression, treatment resistance and glioma stem cell biology [187]. Recently, new evidence has emerged, linking *ID1* to suppression of the anti-tumor immune response in the myeloid compartment and promoting tumor progression [188].

To further explore the underlying biological processes differing between MG in the two compartments, we conducted a gene set enrichment analysis (GSEA) on the results of the differential expression analysis using Gene Ontology (GO) database (Biological Processes). This revealed overall a significant downregulation of GO categories involved in antigen processing and presentation via MHC-I and MHC-II in the peripheral MG relative to the center MG, as well as downregulation of amino acid metabolism and TNF-α signaling pathway (Figure 3B), which supported the conclusion of an impaired activation state of peripheral MG.

When comparing the transcriptional profile of MdMs from the peripheral front to the tumor center, we observed upregulation of proinflammatory genes *MEFV* encoding pyrin [189] and *APOBEC3A,* a cytidine deaminase involved in RNA editing during macrophage M1 polarization and response to interferons (IFN) [190]. Moreover, upregulation of *KCNJ2*, a voltage-dependent potassium channel has been shown to regulate macrophage proliferation [191] whereas *GPR132* serves as lactate sensor in the acidic TME and could potentially facilitate MdM migration to the tumor site [192]. *MIR22HG*, a long non-coding RNA (lncRNA) has been associated with tumor suppressive properties in hepatocellular carcinoma, where it has been linked to chemokine signaling pathways and phagosome activation [193] (Figure 3C).

Along with this, we observed downregulation of anti-inflammatory genes in the peripheral MdMs. This included *RNASE1*, a signature gene of macrophages enriched

in immune checkpoint inhibitor (ICI) non-responding melanoma patients [194], *PLTP*, a negative regulator of NF-κB activation [195], *NRP1*, a key gene required for macrophage attraction towards hypoxic tumor niches and thereby retaining their pro-tumorigenic features [196], and *IL4I1*, a novel metabolic immune checkpoint in the tryptophan/aryl hydrocarbon receptor (AHR) pathway [197] (Figure 3C). Hence, MdMs might display a proinflammatory phenotype in the glioma periphery, however, are less abundant there (Figure 2D).

We observed a marked downregulation of *SDS* in the peripheral MdMs, similar to the peripheral MG population, leading to a presumptive accumulation of L-serine in the peripheral MdMs. In contrast to MG, serine metabolism has been shown to indeed support proinflammatory IL-1β cytokine production in macrophages [198]. Together with the reduced tryptophan metabolism through *IL4I1* and downregulated *SLC39A8*, a transmembrane zinc importer whose reduction has been linked to increased IL-6/IL-1β secretion and increased NF-κB signaling in innate immunity [199], these data shed new light on regional differences in the innate immunometabolism in the iTME of grade 4 glioma.

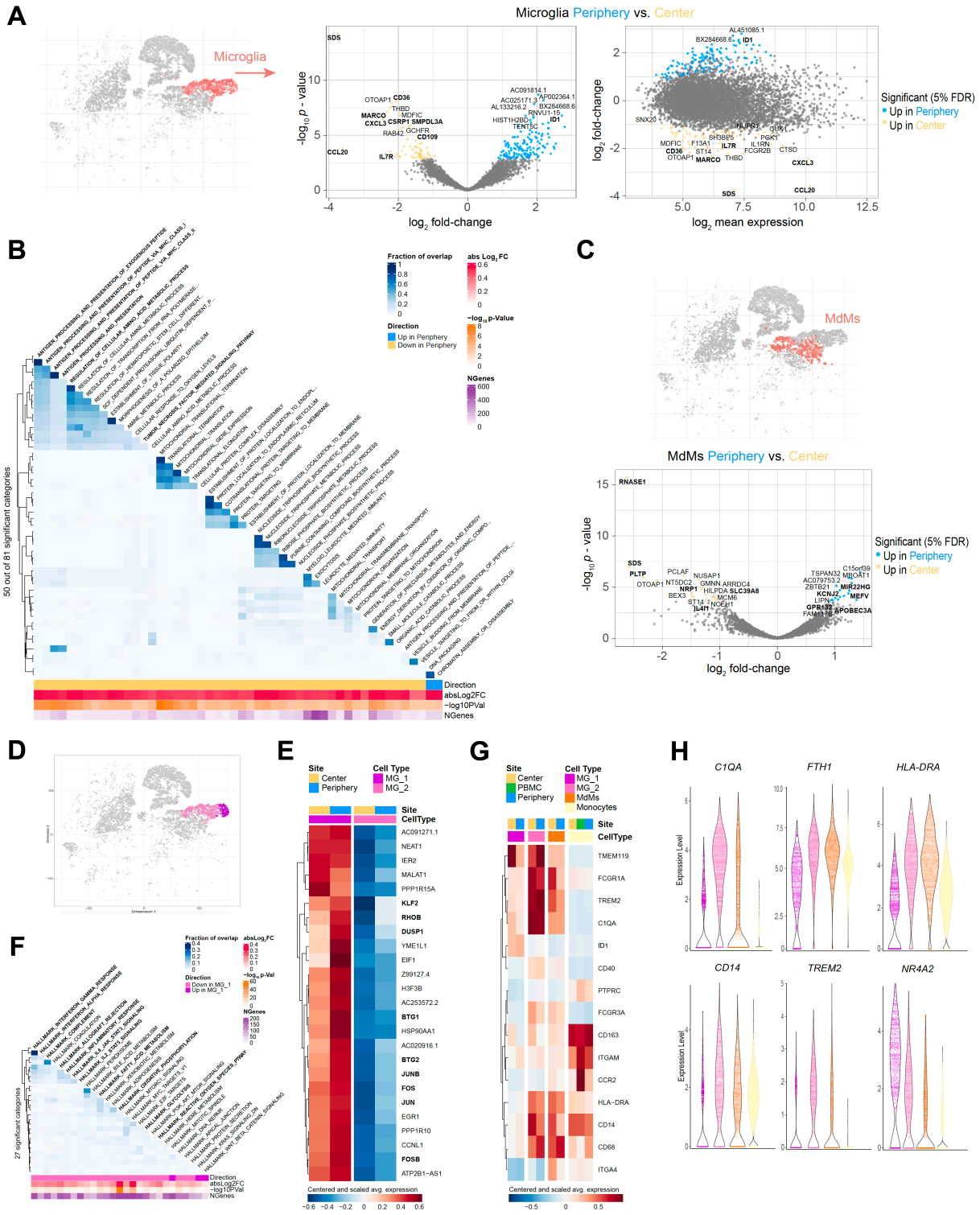

Figure 3 MG and MdMs display distinct regional transcription profiles.
(A) Microglia cluster highlighted on tSNE map and scatterplots showing differentially expressed genes (FDR<5%, indicated by blue and yellow) in Microglia (MG) cells from tumor periphery versus center. Volcano plot showing *p* value versus fold-change (left) and MA plot showing fold-change versus mean expression (right). **(B)** Heatmap representation of Gene set enrichment analysis (GSEA) results between peripheral and center microglia using Gene Ontology (GO) collection (Biological Processes). The fraction of overlap between gene sets is calculated as Jaccard coefficient of overlap between the gene sets. **(C)** Monocyte-derived

macrophages (MdMs) cluster highlighted on tSNE map and volcano plot showing statistical significance (FDR<5%, indicated by blue and yellow) versus fold-change of differentially expressed genes in MdMs from tumor periphery versus tumor center. (**D)** Unsupervised hierarchical sub-clustering of the MG population revealed two transcriptionally distinct subsets of MG, termed MG_1 and MG_2, displayed on the tSNE map. € Heatmap displaying the cluster-specific genes identifying MG_1 and MG_2 subclusters. Columns are ordered by site and cell type, and rows show centered and scaled normalized average expression values, hierarchically clustered. (**F)** Heatmap representation of GSEA between MG_1 and MG_2 subclusters using Hallmark collection of major biological categories. (**G)** Heatmap displaying previously described reactivity markers of MG. Columns are ordered by site and cell type, and rows show centered and scaled normalized average expression values, hierarchically clustered. (**H)** Violin plot showing expression levels of selected reactivity markers among mononuclear phagocyte populations.

3.2.3.3 The iTME of grade 4 glioma harbors two transcriptionally distinct MG subpopulations

Unsupervised hierarchical sub-clustering of the MG population revealed two transcriptionally distinct iTME MG subsets, which we termed MG_1 and MG_2, respectively (Figure 3D and 3E). The MG_1 cluster was highly enriched for the activator protein-1 (AP-1) family of transcription factors including *FOS, FOSB, JUN, JUNB, MAF* and *MAFB* (Figure 3E), which convey a surveilling phenotype to adult MG, but are also involved in numerous processes including cell growth, differentiation and immune activation [200]. Specifically, *FOSB* gene products have been implicated in the excitotoxic MG activation by regulating complement C5a receptor expression [201]. Yet, concomitant upregulation of anti-inflammatory Krüppel-like factor 2 (*KLF2*) [202] and Dual Specificity Protein Phosphatase 1 (*DUSP1*), an inhibitor of innate inflammation by negatively regulating the mitogen-activated protein kinase (MAPK) pathway [203], together with increased expression of anti-proliferative genes like *RHOB, BTG1* and *BTG2* paint a more complex picture of these cells. Particularly, *BTG1* has been identified as an activation-induced apoptotic sensitizer in MG after exposure to inflammatory stimuli [204], serving as an autoregulatory mechanism and possibly hinting towards an exhausted state in these MG_1 cells. GSEA for differences between MG_1 and MG_2 clusters using the MSigDB Hallmark collection of major biological pathways [205] revealed downregulation of many MG effector functions in the MG_1 population including (1) inflammation (“Complement”, “Inflammatory Response”, “Allograft Rejection”, “Reactive Oxygen Species Pathway”), (2) immune cell activation (“IFN-α Response”, “IFN-γ Response”, “IL6 JAK STAT3 Signaling”, “IL2 STAT5 Signaling”) and (3) immunometabolism (“Fatty Acid Metabolism”, Oxidative Phosphorylation”, “Glycolysis”) (Figure

3F). As we examined the expression of previously described reactivity markers of MG including *C1QA,* Ferritin (*FTH1*), *FCGR1A, HLA-DRA, CD14* and *TREM2 [206-209],* and established MG homeostatic genes like *CX3CR1, HEXB* and *SPI1* (PU.1), we noted a marked downregulation of these genes in the MG_1 cluster, while the anti-inflammatory transcription factors *NR4A2* [210] and *NR4A1* [211] were highly upregulated (Figure 3G, 3H, Figure 3 – figure supplement 1A). Additionally, while total MG didn't show differences in abundance between tumor sites (Figure 2D), changes could be observed when stratifying for MG subclusters. We noted in 3 of 4 (75%) paired center-periphery samples an increased abundance of MG_1 cells in the tumor periphery. And, the presumably more reactive MG_2 cells concomitantly decreased significantly in frequency in the tumor periphery (Figure 3 – figure supplement 1B). Collectively, these data argue for the non-reactive/exhausted phenotype of MG_1.

3.2.3.4 The tumor peripheral cytotoxic cell compartment exhibits an impaired activation signature

Next, we investigated the regional differences in the lymphoid compartment composed of $CD4^+$ and $CD8^+$ T cells and natural killer (NK) cells. We observed only very few significant changes in the transcriptomic profiles of $CD4^+$ T cells between tumor center and periphery (Figure 4 – figure supplement 1A). Yet, comparing peripheral $CD8^+$ T cells with $CD8^+$ T cells from tumor center revealed 110 differentially expressed genes (43 genes upregulated and 67 genes downregulated) (Figure 4A). Many downregulated genes in the peripheral $CD8^+$ T cells associated with canonical IFN responses (*IFI6, IFI27, MX1, STAT1, EPSTI1 PARP9, ISG15)* [212] cell proliferation (*STMN1, CENPF, HELLS, NUSAP1* and *DNPH1*) and T cell co-stimulation (*CD28, TMIGD2* (CD28H), *TNFRSF4* (OX40), *CD27* and *TNFRSF18* (GITR)) (Figure 4A). Contrary to our expectations, we saw upregulation of *CTLA4* in the center $CD8^+$ T cells which acts as a negative costimulatory molecule. However, unlike other costimulatory receptors, such as CD27 and CD28, CTLA-4 is not constitutively expressed on T lymphocytes [213]. but only induced following T cell activation, along with positive costimulatory molecules such as OX40 and GITR. In addition, upregulation of CTLA-4 requires entry into the cell cycle [213]. In line with that, we detected an upregulation of proliferative genes in center $CD8^+$ T cells. In summary, CTLA-4 induction in center $CD8^+$ T cells rather suggested T cell activation than exhaustion, especially since other inhibitory receptors like *PDCD1* (PD-1), *LAG3* and *HAVCR2* (TIM-3) were not

differentially expressed between sites. Moreover, we did not observe differential expression of genes involved in CD8⁺ T cell effector functions like cytotoxicity (e.g., *GZMK, GZMB, KLRG1,* PRF1) or cytokines (e.g., *CCL5, XCL1, XCL2, IL10*). Yet, we noted upregulation of inhibitory genes (*TGFB1* and *FCRL6* [214]) in the peripheral CD8⁺ T cells, suggesting that a pool of activated, proliferating and IFN-responsive CD8⁺ T cells is present in the tumor center, but fails to populate the infiltrative tumor periphery.

Similar trends were observed for the peripheral NK cell population with peripherally reduced IFN response (*MX1* and *IFI44L*), and proliferative genes (*STMN1, HELLS, CENPF, PTTG1* and *DNPH1*), downregulated stimulatory receptors (*TMIGD2* (CD28H) and *TNFRSF18* (GITR)), and reduced NF-κB signaling (*NFKB1* and *RELB*) (Figure 4B). Although, we observed upregulation of key genes associated with NK cell effector function in the periphery (e.g., *FCGR3A* (CD16), *FGFBP2, ITGB2, GZMH* and *KIR2DS4*), increased expression of inhibitory receptors like *LILRB1* and *KLRG1*, the latter especially in co-expression with chemokine receptor *CX3CR1*, identified the peripheral NK cells rather to be terminally differentiated with impaired cytotoxic capabilities [215]. This was in line with the observed abrogated cytokine activity profile in the peripheral NK cells with reduced expression of key factors like *XCL1, XCL2, LTB* and *CKLF.* In summary, our data revealed an impaired activation signature in the peripheral cytotoxic cell compartment.

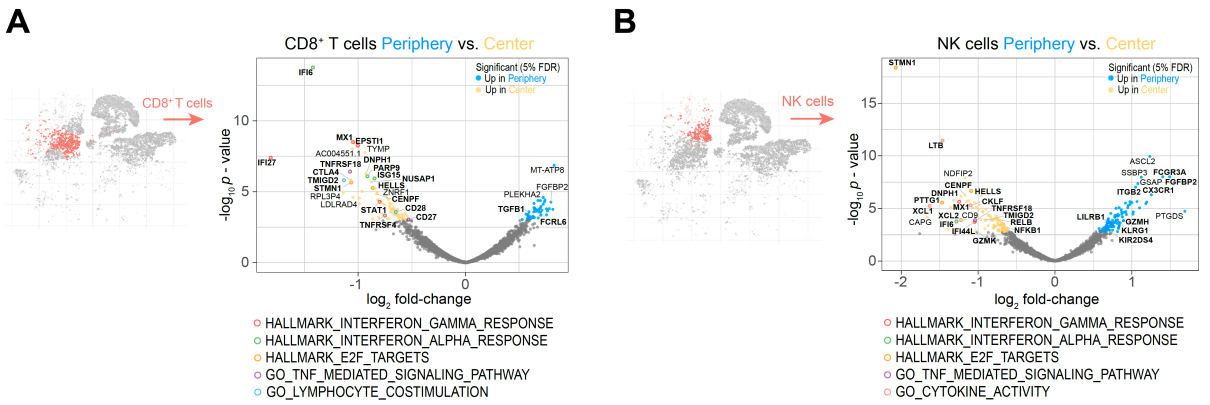

Figure 4 The peripheral cytotoxic cell compartment exhibits an impaired activation signature.
(A, B) Volcano plots showing differentially expressed genes (FDR corrected *p* value < 0.05, indicated by blue and yellow) in CD8⁺ T cells (**A**) and NK cells (**B**) from tumor periphery versus tumor center. Colored rings mark genes belonging to selected GSEA Hallmark or Gene Ontology (GO) pathways as indicated.

3.2.3.5 CX3CR1 labels a specific CD8⁺ T cell population in the circulation of grade 4 glioma patients

Next, we investigated the relationships between circulating $CD8^+$ T cells and those from the tumor milieu and, more specifically, the peripheral, infiltration zone characterized by an abrogated $CD8^+$ T-cell IFN response and activation signature. Strikingly, there were large transcriptomic differences between PBMC and periphery $CD8^+$ T cells (Figure 5A), with 1,417 differentially expressed genes (864 genes upregulated in the tumor periphery and 553 genes upregulated in PBMC) (Figure 5B).

Interestingly, one of the key genes upregulated in PBMC $CD8^+$ T cells was the chemokine receptor *CX3CR1*, whose expression labelled a specific population among these cells (Figure 5C). Flow cytometry of an additional matched glioma grade 4 patient cohort confirmed an increased abundance of $CX3CR1^+$ $CD8^+$ T cells in PBMC compared to almost absent $CX3CR1^+$ $CD8^+$ T cells in tumor periphery (Figure 5D, Figure 5 – figure supplement 1A, Appendix 1 - table 1).

Recently, expression of CX3CR1 was demonstrated to distinguish memory $CD8^+$ T cells with cytotoxic effector function [216]. Further characterization of classical central memory (T_{cm}) and effector memory (T_{em}) populations by varying surface expression levels of CX3CR1 identified a novel $CX3CR1^{int}$ subpopulation, termed peripheral memory (T_{pm}). T_{pm} cells underwent frequent homeostatic divisions, re-acquired CD62L, homed to lymph nodes, and predominantly surveyed peripheral tissues compared to T_{cm} and T_{em} [217]. In our dataset, the circulating $CX3CR1^+$ $CD8^+$ T cells indeed displayed a core signature of memory $CD8^+$ T cells with effector function, comprising expression of LFA-1 (*IGAL- ITGB2*), *EOMES, SELL* (CD62L), $CCR7^{low}$, $CD27^{low}$, $TBX21^{high}$ (Tbet), *IL7R, TCF7, FAS* and *ITGB1,* separating them from circulating $CX3CR1^-$ $CD28^{high}$, $CD27^{high}$ and $IL7R^{high}$ naive $CD8^+$ T cells (Figure 5E and Figure 5 – figure supplement 1B). The observed high expression of cytolytic molecules *GZMB* (Granzyme B) and *PRF1* (Perforin 1) in the $CX3CR1^+$ cells advocated for their cytotoxic effector phenotype (Figure 5N). Flow cytometric analysis confirmed T_{eff} to be $CX3CR1^{high}$, with negligible expression levels in the naive $CD8^+$ T cells, whereas the identified memory $CD8^+$ T cells (T_{em} and T_{pm}) were $CX3CR1^{int}$ (Figure 5F, 5G). Collectively, surface expression analysis of CX3CR1 identified a subset of $CX3CR1^{high}$ T_{eff} and $CX3CR1^{int}$ memory (T_{em}, T_{pm}) $CD8^+$ T cells in the circulation of grade 4 glioma

patients with potentially elevated tissue surveilling properties in the case of T_{pm}, which are, however, largely absent in the tumor microenvironment.

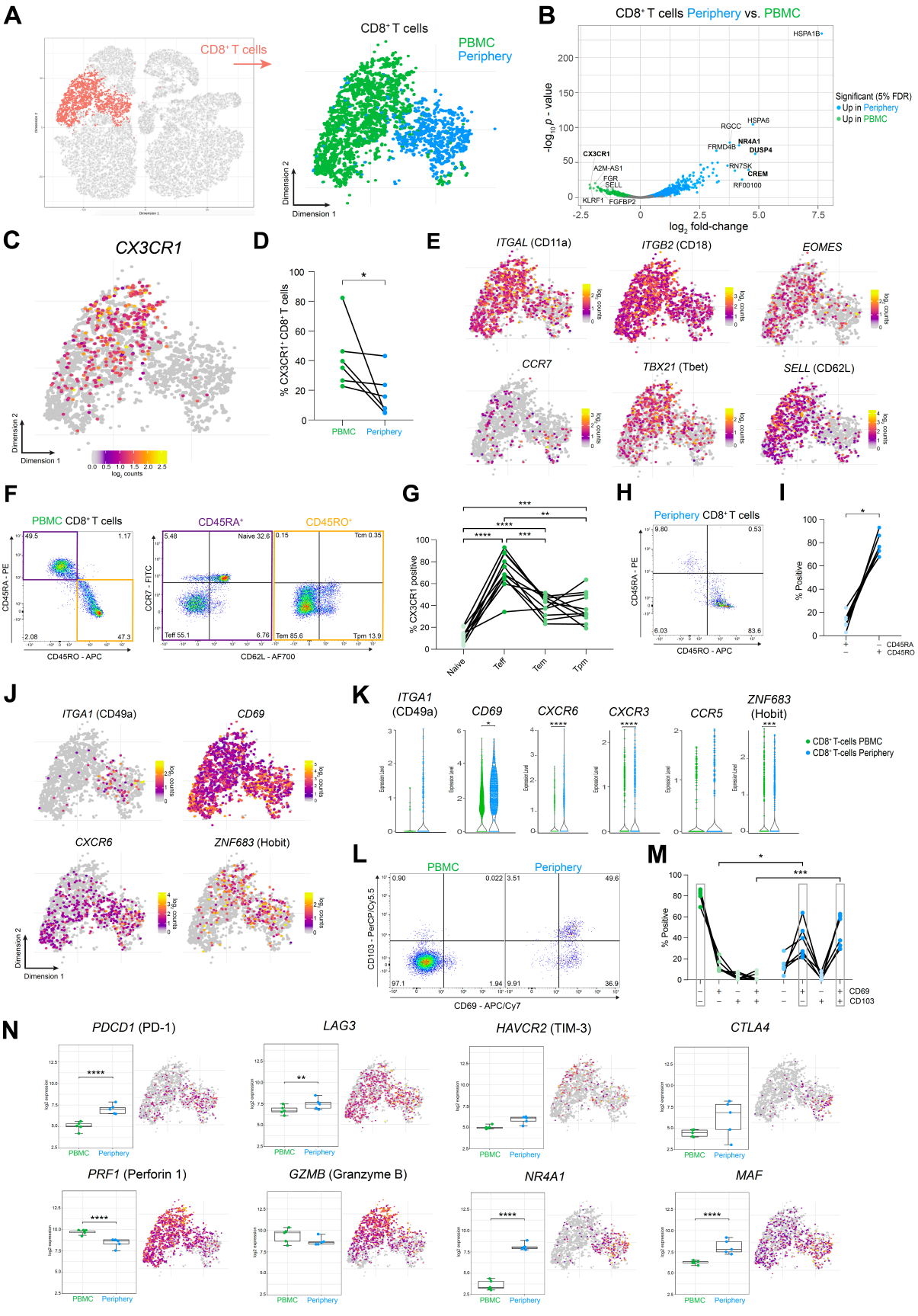

Figure 5 CD8$^+$ T cells in grade 4 glioma show distinct memory phenotypes depending on site.
(A) CD8$^+$ T cell cluster highlighted on tSNE map (left). CD8$^+$ T cell cluster colored by site of origin (right). (**B)** Volcano plot showing differentially expressed genes (FDR corrected *p* value < 0.05, indicated by blue and green) in CD8$^+$ T cells from tumor-periphery versus PBMC. (**C)** Expression of *CX3CR1* overlaid on tSNE CD8$^+$ T cell cluster. (**D)** Frequency of CX3CR1$^+$ CD8$^+$ T cells among all CD8$^+$ T cells in flow cytometry data. (**E)** Expression of genes associated with memory (upper row) and effector memory (lower row) phenotype overlaid on tSNE CD8$^+$ T cell cluster. (**F)** Gating procedure applied to identify CD3$^+$ CD8$^+$ naive, T effector cells (T_{eff}), effector memory (T_{em}), peripheral memory (T_{pm}) and central memory (T_{cm}), eluted from PBMCs. (**G)** Expression of CX3CR1 in CD8$^+$ T cell subpopulations identified in (**F**). (**H)** Representative dot plot of tumor-periphery CD8$^+$ T cells stained for CD45RA and CD45RO. (**I)** Quantification of tumor-periphery CD8$^+$ T cells expressing CD45RA or CD45RO. (**J)** Expression of genes associated with tissue-resident memory (T_{rm}) phenotype overlaid on tSNE CD8$^+$ T cell cluster. (**K)** Average expression levels of selected T_{rm} markers between CD8$^+$ T cells from PBMC versus tumor-periphery. (**L)** Representative dot plots of CD69 and CD103 co-expression in CD8$^+$ T cells from PBMC and tumor-periphery. (**M)** Quantification of CD69 and CD103 co-expression revealed CD69$^-$ CD103$^-$ in PBMC and CD69$^+$ CD103$^-$ and CD69$^+$ CD103$^+$ in tumor-periphery as the dominant phenotypes. (**N)** Expression of selected markers associated with T cell exhaustion/dysfunction, shown as boxplots between CD8$^+$ T cell from PBMC and tumor-periphery and overlaid on tSNE CD8$^+$ T cell cluster. *n* = 6 donors (**D, I, M**), *n* = 11 donors (**G**). Statistics: Wilcoxon matched-pairs signed rank test (**D, I**); repeated measures one-way ANOVA with post-hoc Šidák's correction for multiple comparisons (**G, M**). For detailed statistical analysis of scRNA-seq expression data, please refer to methods section. **p* ≤ 0.05, ***p* ≤ 0.01, ****p* ≤ 0.001, *****p* ≤ 0.0001, no brackets indicate no significant difference.

3.2.3.6 CD8$^+$ T cells in the tumor periphery share features with tissue-resident memory T cells (T_{rm})

We next examined the differing transcriptional and surface-specific features between tumor infiltrating and circulating CD8$^+$ T cells. Surface staining for CD45RA and CD45RO, discriminating naive/effector from memory T cells, attributed a predominant CD45RO$^+$ memory phenotype to the tumor infiltrating CD8$^+$ T cells (Figure 5H, 5I). Interrogation of the transcriptomic profile of these cells revealed a key marker expression signature consistent with tissue-resident memory T cells (T_{rm}): Expression of cellular adhesion molecules (integrins) *ITGA1* (CD49a) and *ITGAE* (CD103), tissue retention marker *CD69*, chemokine receptors implicated in tissue-homing *CXCR3, CXCR6* and *CCR5* [218] and transcription factors, *ZNF683* (Hobit) and *PRDM1* (Blimp1) as well as reduced expression of *TBX21* (Tbet) and *EOMES* [219], strongly suggested a T_{rm} phenotype for these cells (Figure 5J, 5K and Figure 5 – figure supplement 1B). Co-expression analysis of paired PBMC and tumor periphery samples using flow cytometry showed that CD69$^+$ CD103$^-$ and CD69$^+$ CD103$^+$ cells are the dominant

$CD8^+$ T cell populations in the tumor periphery (Figure 5L and 5M). Combined, these data strongly suggest a T_{rm} phenotype for the $CD8^+$ T cells in the tumor periphery.

Previous reports of T_{rm} populating the brain in the aftermath of central or peripheral infections concluded that brain T_{rm} cells surveil the brain tissue and mediate protection by rapid activation and enhanced cytokine production [218]. Indeed, $CD8^+$ T cells in the tumor periphery showed increased expression of genes belonging to costimulatory pathways, including *ICOS, TNFRSF4* (OX40) and *TNFRSF9* (4-1BB) (Figure 5 – figure supplement 1C), albeit accompanied by high levels of inhibitory receptors *PDCD1* (PD-1), *LAG3, HAVCR2* (TIM-3) and *CTLA4* (Figure 5N). Moreover, expression of genes coding for cytotoxic molecules, including Granzyme B and Perforin 1 were decreased in the peripheral $CD8^+$ T cells, suggesting a compromised killing capacity of these cells. And lastly, $CD8^+$ T cells in the tumor periphery exhibited a transcription factor profile of exhausted T cells with high expression of *NR4A1, MAF* and *IRF4* (Figure 5N and Figure 5 – figure supplement 1D), which have been implicated in T cell dysfunction and exhaustion [220, 221]. Collectively, these data indicate that $CD8^+$ T cells in the glioma periphery share features with T_{rm} cells. However, inhibitory receptor expression, functional molecules and transcriptional signature ascribe an exhausted phenotype to these cells.

Noteworthy, we observed high upregulation of similar genes in the comparison tumor periphery vs. PBMC for $CD4^+$ T cells as for $CD8^+$ T cells (Figure 5B and Figure 5 – figure supplement 1E). These included transcription factor family *NRA41-3,* identified as key mediator of T cell dysfunction [221], Dual Specificity Protein Phosphatase 2/4 (*DUSP2, DUSP4*) described as negative regulators of mitogen-activated protein (MAP) kinase superfamily and associated with impaired T cell effector activity [222] and T cell senescence [223], and transcription factor *CREM* which has been implicated in IL-2 suppression [224]. These genes could potentially identify pan T cell dysfunction markers within the GBM iTME [225].

3.2.3.7 Interrogation of cell-cell interactions revealed critical role of SPP1-mediated crosstalk between MG and lymphocytes in the tumor periphery

We next investigated cell-cell interactions based on ligand-receptor expression levels using the CellChat platform [226]. Considering MG and lymphocytes displaying an impaired activation signature in the tumor periphery, we focused our analysis on

the tumor-peripheral crosstalk between these cells (Figure 6A). This revealed SPP1 (Osteopontin) as a leading potential cell-cell interaction mediator between MG and lymphocytes (Figure 6A and 6B). MG SPP1-mediated signaling was as well among the most significant interactions, when investigating cell-cell communication across all cell types and both sites (Figure 6 – figure supplement 1A, 1B). Further, we found that *SPP1* is mainly expressed by MG rather than glioma cells, contrary to previous reports [227] (Figure 6C, Figure 6 – figure supplement 1C, 1D). MG SPP1 conveys different interactions, depending on the recipient cell binding receptor expression profile. The predicted interactions of MG SPP1 with NK cells could be mediated via the integrin complex *ITGA4-ITGB1* (CD49d-CD29) (Figure 6C), whereas $CD4^+$ and $CD8^+$ T cells exhibited strong interactions with MG *SPP1* as well (Figure 6B). However, cell-cell communication between MG and T lymphocytes could be mainly mediated via SPP1/CD44 interaction (Figure 6A and 6C), a ligand-receptor axis recently described to suppress T cell activation and proliferation [228]. Altogether, cell-cell interaction analysis identified MG SPP1 mediated interactions as a potential target to modulate MG-lymphocyte crosstalk in the tumor periphery.

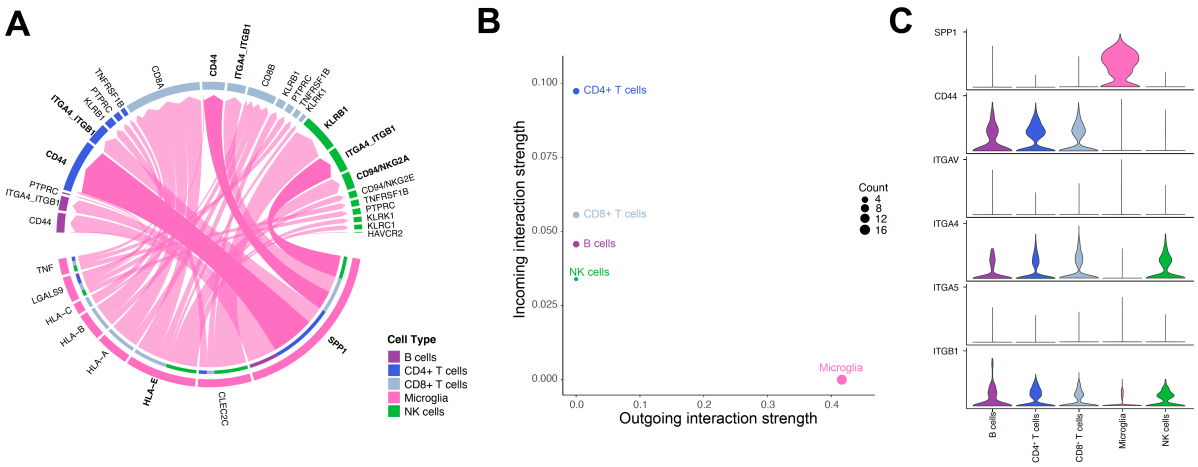

Figure 6 Cell-cell communication analysis using CellChat reveals critical role for SPP1-mediated crosstalk in tumor periphery.
(A) Chord diagram showing significant interactions from microglia to lymphocyte cell clusters. The inner bar colors represent the targets that receive signal from the corresponding outer bar. The inner bar size is proportional to the signal strength received by the targets. Chords indicate ligand-receptor pairs mediating interaction between two cell clusters, size of chords is proportional to signal strength of the given ligand-receptor pair. (**B)** Comparison of incoming and outgoing interaction strength allows identification of main senders and receivers. (**C)** Violin plots showing the expression distribution of signaling genes involved in the inferred SPP1 signaling network.

3.2.4 Discussion

In this study, we combined single-cell RNA sequencing and flow cytometry to interrogate the regional leukocyte activation signature in patient-matched biopsies from contrast-enhancing tumor center, infiltrative peripheral rim, and blood PBMCs of grade 4 glioma patients. Our analyses revealed a distinct, regionally dependent transcriptional profile for most of the investigated cell populations. While peripheral MG and cytotoxic cells predominantly displayed an impaired activation signature, MdMs showed pro-inflammatory traits in the tumor periphery, however, were less abundant there compared to the tumor center, which was reported by others as well [178, 179]. Supplemented with transcriptional analysis of paired PBMC samples, we provide an in-depth characterization of the three main immunological compartments of grade 4 glioma.

Previous studies focused on the description of the TME of grade 4 glioma, which also considered regional differences, yet they focused primarily at neoplastic cells rather than the immune compartment [178]. Others investigated the differences in the iTME composition between primary and metastatic brain tumors [128, 129]. Interestingly, the two latter ones reported differences in the iTME composition between *IDH1*^{wt} and *IDH1*^{mut} glioma. Of note, both authors included low-grade and even pre-treated recurrent glioma patients into the *IDH1*^{mut} group, representing a quite heterogenous patient cohort. In this study, we aimed at providing a representative selection of primary, treatment-naive grade 4 glioma patients including *IDH1*^{wt} and *IDH1*^{mut} to identify common transcriptional differences within the iTME between tumor center, periphery and PBMC of grade 4 glioma. How far these regional differences vary between *IDH1*^{wt} and *IDH1*^{mut} grade 4 glioma merits further investigation.

We identified a transcriptionally distinct MG subcluster, MG_1, which displayed an anti-inflammatory/non-reactive phenotype. A similar MG subpopulation expressing a comparable gene signature has been recently described to be enriched in Alzheimer's disease patients [229]. Along this line, we observed downregulation of *SDS* in the presumably less activated peripheral MG. *SDS* transcribes for the serine dehydratase, an enzyme catalyzing the dehydration of L-serine/L-threonine to yield pyruvate/ketobutyrate [230]. The downregulation of *SDS* in the peripheral MG with reduced metabolization of L-serine to pyruvate could potentially lead to a reduced oxidative phosphorylation in peripheral MG, a metabolic feature described for dysfunctional

MG in Alzheimer's disease models [231]. Concomitantly, increased L-serine levels have been associated with the induction of alternative, M2-like microglial polarization and inhibited secretion of inflammatory factors (TNF-α and IL-1β) [232].

Additionally, the peripheral cytotoxic cell compartment exhibited an impaired activation state, including a downregulated IFN response signature in $CD8^+$ T cells. Induction of an IFN response state has been described as a consequence of T cell receptor-mediated IFN-γ production, likely serving as an autocrine response and inducing the proliferative program [212]. Hence, the reduced autocrine IFN-responsive state in the tumor peripheral $CD8^+$ T cells, together with downregulated proliferative and costimulatory genes emphasized their impaired activation in the peripheral infiltration zone. Recently, our group could show that the response to immunotherapy in GBM is indeed region-dependent. For this, we cultured GBM explants in perfusion bioreactors and treated with anti-CD47, anti-PD1, or their combination which induced an IFN-γ response only in the tumor center, but not periphery [155]. Adding experimental support to the here described impaired activation signature in the tumor periphery.

By exploring the transcriptional trajectory of $CD8^+$ T cells from the blood circulation into the immunosuppressive TME of the tumor periphery, we uncovered $CX3CR1^{high}$ and $CX3CR1^{int}$ effector and memory $CD8^+$ T cells, respectively, to be highly enriched in the PBMC, but absent in the iTME. Recently, adoptive transfer studies of $CX3CR1^+$ $CD8^+$ T cells in a melanoma mouse model significantly suppressed tumor growth [233]. Others identified increased frequencies of $CX3CR1^+$ $CD8^+$ T cells in non-small cell lung and melanoma patients who responded to anti-PD-1 therapy, where these cells exhibited migratory capabilities into the tumor site followed by potent tumor rejection [233, 234]. Thus, the authors proposed T cell CX3CR1 expression as a predictor of response to ICI therapy. Therefore, the absence of ICI therapy-responsive $CD8^+$ T cells in the glioma TME could additionally explain the disappointing outcomes of clinical trials using ICI in glioma patients.

The observed T_{rm} exhaustion phenotype of the glioma residing $CD8^+$ T cells was recently reported as well for tumor-infiltrating $PD\text{-}1^{high}$ $CD8^+$ T cells in hepatocellular carcinoma [220]. Whether these glioma-associated $CD8^+$ T cells really possess tumor-specificity requires further study. Particularly in the light of a recent study by Smolders and colleagues who reported a consistent brain-resident $CD8^+$ T cell population in a miscellaneous autopsy cohort of patients with neurological disorders excluding brain

malignancies (Alzheimer's disease, Parkinson's disease, dementia, depression, multiple sclerosis), as well as patients with no known brain disease. These brain-resident $CD8^+$ T cells displayed a remarkably consistent T_{rm} phenotype [235]. The authors further showed high expression of inhibitory receptors CTLA-4 and PD-1 on the brain-resident $CD8^+$ T_{rm} cells, which is in line with the core phenotypic signature of T_{rm} cells from other tissues [236, 237]. Yet, the brain $CD8^+$ T_{rm} cells showed a preserved inflammatory potential with substantial production of IFN-γ and TNF-α upon *ex vivo* stimulation. They concluded that extensive immune activation with release of highly neurotoxic lytic enzymes, such as perforin and granzyme B, harmfully impacts the brain parenchyma and should be tightly controlled, whilst maintaining the capability to elicit a fast inflammatory response when a neurotropic virus threatens the CNS [235]. Therefore, inhibitory receptors like PD-1 and CTLA-4 on brain $CD8^+$ T_{rm} cells may support CNS homeostasis by preventing uncontrolled T cell reactivity, and the availability of the receptor ligands may determine their inhibitory effect. While this may represent a well-balanced equilibrium under healthy conditions, the tumor setting leads to its disruption with upregulation of inhibitory ligands like PD-L1 on glioma cells and CD86 on GAMs, leading to the dysfunctional state seen in the glioma-residing $CD8^+$ T_{rm} cells.

Another study comprehensively showed, that peripheral infections generate antigen-specific $CD8^+$ T_{rm} cells in the brain, mediating protection against CNS infections [218]. These data could implicate that the glioma-associated $CD8^+$ T cells are devoid of tumor-specific reactivity, but rather represent a pre-existing T cell population generated after peripheral infections, which acquired a dysfunctional state upon glioma formation. To test this hypothesis, further characterization of these cells is required, including analysis of T cell receptor clonality and tumor-specificity by patient-matched T cell/glioma-sphere co-culture assays.

Lastly, our cell-cell interaction analysis revealed signaling pathways between peripheral MG and lymphocytes potentially inducing the observed impaired activation signature. The predicted interaction between MG SPP1 and NK cells integrin complex *ITGA4-ITGB1* (CD49d-CD29), might mediate NK cell adhesion and migration [238]. Which may facilitate interaction of inhibitory NK receptors KLRB1 and CD94/NKG2A with MG C-type lectin-related ligands and HLA-E, respectively, which could explain the observed impaired activation state of peripheral NK cells. Moreover, SPP1/CD44 interaction in T lymphocytes has been described to suppress cell activation and

proliferation [228]. In a comprehensive approach, the group of Marco Prinz mapped the transcriptional states of human MG during aging and disease. Thereby, they found *SPP1* to be differentially expressed in aging-microglia and a doubling of $SPP1^+$ GAMs in GBM samples compared to MG from age-matched controls [239]. Supporting our data of a possible role of MG SPP1 in glioma progression.

Limitations of the study include the limited patient number, thereby our study was neither designed nor powered to explore differences in neoplastic cells, given the high inter- and intra-patient variability in glioma cells [178]. Importantly, our dataset establishes a starting point for further interrogation and provides an in-depth analysis of the transcriptional landscape of the major immune populations in grade 4 glioma within three important regional compartments. Further, we confirmed the observed phenotype of $CD8^+$ T cells in the blood and tumor periphery by flow cytometry in a cohort of ten additional patients, addressing possible generalization concerns. Together, we provide a regionally-resolved map of leukocyte activation in the TME and blood circulation from grade 4 glioma patients, helping the research community to uncover novel therapeutic strategies to combat this fatal disease.

3.2.5 Methods

Ethics statement

Human adult GBM tissue samples were obtained at the Neurosurgical Clinic of the University Hospital of Basel, Switzerland in accordance with the Swiss Human Research Act and institutional ethics commission (EKNZ 02019-02358). All patients gave written informed consent for tumor biopsy collection and signed a declaration permitting the use of their biopsy specimens in scientific research, including storage in our brain tumor biobank (Req-2019-00553). All patient identifying information was removed and tissue was coded for identification.

Glioma tissue dissociation

Resected glioma tissue samples were immediately placed on ice and transferred to the laboratory for single cell dissociation within 2-3 h after resection. Human brain tissue was manually minced using razor blades and enzymatically dissociated at 37°C for 30 minutes with 1 mg/ml collagenase-4 (#LS004188, Worthington Biochemical Corporation, USA) and 250 U/ml DNAse1 (#10104159001, Roche, Switzerland) in a buffer containing Hank's Balanced Salt Solution (HBSS) with Ca^{2+}/Mg^{2+}, 1% MEM

non-essential amino acids (Gibco, USA), 1 mM sodium pyruvate (Gibco), 44 mM sodium bi-carbonate (Gibco), 25 mM HEPES (Gibco), 1% GlutaMAX (Gibco) and 1% antibiotic-antimycotic (Sigma-Aldrich, USA). Cells were filtered and separated from dead cells, debris and myelin by a 0.9 M sucrose (#84100, Simga Aldrich) density gradient centrifugation. Upon ACK-lysis for removal of erythrocytes (#A1049201, Gibco) the now generated single-cell suspension (SCS) was washed, counted and frozen in Bambanker (#BB01, Nippon Genetics, Germany) in liquid nitrogen until use.

PBMCs (Peripheral blood mononuclear cells) preparation

Patient blood samples were directly placed on ice and transferred to the laboratory for PBMC isolation. Blood samples were centrifuged to separate buffy coat from plasma and erythrocytes, followed by standard density gradient centrifugation protocol (#17144002, Ficoll-Paque PLUS, Cytiva, USA) to isolate PBMCs. PBMCs were frozen in Bambanker (#BB01, Nippon Genetics, Germany) in liquid nitrogen until use.

FACS sorting for single cell RNA sequencing (scRNA-seq)

Cryopreserved tumor digests from glioma samples (center and periphery), as well as autologous PBMCs were thawed and washed with excess ice-cold 1xPBS and spun down at 350xg for 5 min. Subsequently, the cells were stained with Live/Dead (APC-Cy7 (Near IR), # L34976, Thermo Fischer) and a cocktail of fluorescently-conjugated antibodies CD11b (FITC, clone M1/70, #101206, BioLegend) and CD45 (FITC, clone 2D1, #368508, BioLegend), and large debris were removed with a 40-µm strainer. All samples were acquired on the BD FACS ARIA Fusion III (Becton Dickinson GmbH, Germany). For single-cell RNA-seq experiments, live and single gated cells were sorted into non-immune cell ($CD45^-CD11b^-$) and immune cell ($CD45^+CD11b^+$) populations. Both populations were directly sorted into Eppendorf tubes with 1xPBS supplemented with 1% BSA for single cell RNA sequencing.

Single cell RNA sequencing (scRNA-seq) – Library preparation and sequencing

Single-cell RNA-seq was performed using Chromium Single Cell 3' GEM, Library & Gel Bead Kit v3 (#CG000183, 10x Genomics, Pleasanton, CA, USA) following the manufacturer's protocol. Briefly, non-immune cells and immune cells were mixed at a defined ratio of 1:4. Roughly 8000-10000 cells per sample, diluted at a density of 100–800 cells/µL in PBS plus 1% BSA determined by Cellometer Auto 2000 Cell Viability Counter (Nexelom Bioscience, Lawrence, MA USA), and were loaded onto the

chip. The quality and concentration of both cDNA and libraries were assessed using an Agilent BioAnalyzer with High Sensitivity kit (#5067-4626, Agilent, Santa Clara, CA USA) and Qubit Fluorometer with dsDNA HS assay kit (#Q33230, Thermo Fischer Scientific, Waltham, MA USA) according to the manufacturer's recommendation. For sequencing, samples were mixed in equimolar fashion and sequenced on an Illumina HiSeq 4000 with a targeted read depth of 50,000 reads/cell and sequencing parameters were set for Read1 (28 cycles), Index1 (8 cycles), and Read2 (91 cycles).

Single cell RNA sequencing (scRNA-seq) - Computational analysis

The dataset was analyzed by the Bioinformatics Core Facility, Department of Biomedicine, University of Basel. Read quality was controlled with the FastQC tool (version 0.11.5). Sequencing files were processed using the Salmon Alevin tool (v 1.3.0) [240] to perform quality control, sample demultiplexing, cell barcode processing, pseudo-alignment of cDNA reads to the human Gencode v35 reference and counting of UMIs. Parameters *--keepCBFraction 1* and *--maxNumBarcodes 100000* were used.

Processing of the UMI counts matrix was performed using the Bioconductor packages DropletUtils (version 1.8.0) [241, 242], scran (version 1.16.0) [243, 244] and scater (version 1.16.2) [245], following mostly the steps illustrated in the OSCA book (http://bioconductor.org/books/release/OSCA/) [244, 246]. Filtering for high-quality cells was done based on library size (at least 2,000 UMI counts per cell), the number of detected genes (at least 700 genes detected) and the percentage of reads mapping to mitochondrial genes (larger than 0% and lower than 15%), based on the distribution observed across cells. Low-abundance genes with average counts per cell lower than 0.006 were filtered out. The presence of doublet cells was investigated with the scDblFinder package (version 1.2.0), and suspicious cells were filtered out (score > 0.6). After quality filtering, the resulting dataset consisted of UMI counts for 15,523 genes and 45,466 cells, ranging from 803 to 9,121 per sample.

UMI counts were normalized with size factors estimated from pools of cells created with the scran package *quickCluster()* function [243, 247]. To distinguish between genuine biological variability and technical noise we modeled the variance of the log-expression across genes using a Poisson-based mean-variance trend. The scran package *denoisePCA()* function was used denoise log-expression data by removing principal components corresponding to technical noise. A t-stochastic neighbor embedding (t-SNE) was built with a perplexity of 50 using the top most variable genes

(141 genes with estimated biological variance > 0.3, excluding genes with highest proportion of reads in the ambient RNA pool estimated from empty droplets), and the denoised principal components as input (5 top PCs). Clustering of cells was performed with hierarchical clustering on the Euclidean distances between cells (with Ward's criterion to minimize the total variance within each cluster [248]; package cluster version 2.1.0). The number of clusters used for following analyses was identified by applying a dynamic tree cut (package dynamicTreeCut, version 1.63-1) [249], resulting in 10, or 22 clusters with argument *deepSplit* set to 2.

The Bioconductor package SingleR (version 1.2.4) was used for cell-type annotation of the cells [250] using as references (i) a public bulk RNA-seq dataset of sorted immune cell types from human PBMC samples [182], available through the *celldex* Bioconductor package; (ii) a bulk RNA-seq dataset of sorted immune cell types from the tumor microenvironment of human gliomas [128] (UMI count matrix and annotation downloaded from https://joycelab.shinyapps.io/braintime/); (iii) a Smartseq2 scRNA-seq dataset of IDH-wild-type glioblastoma tumors [183] (downloaded from GEO accession GSE131928). A microglia and a macrophage signature scores were defined by averaging the center and scaled expression levels of gene lists obtained in [173]. An endothelial score was defined by averaging the center and scaled expression levels of the genes *CDH5*, *VWF*, *CD34* and *PECAM1*. The SingleR high-quality assignments (pruned scores) and the signature scores were used to manually derive a consensus cell type annotation for each cluster.

The *findMarkers* function of the scran package was used to find the best markers across annotated cell types (parameters *direction="up"* and *pval.type="any"*). The top 10 markers for each cell type were extracted and pooled to from a list of 68 markers.

Differential abundance analysis of identified cell types between tumor sites was performed using *diffcyt-DA-voom* method [251]. Differential abundance of cell types was considered to be significant at a false discovery rate (FDR) lower than 5 %.

Differential expression between tumor sites, or between PBMC cells and tumor periphery cells, stratified by annotated cell type, was performed using a pseudo-bulk approach, summing the UMI counts of cells from each cell type in each sample when at least 20 cells could be aggregated. The aggregated samples were then treated as

bulk RNA-seq samples [252] and for each pairwise comparison genes were filtered to keep genes detected in at least 5% of the cells aggregated. The package edgeR (version 3.30.3) [253] was used to perform TMM normalization [254] and to test for differential expression with the Generalized Linear Model (GLM) framework, using a model accounting for patient-specific effects. Genes with a FDR lower than 5 % were considered differentially expressed. Gene set enrichment analysis was performed with the function camera [255] on gene sets from the Molecular Signature Database (MSigDB, version 7.4) [205, 256]. We retained only sets containing more than 5 genes, and gene sets with a FDR lower than 5% were considered as significant.

Cell chat analysis

The R package CellChat (1.1.3) [226] was used to analyze cell-cell interactions in our dataset (with previously annotated 9 cell types). We followed the recommended workflow to infer the cell state-specific communications (using *identifyOverExpressedGenes*, *identifyOverExpressedInteractions* and *projectData* with the default parameters). We performed 3 separate analyses, on the center and the periphery subsets and a comparison analysis as described in the official workflow. We visualized the significant interactions for the microglia cluster using *netVisual_chord_gene* and used *plotGeneExpression* to display of the expression of all genes involved SPP1 signaling pathway in the cell populations. Finally, *netAnalysis_signalingRole_scatter* was used to calculate and visualize incoming and outgoing signaling strength.

Flow cytometry analysis of paired PBMC and periphery samples

Cryopreserved samples were thawed and washed with excess ice-cold 1xPBS and spun down at 350xg for 5 min. Cells were resuspended in FACS buffer (PBS plus 2% FBS) and blocked with monoclonal antibody to CD16/32 (Human TruStain FcX, #422302, Biolegend) for 10 min at 4°C before staining with surface antibodies: CD45RA (PE, clone HI100, #304108), CD45RO (APC, clone UCHL1, #304210), CD3e (BV650, clone UCHT1, #300468), CD8a (BV421, clone RPA-T8, #301036), CCR7 (FITC, clone G043H7, #353216), CD62L (AF700, clone DREG-56, #304820), CD69 (APC-Cy7, clone FN50, #310914), CD103 (PerCP/Cy5.5, clone Ber-ACT8, #350226) and CX3CR1 (PE/Cy7, clone 2A9-1, #341612). All antibodies were purchased from BioLegend, USA. Cells were stained for 30 min at 4°C, and subsequently washed with FACS buffer. To exclude dead cells Zombie Aqua Fixable Viability Kit (#423102, 1:100, BioLegend) was added. Acquisition was performed on a CytoFLEX (Beckman). Data

was analyzed using FlowJo software, version 10.8.1 (TreeStar). Gates were drawn by using Fluorescent Minus One (FMO) controls.

Statistical analysis of flow cytometry data

Data analysis and graph generation was performed using GraphPad Prism 9 (GraphPad Prism Software Inc.). Paired comparisons between two groups were performed using Wilcoxon matched-pairs signed rank test. Differences of more than two paired groups were assessed using repeated measures one-way ANOVA test, followed by post-hoc Šidák's multiple comparisons correction. A p value < 0.05 was considered statistically significant. *$p \leq 0.05$, **$p \leq 0.01$, ***$p \leq 0.001$, ****$p \leq 0.0001$.

Graphical illustrations

All graphical illustrations were created with BioRender.com.

3.2.6 Data availability

The UMI count matrix and cell metadata from the scRNA-seq dataset are available on GEO under accession number GSE197543. The remaining data are available within the Article and Supplementary Information.

3.2.7 Acknowledgements

We are grateful to the patients and their families for their consent to donate tissue to our brain tumor biobank. We thank Tamara Hüssen, Alison Riberio and Florian Limani for experimental support and Cecile Buenter for critical revision of the manuscript. Calculations were performed at sciCORE (http://scicore.unibas.ch/) scientific computing center at the University of Basel. This work was supported by a Swiss Cancer Research MD-PhD Grant (MD-PhD-4818-06-2019) to P.S. as well an Alumni Medizin Basel grant to P.S.; Swiss National Science Foundation Professorial Fellowship (PP00P3_176974); the ProPatient Forschungsstiftung, University Hospital Basel (Annemarie Karrasch Award 2019); Swiss Cancer Research Grant (KFS- 4382-02-2018) to G.H.; the Department of Surgery, University Hospital Basel, to G.H. and P.S.; and by The Brain Tumour Charity Foundation, London, UK (GN- 000562) to G.H.

3.2.8 Author contribution

G.H., S. Herter, M.B., S.D. and P.S., conceived and planned the project. P.S. performed most of the experiments, interpreted the results and wrote the manuscript. J.R. and S. Hogan analyzed the scRNA-sequencing data and performed statistical

analysis. S.D., T.S., T.A.M. and M.-F.R. helped coordinating experiments. G.H. supervised and coordinated the study and critically revised the manuscript. All authors reviewed the paper and approved its final version.

3.2.9 Competing interests

G.H. has equity in, and is a cofounder of Incephalo Inc. S.D., S. Herter and M.B. are affiliated with Roche Pharmaceutical Research and Early Development, but have no financial interests to declare.

3.2.10 Supplementary data

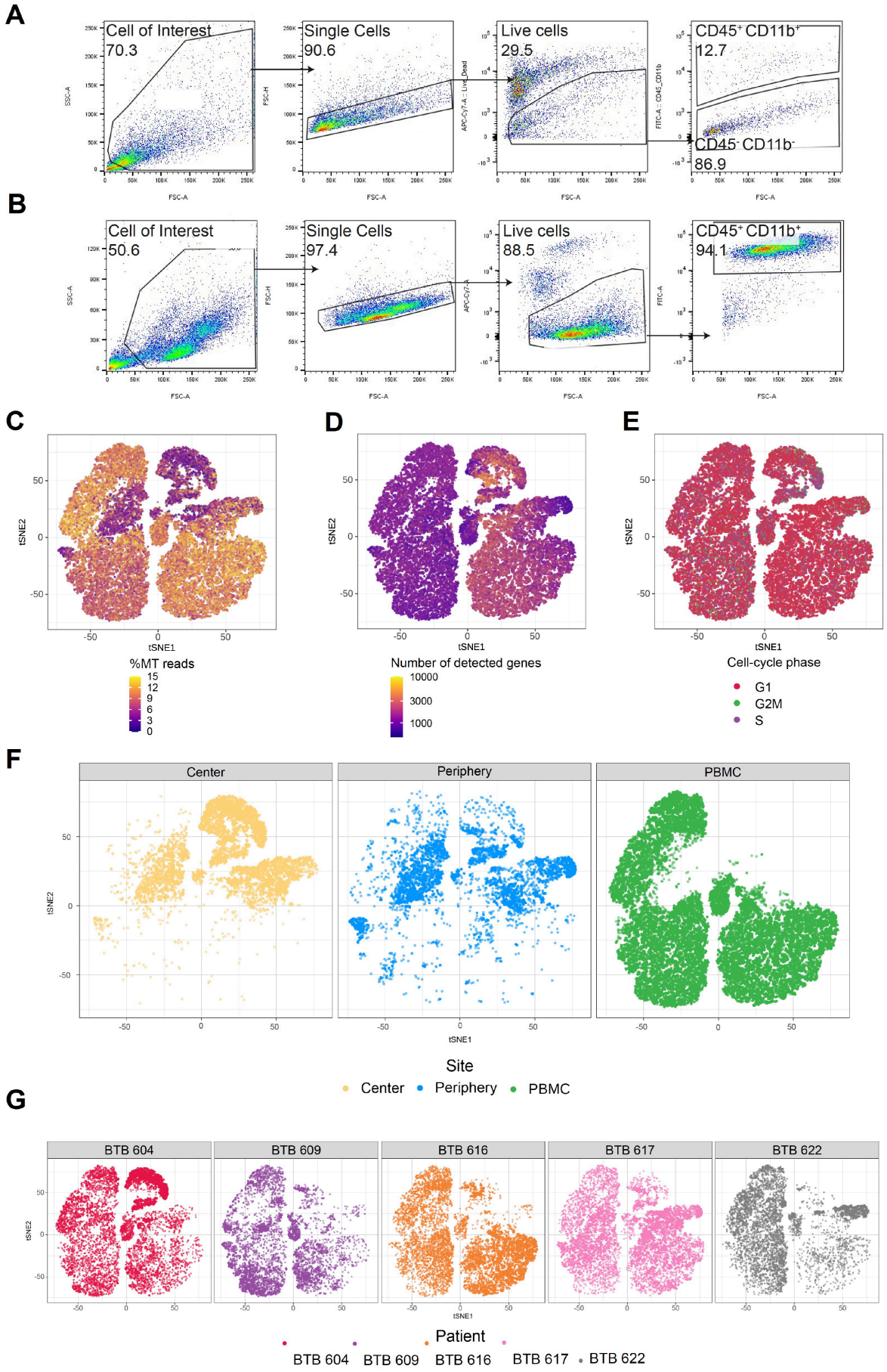

Figure 1 – figure supplement 1. CD45+ CD11b+ immune cells gating strategy and quality control of scRNA-seq data.
(A, B) Gating strategy for paired tumor-derived (**A**) and PBMCs (**B**); after debris, doublet and dead cell removal, immune cells were assessed as CD45+ and/or CD11b+. **(C-E)** Percentage of mitochondrial (MT) reads (**C**) number of detected genes (**D**) and cell-cycle phase (**E**) overlaid on tSNE representation. **(F, G)** tSNE map stratified according to site (**F**) and patient (**G**).

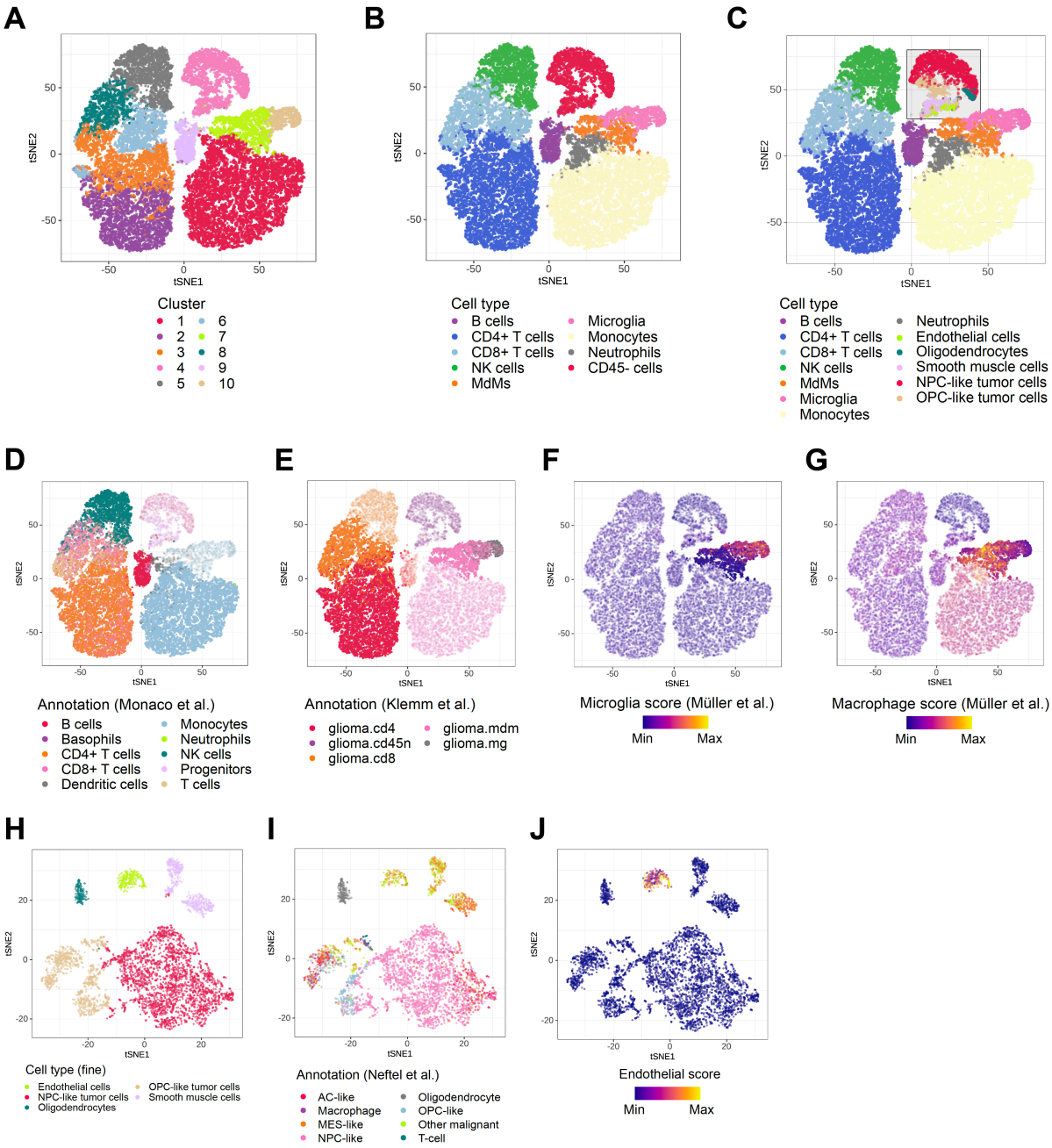

Figure 2 – figure supplement 1. Cross-referencing scRNA-seq data with published datasets.
(A-C) Using hierarchical clustering, identified cell clusters (**A**) which were then annotated into eight distinct cell types for the immune subset (**B**) and five cell types for the CD45neg subset (**C**). (**D-G)** Immune cell types were annotated by referencing to a dataset of bulk RNA-seq samples of sorted immune cell types from human PBMC (**D**) [182]; MdMs and microglia were

annotated by comparing to a dataset of bulk RNA-seq samples of sorted immune cell types from the tumor microenvironment of human gliomas € [128] and by using signature scores defined from scRNA-seq of glioma TAMs (**F, G**) [173]. Clusters are highlighted which were annotated using each respective reference dataset. (**H, I)** Grey panel in (**C**) zooms in on CD45neg subset and is shown in (**H**). CD45neg cells were annotated by whole-transcriptome comparison to a scRNA-seq dataset of IDH1wt GBM (**I**) [183]. (**J)** Endothelial score was defined by averaging the center and scaled expression levels of the genes CDH5, VWF, CD34 and PECAM1.

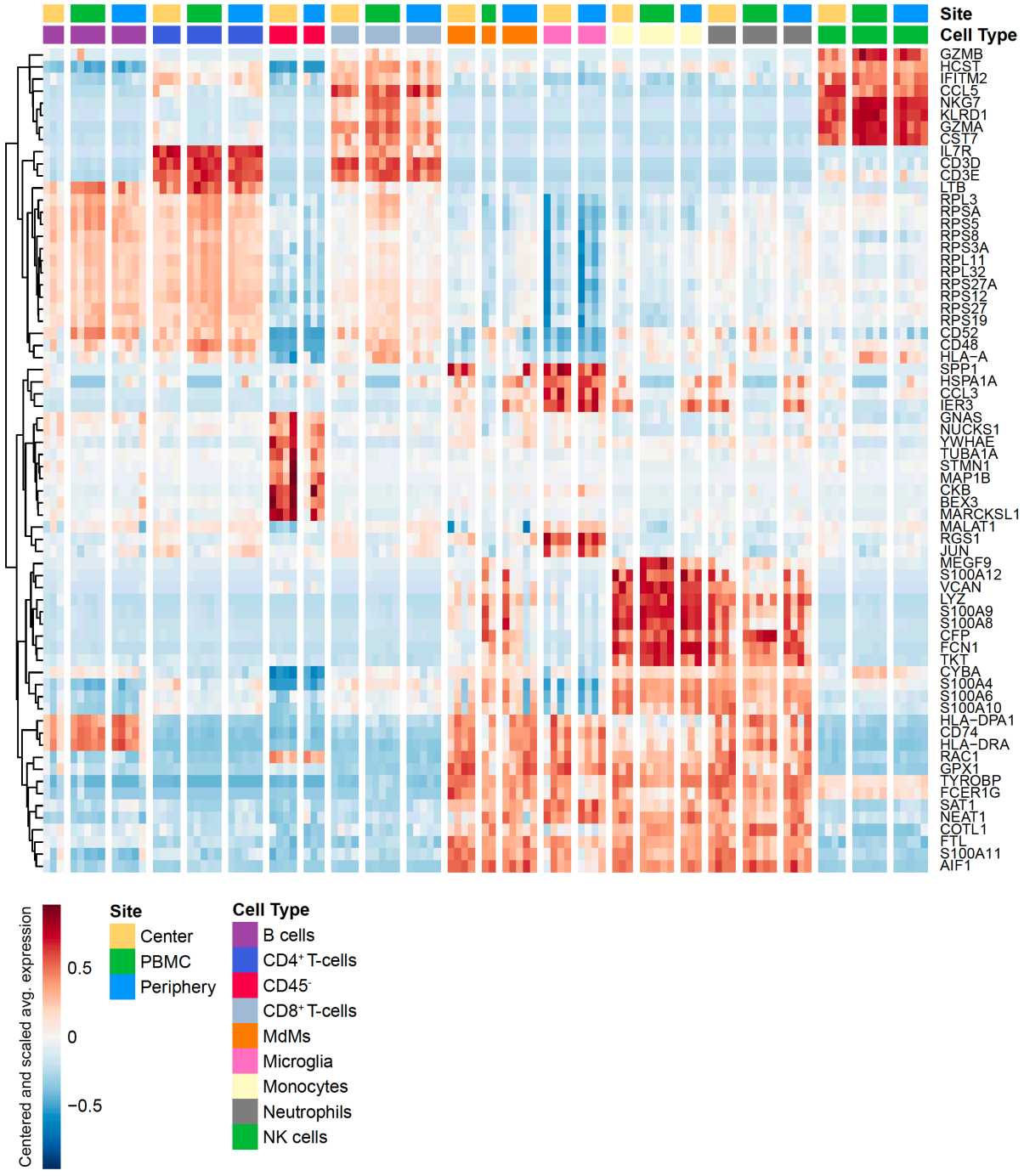

Figure 2 – figure supplement 2. Cell type specific gene expression.

Heatmap displaying genes whose expression is most specific to each cell type. Columns are ordered by site and cell type, and rows show centered and scaled expression values, hierarchically clustered.

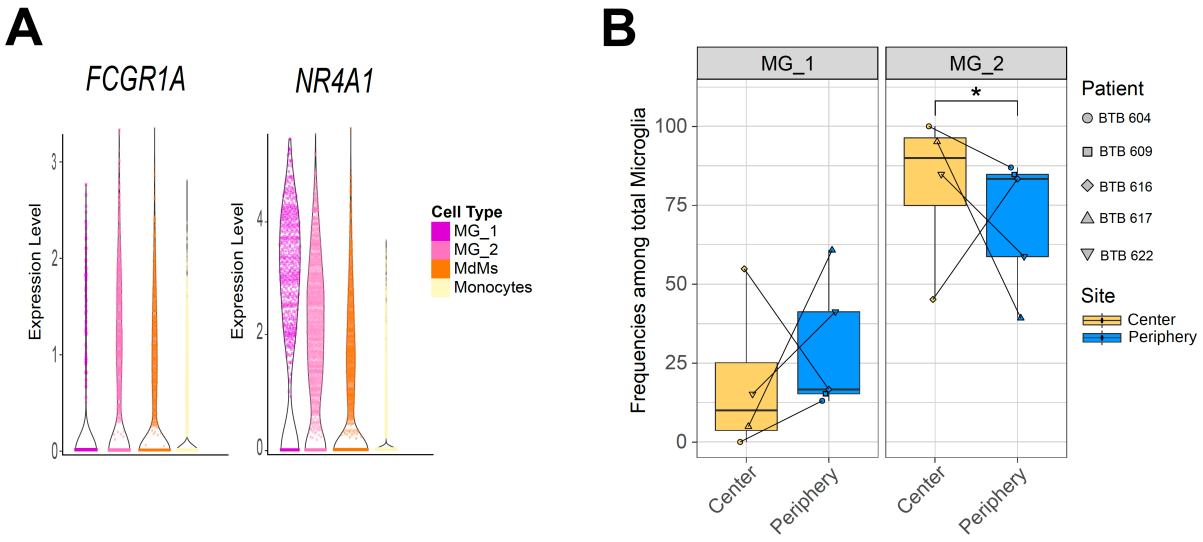

Figure 3 -figure supplement 1. MG subclusters MG_1 and MG_2.
(**A**) Violin plot showing average expression levels of selected reactivity markers among mononuclear phagocyte populations. (**B**) Frequencies of MG_1 and MG_2 subpopulations among total microglia between center and periphery. Symbols represent individual patients and paired samples are indicated by connecting lines. 3 of 4 (75%) paired samples showed an increased abundance of MG_1 cells in the tumor periphery and decreased frequency of MG_2 cells. Statistical significance was assessed by diffcyt-DA-voom method, *FDR corrected p value < 0.05.

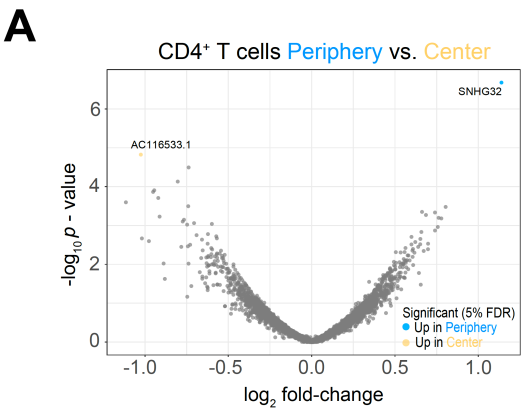

Figure 4 – figure supplement 1. Differential expression analysis between tumor center and peripheral CD4+ T cells.
(**A**) Volcano plot showing differentially expressed genes (FDR corrected p value < 0.05, indicated by blue and yellow) in CD4+ T cells from tumor periphery versus tumor center.

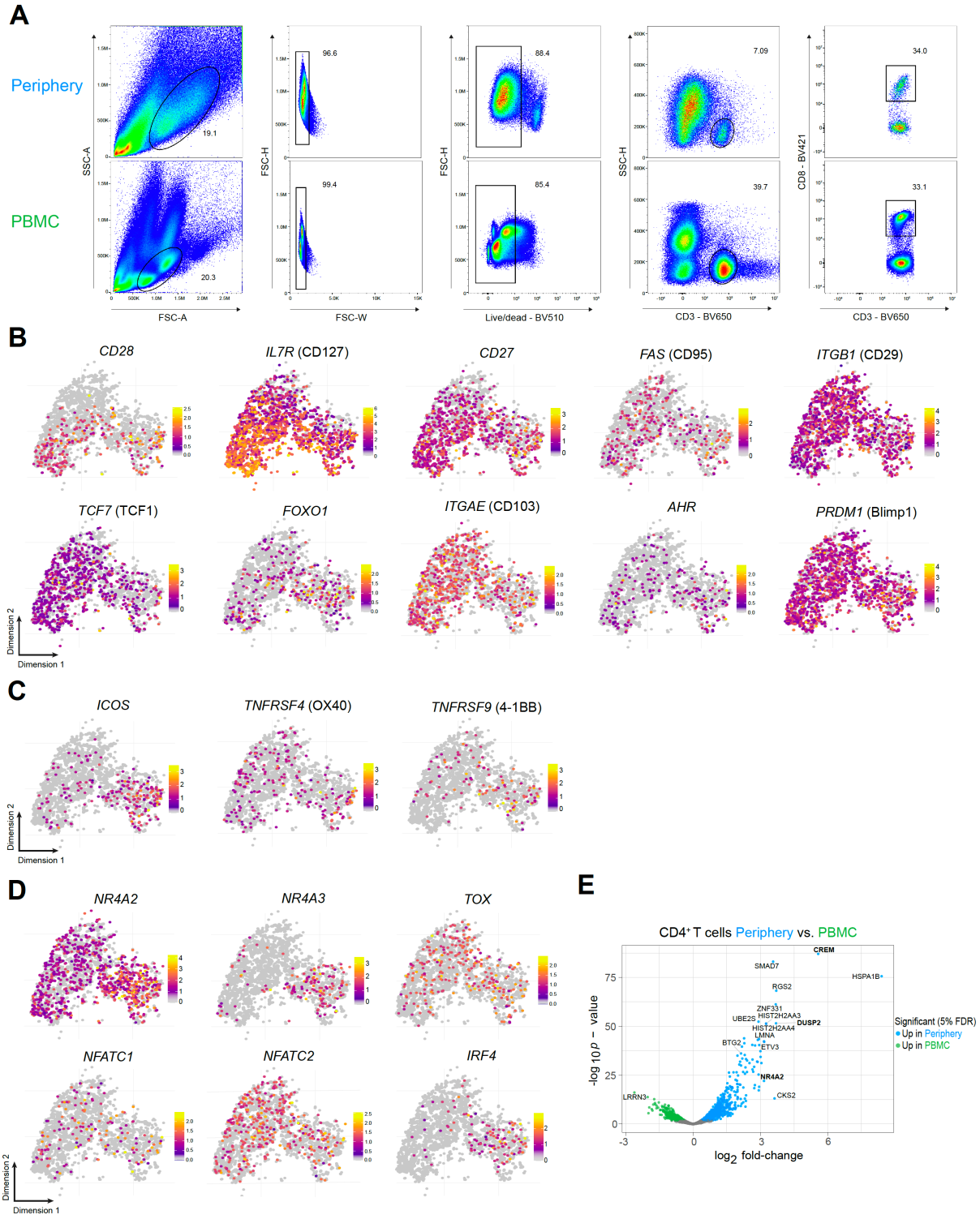

Figure 5 – figure supplement 1. CD8+ T cell phenotype is site-specific.
(**A**) Gating strategy for paired tumor-periphery and PBMC cells; after debris, doublet and dead cell removal, CD8+ T cells were identified as CD3+ CD8+ events. (**B-D**) Single-cell expression of markers associated with naive/memory (CD28, IL7R, CD27, FAS, CD29, TCF, FOXO1) and tissue-resident memory (ITGAE, AHR, PRDM1) (**B**) T cell co-stimulation (**C**) and T cell exhaustion/dysfunction (**D**) overlaid on tSNE CD8+ T cell cluster. (**E**) Volcano plot showing differentially expressed genes (FDR corrected p value < 0.05, indicated by blue and green) in CD4+ T cells from tumor-periphery versus PBMC.

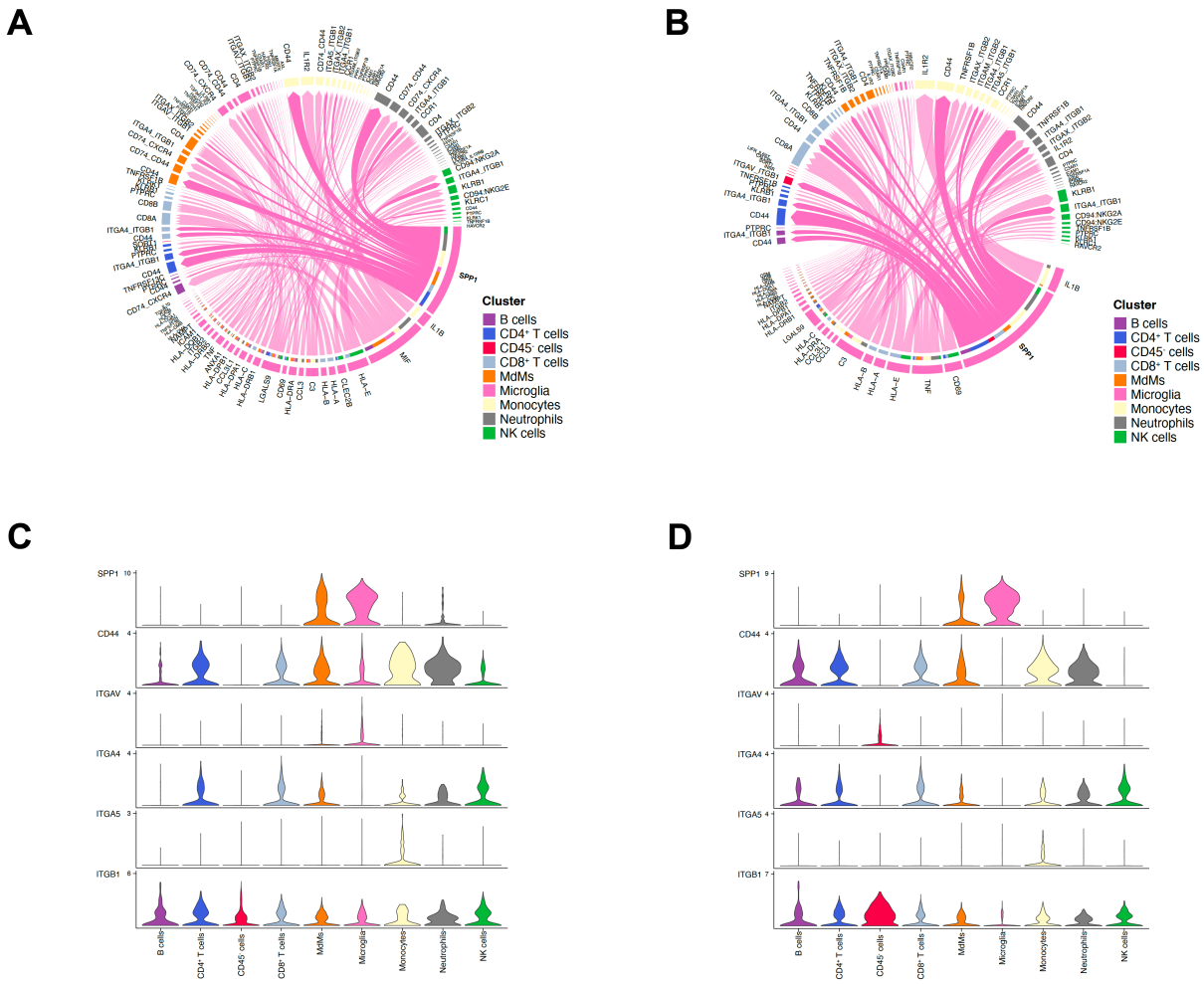

Figure 6 – figure supplement 1. Cell-cell communication analysis using CellChat.
(**A, B**) Chord diagram showing significant interactions from microglia to all cell clusters in center (**A**) and periphery (**B**). The inner bar colors represent the targets that receive signal from the corresponding outer bar. The inner bar size is proportional to the signal strength received by the targets. Chords indicate ligand-receptor pairs mediating interaction between two cell clusters, size of chords is proportional to signal strength of the given ligand-receptor pair. (**C, D**) Violin plots showing the expression distribution of signaling genes involved in the inferred SPP1 signaling network in center (**C**) and periphery (**D**).

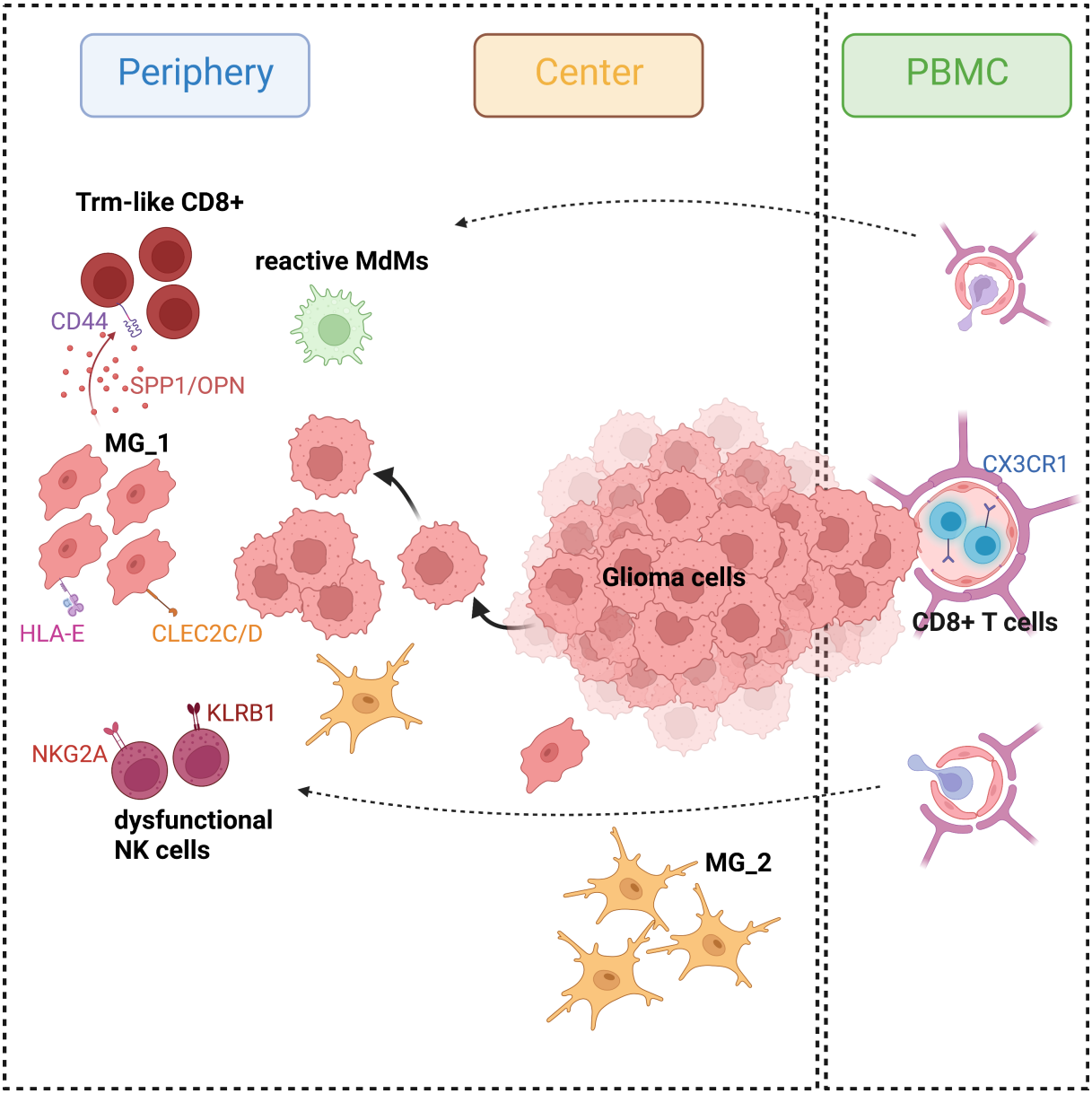

Appendix - Graphical abstract.
Proposed schematic of grade 4 glioma-associated immune cells in the three regional compartments. Created with BioRender.com.

Appendix 1 – table 1. Patient characteristics.

	Sex	Age	Histology & Grade	Status	IDH Status	MGMT promoter	EGFR ampl.	Subclassification
BTB 604	M	62	GBM, 4	primary	wild type	unmethylated	not amplified	mesenchymal
BTB 609	M	50	GBM, 4	primary	mutated	methylated	not amplified	high grade astrocytoma
BTB 616	F	80	GBM, 4	primary	wild type	unmethylated	not amplified	proneural
BTB 617	M	64	GBM, 4	primary	wild type	unmethylated	not amplified	proneural
BTB 622	F	51	GBM, 4	primary	mutated	unmethylated	not amplified	high grade astrocytoma
BTB 642	F	56	GBM, 4	primary	wild type	unmethylated	not amplified	classical
BTB 626	M	25	GBM, 4	primary	mutated	unmethylated	not amplified	high grade astrocytoma
BTB 649	M	77	GBM, 4	primary	wild type	methylated	amplified	classical
BTB 653	M	57	GBM, 4	primary	wild type	unmethylated	not amplified	proneural
BTB 659	M	43	GBM, 3	primary	mutated	methylated	not amplified	anaplastic oligodendroglioma
BTB 610	F	69	GBM, 4	primary	wild type	methylated	not amplified	mesenchymal
BTB 644	M	64	GBM, 4	primary	wild type	unmethylated	amplified	classical
BTB 643	M	66	GBM, 4	primary	wild type	unmethylated	not amplified	proneural
BTB 666	M	68	GBM, 4	primary	wild type	unmethylated	amplified	classical
BTB 668	M	65	GBM, 4	primary	wild type	unmethylated	amplified	classical

Pat	pre-OP steroids	scRNAseq Center	scRNAseq Periphery	scRNAseq PBMC	Flow Cytometry Periphery	Flow Cytometry PBMC
BTB 604	4 mg	Yes	Yes	Yes	Yes	Yes
BTB 609	96 mg	No	Yes	Yes	No	No
BTB 616	80 mg	Yes	Yes	Yes	No	No
BTB 617	none	Yes	Yes	Yes	No	No
BTB 622	68 mg	Yes	Yes	Yes	No	No
BTB 642	88 mg	No	No	No	Yes	Yes
BTB 626	56 mg	No	No	No	Yes	Yes
BTB 649	8 mg	No	No	No	Yes	Yes
BTB 653	80 mg	No	No	No	Yes	Yes
BTB 659	64 mg	No	No	No	Yes	Yes
BTB 610	2 mg	No	No	No	No	Yes
BTB 644	4 mg	No	No	No	No	Yes
BTB 643	none	No	No	No	No	Yes
BTB 666	96 mg	No	No	No	No	Yes
BTB 668	76 mg	No	No	No	No	Yes

4 Review

4.1 Microglia-Centered Combinatorial Strategies Against Glioblastoma

Tomás A. Martins[1+], Philip Schmassmann[1+], Tala Shekarian[1+], Jean-Louis Boulay[1,2], Marie-Françoise Ritz[1,2], Steven Zanganeh[3,4], Johannes vom Berg[5], Gregor Hutter[1,2]

[1]Department of Biomedicine, University of Basel, Basel, Switzerland

[2]Department of Neurosurgery, University Hospital Basel, Basel, Switzerland

[3]Sloan Kettering Institute, Memorial Sloan Kettering Cancer Center, New York, USA

[4]Department of Chemical and Biomolecular Engineering, New York University, New York, USA

[5]Institute of Laboratory Animal Science, University of Zurich, Schlieren, Switzerland

[+]These authors contributed equally

- published -

on September 29, 2020 in Frontiers in Immunology

4.1.1 Abstract

Tumor-associated microglia (MG) and macrophages (MΦ) are important components of the glioblastoma (GBM) immune tumor microenvironment (iTME). From the recent advances in understanding how MG and GBM cells evolve and interact during tumorigenesis, we emphasize the cooperation of MG with other immune cell types of the GBM-iTME, mainly MΦ and T cells. We provide a comprehensive overview of current immunotherapeutic clinical trials and approaches for the treatment of GBM, which in general, underestimate the counteracting contribution of immunosuppressive MG as a main factor for treatment failure. Furthermore, we summarize new developments and strategies in MG reprogramming/re-education in the GBM context, with a focus on ways to boost MG-mediated tumor cell phagocytosis and associated experimental models and methods. This ultimately converges in our proposal of novel combinatorial regimens that locally modulate MG as a central paradigm, and therefore may lead to additional, long-lasting, and effective tumoricidal responses.

4.1.2 Development and classification of glioblastoma

Glioblastoma (GBM) is the most aggressive and common primary brain tumor. Despite current treatment modalities, consisting of surgical resection followed by chemo-irradiation, the median overall survival of GBM patients remains only 15 months [257]. These tumors arise from astrocytes or their precursors within the central nervous system (CNS) and are genetically and phenotypically heterogeneous [258]. World Health Organization (WHO) grade IV glioma that arises *de novo* is designated primary GBM while that developing from the progression of previously diagnosed lower-grade glioma is named secondary GBM [259].

In the course of primary GBM development, chromosome 7 gain and chromosome 10 loss have led to the identification of platelet-derived growth factor subunit A (*PDGF*A) and phosphatase and tensin homolog (*PTEN*) as driver genes [260]. Based on genomic, transcriptomic, and proteomic profiles, primary GBM has been further subclassified into classical (CL), proneural (PN), or mesenchymal (MES) subgroups [261-264]. While CL-GBM shows frequent epidermal growth factor receptor (*EGFR*) amplification and cyclin-dependent kinase inhibitor 2A (*CDKN2A*) homozygous deletion, PN-GBM is associated with amplification of platelet-derived growth factor receptor alpha (*PDGFRA*) and tumor protein p53 (*TP53*) mutations. Finally, MES-GBM, is associated with additional loss of neurofibromin 1 (*NF1*) gene, and co-mutated *PTEN*

and *TP53* tumor suppressor genes [260, 261]. In sum, the genetic alterations that distinguish all 3 GBM subgroups commonly hit the same 3 major glioma signaling pathways: the RTK/RAS/PI3K (proliferation), TP53 (apoptosis) and RB (cell division) pathways [265]. At the clinical level, MES-GBM shows the shortest median survival (11.5 months), compared to CL- and PN-GBM (14.7 and 17 months, respectively) [266] (Figure 1). Within these 3 GBM subgroups, limited therapeutic benefit has been observed [261, 262]. Additionally, NFKB inhibitor alpha (*NFKBIA*) deletion confers radio-resistance in MES-GBM [267, 268].

Secondary GBM and its precursors harbor isocitrate dehydrogenase (NADP(+)) 1 (*IDH1*) and 2 (*IDH2*) mutations (collectively IDH^{mut}), in addition to either *TP53* mutations in low-grade astrocytoma (LGA) and high-grade astrocytoma (HGA), or co-deletion of chromosome 1p/19q in oligodendroglioma (ODG) [269, 270]. In contrast to IDH^{wt}, glioma patients retrospectively identified as IDH^{mut} showed improved survival upon standard of care temozolomide (TMZ) treatment [271]. Together with histopathology, *IDH* mutation and 1p/19q co-deletion statuses are now used resulting in the current integrated WHO classification [1]. The classification of brain tumors into IDH^{mut} (HGA, LGA, and ODG) or *IDH* wild type (IDH^{wt}; CL-, MES-, and PN-GBM) has been further supported by methylomics [264] (Figure 1).

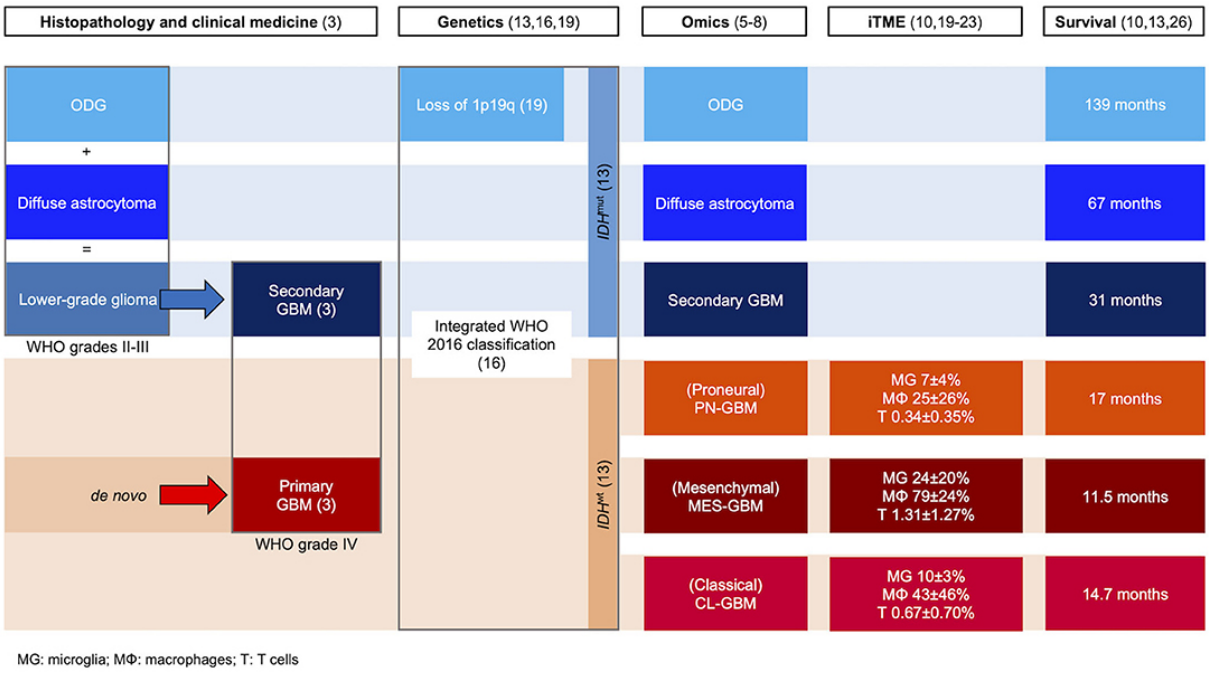

Figure 1: Classification of GBM based on histological, clinical, genetic, -omic and immune features.

IDH^{mut} and *IDH*^{wt} glioma subtypes are indicated in shades of blue and red, respectively. Arrows indicate tumor progression. The definition of iTME composition is described in the relevant publications. Median survival of ODG and diffuse astrocytoma is based on WHO grade II [1, 259, 261-264, 266, 269, 272-278].

4.1.3 Implications of GBM subtype on immune cell infiltrates

GBMs frequently contain high proportions of non-neoplastic immune cells that collectively form the immune tumor microenvironment (iTME). The considerable number of immune cells within these tumors may account for the gene expression variability observed between GBM patient biopsies [279]. Tumor-associated immune cells primarily enrolled for cytotoxicity against tumor cells, are typically hijacked by the tumor to promote its progression through mutual tumor-immune cell paracrine interactions and genetic reprogramming. Furthermore, the high content of macrophages (MΦ) and microglia (MG) and low frequency of lymphocytes in the GBM-iTME classify GBM as a lymphocyte-depleted tumor [280]. Since studies describing the immune cell composition of glioma biopsies *in situ* have used distinct methodologies and calculation modes, interstudy comparison is not quantifiable. Nevertheless, the superimposition of those data shows consistent trends. First, *IDH*^{wt} primary GBM patients, having shorter overall survival relative to *IDH*^{mut} secondary GBM patients, show globally higher MG, MΦ, and T lymphocyte composition [273]. Then, among *IDH*^{mut}, from WHO grade II to IV secondary GBM, progressively reduced patient outcome correlates with increased MG, MΦ and T cell contents [274]. Finally, primary GBM subgroups show differences in their immune composition, again linking tumor progression and reduced patient survival with higher proportions of immune cells [275, 277, 278]. Importantly, *NF1* loss (MES subtype) resulted in increased glioma-associated microglia and macrophage (GAM) infiltration, which was even more pronounced in recurrent GBM [266] (Figure 1). Thus, there is convincing evidence of increased recruitment of tumor-associated immune cells during brain tumor development, suggesting an oncogenic contribution of the iTME. Hampering this paracrine symbiotic association may lead to greater control of tumor progression. Mechanistically, the accumulation of 2-hydroxyglutarate resulting from *IDH* mutations suppresses the accumulation and activity of infiltrating T cells by impairing the nuclear factor of activated T cells (NFAT) expression in a paracrine manner [281, 282]. Further, NF-κB activation of GAMs mediates PN- to MES-GBM transition, while *NF1* inactivation, a hallmark of MES-GBM, results in higher numbers of infiltrating, anti-inflammatory, M2 GAMs and $CD4^+$ memory T cells [266, 268].

In parallel to *IDH*^{mut} tumors and their hypermethylator phenotype, GBM can acquire a hypermutator phenotype resulting from TMZ-based chemotherapy [276, 283-286]. Concurrently, the accumulation of neoantigens stimulates the recruitment of $CD8^+$ T cells into the tumor [266]. Thus, the occurrence of spontaneous or TMZ-induced tumor-specific neoantigens represents a potential modulator of iTME composition and T cell-mediated anticancer cytotoxicity in GBM. Altogether, the crosstalk between tumor and infiltrating immune cells suggests possible therapeutic interventions to redirect immune cells against neoplastic cells to further control glioma progression.

4.1.4 Characterization of the GBM-iTME

The brain has historically been considered an immune-privileged organ [287, 288]. This concept was long supported by 3 main observations: (a) the existence of a specialized vasculature in the brain, termed the blood-brain barrier (BBB) [289], (b) the lack of a conventional lymphatic system, (c) and a poorly characterized brain-specific immune cell population – MG. This classical dogma has been challenged by several studies that demonstrated that the CNS is in fact actively interacting with the immune system [290]. Increasing evidence suggests that inflammation is the prime cause of many neurodegenerative diseases, and it is now generally accepted that the CNS undergoes constant intrinsic and peripheral immune surveillance [291-293]. One such mechanism of immunosurveillance has been elucidated by the discovery of a CNS-specific lymphatic system. This study established that antigens and T cells can reach the cervical lymph nodes through cerebrospinal fluid-filled channels [294]. In addition, antigens may also enter the cerebral arteries and cervical lymph nodes through the Virchow Robin perivascular spaces, and immunoglobulins are able to cross the BBB via carrier-mediated transport [295, 296]. Taken together, these observations point towards the existence of important interactions between the CNS and the immune system, and underscore the role of the immune system in the induction and progression of brain cancers. Moreover, they emphasize the potential for immunotherapeutic approaches in the treatment of brain tumors.

The complex GBM-iTME is dominated by immunosuppressive cytokines such as prostaglandin E_2 (PGE2), transforming growth factor beta 1 (TGFB1), and interleukin (IL) -6 and -10 [297, 298]. Important “hubs of immunosuppression” such as high expression of STAT3 or FGL2 by GBM cells might directly act as paracrine mediators on the pleiotropic iTME, and could be universally targeted [299]. In parallel, regulatory

$CD4^+$ T-helper cells (Tregs) are an important immune population in the GBM-iTME [300]. Both natural Tregs (nTregs) – naturally occurring in the thymus – and induced Tregs (iTregs) – induced by activation with antigen or by antigen-presenting cells (APCs) – have been reported to contribute to GBM-mediated immunosuppression, with nTregs reportedly having a dominant role in the GBM-iTME [301]. Cytotoxic $CD8^+$ T cells are very rare, accounting for under 20% of all $CD3^+$ lymphocytes, and appear loosely distributed in the GBM parenchyma [302]. In an immunohistochemical (IHC) study of tissue microarray cores from 284 gliomas, the number of $CD8^+$ tumor-infiltrating lymphocytes (TILs) correlated negatively with tumor grade whereas the number of $CD4^+$ TILs displayed a positive correlation [303]. Another recent study reported that GBM-TILs increased their expression of indoleamine 2,3-dioxygenase (IDO1), an enzyme that catalyzes tryptophan (TRP) degradation, resulting in the depletion of TRP in the local iTME and consequent inhibition of T cell responses [304]. Moreover, another study demonstrated that GBM patients and GBM-grafted mice may harbor peripheral blood $CD4^+$ T cell counts as low as acquired immune deficiency syndrome subjects and show T cell-deficient lymphoid organs. Concomitantly, large numbers of T cells were instead found sequestered in the bone marrow (BM), accompanied by tumor-imposed loss of sphingosine 1 phosphate receptor 1 (S1PR1) from the T cell surface [305].

Yet, perhaps the most notable aspect of the GBM-iTME is its population of tumor-associated MΦ and MG – collectively referred to as GAMs. These are the most abundant GBM-infiltrating immune cells and may contribute to up to half of the total tumor mass [12, 13]. In addition to the recruitment of brain-resident MG to the tumor site, the high number of GAMs in glioma is a cumulative result of the influx of myeloid-derived MΦ into the brain as a consequence of tumor-induced neoangiogenesis and inflammatory stimuli. This inflammatory iTME acts in an immunosuppressive manner to promote tumor progression e.g. via reprogramming of GAMs to anti-inflammatory states by paracrine tumor cell-GAM crosstalk [10, 11, 34, 306]. The contribution of GAMs to gliomagenesis continues to unveil the complex interactions of GBM cells with their microenvironment [10, 11, 14]. Together, these data suggest that in addition to T cells, GAMs represent an attractive cell population with an intrinsic functional repertoire that may be reprogrammed to target tumor cells. In the supplementary information and table of this review, we provide a comprehensive overview of the most recent clinical trials and their strategies in interfering with the innate and adaptive GBM-iTME.

4.1.5 Distinction of BM-derived MΦ from brain-resident MG

MG are dynamic and specialized CNS-resident immune cells. Their name was first coined by Pío Del Río Hortega, then a student of Santiago Ramón y Cajal, and published in the Bulletin of the Spanish Society of Biology in 1919. MG are constantly monitoring the CNS and become activated in response to pathogens or CNS injury [50, 307].

Various experiments including parabiosis, adoptive transfer and fate mapping studies conducted in mouse models have elucidated our understanding of MG and their distinction from peripheral, BM-derived MΦ [12, 15-20]. MG and MΦ are thus distinct and ontogenically different cell populations [11].

Despite the separate origins of MG and MΦ, GAM accumulation within and around GBM has raised interest in dissecting the roles of these cells in tumor progression. Many common chemoattractant factors have been identified for MG and MΦ [14]. In the healthy brain, the CX3C motif chemokine receptor 1 (CX3CR1) is mostly expressed by MG and has been established as a reliable marker for MG imaging [14]. Notably, a polymorphism in the *CX3CR1* gene has been associated with reduced tumor infiltration by MG which led to increased survival of GBM patients [21]. Others reported conflicting findings regarding the importance of CX3CR1 and its ligand – CX3C motif chemokine ligand 1 (CX3CL1) – in tumor-directed MG migration [22, 23]. However, infiltrating monocytes, differentiating into MΦ express it as well, implying that CX3CR1 does not represent a MG-specific marker, especially in the context of glioma [22]. Notably, a recent study identified perivascular, meningeal, and choroid plexus MΦ as non-parenchymal brain MΦ that mediate immune responses at the brain boundaries and, like MG, express CX3CR1 in the healthy brain [49]. One of the first chemoattractant factors identified is CC motif chemokine ligand 2 (CCL2) or MCP1. Ectopic expression of CCL2 in rat glioma cells showed increased tumor growth, with massive infiltration of MG/MΦ, resulting in reduced survival [308]. Interestingly, it has been recently described that in mice, MG, in contrast to MΦ, do not express the CCL2 receptor, CC motif chemokine receptor 2 (CCR2), providing a novel model to investigate monocyte subset trafficking within the GBM-iTME [309]. In fact, Hutter and colleagues used a *Ccr2* knockout mouse model which limits MΦ infiltration into the tumor site, enabling the specific study of MG within the GBM iTME [71]. Colony stimulating factor 1 (CSF1) or M-CSF is another potent GAM-recruiting cytokine. Blocking its receptor, colony

stimulating factor 1 receptor (CSF1R) reduced GAM density and attenuated GBM invasion *in vivo* [25, 310]. Similar results were reported by a knockdown of its close relative, CSF2, which resulted in reduced MG-dependent invasion in organotypic brain slices as well as diminished growth of intracranial gliomas accompanied by extended survival in animal models [311].

Approaches to distinguish these cell populations have traditionally relied on the expression of the hematopoietic marker CD45, with yolk sac-derived MG being $CD45^{low}$ and infiltrating MΦ of hematopoietic origin $CD45^{high}$ [44]. This paradigm has been recently challenged by a study using irradiated chimeras with head protection which impeded the massive unspecific influx of monocytes due to a disrupted BBB. The authors showed that MG are able to upregulate CD45 and represent an inherent part of the $CD45^{high}$ population in the tumor context [312].

Therefore, better targets are needed to accurately distinguish resident MG from infiltrating inflammatory monocytes and non-parenchymal brain MΦ to better understand their contribution in glioma formation, maintenance, and progression.

In a traumatic brain injury model, *in vivo* time-lapse 2-photon imaging of MG revealed their rapid and targeted migration and process extension to the site of injury, establishing a barrier between the healthy and injured tissue. This rapid chemotactic response is mediated by the release of nucleotides following CNS injuries [50]. MG express several G protein-coupled receptors, including the G protein-coupled purinergic receptor P2Y 12 (P2RY12), a putative primary site where nucleotides act to induce MG chemotaxis. P2RY12 is also expressed on platelets and required for normal platelet aggregation and blood coagulation [313]. In the brain parenchyma, its expression is well limited to MG, making it a very useful marker in MG identification [52]. Another useful marker to distinguish MG from infiltrating MΦ is integrin subunit alpha 4 (ITGA4) or CD49D, which was specifically repressed in the MG of different mouse models of glioma. Its translational relevance has also been shown in human GBM biopsies [10].

Recent advances in RNA sequencing and other cell profiling technologies have enabled the discovery of cell-type-specific signature genes. Among these, a transmembrane protein of unknown function – transmembrane protein 119 (TMEM119) – is exclusively expressed by MG in the human and mouse brain [53]. Hence, TMEM119-specific antibodies are now widely used in IHC and flow cytometric (FC) applications.

The ongoing large-scale transcriptional profiling of MG further identified novel cell lineage-specific genes like hexosaminidase subunit beta (*HEXB*), which is highly expressed in MG and encodes a subunit of the lysosomal enzyme hexosaminidase, that catalyzes the degradation of gangliosides [58]. These novel instruments for cell-specific tracking and genetic modulation will enhance the specificity and sophistication of MG studies as well as our understanding of MG functions in the context of glioma.

4.1.6 MG activation and immune cell interactions in the GBM-iTME

MG accumulated within GBM typically undergo a morphological transformation from a ramified, resting phenotype, to an amoeboid, activated state [12]. For MΦ, different types of activation have been defined following *in vitro* stimulation. The proinflammatory M1 phenotype is typically acquired after stimulation with IFNγ, alone or in concert with microbial cues such as LPS. Whereas anti-inflammatory molecules, such as IL-4, -10, and -13, are inhibitors of MΦ activation and induce the alternative M2 phenotype [27, 28]. These polarized MΦ subpopulations differ in terms of receptor expression, effector function, and cytokine and chemokine production [28]. Given that these definitions of the different activation states are based on *in vitro* conditions, and the M1 and M2 phenotypes represent the extremes of a broader spectrum of functional states, they are only to some extent translatable to the *in vivo* settings. In the era of single cell sequencing and mass cytometry, and much more detailed functional state analysis, this polarization classification may soon become obsolete in the MG field. Nevertheless, several studies have analyzed the expression of M1 and M2 markers among GBM-associated GAMs and concluded that, similarly to other solid tumor types, they predominantly exhibit an anti-inflammatory M2 polarization and reduced phagocytic activity [11, 29-32]. It is believed that glioma-derived molecules such as CSF1 induce the shift of MG and MΦ toward the M2 phenotype and thus create a favorable microenvironment for GBM growth [31]. In addition, GAM expression of CD163 and macrophage scavenger receptor 1 (MSR1) or CD204, both of which are considered M2 MΦ markers, was significantly higher in grade IV GBM when compared to low-grade glioma (LGG), indicating that polarization of GBM-associated MG and MΦ toward the M2 phenotype correlates with a more malignant histological grade [34]. Accordingly, others identified the expression of CD74, an M1 polarization marker, by human GAMs to be positively correlated with the overall survival of GBM patients [35]. However useful they may have been in establishing and dissecting the functions of

MG, the traditional M1 and M2 phenotypes, and the resulting classification of MG responses into a binary system of pro- or anti-inflammatory has so far produced an oversimplified insight to their complex roles in the context of brain diseases [314, 315].

Studies of human and murine neurodegenerative diseases, as well as brain tumors, have identified genes and their encoded proteins previously known to be expressed in the DC compartment of the peripheral immune system. Moreover, transcriptomics data from diverse neurodegenerative disease studies show MG upregulation of genes involved in APC-T cell interactions [316]. Interestingly, similar trends have been found in MG isolated from GL261 syngeneic GBM mouse models as well as in tumor biopsies of GBM patients. This upregulated gene set included human and mouse homologs of immunosuppressive modulators (C type lectin domain containing 7A, *CLEC7A*; glycoprotein nmb, *GPNMB*; leukocyte immunoglobulin like receptor B4, *LILRB4*; and *PDCD1*) as well as stimulators (integrin subunit alpha X, *ITGAX* or *CD11C*; and secreted phosphoprotein 1, *SPP1*) of the adaptive immune system. Collectively, these studies show that MG derived from tumor and neurodegenerative states both contribute to immunosuppression and altered T cell responses in the brain [317-319].

In fact, a recent study showed that in the context of Alzheimer's disease (AD), chronically activated MG limit $CD3^+/CD8^+$ T cell recruitment to the brain [320]. Another study with GL261 murine glioma models demonstrated that MG are functional APCs and are required for complete antigen-specific $CD8^+$ T cell responses in an MHC class I-dependent manner [321]. Given the parallels between the inflammatory states resulting from brain tumors and neurodegenerative diseases, a better understanding of the link between innate and adaptive immune responses in the brain in combination with an improved characterization of MG heterogeneity, remain future directions for targeted immunotherapies against GBM.

Recently, combined high-throughput technologies of regionally annotated MG cells and intratumoral MG have mapped specific functional differences of MG in healthy vs. GBM-burdened brains. In non-neoplastic brains, 9 clusters of heterogeneous MG functional states were identified whereas in GBM-associated MG, single-cell RNA sequencing (scRNA-seq) revealed even more heterogeneity – 15 clusters – with upregulation of proinflammatory and metabolic genes, including *SPP1*, and several type I interferon genes, including apolipoprotein E (*APOE*) and *CD163.* By concurrent

mass cytometry, the upregulation of HLA-DR, triggering receptor expressed on myeloid cells 2 (TREM2) , APOE, adhesion G protein-coupled receptor G1 (ADGRG1) or GPR56, solute carrier family 2 member 5 (SLC2A5) or GLUT5, and Fc fragment of IgG receptor Ia (FCGR1A) or CD64 was confirmed in GBM-associated MG vs. normal control MG [322]. This underscores the diversity and plasticity of MG in the healthy brain and the GBM-iTME, and reiterates the difficulty in targeting these cells for treatment.

4.1.7 MG in GBM progression

Early co-culture studies noted that the motility of murine glioma cells was increased in the presence of MG, and that this glioma-promoting effect could be further enhanced by MG-activating substances like CSF2 [323]. GBM cells are known to constitutively release CSF1 and CSF2, which act as chemoattractants for MG and convert GAMs to protumoral phenotypes [310]. Consistent with the tumor-promoting effect of CSF1, blockade of CSF1R led to decreased expression of M2 markers in GAMs, resulting in regression of established tumors and increased survival in a mouse GBM model [310]. To summarize, once MG and MΦ are recruited to the tumor site and re-educated to a protumorigenic phenotype, mutual paracrine signaling between GAM and GBM cells is established whereby glioma growth and invasion are promoted. Similar effects on glioma cells could be shown by using GAM-conditioned media instead of co-cultures [323]. Many of the soluble factors involved in GAM-glioma crosstalk have been identified, such as epidermal growth factor (EGF), which is released by MG and stimulates GBM cell migration and invasion via the commonly upregulated epidermal growth factor receptor (EGFR) on glioma cells [25]. Other factors include anti-inflammatory TGFB1 and IL-10, pro-inflammatory molecules like TNF, IL-1B, and IL-6, as well as pro-angiogenic factors like vascular endothelial growth factor A (VEGFA). TGFB1 promotes the migration of glioma cells via processes that likely involve the upregulation of integrin expression and function [324]. Furthermore, TGFB1 induces the release of matrix metallopeptidase 2 (MMP2) in its inactive form – pro-MMP2 – which becomes activated upon cleavage by the membrane-bound matrix metallopeptidase 14 (MMP14) [39, 324]. GBM-associated MG upregulate MMP14 and thereby facilitate the invasion of glioma cells into the brain parenchyma by metalloproteinase-mediated degradation of the extracellular matrix [39]. A recent study by Walentynowicz et al. sought to assess the role of human GBM conditioned media on human MG cell

lines on the MG transcriptome. *TGM2* and *GPNMB* were identified across various datasets, but their relevance is awaiting further experimental validation [325].

Along with this paracrine glioma-promoting effect, GAMs also enable GBM engraftment and invasion by failing to efficiently eliminate cancer cells by phagocytosis. Their role as phagocytic innate immune cells is perturbed by glioma cells rendering MG and MΦ to an anti-inflammatory, antiphagocytic M2 phenotype [36]. Moreover, upregulation of the so-called “don’t eat me” signals on the surface of glioma cells and masking of antigenic sites by overexpressing sialic acid-rich glycoproteins are both effective strategies to inhibit phagocytosis and evade innate immune surveillance [41, 42, 326].

4.1.8 Modeling MG-GBM interactions

The generation of a mouse strain in which the *Cx3cr1* locus was replaced by a green fluorescent protein (GFP) reporter gene (*Cx3cr1*$^{+/GFP}$) allowed for the first time the direct study of MG *in vivo* using 2-photon-microscopy [327, 328]. This mouse line strongly labels MG and is the best-studied model in MG research [327, 329]. To further exploit the *Cx3cr1* promoter activity, the *Cx3cr1* gene was replaced with sequences encoding either Cre recombinase (*Cx3cr1*^{Cre}) or a Cre recombinase fused to a mutant estrogen ligand-binding domain that requires the presence of the estrogen antagonist tamoxifen for activity (*Cx3cr1*^{CreERT2}) [48]. These mouse lines enabled a conditional, MG-specific constitutive or inducible gene knockout, which advanced the specificity of MG research significantly (Table 1).

Target gene	Modifications	Reference
Cx3cr1	*Cx3cr1*$^{+/GFP}$ *Cx3cr1*$^{GFP/GFP}$	[46]
	Cx3cr1^{Cre} *Cx3cr1*^{CreERT2}	[48, 148]
P2ry12	*P2ry12*$^{-/-}$ *Cx3cr1*$^{+/GFP}$	[52]
Sall1	*Sall1*^{GFP}	[56]
	Sall1^{CreERT2}	[57]
Tmem119	*Tmem119*^{EGFP}	[54]
	Tmem119^{CreERT2}	[54]

Table 1 Current MG mouse models.

Even though CX3CR1 is highly expressed on MG, it is expressed as well on MΦ, monocytes, and DCs [327]. P2RY12, on the other hand, was initially investigated for its function as a regulator of platelet adhesion and activation. P2RY12-deficient mice were therefore primarily used to study platelet physiology and blood coagulation [330, 331]. Eventually, P2RY12 was identified as a MG-specific marker in the brain parenchyma and *P2ry12*$^{-/-}$ MG reporter mice were generated, allowing the study of P2RY12-mediated MG chemotaxis to the site of BBB injuries [52, 332].

Gene expression profiling not only identified MG specific surface proteins but also MG signature genes such as spalt like transcription factor 1 (*Sall1*), which encodes a transcriptional regulator [55]. Accordingly, the introduction of *Sall1*^{GFP} and *Sall1*^{CreERT2} knock-in mouse lines represent more distinct models for MG tracking and genetic modulation *in vivo* [56, 57]. The ongoing efforts, mainly based on large-scale transcriptional analysis of MG cells, will keep providing novel targets for even more specific *in vivo* imaging and modulation. Very recently demonstrated by the discovery of TMEM119 which was shortly followed by the introduction of a knock-in *Tmem119*^{EGFP} reporter mouse line and *Tmem119*^{CreERT2} mice [53, 333].

With the increased interest in MΦ-focused immuno-oncology, assays that robustly and reproducibly determine the prophagocytic effect of a therapeutic agent of interest, are constantly evolving as well. While the first reports of the beneficial effect of CD47 disruption in leukemia cells, were mainly based on classical fluorescence microscopy, calculating the phagocytic index by dividing ingested cells by the total number of MΦ, they were soon replaced by FC-based approaches to better identify also smaller effect sizes in other tumor models [41, 66-70]. In these experiments, phagocytes were identified by specific markers and co-incubated with cell-dye labeled tumor cells. MΦ that had successfully phagocytosed tumor cells were also positive for the tumor cell stain. However, this method lacks the optical confirmation that the tumor cell has been really engulfed by the phagocytic cell, which is why many studies still included a microscopic assessment or use more elaborately time-lapse live-cell microscopy which offers not only spatial but also temporal information [120]. Technological advances enable the better identification of phagocytic events as well, as seen with the introduction of imaging FC, which combines the high throughput analysis of FC with the detailed morphometric information of fluorescence microscopy [334]. Besides these *in vitro* phagocytosis assays, many efforts are undertaken to make the complex

interplay between tumor cells and phagocytes visible. In many studies, after a specific treatment *in vivo*, the tumor mass is resected and dissociated and within the single-cell suspension, phagocytosis is measured as the ratio of the double-positive MΦ population by FC [68, 69, 120]. This approach compared to *in vitro* models allows for a better understanding of the complex interface between innate and adaptive immune systems as they orchestrate the antitumor immune response together [153]. More sophisticated and direct approaches employ specific reporter mice that enable *in vivo* imaging using 2-photon microscopy. As shown in their recent publication, Hutter and colleagues were able to demonstrate real-time phagocytosis of living glioma cells by MG and MΦ upon CD47 disruption using *Ccr2*$^{+/RFP}$ *Cx3cr1*$^{+/GFP}$ reporter mice, allowing the direct study of these cells in the TME [71]. As new targets in innate immunotherapy are emerging, sophisticated methods will be needed to validate their prophagocytic capacity and clinical potential in cancer therapy, such as 3D cultures and tissue culture bioreactors for improved *ex vivo* tissue preservation [335]. Another promising technology to study cell interactions, tissue composition, and spatial distribution of the iTME is high-dimensional multiplexing – CO-Detection by indEXing (CODEX) – that allows *in situ* tissue cytometry with the detection of over 50 parameters [336].

4.1.9 MG targeting and modulation

As the largest immune cell population and one that positively correlates with glioma malignancy, invasiveness, and grade, MG represent the primordial target for modulation and antitumor immunotherapy. In this context, most strategies so far aimed at impairing GAM recruitment to the tumor site, thereby preventing their glioma-promoting effects. This included the previously mentioned blockade of CSF1R, disruption of periostin (POSTN), which is secreted by GSCs, and recruits GAMs through integrin $\alpha_v\beta_3$ signaling, or inhibition of the CXC motif chemokine receptor 4 (CXCR4) chemotactic pathway [10, 310]. The latter has been mainly implicated in MΦ mobilization through increased CXC motif chemokine ligand 12 (CXCL12) expression after radiation therapy [337]. In combination with radiotherapy, a small molecule inhibitor of CXCL12/CXCR4 interactions prevented GAM infiltration and tumor recurrence [338]. Another approach aimed at reversing the MG tumor-promoting effects and re-educating them to an antitumor phenotype. One report showed that activated NK cells combined with an antibody against chondroitin sulfate proteoglycan 4 (CSPG4) on GBM cells, were able to reverse the GAM phenotype [62]. Osteopontin (OPN/encoded by

SPP1) is another promising candidate protein secreted by GBM cells, which has prognostic implications and drives the protumorigenic reprogramming of MG, which can be therapeutically targeted [339, 340].

Recently, the focus has shifted towards the phagocytic role of MG as part of innate immune surveillance, most often targeted through the CD47/signal regulatory protein alpha (SIRPA) and the sialic acid/sialic acid binding immunoglobulin like lectin (SIGLEC) phagocytosis axes. CD47 is a widely expressed transmembrane protein with numerous functions, among which the inhibition of phagocytosis [63]. Upon binding and activating its receptor SIRPA on the surface of mononuclear cells, CD47 inhibits the phagocytic activity of MΦ and MG [64]. This antiphagocytic signal is transmitted via phosphorylation of the immunoreceptor tyrosine-based inhibitory motif (ITIM) on the cytoplasmic tail of SIRPA. Subsequent binding and activation of the protein-tyrosine phosphatase non receptor type 6 (PTPN6) and 11 (PTPN11) blocks phagocytosis, putatively by preventing the accumulation of myosin-IIA at the phagocytic synapse [341]. However, CD47 expression is best characterized for its role in hematopoietic cell homeostasis, particularly in red blood cells and platelets, where it is required to prevent their elimination by splenic MΦ. CD47 is thus considered a marker of self [64]. In pathological processes, inflammation-mobilized hematopoietic stem cells protect themselves from phagocytosis by upregulating CD47 on their surface [66]. This CD47 overexpression is co-opted by tumor cells and represents a common feature of hematologic and solid tumors, allowing them to evade innate immune surveillance [41, 66-68].

As a major “don’t eat me” signal, CD47 is highly upregulated on the surface of nearly all human tumor cell types, including GBM cells. Transcriptional analysis of glioma patients revealed that high *CD47* mRNA expression levels were associated with decreased progression-free and overall survival, suggesting that *CD47* expression levels may serve as a clinically relevant prognostic factor [41]. Willingham et al. were the first to describe the GAM re-educating effect of CD47 blockade in models of GBM. Using targeted monoclonal antibodies against CD47 enabled MΦ-dependent phagocytosis of patient-derived GBM neurospheres *in vitro*. Furthermore, the administration of anti-CD47 antibodies inhibited tumor growth and increased the survival of orthotopic immunodeficient mice transplanted with patient derived GBM cells, providing the first preclinical validation of CD47 as a therapeutic target in GBM [41]. Additional studies

showed that anti-CD47 treatment repolarized GAMs *in vivo* to an M1 phenotype and that both M1- and M2-polarized MΦ alike displayed a higher GBM cell phagocytosis rate under anti-CD47 treatment [69]. The therapeutic safety and efficacy of anti-CD47 treatment was also demonstrated in mouse models of murine high-grade glioma as well as 5 aggressive and etiologically distinct human pediatric brain tumors (medulloblastoma, atypical teratoid/rhabdoid tumor, primitive neuroectodermal tumor, pediatric GBM, and diffuse intrinsic pontine glioma) [70].

More recently, Hutter and colleagues dissected the response of MG and infiltrating peripheral MΦ upon anti-CD47 treatment in GBM. Using a mouse model with genetically color-coded MΦ (*Ccr2*^{RFP}) and MG (*Cx3cr1*^{GFP}), they showed that even in mice lacking Ccr2-mediated MΦ recruitment to the brain (*Ccr2*$^{RFP/RFP}$ *Cx3cr1*$^{GFP/+}$), MG-mediated GBM phagocytosis was sufficient to reduce tumor burden and prolong survival under anti-CD47 treatment. This observation led to the identification of MG as effector cells of GBM cell phagocytosis in response to CD47 blockade [71].

Comparable to CD47 overexpression, the aberrant glycosylation of cancer cells represents a common feature of malignant transformation [73, 74]. These glycoproteins and glycolipids are often terminated by negatively charged sialic acids. Sialic acids are derivatives of neuraminic acid, and the predominant sialic acid found in mammalian cells bears at its amino site an acetyl group, therefore termed *N*-acetyl-neuraminic acid. The addition of sialic acids is mediated by sialyltransferases, a family of glycosyltransferases [342]. Hypersialylation, meaning the upregulation of sialic acid-containing glycans (sialoglycan) on the cell surface through altered sialyltransferase expression and the increased introduction of non-human sialic acids like *N*-glycolyl-neuraminic acid (xenosialylation) are, together with the altered glycosylation itself, key changes of malignant tissue and important for cancer progression [79, 80].

Sialic acids can modulate the iTME through SIGLEC engagement. To date, 14 human and 9 mouse SIGLECs have been identified, differing in their sialic acid ligand specificity and intracellular signaling cascades. SIGLECs are expressed on most cells of the immune system and can transmit immunosuppressive signals upon binding to sialic acids. Similar to the inhibitory SIRPA receptor – inhibitory SIGLEC receptors contain ITIMs in their intracellular domain that signal negatively via the recruitment of PTPN6 and 11 [84]. The physiological role of SIGLECs to recognize sialic acids as self-associated patterns and therefore counter-regulate overshooting immune

reactions and limit tissue damage during inflammation can be exploited by cancer cells [90]. Hypersialylation of tumor cells can thus contribute to tumor immune evasion [42].

Initially, immunoinhibitory SIGLECs in brain pathologies were primarily associated with CD33 or SIGLEC3 as a genetic risk factor for AD [104, 343, 344]. Subsequent functional studies showed that CD33 inhibits MG uptake of amyloid-β plaques in diseased brains [106]. More recently, CD22 or SIGLEC2 was also identified as a negative regulator of phagocytosis that is upregulated on aged MG. Inhibition of CD22 promoted the clearance of myelin debris, amyloid-β oligomers, and α-synuclein fibrils in an AD model [107]. Other studies identified important roles of SIGLECs in neuroinflammatory diseases, where immunoinhibitory SIGLECs convey neuroprotective functions by alleviating especially MG neurotoxicity [108, 109].

With the paradigm shift in cancer therapy that came with the discovery of immune checkpoint inhibitors, the sialoglycan-SIGLEC pathway attracted recently a great deal of attention as a novel target for cancer immunotherapy. This holds especially true in brain malignancies, since phase II and III clinical trials of classical immunotherapeutic agents like PDCD1 and CD274 inhibitors showed no significant improvement in the median overall survival of GBM patients [111]. Correlative single-cell transcriptomic analysis, including The Cancer Genome Atlas (TCGA) data, showed that most members of the SIGLEC family are differentially expressed in glioma. Interestingly, several SIGLEC receptors are predominantly expressed on MΦ and GAMs with higher expression levels observed in high-grade gliomas [112].

In a more translational approach, others investigated the role of immunomodulatory SIGLECs in the treatment with glucocorticosteroids, including dexamethasone, which is frequently used to control tumor-induced edema in brain tumor patients. They found alterations in tumor cell surface sialylation and SIGLEC recognition in response to dexamethasone treatment [114]. Specifically, MG showed an upregulation of SIGLEC receptors together with induction of an anti-inflammatory cytokine profile, indicating a crucial role of SIGLECs in dampening the dexamethasone-induced antitumor immunity [115]. The first experimental evidence that linked SIGLECs with whole tumor cell phagocytosis in glioma dates back to 2013, when Siglec H, a MG-specific marker, was suggested to be a phagocytic receptor for glioma cells [117-119]. Novel insights into the sialic acid-SIGLEC antiphagocytic axis have recently emerged. In particular, SIGLEC10 was identified as the receptor of CD24, an additional “don’t eat me” signal.

Tumor-expressed CD24 promoted innate immune evasion through its interaction with GAM-expressed SIGLEC10 [120]. Another study focused on SIGLEC15 as an immune suppressor and potential target for cancer immunotherapy. Using a genetic mouse model and intracranial injection of murine glioma cells, the authors found significantly slower tumor growth associated with more MΦ and $CD8^+$ T cells in the TME upon genetic ablation of SIGLEC15. Together with *ex vivo* restimulation assays, their data support a role for SIGLEC15 in MΦ-mediated suppression of tumor immunity [122]. The mounting evidence of SIGLEC engagement by cancer cells to evade the antitumor immune response, especially innate immune response, make sialic acid-SIGLEC interactions very attractive candidates for potentiating antitumor immunity in GBM.

4.1.10 Discussion: Emerging local and combinatorial approaches for the treatment of GBM place MG at the center stage

Despite advances in surgical techniques, radiation therapy, and chemotherapy, effective treatment of GBM remains an unresolved challenge. Today's unspecific approach of alkylating chemotherapy and radiation therapy causes major toxicities and debilitating side effects. Better ways to control this devastating disease are urgently needed.

We previously showed that modulation of MG within GBM, e.g. by CD47-SIRPA disruption, can control GBM progression by rendering MG tumor-phagocytic. Although disrupting CD47-SIRPA modulates MΦ and MG anti-GBM activity and reprograms the immunosuppressive iTME, GBM represents a heterogeneous tumor entity with a multitude of deregulated cancer pathways. Therefore, a subset of tumor cells will evade the MG-mediated antitumor response and develop resistance. We are thus convinced that reprogramming of MG within the tumor will not suffice by itself to halt GBM entirely, especially in view of emerging insights into MG heterogeneity. On the other hand, pure tumor-targeting approaches, vaccinations with tumor antigens, monoantigenic CAR T cells, or intratumoral cytokine deliveries are all prone to failure because of the overwhelming immunosuppressive contribution of the iTME, and specifically tumor-educated MG. Therefore, more sophisticated combinatorial approaches that target MG, adaptive immunity, and tumor cells at once are mandated.

We believe that MG are at the centerstage for modulation in the iTME, since this will also influence the antitumoral capacity of other components of the iTME such as

TILs, e.g. via enhanced antigen presentation [345]. The capacity to of MG to present antigens e.g. after tumor cell phagocytosis needs to be evaluated further and with novel techniques in various experimental contexts since this might offer key insights into potential combinatorial strategies with vaccination studies or T cell checkpoint inhibitor treatments. How MG modulation and reprogramming is best achieved, and which – often redundant – immune evasion mechanisms should be targeted to achieve a durable induction of antitumoral activity is largely unknown. On top, the additional MΦ modulation and recruitment effects caused by the treatments should be considered, since additional recruitment of BM-derived MΦ might cause increased unwanted side effects such as enhanced edema. Prophagocytic pathways beyond CD47-SIRPA with higher MG specificity might be particularly attractive to tailor the MG response. However, an overshooting MG induction might as well lead to deleterious effects in the brain (e.g. via hyperphagocytosis), and treatment effects, timing, and delivery need to be carefully validated in future clinical trials. Since most systemic treatments in brain tumors do not effectively reach the tumor because of the BBB, local/continuous application of these treatment regimens might be most effective, and application of these treatments in the early phase of the disease would be preferable over the post-treatment recurrent situation, where the iTME and tumor resistance mechanisms are even more deranged. Besides that, it remains to be studied, whether these treatments should be applied before or after tumor resection, and whether targeting of the peripheral invasion zone of the tumor, where presumably a lot of iTME reprogramming happens, might be advantageous. A multitude of strategies for MG modulation may unleash the inherent antitumoral armamentarium of MG and have translational potential; future translational research and clinical trials should pave the way on how to optimally design these approaches against GBM. In Figure 2, we summarize promising combinatorial treatment strategies to overcome these challenges.

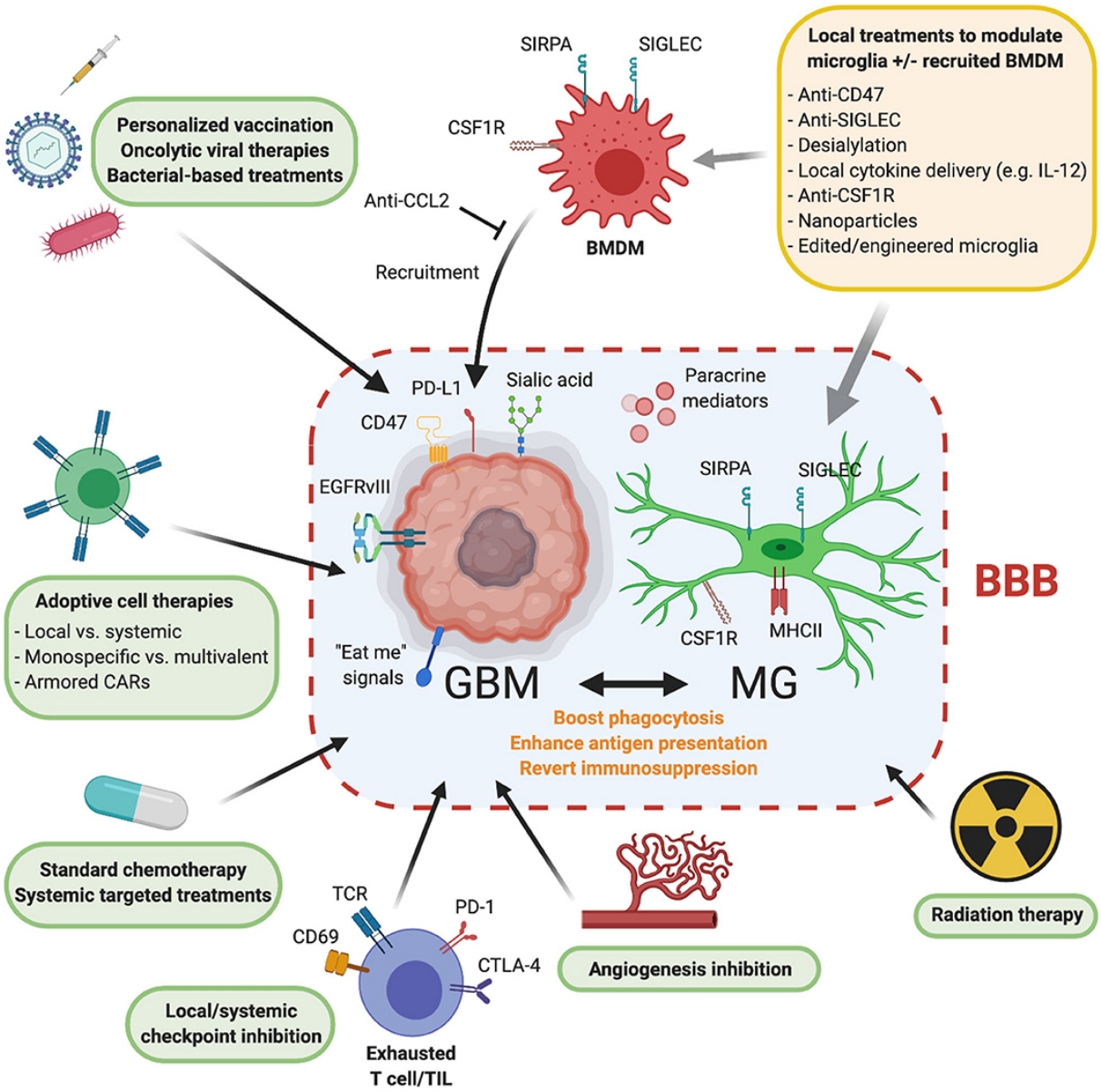

Figure 2 Combinatorial approaches of local MG modulation and other treatment modalities against GBM.

Means of local MG modulation (upper right): MG can be targeted locally beyond the BBB by various approaches to influence MG phagocytosis, enhance antigen presentation and revert generalized immunosuppression. Prominent potential means to locally modulate MG include anti-CD47 or anti-Siglec treatments, intratumoral desialylation, application of pro-inflammatory cytokines, “reprogramming” by blocking CSF1 signaling, or addition of immunomodulatory nanoparticles. Some of these modalities would also interfere with infiltrating BMDMs, e.g anti-CCL2 blockade. Overall, this would enable other tumor specific or immunotherapeutic regimens to exert their antitumorigenic activity.

Combinatorial approaches with MG modulation: *Personalized vaccination, oncolytic viral therapy, or bacterial based approaches:* the effect of tumor-specific vaccinations, oncolytic viruses or tumor-targeting bacteria might be significantly enhanced when tumor-associated MG is reverted to a less immunosuppressive phenotype. *MG modulation + tumor-targeting CAR T cell therapy:* combining MG modulation with tumor antigen-specific CAR T cell therapy poses

another way to circumvent current obstacles in GBM therapy. Local application of MG modulation and tumor-specific CAR T cells might result in better GBM control. Novel CAR T products could combine MG modulation, e.g. by reprogramming MG and targeting the tumor at once. *MG modulation + chemotherapy or targeted treatments:* tumor cells respond to established chemotherapy with increased expression of “eat-me” signals. Combinatorial strategies of already established chemotherapies with inducers of MG phagocytosis could improve treatment responses. *MG modulation + T cell checkpoint therapy:* this dual strategy of targeting the major players of the GBM-iTME – MG – and facilitating an intratumoral T cell response in addition to a putative MG-mediated T cell response might boost tumor regression. Further, the thorough analysis of tumor-phagocytosing MG vs. non-phagocytosing MG, their MHC molecules and linked, presented antigens, could lead to the discovery of novel tumor antigens and result in potential vaccination candidates. *MG modulation + angiogenesis inhibition:* anti-VEGFR treatment serves as a salvage therapy in recurrent GBM. Additional MG activation might prevent development of early resistance. *MG modulation + radiation therapy:* in line with chemotherapy, radiation therapy enhances immune responses and upregulates “eat-me” signals on tumor cells. Additional MG modulation could increase efficacy and long-term treatment responses.

4.1.11 Acknowledgements

This work was supported by a Swiss National Science Foundation Professorial Fellowship (PP00P3_176974); the ProPatient Forschungsstiftung, University Hospital Basel (Annemarie Karrasch Award 2019); Swiss Cancer Research Grant (KFS-4382-02-2018) to G.H.; Swiss Cancer Research MD-PhD Grant (MD-PhD-4818-06-2019) to P.S.; the Department of Surgery, University Hospital Basel, to G.H. and P.S.; and by The Brain Tumour Charity Foundation, London, UK (GN-000562) to G.H. and T.S. was supported by a UICC Technical Fellowship (TF/18/625070). We would like to thank Dr. Selina Ackermann for editorial support and critical revision of the manuscript.

4.1.12 Author contribution

Conception or design of the work (G.H., T.S.), Literature Collection (T.M., P.S., T.S.), Drafting the article (T.M., P.S., T.S., JL.B., M.R. J.v.B., S.Z., G.H.) Critical revision of the article (G.H.) Final approval of the version to be published (all authors).

4.1.13 Conflict of Interest

The authors declare that the research was conducted in the absence of any commercial or financial relationships that could be construed as a potential conflict of interest.

5 General conclusions and future plans

Our data highlight the Siglec-sialic acid axis as an attractive therapeutic target in GBM patients. We show that Siglec-E depletion leads to increased tumor cell phagocytosis by MG and MdCs, elevated expression of NF-κB target genes in MdCs, which mediates cross-priming of $CD8^+$ T cells and ultimately synergizes with cancer immunotherapy to convey a substantial survival benefit in a highly aggressive and poorly immunogenic CT-2A GBM preclinical model. We further showcased the translational relevance of Siglec-9/E disruption within GBM, by using Siglec-9 blocking antibody on cultured, perfused 3D tumor explants (as recently described by us [155]) and observed increased anti-tumoral cytokine production in 60% of patients. Second, we took advantage of an image-based ex-vivo drug screening platform, which demonstrated that Siglec-9 disruption efficiently reduced the number of glioma cells despite interpatient heterogeneity.

Together with recent findings, our study further underlines the importance of combining innate and adaptive immunotherapies, especially in less immunogenic and ICI-resistant tumors such as GBM.

These combinations could include established treatment regimens, as we were able to show additive effects when combining Siglec-E depletion with anti-CD47 and anti-PD1. Yet, exploring the transcriptional landscape of the GBM iTME on a single-cell level, revealed novel potential targets for combinatorial immunotherapeutic approaches.

One focus in this regard might be the described regional transcription profile of MG, with downregulated gene sets involved in antigen processing and presentation via MHC-I and MHC-II in the tumor peripheral MG. Along this line, *ID1* was identified as one of the signature genes in these presumably less immunogenic peripheral MG. Based on our data and evidence from the literature, which linked *ID1* to suppression of anti-tumor immune responses in the myeloid compartment [188], we hypothesized that *ID1* could act as an innate immune checkpoint in GBM-associated MG. Opening up a potential new avenue for rendering MG pro-inflammatory by blocking ID1-mediated signaling. A project which is currently followed up on by Deniz Kaymak, a new MD-PhD student in our lab. He characterizes *Id1* overexpressing murine BV2 microglia cell line in regard to their antigen processing and presentation capabilities, and

eventually testing the effects of *Id1* conditional innate knock-out in vivo, by using the same inducible *Sall1*^{CreERT2} and *Cx3cr1*^{CreERT2} mouse lines, crossed to *Id1*$^{fl/fl}$ mice [346].

Exploring further the distinct region-dependent phenotype of MG in the human GBM iTME by performing cell-cell interaction analysis based on ligand-receptor expression levels, revealed SPP1 as a leading potential cell-cell interaction mediator between the peripheral MG and lymphocytes. SPP1-mediated signaling has been described to suppress T cell activation and proliferation through binding with T cell expressed CD44 [228]. Possibly identifying SPP1 as mediator between the less immunogenic peripheral MG and the inadequately activated peripheral lymphocytes, which might be amenable to therapeutic intervention.

Comparing this impaired activation signature of lymphocytes, specifically CD8$^+$ T cells from the tumor periphery to circulating CD8$^+$ T cells, identified *CX3CR1*$^+$ CD8$^+$ T cells to be enriched in the patient's blood, but nearly absent in the TME. Recent studies proposed T cell expressed *CX3CR1* as a predictor of response to ICI therapy [233, 234]. Therefore, the absence of presumably ICI therapy-responsive CD8$^+$ T cells in the glioma iTME could serve as an additional explanation for the disappointing outcomes of clinical trials using traditional ICI in glioma patients. Yet, opening up another possible avenue to render cancer immunity anti-tumorigenic. This could be achieved by adoptive transfer of *Cx3cr1*-expressing CD8$^+$ T cells into our GBM mouse model, combined with ICI. This approach could eventually be translated into clinics in the form of autologous CX3CR1-expressing lymphocyte transfer into the tumor resection cavity and combined with ICI. The transferred cells might replace the glioma residing CD8$^+$ T cells which display a T_{rm} exhaustion phenotype, potentially leading to an improved response to the ICI treatment.

Taken together, our data identifies the Siglec-sialic acid-axis as a promising innate immune checkpoint and underscores the value of Siglec blockade in combinatorial approaches to liberate anti-tumor immunity. Further, we offer a transcriptional landscape of the GBM-associated immune cells in three tumor compartments, which could help to uncover novel therapeutic strategies to combat this fatal disease.

6 References

1. Louis, D.N., et al., *The 2016 World Health Organization Classification of Tumors of the Central Nervous System: a summary.* Acta Neuropathol, 2016. **131**(6): p. 803-20.
2. Ohgaki, H., *Epidemiology of Brain Tumors*, in *Cancer Epidemiology: Modifiable Factors*, M. Verma, Editor. 2009, Humana Press: Totowa, NJ. p. 323-342.
3. Yan, H., et al., *IDH1 and IDH2 mutations in gliomas.* N Engl J Med, 2009. **360**(8): p. 765-73.
4. Ohgaki, H. and P. Kleihues, *The definition of primary and secondary glioblastoma.* Clin Cancer Res, 2013. **19**(4): p. 764-72.
5. Stupp, R., et al., *Effects of radiotherapy with concomitant and adjuvant temozolomide versus radiotherapy alone on survival in glioblastoma in a randomised phase III study: 5-year analysis of the EORTC-NCIC trial.* Lancet Oncol, 2009. **10**(5): p. 459-66.
6. Stummer, W., et al., *Intraoperative detection of malignant gliomas by 5-aminolevulinic acid-induced porphyrin fluorescence.* Neurosurgery, 1998. **42**(3): p. 518-25; discussion 525-6.
7. Lima, F.R., et al., *Glioblastoma: therapeutic challenges, what lies ahead.* Biochim Biophys Acta, 2012. **1826**(2): p. 338-49.
8. Stupp, R., et al., *Radiotherapy plus concomitant and adjuvant temozolomide for glioblastoma.* N Engl J Med, 2005. **352**(10): p. 987-96.
9. Verhaak, R.G., et al., *Integrated genomic analysis identifies clinically relevant subtypes of glioblastoma characterized by abnormalities in PDGFRA, IDH1, EGFR, and NF1.* Cancer Cell, 2010. **17**(1): p. 98-110.
10. Bowman, R.L., et al., *Macrophage Ontogeny Underlies Differences in Tumor-Specific Education in Brain Malignancies.* Cell Rep, 2016. **17**(9): p. 2445-2459.
11. Kennedy, B.C., et al., *Tumor-associated macrophages in glioma: friend or foe?* J Oncol, 2013. **2013**: p. 486912.
12. Charles, N.A., et al., *The brain tumor microenvironment.* Glia, 2011. **59**(8): p. 1169-80.
13. Morantz, R.A., et al., *Macrophages in experimental and human brain tumors. Part 2: studies of the macrophage content of human brain tumors.* J Neurosurg, 1979. **50**(3): p. 305-11.
14. Hambardzumyan, D., D.H. Gutmann, and H. Kettenmann, *The role of microglia and macrophages in glioma maintenance and progression.* Nat Neurosci, 2016. **19**(1): p. 20-7.
15. Hickey, W.F. and H. Kimura, *Perivascular microglial cells of the CNS are bone marrow-derived and present antigen in vivo.* Science, 1988. **239**(4837): p. 290-2.
16. Massengale, M., et al., *Hematopoietic cells maintain hematopoietic fates upon entering the brain.* J Exp Med, 2005. **201**(10): p. 1579-89.
17. Simard, A.R. and S. Rivest, *Bone marrow stem cells have the ability to populate the entire central nervous system into fully differentiated parenchymal microglia.* Faseb j, 2004. **18**(9): p. 998-1000.
18. Ajami, B., et al., *Local self-renewal can sustain CNS microglia maintenance and function throughout adult life.* Nat Neurosci, 2007. **10**(12): p. 1538-43.
19. Ajami, B., et al., *Infiltrating monocytes trigger EAE progression, but do not contribute to the resident microglia pool.* Nat Neurosci, 2011. **14**(9): p. 1142-9.
20. Ginhoux, F., et al., *Fate mapping analysis reveals that adult microglia derive from primitive macrophages.* Science, 2010. **330**(6005): p. 841-5.

21. Rodero, M., et al., *Polymorphism in the microglial cell-mobilizing CX3CR1 gene is associated with survival in patients with glioblastoma.* J Clin Oncol, 2008. **26**(36): p. 5957-64.
22. Feng, X., et al., *Loss of CX3CR1 increases accumulation of inflammatory monocytes and promotes gliomagenesis.* Oncotarget, 2015. **6**(17): p. 15077-94.
23. Liu, C., et al., *CX3CL1 and CX3CR1 in the GL261 murine model of glioma: CX3CR1 deficiency does not impact tumor growth or infiltration of microglia and lymphocytes.* J Neuroimmunol, 2008. **198**(1-2): p. 98-105.
24. Pyonteck, S.M., et al., *CSF-1R inhibition alters macrophage polarization and blocks glioma progression.* Nature Medicine, 2013. **19**: p. 1264.
25. Coniglio, S.J., et al., *Microglial stimulation of glioblastoma invasion involves epidermal growth factor receptor (EGFR) and colony stimulating factor 1 receptor (CSF-1R) signaling.* Mol Med, 2012. **18**: p. 519-27.
26. Sielska, M., et al., *Distinct roles of CSF family cytokines in macrophage infiltration and activation in glioma progression and injury response.* The Journal of Pathology, 2013. **230**(3): p. 310-321.
27. Mantovani, A., et al., *The chemokine system in diverse forms of macrophage activation and polarization.* Trends Immunol, 2004. **25**(12): p. 677-86.
28. Mantovani, A., et al., *Macrophage polarization: tumor-associated macrophages as a paradigm for polarized M2 mononuclear phagocytes.* Trends Immunol, 2002. **23**(11): p. 549-55.
29. Gabrusiewicz, K., et al., *Characteristics of the alternative phenotype of microglia/macrophages and its modulation in experimental gliomas.* PLoS One, 2011. **6**(8): p. e23902.
30. Kees, T., et al., *Microglia isolated from patients with glioma gain antitumor activities on poly (I:C) stimulation.* Neuro Oncol, 2012. **14**(1): p. 64-78.
31. Li, W. and M.B. Graeber, *The molecular profile of microglia under the influence of glioma.* Neuro Oncol, 2012. **14**(8): p. 958-78.
32. Sica, A., et al., *Tumour-associated macrophages are a distinct M2 polarised population promoting tumour progression: potential targets of anti-cancer therapy.* Eur J Cancer, 2006. **42**(6): p. 717-27.
33. Heusinkveld, M. and S.H. van der Burg, *Identification and manipulation of tumor associated macrophages in human cancers.* Journal of translational medicine, 2011. **9**: p. 216-216.
34. Komohara, Y., et al., *Possible involvement of the M2 anti-inflammatory macrophage phenotype in growth of human gliomas.* J Pathol, 2008. **216**(1): p. 15-24.
35. Zeiner, P.S., et al., *MIF Receptor CD74 is Restricted to Microglia/Macrophages, Associated with a M1-Polarized Immune Milieu and Prolonged Patient Survival in Gliomas.* Brain Pathol, 2015. **25**(4): p. 491-504.
36. Wu, A., et al., *Glioma cancer stem cells induce immunosuppressive macrophages/microglia.* Neuro Oncol, 2010. **12**(11): p. 1113-25.
37. Bettinger, I., S. Thanos, and W. Paulus, *Microglia promote glioma migration.* Acta Neuropathologica, 2002. **103**(4): p. 351-355.
38. Wick, W., M. Platten, and M. Weller, *Glioma Cell Invasion: Regulation of Metalloproteinase Activity by TGF-β.* Journal of Neuro-Oncology, 2001. **53**(2): p. 177-185.
39. Markovic, D.S., et al., *Gliomas induce and exploit microglial MT1-MMP expression for tumor expansion.* Proceedings of the National Academy of Sciences, 2009. **106**(30): p. 12530-12535.

40. Wesolowska, A., et al., *Microglia-derived TGF-beta as an important regulator of glioblastoma invasion--an inhibition of TGF-beta-dependent effects by shRNA against human TGF-beta type II receptor.* Oncogene, 2008. **27**(7): p. 918-30.
41. Willingham, S.B., et al., *The CD47-signal regulatory protein alpha (SIRPa) interaction is a therapeutic target for human solid tumors.* Proc Natl Acad Sci U S A, 2012. **109**(17): p. 6662-7.
42. Bull, C., et al., *Sialic acids sweeten a tumor's life.* Cancer Res, 2014. **74**(12): p. 3199-204.
43. Veillon, L., et al., *Glycosylation Changes in Brain Cancer.* ACS chemical neuroscience, 2018. **9**(1): p. 51-72.
44. Ford, A.L., et al., *Normal adult ramified microglia separated from other central nervous system macrophages by flow cytometric sorting. Phenotypic differences defined and direct ex vivo antigen presentation to myelin basic protein-reactive CD4+ T cells compared.* The Journal of Immunology, 1995. **154**(9): p. 4309-4321.
45. Muller, A., et al., *Resident microglia, and not peripheral macrophages, are the main source of brain tumor mononuclear cells.* Int J Cancer, 2015. **137**(2): p. 278-88.
46. Jung, S., et al., *Analysis of Fractalkine Receptor CX3CR1 Function by Targeted Deletion and Green Fluorescent Protein Reporter Gene Insertion.* Molecular and Cellular Biology, 2000. **20**(11): p. 4106-4114.
47. Wieghofer, P. and M. Prinz, *Genetic manipulation of microglia during brain development and disease.* Biochimica et Biophysica Acta (BBA) - Molecular Basis of Disease, 2016. **1862**(3): p. 299-309.
48. Yona, S., et al., *Fate mapping reveals origins and dynamics of monocytes and tissue macrophages under homeostasis.* Immunity, 2013. **38**(1): p. 79-91.
49. Goldmann, T., et al., *Origin, fate and dynamics of macrophages at central nervous system interfaces.* Nat Immunol, 2016. **17**(7): p. 797-805.
50. Davalos, D., et al., *ATP mediates rapid microglial response to local brain injury in vivo.* Nat Neurosci, 2005. **8**(6): p. 752-8.
51. Srinivasan, S., et al., *The P2Y12 antagonists, 2-methylthioadenosine 5'-monophosphate triethylammonium salt and cangrelor (ARC69931MX), can inhibit human platelet aggregation through a Gi-independent increase in cAMP levels.* The Journal of biological chemistry, 2009. **284**(24): p. 16108-16117.
52. Haynes, S.E., et al., *The P2Y12 receptor regulates microglial activation by extracellular nucleotides.* Nat Neurosci, 2006. **9**(12): p. 1512-9.
53. Bennett, M.L., et al., *New tools for studying microglia in the mouse and human CNS.* Proc Natl Acad Sci U S A, 2016. **113**(12): p. E1738-46.
54. Kaiser, T. and G. Feng, *Tmem119-EGFP and Tmem119-CreERT2 Transgenic Mice for Labeling and Manipulating Microglia.* eNeuro, 2019. **6**(4): p. ENEURO.0448-18.2019.
55. Buttgereit, A., et al., *Sall1 is a transcriptional regulator defining microglia identity and function.* Nat Immunol, 2016. **17**(12): p. 1397-1406.
56. Takasato, M., et al., *Identification of kidney mesenchymal genes by a combination of microarray analysis and Sall1-GFP knockin mice.* Mech Dev, 2004. **121**(6): p. 547-57.
57. Inoue, S., et al., *A mouse line expressing Sall1-driven inducible Cre recombinase in the kidney mesenchyme.* Genesis, 2010. **48**(3): p. 207-12.
58. Butovsky, O., et al., *Identification of a unique TGF-beta-dependent molecular and functional signature in microglia.* Nat Neurosci, 2014. **17**(1): p. 131-43.

59. Zhou, W., et al., *Periostin secreted by glioblastoma stem cells recruits M2 tumour-associated macrophages and promotes malignant growth.* Nature Cell Biology, 2015. **17**(2): p. 170-182.
60. Wang, S.-C., et al., *Radiation Therapy-Induced Tumor Invasiveness Is Associated with SDF-1-Regulated Macrophage Mobilization and Vasculogenesis.* PLOS ONE, 2013. **8**(8): p. e69182.
61. Kioi, M., et al., *Inhibition of vasculogenesis, but not angiogenesis, prevents the recurrence of glioblastoma after irradiation in mice.* The Journal of clinical investigation, 2010. **120**(3): p. 694-705.
62. Poli, A., et al., *Targeting glioblastoma with NK cells and mAb against NG2/CSPG4 prolongs animal survival.* Oncotarget, 2013. **4**(9): p. 1527-46.
63. Brown, E.J. and W.A. Frazier, *Integrin-associated protein (CD47) and its ligands.* Trends Cell Biol, 2001. **11**(3): p. 130-5.
64. Barclay, A.N. and T.K. Van den Berg, *The interaction between signal regulatory protein alpha (SIRPalpha) and CD47: structure, function, and therapeutic target.* Annu Rev Immunol, 2014. **32**: p. 25-50.
65. Tsai, R.K. and D.E. Discher, *Inhibition of "self" engulfment through deactivation of myosin-II at the phagocytic synapse between human cells.* The Journal of cell biology, 2008. **180**(5): p. 989-1003.
66. Jaiswal, S., et al., *CD47 is upregulated on circulating hematopoietic stem cells and leukemia cells to avoid phagocytosis.* Cell, 2009. **138**(2): p. 271-85.
67. Edris, B., et al., *Antibody therapy targeting the CD47 protein is effective in a model of aggressive metastatic leiomyosarcoma.* Proc Natl Acad Sci U S A, 2012. **109**(17): p. 6656-61.
68. Majeti, R., et al., *CD47 is an adverse prognostic factor and therapeutic antibody target on human acute myeloid leukemia stem cells.* Cell, 2009. **138**(2): p. 286-99.
69. Zhang, M., et al., *Anti-CD47 Treatment Stimulates Phagocytosis of Glioblastoma by M1 and M2 Polarized Macrophages and Promotes M1 Polarized Macrophages In Vivo.* PLoS One, 2016. **11**(4): p. e0153550.
70. Gholamin, S., et al., *Disrupting the CD47-SIRPalpha anti-phagocytic axis by a humanized anti-CD47 antibody is an efficacious treatment for malignant pediatric brain tumors.* Sci Transl Med, 2017. **9**(381).
71. Hutter, G., et al., *Microglia are effector cells of CD47-SIRPalpha antiphagocytic axis disruption against glioblastoma.* Proc Natl Acad Sci U S A, 2019. **116**(3): p. 997-1006.
72. Hakomori, S.-i., *Tumor-Associated Carbohydrate Antigens.* Annual Review of Immunology, 1984. **2**(1): p. 103-126.
73. Fuster, M.M. and J.D. Esko, *The sweet and sour of cancer: glycans as novel therapeutic targets.* Nat Rev Cancer, 2005. **5**(7): p. 526-42.
74. Pinho, S.S. and C.A. Reis, *Glycosylation in cancer: mechanisms and clinical implications.* Nat Rev Cancer, 2015. **15**(9): p. 540-55.
75. Boligan, K.F., et al., *Cancer intelligence acquired (CIA): tumor glycosylation and sialylation codes dismantling antitumor defense.* Cellular and Molecular Life Sciences, 2015. **72**(7): p. 1231-1248.
76. Rabinovich, Gabriel A. and Diego O. Croci, *Regulatory Circuits Mediated by Lectin-Glycan Interactions in Autoimmunity and Cancer.* Immunity, 2012. **36**(3): p. 322-335.
77. Adams, O.J., et al., *Targeting sialic acid–Siglec interactions to reverse immune suppression in cancer.* Glycobiology, 2018. **28**(9): p. 640-647.

78. Dall'Olio, F., et al., *Sialosignaling: Sialyltransferases as engines of self-fueling loops in cancer progression.* Biochimica et Biophysica Acta (BBA) - General Subjects, 2014. **1840**(9): p. 2752-2764.
79. Varki, A., *Loss of N-glycolylneuraminic acid in humans: Mechanisms, consequences, and implications for hominid evolution.* American journal of physical anthropology, 2001. **Suppl 33**: p. 54-69.
80. Pearce, O.M. and H. Laubli, *Sialic acids in cancer biology and immunity.* Glycobiology, 2016. **26**(2): p. 111-28.
81. Freire-de-Lima, L., et al., *Sialic acid: a sweet swing between mammalian host and Trypanosoma cruzi.* Frontiers in Immunology, 2012. **3**(356).
82. Sedlacek, H.H., H. Meesmann, and F.R. Seiler, *Regression of spontaneous mammary tumors in dogs after injection of neuraminidase-treated tumor cells.* Int J Cancer, 1975. **15**(3): p. 409-16.
83. Schultz, M.J., A.F. Swindall, and S.L. Bellis, *Regulation of the metastatic cell phenotype by sialylated glycans.* Cancer and Metastasis Reviews, 2012. **31**(3): p. 501-518.
84. Schwarz, F., J.J. Fong, and A. Varki, *Human-specific evolutionary changes in the biology of siglecs.* Adv Exp Med Biol, 2015. **842**: p. 1-16.
85. Macauley, M.S., P.R. Crocker, and J.C. Paulson, *Siglec-mediated regulation of immune cell function in disease.* Nat Rev Immunol, 2014. **14**(10): p. 653-66.
86. Cao, H. and P.R. Crocker, *Evolution of CD33-related siglecs: regulating host immune functions and escaping pathogen exploitation?* Immunology, 2011. **132**(1): p. 18-26.
87. Jandus, C., H.-U. Simon, and S. von Gunten, *Targeting Siglecs—A novel pharmacological strategy for immuno- and glycotherapy.* Biochemical Pharmacology, 2011. **82**(4): p. 323-332.
88. Angata, T., et al., *Large-scale sequencing of the CD33-related Siglec gene cluster in five mammalian species reveals rapid evolution by multiple mechanisms.* Proc Natl Acad Sci U S A, 2004. **101**(36): p. 13251-6.
89. Angata, T., *Molecular diversity and evolution of the Siglec family of cell-surface lectins.* Molecular Diversity, 2006. **10**(4): p. 555-566.
90. Varki, A., *Since there are PAMPs and DAMPs, there must be SAMPs? Glycan "self-associated molecular patterns" dampen innate immunity, but pathogens can mimic them.* Glycobiology, 2011. **21**(9): p. 1121-4.
91. Padler-Karavani, V., et al., *Rapid evolution of binding specificities and expression patterns of inhibitory CD33-related Siglecs in primates.* Faseb j, 2014. **28**(3): p. 1280-93.
92. Carlin, A.F., et al., *Group B Streptococcus suppression of phagocyte functions by protein-mediated engagement of human Siglec-5.* J Exp Med, 2009. **206**(8): p. 1691-9.
93. Chang, Y.-C. and V. Nizet, *The interplay between Siglecs and sialylated pathogens.* Glycobiology, 2014. **24**(9): p. 818-825.
94. Hudak, J.E., S.M. Canham, and C.R. Bertozzi, *Glycocalyx engineering reveals a Siglec-based mechanism for NK cell immunoevasion.* Nat Chem Biol, 2014. **10**(1): p. 69-75.
95. Jandus, C., et al., *Interactions between Siglec-7/9 receptors and ligands influence NK cell-dependent tumor immunosurveillance.* J Clin Invest, 2014. **124**(4): p. 1810-20.
96. Laubli, H., et al., *Engagement of myelomonocytic Siglecs by tumor-associated ligands modulates the innate immune response to cancer.* Proc Natl Acad Sci U S A, 2014. **111**(39): p. 14211-6.

97. Laubli, H., et al., *Lectin galactoside-binding soluble 3 binding protein (LGALS3BP) is a tumor-associated immunomodulatory ligand for CD33-related Siglecs.* J Biol Chem, 2014. **289**(48): p. 33481-91.
98. Beatson, R., et al., *The mucin MUC1 modulates the tumor immunological microenvironment through engagement of the lectin Siglec-9.* Nat Immunol, 2016. **17**(11): p. 1273-1281.
99. Ding, Y., et al., *The lectin Siglec-G inhibits dendritic cell cross-presentation by impairing MHC class I-peptide complex formation.* Nat Immunol, 2016. **17**(10): p. 1167-75.
100. Silva, M., et al., *Sialic acid removal from dendritic cells improves antigen cross-presentation and boosts anti-tumor immune responses.* Oncotarget, 2016. **7**(27): p. 41053-41066.
101. Perdicchio, M., et al., *Tumor sialylation impedes T cell mediated anti-tumor responses while promoting tumor associated-regulatory T cells.* Oncotarget, 2016. **7**(8): p. 8771-82.
102. Stanczak, M.A., et al., *Self-associated molecular patterns mediate cancer immune evasion by engaging Siglecs on T cells.* J Clin Invest, 2018. **128**(11): p. 4912-4923.
103. Bertram, L., et al., *Genome-wide Association Analysis Reveals Putative Alzheimer's Disease Susceptibility Loci in Addition to APOE.* The American Journal of Human Genetics, 2008. **83**(5): p. 623-632.
104. Hollingworth, P., et al., *Common variants at ABCA7, MS4A6A/MS4A4E, EPHA1, CD33 and CD2AP are associated with Alzheimer's disease.* Nat Genet, 2011. **43**(5): p. 429-35.
105. Naj, A.C., et al., *Common variants at MS4A4/MS4A6E, CD2AP, CD33 and EPHA1 are associated with late-onset Alzheimer's disease.* Nature genetics, 2011. **43**(5): p. 436-441.
106. Griciuc, A., et al., *Alzheimer's disease risk gene CD33 inhibits microglial uptake of amyloid beta.* Neuron, 2013. **78**(4): p. 631-43.
107. Pluvinage, J.V., et al., *CD22 blockade restores homeostatic microglial phagocytosis in ageing brains.* Nature, 2019. **568**(7751): p. 187-192.
108. Claude, J., et al., *Microglial CD33-related Siglec-E inhibits neurotoxicity by preventing the phagocytosis-associated oxidative burst.* J Neurosci, 2013. **33**(46): p. 18270-6.
109. Wang, Y. and H. Neumann, *Alleviation of neurotoxicity by microglial human Siglec-11.* J Neurosci, 2010. **30**(9): p. 3482-8.
110. Reardon, D.A., et al., *Phase 2 study to evaluate safety and efficacy of MEDI4736 (durvalumab [DUR]) in glioblastoma (GBM) patients: An update.* Journal of Clinical Oncology, 2017. **35**(15_suppl): p. 2042-2042.
111. Reardon, D.A., et al., *OS10.3 Randomized Phase 3 Study Evaluating the Efficacy and Safety of Nivolumab vs Bevacizumab in Patients With Recurrent Glioblastoma: CheckMate 143.* Neuro-Oncology, 2017. **19**(Suppl 3): p. iii21-iii21.
112. Li, G.Z., et al., *Siglecs, Novel Immunotherapy Targets, Potentially Enhance The Effectiveness of Existing Immune Checkpoint Inhibitors in Glioma Immunotherapy.* Onco Targets Ther, 2019. **12**: p. 10263-10273.
113. Santegoets, K.C.M., et al., *Expression profiling of immune inhibitory Siglecs and their ligands in patients with glioma.* Cancer Immunol Immunother, 2019. **68**(6): p. 937-949.

114. Wielgat, P., et al., *Sialic acids as cellular markers of immunomodulatory action of dexamethasone on glioma cells of different immunogenicity.* Mol Cell Biochem, 2019. **455**(1-2): p. 147-157.
115. Wielgat, P., et al., *The sialoglycan-Siglec-E checkpoint axis in dexamethasone-induced immune subversion in glioma-microglia transwell co-culture system.* Immunol Res, 2019. **67**(4-5): p. 348-357.
116. Dusoswa, S.A., et al., *Glycan modification of glioblastoma-derived extracellular vesicles enhances receptor-mediated targeting of dendritic cells.* J Extracell Vesicles, 2019. **8**(1): p. 1648995.
117. Gautier, E.L., et al., *Gene-expression profiles and transcriptional regulatory pathways that underlie the identity and diversity of mouse tissue macrophages.* Nat Immunol, 2012. **13**(11): p. 1118-28.
118. Konishi, H., et al., *Siglec-H is a microglia-specific marker that discriminates microglia from CNS-associated macrophages and CNS-infiltrating monocytes.* Glia, 2017. **65**(12): p. 1927-1943.
119. Kopatz, J., et al., *Siglec-h on activated microglia for recognition and engulfment of glioma cells.* Glia, 2013. **61**(7): p. 1122-33.
120. Barkal, A.A., et al., *CD24 signalling through macrophage Siglec-10 is a target for cancer immunotherapy.* Nature, 2019. **572**(7769): p. 392-396.
121. Takamiya, R., et al., *The interaction between Siglec-15 and tumor-associated sialyl-Tn antigen enhances TGF-beta secretion from monocytes/macrophages through the DAP12-Syk pathway.* Glycobiology, 2013. **23**(2): p. 178-87.
122. Wang, J., et al., *Siglec-15 as an immune suppressor and potential target for normalization cancer immunotherapy.* Nat Med, 2019. **25**(4): p. 656-666.
123. Weller, M., et al., *EANO guidelines on the diagnosis and treatment of diffuse gliomas of adulthood.* Nature Reviews Clinical Oncology, 2021. **18**(3): p. 170-186.
124. Topalian, S.L., C.G. Drake, and D.M. Pardoll, *Immune checkpoint blockade: a common denominator approach to cancer therapy.* Cancer cell, 2015. **27**(4): p. 450-461.
125. Reardon, D.A., et al., *Effect of Nivolumab vs Bevacizumab in Patients With Recurrent Glioblastoma: The CheckMate 143 Phase 3 Randomized Clinical Trial.* JAMA Oncology, 2020. **6**(7): p. 1003-1010.
126. Lim, M., et al., *Phase 3 Trial of Chemoradiotherapy With Temozolomide Plus Nivolumab or Placebo for Newly Diagnosed Glioblastoma With Methylated MGMT Promoter.* Neuro Oncol, 2022.
127. Omuro, A., et al., *Radiotherapy Combined With Nivolumab or Temozolomide for Newly Diagnosed Glioblastoma With Unmethylated MGMT Promoter: An International Randomized Phase 3 Trial.* Neuro Oncol, 2022.
128. Klemm, F., et al., *Interrogation of the Microenvironmental Landscape in Brain Tumors Reveals Disease-Specific Alterations of Immune Cells.* Cell, 2020. **181**(7): p. 1643-1660.e17.
129. Friebel, E., et al., *Single-Cell Mapping of Human Brain Cancer Reveals Tumor-Specific Instruction of Tissue-Invading Leukocytes.* Cell, 2020. **181**(7): p. 1626-1642.e20.
130. Rodriguez, E., et al., *Sialic acids in pancreatic cancer cells drive tumour-associated macrophage differentiation via the Siglec receptors Siglec-7 and Siglec-9.* Nature Communications, 2021. **12**(1): p. 1270.
131. Perdicchio, M., et al., *Sialic acid-modified antigens impose tolerance via inhibition of T-cell proliferation and de novo induction of regulatory T cells.*

Proceedings of the National Academy of Sciences of the United States of America, 2016. **113**(12): p. 3329-3334.
132. Bowman, R.L., et al., *GlioVis data portal for visualization and analysis of brain tumor expression datasets.* Neuro-Oncology, 2016. **19**(1): p. 139-141.
133. Schmassmann, P., et al., *Single-cell characterization of human GBM reveals regional differences in tumor-infiltrating leukocyte activation.* bioRxiv, 2022: p. 2022.06.17.496574.
134. Müller, J., et al., *CD22 ligand-binding and signaling domains reciprocally regulate B-cell Ca2+ signaling.* Proc Natl Acad Sci U S A, 2013. **110**(30): p. 12402-7.
135. Chen, G.-Y., et al., *Siglec-G/10 in self-nonself discrimination of innate and adaptive immunity.* Glycobiology, 2014. **24**(9): p. 800-806.
136. Hinderlich, S., et al., *UDP-GlcNAc 2-Epimerase/ManNAc Kinase (GNE): A Master Regulator of Sialic Acid Synthesis.* Top Curr Chem, 2015. **366**: p. 97-137.
137. Seyfried, T.N., M. el-Abbadi, and M.L. Roy, *Ganglioside distribution in murine neural tumors.* Mol Chem Neuropathol, 1992. **17**(2): p. 147-67.
138. Giachino, C., et al., *A Tumor Suppressor Function for Notch Signaling in Forebrain Tumor Subtypes.* Cancer Cell, 2015. **28**(6): p. 730-742.
139. Wang, J., et al., *Siglec Receptors Modulate Dendritic Cell Activation and Antigen Presentation to T Cells in Cancer.* Front Cell Dev Biol, 2022. **10**: p. 828916.
140. Keren-Shaul, H., et al., *A Unique Microglia Type Associated with Restricting Development of Alzheimer's Disease.* Cell, 2017. **169**(7): p. 1276-1290.e17.
141. Hansen, D.V., J.E. Hanson, and M. Sheng, *Microglia in Alzheimer's disease.* Journal of Cell Biology, 2017. **217**(2): p. 459-472.
142. Friedman, B.A., et al., *Diverse Brain Myeloid Expression Profiles Reveal Distinct Microglial Activation States and Aspects of Alzheimer's Disease Not Evident in Mouse Models.* Cell Reports, 2018. **22**(3): p. 832-847.
143. Chen, Y. and M. Colonna, *Microglia in Alzheimer's disease at single-cell level. Are there common patterns in humans and mice?* Journal of Experimental Medicine, 2021. **218**(9).
144. Liberzon, A., et al., *The Molecular Signatures Database (MSigDB) hallmark gene set collection.* Cell Syst, 2015. **1**(6): p. 417-425.
145. Belz, G.T. and S.L. Nutt, *Transcriptional programming of the dendritic cell network.* Nature Reviews Immunology, 2012. **12**(2): p. 101-113.
146. Agliardi, G., et al., *Intratumoral IL-12 delivery empowers CAR-T cell immunotherapy in a pre-clinical model of glioblastoma.* Nature Communications, 2021. **12**(1): p. 444.
147. Qian, B.-Z., et al., *CCL2 recruits inflammatory monocytes to facilitate breast-tumour metastasis.* Nature, 2011. **475**(7355): p. 222-225.
148. Parkhurst, Christopher N., et al., *Microglia Promote Learning-Dependent Synapse Formation through Brain-Derived Neurotrophic Factor.* Cell, 2013. **155**(7): p. 1596-1609.
149. Curtsinger, J.M. and M.F. Mescher, *Inflammatory cytokines as a third signal for T cell activation.* Curr Opin Immunol, 2010. **22**(3): p. 333-40.
150. Kanehisa, M. and S. Goto, *KEGG: kyoto encyclopedia of genes and genomes.* Nucleic Acids Res, 2000. **28**(1): p. 27-30.
151. McGeachy, M.J., D.J. Cua, and S.L. Gaffen, *The IL-17 Family of Cytokines in Health and Disease.* Immunity, 2019. **50**(4): p. 892-906.

152. Prescott, J.A., J.P. Mitchell, and S.J. Cook, *Inhibitory feedback control of NF-κB signalling in health and disease.* Biochem J, 2021. **478**(13): p. 2619-2664.
153. von Roemeling, C.A., et al., *Therapeutic modulation of phagocytosis in glioblastoma can activate both innate and adaptive antitumour immunity.* Nat Commun, 2020. **11**(1): p. 1508.
154. Garcia-Diaz, A., et al., *Interferon Receptor Signaling Pathways Regulating PD-L1 and PD-L2 Expression.* Cell Reports, 2017. **19**(6): p. 1189-1201.
155. Shekarian, T., et al., *Immunotherapy of glioblastoma explants induces interferon-γ responses and spatial immune cell rearrangements in tumor center, but not periphery.* Science Advances, 2022. **8**(26): p. eabn9440.
156. Snijder, B., et al., *Image-based ex-vivo drug screening for patients with aggressive haematological malignancies: interim results from a single-arm, open-label, pilot study.* The Lancet Haematology, 2017. **4**(12): p. e595-e606.
157. Khalsa, J.K., et al., *Immune phenotyping of diverse syngeneic murine brain tumors identifies immunologically distinct types.* Nature Communications, 2020. **11**(1): p. 3912.
158. Delaveris, C.S., et al., *Modulation of immune cell reactivity with cis-binding Siglec agonists.* Proceedings of the National Academy of Sciences, 2021. **118**(3): p. e2012408118.
159. Theruvath, J., et al., *Anti-GD2 synergizes with CD47 blockade to mediate tumor eradication.* Nature Medicine, 2022. **28**(2): p. 333-344.
160. Yeo, A.T., et al., *Single-cell RNA sequencing reveals evolution of immune landscape during glioblastoma progression.* Nat Immunol, 2022.
161. Ikehara, Y., S.K. Ikehara, and J.C. Paulson, *Negative regulation of T cell receptor signaling by Siglec-7 (p70/AIRM) and Siglec-9.* J Biol Chem, 2004. **279**(41): p. 43117-25.
162. Dangaj, D., et al., *Cooperation between Constitutive and Inducible Chemokines Enables T Cell Engraftment and Immune Attack in Solid Tumors.* Cancer Cell, 2019. **35**(6): p. 885-900.e10.
163. Romero, J.M., et al., *A Four-Chemokine Signature Is Associated with a T-cell-Inflamed Phenotype in Primary and Metastatic Pancreatic Cancer.* Clin Cancer Res, 2020. **26**(8): p. 1997-2010.
164. Kirchhammer, N., et al., *NK cells with tissue-resident traits shape response to immunotherapy by inducing adaptive antitumor immunity.* Science Translational Medicine, 2022. **14**(653): p. eabm9043.
165. Jiao, X., et al., *CCR5 Governs DNA Damage Repair and Breast Cancer Stem Cell Expansion.* Cancer Res, 2018. **78**(7): p. 1657-1671.
166. Liu, C., et al., *Macrophage-derived CCL5 facilitates immune escape of colorectal cancer cells via the p65/STAT3-CSN5-PD-L1 pathway.* Cell Death Differ, 2020. **27**(6): p. 1765-1781.
167. Gray, M.A., et al., *Targeted glycan degradation potentiates the anticancer immune response in vivo.* Nature Chemical Biology, 2020. **16**(12): p. 1376-1384.
168. Büll, C., et al., *Sialic Acid Blockade Suppresses Tumor Growth by Enhancing T-cell-Mediated Tumor Immunity.* Cancer Res, 2018. **78**(13): p. 3574-3588.
169. Stanczak, M.A., et al., *Targeting cancer glycosylation repolarizes tumor-associated macrophages allowing effective immune checkpoint blockade.* bioRxiv, 2021: p. 2021.04.11.439323.
170. Macauley, M.S., et al., *Systemic blockade of sialylation in mice with a global inhibitor of sialyltransferases.* J Biol Chem, 2014. **289**(51): p. 35149-58.

171. Weller, M., et al., *Rindopepimut with temozolomide for patients with newly diagnosed, EGFRvIII-expressing glioblastoma (ACT IV): a randomised, double-blind, international phase 3 trial.* The Lancet Oncology, 2017. **18**(10): p. 1373-1385.
172. Wang, B. and J. Brand-Miller, *The role and potential of sialic acid in human nutrition.* European Journal of Clinical Nutrition, 2003. **57**(11): p. 1351-1369.
173. Müller, S., et al., *Single-cell profiling of human gliomas reveals macrophage ontogeny as a basis for regional differences in macrophage activation in the tumor microenvironment.* Genome Biology, 2017. **18**(1): p. 234.
174. Abdelfattah, N., et al., *Single-cell analysis of human glioma and immune cells identifies S100A4 as an immunotherapy target.* Nature Communications, 2022. **13**(1): p. 767.
175. Pombo Antunes, A.R., et al., *Single-cell profiling of myeloid cells in glioblastoma across species and disease stage reveals macrophage competition and specialization.* Nature Neuroscience, 2021. **24**(4): p. 595-610.
176. Goswami, S., et al., *Immune profiling of human tumors identifies CD73 as a combinatorial target in glioblastoma.* Nature Medicine, 2020. **26**(1): p. 39-46.
177. Chen, A.X., et al., *Single-cell characterization of macrophages in glioblastoma reveals MARCO as a mesenchymal pro-tumor marker.* Genome Medicine, 2021. **13**(1): p. 88.
178. Darmanis, S., et al., *Single-Cell RNA-Seq Analysis of Infiltrating Neoplastic Cells at the Migrating Front of Human Glioblastoma.* Cell Rep, 2017. **21**(5): p. 1399-1410.
179. Landry, A.P., et al., *Distinct regional ontogeny and activation of tumor associated macrophages in human glioblastoma.* Scientific Reports, 2020. **10**(1): p. 19542.
180. Louis, D.N., et al., *The 2021 WHO Classification of Tumors of the Central Nervous System: a summary.* Neuro-Oncology, 2021. **23**(8): p. 1231-1251.
181. Linderman, G.C., et al., *Fast interpolation-based t-SNE for improved visualization of single-cell RNA-seq data.* Nat Methods, 2019. **16**(3): p. 243-245.
182. Monaco, G., et al., *RNA-Seq Signatures Normalized by mRNA Abundance Allow Absolute Deconvolution of Human Immune Cell Types.* Cell Rep, 2019. **26**(6): p. 1627-1640.e7.
183. Neftel, C., et al., *An Integrative Model of Cellular States, Plasticity, and Genetics for Glioblastoma.* Cell, 2019. **178**(4): p. 835-849.e21.
184. Baek, M., et al., *The BET inhibitor attenuates the inflammatory response and cell migration in human microglial HMC3 cell line.* Scientific Reports, 2021. **11**(1): p. 8828.
185. Hagiwara, S., et al., *Processing of CD109 by furin and its role in the regulation of TGF-β signaling.* Oncogene, 2010. **29**(15): p. 2181-2191.
186. Traini, M., et al., *Sphingomyelin phosphodiesterase acid-like 3A (SMPDL3A) is a novel nucleotide phosphodiesterase regulated by cholesterol in human macrophages.* J Biol Chem, 2014. **289**(47): p. 32895-913.
187. Soroceanu, L., et al., *Id-1 is a key transcriptional regulator of glioblastoma aggressiveness and a novel therapeutic target.* Cancer Res, 2013. **73**(5): p. 1559-69.
188. Papaspyridonos, M., et al., *Id1 suppresses anti-tumour immune responses and promotes tumour progression by impairing myeloid cell maturation.* Nature Communications, 2015. **6**(1): p. 6840.

189. Grandemange, S., et al., *The regulation of MEFV expression and its role in health and familial Mediterranean fever.* Genes & Immunity, 2011. **12**(7): p. 497-503.
190. Sharma, S., et al., *APOBEC3A cytidine deaminase induces RNA editing in monocytes and macrophages.* Nature Communications, 2015. **6**(1): p. 6881.
191. Vicente, R., et al., *Differential voltage-dependent K+ channel responses during proliferation and activation in macrophages.* J Biol Chem, 2003. **278**(47): p. 46307-20.
192. Chen, P., et al., *Gpr132 sensing of lactate mediates tumor-macrophage interplay to promote breast cancer metastasis.* Proc Natl Acad Sci U S A, 2017. **114**(3): p. 580-585.
193. Gao, L., et al., *MIR22HG As A Tumor Suppressive lncRNA In HCC: A Comprehensive Analysis Integrating RT-qPCR, mRNA-Seq, And Microarrays.* Onco Targets Ther, 2019. **12**: p. 9827-9848.
194. Xiong, D., Y. Wang, and M. You, *A gene expression signature of TREM2hi macrophages and γδ T cells predicts immunotherapy response.* Nature Communications, 2020. **11**(1): p. 5084.
195. Vuletic, S., et al., *PLTP regulates STAT3 and NFκB in differentiated THP1 cells and human monocyte-derived macrophages.* Biochimica et Biophysica Acta (BBA) - Molecular Cell Research, 2011. **1813**(10): p. 1917-1924.
196. Casazza, A., et al., *Impeding Macrophage Entry into Hypoxic Tumor Areas by Sema3A/Nrp1 Signaling Blockade Inhibits Angiogenesis and Restores Antitumor Immunity.* Cancer Cell, 2013. **24**(6): p. 695-709.
197. Sadik, A., et al., *IL4I1 Is a Metabolic Immune Checkpoint that Activates the AHR and Promotes Tumor Progression.* Cell, 2020. **182**(5): p. 1252-1270.e34.
198. Rodriguez, A.E., et al., *Serine Metabolism Supports Macrophage IL-1β Production.* Cell Metabolism, 2019. **29**(4): p. 1003-1011.e4.
199. Tseng, W.C., et al., *Schizophrenia-associated SLC39A8 polymorphism is a loss-of-function allele altering glutamate receptor and innate immune signaling.* Translational Psychiatry, 2021. **11**(1): p. 136.
200. Holtman, I.R., D. Skola, and C.K. Glass, *Transcriptional control of microglia phenotypes in health and disease.* The Journal of Clinical Investigation, 2017. **127**(9): p. 3220-3229.
201. Nomaru, H., et al., *Fosb gene products contribute to excitotoxic microglial activation by regulating the expression of complement C5a receptors in microglia.* Glia, 2014. **62**(8): p. 1284-98.
202. Sweet, D.R., et al., *Myeloid Krüppel-like factor 2 is a critical regulator of metabolic inflammation.* Nature Communications, 2020. **11**(1): p. 5872.
203. Salojin, K.V., et al., *Essential role of MAPK phosphatase-1 in the negative control of innate immune responses.* J Immunol, 2006. **176**(3): p. 1899-907.
204. Lee, H., et al., *Role of antiproliferative B cell translocation gene-1 as an apoptotic sensitizer in activation-induced cell death of brain microglia.* J Immunol, 2003. **171**(11): p. 5802-11.
205. Liberzon, A., et al., *The Molecular Signatures Database (MSigDB) hallmark gene set collection.* Cell systems, 2015. **1**(6): p. 417-425.
206. Walker, D.G. and L.F. Lue, *Immune phenotypes of microglia in human neurodegenerative disease: challenges to detecting microglial polarization in human brains.* Alzheimers Res Ther, 2015. **7**(1): p. 56.
207. Hopperton, K.E., et al., *Markers of microglia in post-mortem brain samples from patients with Alzheimer's disease: a systematic review.* Molecular Psychiatry, 2018. **23**(2): p. 177-198.

208. Hammond, T.R., et al., *Single-Cell RNA Sequencing of Microglia throughout the Mouse Lifespan and in the Injured Brain Reveals Complex Cell-State Changes.* Immunity, 2019. **50**(1): p. 253-271.e6.
209. McQuade, A., et al., *Gene expression and functional deficits underlie TREM2-knockout microglia responses in human models of Alzheimer's disease.* Nature Communications, 2020. **11**(1): p. 5370.
210. Saijo, K., et al., *A Nurr1/CoREST pathway in microglia and astrocytes protects dopaminergic neurons from inflammation-induced death.* Cell, 2009. **137**(1): p. 47-59.
211. Rothe, T., et al., *The Nuclear Receptor Nr4a1 Acts as a Microglia Rheostat and Serves as a Therapeutic Target in Autoimmune-Driven Central Nervous System Inflammation.* Journal of immunology (Baltimore, Md. : 1950), 2017. **198**(10): p. 3878-3885.
212. Szabo, P.A., et al., *Single-cell transcriptomics of human T cells reveals tissue and activation signatures in health and disease.* Nature Communications, 2019. **10**(1): p. 4706.
213. Alegre, M.L., et al., *Regulation of surface and intracellular expression of CTLA4 on mouse T cells.* J Immunol, 1996. **157**(11): p. 4762-70.
214. Johnson, D.B., et al., *Tumor-specific MHC-II expression drives a unique pattern of resistance to immunotherapy via LAG-3/FCRL6 engagement.* JCI insight, 2018. **3**(24): p. e120360.
215. Sciumè, G., et al., *CX3CR1 expression defines 2 KLRG1+ mouse NK-cell subsets with distinct functional properties and positioning in the bone marrow.* Blood, 2011. **117**(17): p. 4467-4475.
216. Böttcher, J.P., et al., *Functional classification of memory CD8+ T cells by CX3CR1 expression.* Nature Communications, 2015. **6**(1): p. 8306.
217. Gerlach, C., et al., *The Chemokine Receptor CX3CR1 Defines Three Antigen-Experienced CD8 T Cell Subsets with Distinct Roles in Immune Surveillance and Homeostasis.* Immunity, 2016. **45**(6): p. 1270-1284.
218. Urban, S.L., et al., *Peripherally induced brain tissue–resident memory CD8+ T cells mediate protection against CNS infection.* Nature Immunology, 2020. **21**(8): p. 938-949.
219. Mackay, L.K., et al., *Hobit and Blimp1 instruct a universal transcriptional program of tissue residency in lymphocytes.* Science, 2016. **352**(6284): p. 459-63.
220. Ma, J., et al., *PD1(Hi) CD8(+) T cells correlate with exhausted signature and poor clinical outcome in hepatocellular carcinoma.* Journal for immunotherapy of cancer, 2019. **7**(1): p. 331-331.
221. Liu, X., et al., *Genome-wide analysis identifies NR4A1 as a key mediator of T cell dysfunction.* Nature, 2019. **567**(7749): p. 525-529.
222. Dan, L., et al., *The phosphatase PAC1 acts as a T cell suppressor and attenuates host antitumor immunity.* Nature Immunology, 2020. **21**(3): p. 287-297.
223. Bignon, A., et al., *DUSP4-mediated accelerated T-cell senescence in idiopathic CD4 lymphopenia.* Blood, 2015. **125**(16): p. 2507-18.
224. Maine, C.J., et al., *PTPN22 contributes to exhaustion of T lymphocytes during chronic viral infection.* Proceedings of the National Academy of Sciences, 2016. **113**(46): p. E7231-E7239.
225. Li, H., et al., *Dysfunctional CD8 T Cells Form a Proliferative, Dynamically Regulated Compartment within Human Melanoma.* Cell, 2019. **176**(4): p. 775-789.e18.

226. Jin, S., et al., *Inference and analysis of cell-cell communication using CellChat.* Nature Communications, 2021. **12**(1): p. 1088.
227. Wei, J., et al., *Osteopontin mediates glioblastoma-associated macrophage infiltration and is a potential therapeutic target.* J Clin Invest, 2019. **129**(1): p. 137-149.
228. Klement, J.D., et al., *An osteopontin/CD44 immune checkpoint controls CD8+ T cell activation and tumor immune evasion.* J Clin Invest, 2018. **128**(12): p. 5549-5560.
229. Olah, M., et al., *Single cell RNA sequencing of human microglia uncovers a subset associated with Alzheimer's disease.* Nature Communications, 2020. **11**(1): p. 6129.
230. Yamada, T., et al., *A catalytic mechanism that explains a low catalytic activity of serine dehydratase like-1 from human cancer cells: crystal structure and site-directed mutagenesis studies.* Biochim Biophys Acta, 2008. **1780**(5): p. 809-18.
231. Pan, R.-Y., et al., *Sodium rutin ameliorates Alzheimer’s disease–like pathology by enhancing microglial amyloid-β clearance.* Science Advances, 2019. **5**(2): p. eaau6328.
232. Wang, G., et al., *Neuroprotective effect of l-serine against white matter demyelination by harnessing and modulating inflammation in mice.* Neuropharmacology, 2019. **146**: p. 39-49.
233. Yan, Y., et al., *CX3CR1 identifies PD-1 therapy-responsive CD8+ T cells that withstand chemotherapy during cancer chemoimmunotherapy.* JCI Insight, 2018. **3**(8).
234. Yamauchi, T., et al., *T-cell CX3CR1 expression as a dynamic blood-based biomarker of response to immune checkpoint inhibitors.* Nature Communications, 2021. **12**(1): p. 1402.
235. Smolders, J., et al., *Tissue-resident memory T cells populate the human brain.* Nature Communications, 2018. **9**(1): p. 4593.
236. Kumar, B.V., et al., *Human Tissue-Resident Memory T Cells Are Defined by Core Transcriptional and Functional Signatures in Lymphoid and Mucosal Sites.* Cell Rep, 2017. **20**(12): p. 2921-2934.
237. Mackay, L.K., et al., *The developmental pathway for CD103(+)CD8+ tissue-resident memory T cells of skin.* Nat Immunol, 2013. **14**(12): p. 1294-301.
238. Gandoglia, I., et al., *In vitro VLA-4 blockade results in an impaired NK cell-mediated immune surveillance against melanoma.* Immunology Letters, 2017. **181**: p. 109-115.
239. Sankowski, R., et al., *Mapping microglia states in the human brain through the integration of high-dimensional techniques.* Nature Neuroscience, 2019. **22**(12): p. 2098-2110.
240. Srivastava, A., et al., *Alevin efficiently estimates accurate gene abundances from dscRNA-seq data.* Genome Biol, 2019. **20**(1): p. 65.
241. Griffiths, J.A., et al., *Detection and removal of barcode swapping in single-cell RNA-seq data.* Nat Commun, 2018. **9**(1): p. 2667.
242. Lun, A.T.L., et al., *EmptyDrops: distinguishing cells from empty droplets in droplet-based single-cell RNA sequencing data.* Genome Biol, 2019. **20**(1): p. 63.
243. Vallejos, C.A., et al., *Normalizing single-cell RNA sequencing data: challenges and opportunities.* Nat Meth, 2017. **14**(6): p. 565-571.
244. Lun, A., D. McCarthy, and J. Marioni, *A step-by-step workflow for low-level analysis of single-cell RNA-seq data with Bioconductor [version 2; referees: 3 approved, 2 approved with reservations].* F1000Research, 2016. **5**(2122).

245. McCarthy, D.J., et al., *Scater: pre-processing, quality control, normalization and visualization of single-cell RNA-seq data in R.* Bioinformatics, 2017. **33**(8): p. 1179-1186.
246. Amezquita, R.A., et al., *Orchestrating single-cell analysis with Bioconductor.* Nat Methods, 2019.
247. Lun, A.T., D.J. McCarthy, and J.C. Marioni, *A step-by-step workflow for low-level analysis of single-cell RNA-seq data with Bioconductor.* F1000Res, 2016. **5**: p. 2122.
248. Murtagh, F. and P. Legendre, *Ward's Hierarchical Agglomerative Clustering Method: Which Algorithms Implement Ward's Criterion?* J. Classif., 2014. **31**(3): p. 274–295.
249. Langfelder, P., B. Zhang, and S. Horvath, *Defining clusters from a hierarchical cluster tree: the Dynamic Tree Cut package for R.* Bioinformatics, 2008. **24**(5): p. 719-20.
250. Aran, D., et al., *Reference-based analysis of lung single-cell sequencing reveals a transitional profibrotic macrophage.* Nat Immunol, 2019. **20**(2): p. 163-172.
251. Weber, L.M., et al., *diffcyt: Differential discovery in high-dimensional cytometry via high-resolution clustering.* Communications Biology, 2019. **2**(1): p. 183.
252. Lun, A.T.L. and J.C. Marioni, *Overcoming confounding plate effects in differential expression analyses of single-cell RNA-seq data.* Biostatistics, 2017. **18**(3): p. 451-464.
253. Robinson, M.D., D.J. McCarthy, and G.K. Smyth, *edgeR: a Bioconductor package for differential expression analysis of digital gene expression data.* Bioinformatics, 2010. **26**(1): p. 139-140.
254. Robinson, M.D. and A. Oshlack, *A scaling normalization method for differential expression analysis of RNA-seq data.* Genome Biol, 2010. **11**(3): p. R25.
255. Wu, D. and G.K. Smyth, *Camera: a competitive gene set test accounting for inter-gene correlation.* Nucleic Acids Res, 2012. **40**(17): p. e133.
256. Subramanian, A., et al., *Gene set enrichment analysis: A knowledge-based approach for interpreting genome-wide expression profiles.* Proc Natl Acad Sci U S A, 2005. **102**(43): p. 15545-15550.
257. Koshy, M., et al., *Improved survival time trends for glioblastoma using the SEER 17 population-based registries.* J Neurooncol, 2012. **107**(1): p. 207-12.
258. Urbańska, K., et al., *Glioblastoma multiforme - an overview.* Contemp Oncol (Pozn), 2014. **18**(5): p. 307-12.
259. Scherer, H.J., *A Critical Review: The Pathology of Cerebral Gliomas.* J Neurol Psychiatry, 1940. **3**(2): p. 147-77.
260. Ozawa, T., et al., *Most human non-GCIMP glioblastoma subtypes evolve from a common proneural-like precursor glioma.* Cancer Cell, 2014. **26**(2): p. 288-300.
261. Phillips, H.S., et al., *Molecular subclasses of high-grade glioma predict prognosis, delineate a pattern of disease progression, and resemble stages in neurogenesis.* Cancer Cell, 2006. **9**(3): p. 157-73.
262. Verhaak, R.G., et al., *Integrated genomic analysis identifies clinically relevant subtypes of glioblastoma characterized by abnormalities in PDGFRA, IDH1, EGFR, and NF1.* Cancer Cell, 2010. **17**(1): p. 98-110.
263. Brennan, C., et al., *Glioblastoma subclasses can be defined by activity among signal transduction pathways and associated genomic alterations.* PLoS One, 2009. **4**(11): p. e7752.
264. Capper, D., et al., *DNA methylation-based classification of central nervous system tumours.* Nature, 2018. **555**(7697): p. 469-474.

265. Cancer Genome Atlas Research Network, *Comprehensive genomic characterization defines human glioblastoma genes and core pathways.* Nature, 2008. **455**(7216): p. 1061-8.
266. Wang, Q., et al., *Tumor Evolution of Glioma-Intrinsic Gene Expression Subtypes Associates with Immunological Changes in the Microenvironment.* Cancer Cell, 2017. **32**(1): p. 42-56 e6.
267. Bredel, M., et al., *NFKBIA deletion in glioblastomas.* N Engl J Med, 2011. **364**(7): p. 627-37.
268. Bhat, K.P.L., et al., *Mesenchymal differentiation mediated by NF-kappaB promotes radiation resistance in glioblastoma.* Cancer Cell, 2013. **24**(3): p. 331-46.
269. Yan, H., et al., *IDH1 and IDH2 mutations in gliomas.* N Engl J Med, 2009. **360**(8): p. 765-73.
270. Parsons, D.W., et al., *An integrated genomic analysis of human glioblastoma multiforme.* Science, 2008. **321**(5897): p. 1807-12.
271. Hegi, M.E., et al., *MGMT gene silencing and benefit from temozolomide in glioblastoma.* N Engl J Med, 2005. **352**(10): p. 997-1003.
272. Bigner, S.H., et al., *Molecular genetic aspects of oligodendrogliomas including analysis by comparative genomic hybridization.* Am J Pathol, 1999. **155**(2): p. 375-86.
273. Amankulor, N.M., et al., *Mutant IDH1 regulates the tumor-associated immune system in gliomas.* Genes Dev, 2017. **31**(8): p. 774-786.
274. Annovazzi, L., et al., *Microglia immunophenotyping in gliomas.* Oncol Lett, 2018. **15**(1): p. 998-1006.
275. Martinez-Lage, M., et al., *Immune landscapes associated with different glioblastoma molecular subtypes.* Acta Neuropathol Commun, 2019. **7**(1): p. 203.
276. Ohgaki, H., et al., *Genetic pathways to glioblastoma: a population-based study.* Cancer Res, 2004. **64**(19): p. 6892-9.
277. Friebel, E., et al., *Single-Cell Mapping of Human Brain Cancer Reveals Tumor-Specific Instruction of Tissue-Invading Leukocytes.* Cell, 2020.
278. Klemm, F., et al., *Interrogation of the Microenvironmental Landscape in Brain Tumors Reveals Disease-Specific Alterations of Immune Cells.* Cell, 2020.
279. Patel, A.P., et al., *Single-cell RNA-seq highlights intratumoral heterogeneity in primary glioblastoma.* Science, 2014. **344**(6190): p. 1396-401.
280. Thorsson, V., et al., *The Immune Landscape of Cancer.* Immunity, 2018. **48**(4): p. 812-830 e14.
281. Kohanbash, G., et al., *Isocitrate dehydrogenase mutations suppress STAT1 and CD8+ T cell accumulation in gliomas.* J Clin Invest, 2017. **127**(4): p. 1425-1437.
282. Bunse, L., et al., *Suppression of antitumor T cell immunity by the oncometabolite (R)-2-hydroxyglutarate.* Nat Med, 2018. **24**(8): p. 1192-1203.
283. Turcan, S., et al., *IDH1 mutation is sufficient to establish the glioma hypermethylator phenotype.* Nature, 2012. **483**(7390): p. 479-83.
284. Mathur, R., et al., *MGMT promoter methylation level in newly diagnosed low-grade glioma is a predictor of hypermutation at recurrence.* Neuro Oncol, 2020.
285. Johnson, B.E., et al., *Mutational analysis reveals the origin and therapy-driven evolution of recurrent glioma.* Science, 2014. **343**(6167): p. 189-193.
286. Choi, S., et al., *Temozolomide-associated hypermutation in gliomas.* Neuro Oncol, 2018. **20**(10): p. 1300-1309.

287. Barker, C.F. and R.E. Billingham, *Immunologically privileged sites.* Adv Immunol, 1977. **25**: p. 1-54.
288. Medawar, P.B., *Immunity to homologous grafted skin; the fate of skin homografts transplanted to the brain, to subcutaneous tissue, and to the anterior chamber of the eye.* Br J Exp Pathol, 1948. **29**(1): p. 58-69.
289. Graham, M., et al., *High-dose chemotherapy with autologous stem-cell rescue in patients with recurrent and high-risk pediatric brain tumors.* J Clin Oncol, 1997. **15**(5): p. 1814-23.
290. Bechmann, I., *Failed central nervous system regeneration: a downside of immune privilege?* Neuromolecular Med, 2005. **7**(3): p. 217-28.
291. Grigoriadis, N., et al., *Neuroinflammation in multiple sclerosis: evidence for autoimmune dysregulation, not simple autoimmune reaction.* Clin Neurol Neurosurg, 2006. **108**(3): p. 241-4.
292. Pardo, L.M. and C.M. van Duijn, *In search of genes involved in neurodegenerative disorders.* Mutat Res, 2005. **592**(1-2): p. 89-101.
293. Gelders, G., V. Baekelandt, and A. Van der Perren, *Linking Neuroinflammation and Neurodegeneration in Parkinson's Disease.* J Immunol Res, 2018. **2018**: p. 4784268.
294. Louveau, A., et al., *Structural and functional features of central nervous system lymphatic vessels.* Nature, 2015. **523**(7560): p. 337-41.
295. Cserr, H.F., C.J. Harling-Berg, and P.M. Knopf, *Drainage of brain extracellular fluid into blood and deep cervical lymph and its immunological significance.* Brain Pathol, 1992. **2**(4): p. 269-76.
296. Roopenian, D.C. and S. Akilesh, *FcRn: the neonatal Fc receptor comes of age.* Nat Rev Immunol, 2007. **7**(9): p. 715-25.
297. Jackson, C., et al., *Challenges in immunotherapy presented by the glioblastoma multiforme microenvironment.* Clin Dev Immunol, 2011. **2011**: p. 732413.
298. Frei, K., et al., *Transforming growth factor-beta pathway activity in glioblastoma.* Oncotarget, 2015. **6**(8): p. 5963-77.
299. Nduom, E., M. Weller, and A. Heimberger, *Immunosuppressive mechanisms in glioblastoma.* Neuro-Oncology, 2015. **17**: p. 9-14.
300. Elliott, L.H., W.H. Brooks, and T.L. Roszman, *Activation of immunoregulatory lymphocytes obtained from patients with malignant gliomas.* J Neurosurg, 1987. **67**(2): p. 231-6.
301. Wainwright, D.A., et al., *Thymus-derived rather than tumor-induced regulatory T cells predominate in brain tumors.* Neuro Oncol, 2011. **13**(12): p. 1308-23.
302. Han, S., et al., *Rescuing defective tumor-infiltrating T-cell proliferation in glioblastoma patients.* Oncol Lett, 2016. **12**(4): p. 2924-2929.
303. Han, S., et al., *Tumour-infiltrating CD4(+) and CD8(+) lymphocytes as predictors of clinical outcome in glioma.* Br J Cancer, 2014. **110**(10): p. 2560-8.
304. Zhai, L., et al., *Infiltrating T Cells Increase IDO1 Expression in Glioblastoma and Contribute to Decreased Patient Survival.* Clin Cancer Res, 2017. **23**(21): p. 6650-6660.
305. Chongsathidkiet, P., et al., *Sequestration of T cells in bone marrow in the setting of glioblastoma and other intracranial tumors.* Nat Med, 2018. **24**(9): p. 1459-1468.
306. Engler, J.R., et al., *Increased microglia/macrophage gene expression in a subset of adult and pediatric astrocytomas.* PLoS One, 2012. **7**(8): p. e43339.
307. Hanisch, U.K. and H. Kettenmann, *Microglia: active sensor and versatile effector cells in the normal and pathologic brain.* Nat Neurosci, 2007. **10**(11): p. 1387-94.

308. Platten, M., et al., *Monocyte chemoattractant protein-1 increases microglial infiltration and aggressiveness of gliomas.* Ann Neurol, 2003. **54**(3): p. 388-92.
309. Mizutani, M., et al., *The fractalkine receptor but not CCR2 is present on microglia from embryonic development throughout adulthood.* J Immunol, 2012. **188**(1): p. 29-36.
310. Pyonteck, S.M., et al., *CSF-1R inhibition alters macrophage polarization and blocks glioma progression.* Nat Med, 2013. **19**(10): p. 1264-72.
311. Sielska, M., et al., *Distinct roles of CSF family cytokines in macrophage infiltration and activation in glioma progression and injury response.* J Pathol, 2013. **230**(3): p. 310-21.
312. Müller, A., et al., *Resident microglia, and not peripheral macrophages, are the main source of brain tumor mononuclear cells.* Int J Cancer, 2015. **137**(2): p. 278-88.
313. Srinivasan, S., et al., *The P2Y12 antagonists, 2-methylthioadenosine 5'-monophosphate triethylammonium salt and cangrelor (ARC69931MX), can inhibit human platelet aggregation through a Gi-independent increase in cAMP levels.* J Biol Chem, 2009. **284**(24): p. 16108-17.
314. Ransohoff, R.M., *A polarizing question: do M1 and M2 microglia exist?* Nat Neurosci, 2016. **19**(8): p. 987-91.
315. Masuda, T., et al., *Spatial and temporal heterogeneity of mouse and human microglia at single-cell resolution.* Nature, 2019. **566**(7744): p. 388-392.
316. Schetters, S.T.T., et al., *Neuroinflammation: Microglia and T Cells Get Ready to Tango.* Front Immunol, 2017. **8**: p. 1905.
317. Szulzewsky, F., et al., *Glioma-associated microglia/macrophages display an expression profile different from M1 and M2 polarization and highly express Gpnmb and Spp1.* PLoS One, 2015. **10**(2): p. e0116644.
318. See, A.P., J.J. Parker, and A. Waziri, *The role of regulatory T cells and microglia in glioblastoma-associated immunosuppression.* J Neurooncol, 2015. **123**(3): p. 405-12.
319. Schwartz, M. and Y. Ziv, *Immunity to self and self-maintenance: what can tumor immunology teach us about ALS and Alzheimer's disease?* Trends Pharmacol Sci, 2008. **29**(6): p. 287-93.
320. Unger, M.S., et al., *Microglia prevent peripheral immune cell invasion and promote an anti-inflammatory environment in the brain of APP-PS1 transgenic mice.* J Neuroinflammation, 2018. **15**(1): p. 274.
321. Malo, C.S., *MHC class I expression by microglia is required for generating a complete antigen-specific CD8 T cell response in the CNS.* J Immunol, 2018. **200**(1).
322. Sankowski, R., et al., *Mapping microglia states in the human brain through the integration of high-dimensional techniques.* Nat Neurosci, 2019. **22**(12): p. 2098-2110.
323. Bettinger, I., S. Thanos, and W. Paulus, *Microglia promote glioma migration.* Acta Neuropathol, 2002. **103**(4): p. 351-5.
324. Wick, W., M. Platten, and M. Weller, *Glioma cell invasion: regulation of metalloproteinase activity by TGF-beta.* J Neurooncol, 2001. **53**(2): p. 177-85.
325. Walentynowicz, K.A., et al., *In Search for Reliable Markers of Glioma-Induced Polarization of Microglia.* Front Immunol, 2018. **9**: p. 1329.
326. Veillon, L., et al., *Glycosylation Changes in Brain Cancer.* ACS Chem Neurosci, 2018. **9**(1): p. 51-72.

327. Jung, S., et al., *Analysis of fractalkine receptor CX(3)CR1 function by targeted deletion and green fluorescent protein reporter gene insertion.* Mol Cell Biol, 2000. **20**(11): p. 4106-14.
328. Nimmerjahn, A., F. Kirchhoff, and F. Helmchen, *Resting microglial cells are highly dynamic surveillants of brain parenchyma in vivo.* Science, 2005. **308**(5726): p. 1314-8.
329. Wieghofer, P. and M. Prinz, *Genetic manipulation of microglia during brain development and disease.* Biochim Biophys Acta, 2016. **1862**(3): p. 299-309.
330. Foster, C.J., et al., *Molecular identification and characterization of the platelet ADP receptor targeted by thienopyridine antithrombotic drugs.* The Journal of clinical investigation, 2001. **107**(12): p. 1591-1598.
331. Andre, P., et al., *P2Y12 regulates platelet adhesion/activation, thrombus growth, and thrombus stability in injured arteries.* J Clin Invest, 2003. **112**(3): p. 398-406.
332. Lou, N., et al., *Purinergic receptor P2RY12-dependent microglial closure of the injured blood-brain barrier.* Proc Natl Acad Sci U S A, 2016. **113**(4): p. 1074-9.
333. Kaiser, T. and G. Feng, *Tmem119-EGFP and Tmem119-CreERT2 Transgenic Mice for Labeling and Manipulating Microglia.* eNeuro, 2019. **6**(4).
334. Klichinsky, M., et al., *Human chimeric antigen receptor macrophages for cancer immunotherapy.* Nat Biotechnol, 2020.
335. Muraro, M.G., et al., *Ex-vivo assessment of drug response on breast cancer primary tissue with preserved microenvironments.* Oncoimmunology, 2017. **6**(7): p. e1331798.
336. Goltsev, Y., et al., *Deep Profiling of Mouse Splenic Architecture with CODEX Multiplexed Imaging.* Cell, 2018. **174**(4): p. 968-981 e15.
337. Wang, S.C., et al., *Radiation therapy-induced tumor invasiveness is associated with SDF-1-regulated macrophage mobilization and vasculogenesis.* PLoS One, 2013. **8**(8): p. e69182.
338. Kioi, M., et al., *Inhibition of vasculogenesis, but not angiogenesis, prevents the recurrence of glioblastoma after irradiation in mice.* J Clin Invest, 2010. **120**(3): p. 694-705.
339. Gieryng, A., et al., *Immune microenvironment of gliomas.* Lab Invest, 2017. **97**(5): p. 498-518.
340. Ellert-Miklaszewska, A., et al., *Tumour-processed osteopontin and lactadherin drive the protumorigenic reprogramming of microglia and glioma progression.* Oncogene, 2016. **35**(50): p. 6366-6377.
341. Tsai, R.K. and D.E. Discher, *Inhibition of "self" engulfment through deactivation of myosin-II at the phagocytic synapse between human cells.* J Cell Biol, 2008. **180**(5): p. 989-1003.
342. Dall'Olio, F., et al., *Sialosignaling: sialyltransferases as engines of self-fueling loops in cancer progression.* Biochim Biophys Acta, 2014. **1840**(9): p. 2752-64.
343. Bertram, L., et al., *Genome-wide association analysis reveals putative Alzheimer's disease susceptibility loci in addition to APOE.* Am J Hum Genet, 2008. **83**(5): p. 623-32.
344. Naj, A.C., et al., *Common variants at MS4A4/MS4A6E, CD2AP, CD33 and EPHA1 are associated with late-onset Alzheimer's disease.* Nat Genet, 2011. **43**(5): p. 436-41.
345. Watters, J.J., J.M. Schartner, and B. Badie, *Microglia function in brain tumors.* J Neurosci Res, 2005. **81**(3): p. 447-55.
346. Barrett, Lindy E., et al., *Self-Renewal Does Not Predict Tumor Growth Potential in Mouse Models of High-Grade Glioma.* Cancer Cell, 2012. **21**(1): p. 11-24.

7 Acknowledgements

First of all, I would like to thank Prof. Dr. Gregor Hutter for giving me the great opportunity to perform my MD-PhD thesis in his laboratory. I appreciate his enthusiasm and great commitment for science, which motivated me as well and allowed me to develop new ideas and experiments, but also to critically view the research of others and my own.

Secondly, I am grateful to the current and previous members of the Hutter/Mariani laboratory for technical inputs, critical questions, discussions and fun moments.

In addition, special thanks go to the lab of Prof. Dr. Heinz Läubli, in particular Dr. Anne Bärenwaldt, Dr. Natalia Rodrigues Mantuano and Dr. Jinyu Wang for significant technical support, and scientific discussions.

A particular thank you goes to the genomics, proteomics, flow cytometry, bioinformatics and animal core facilities of the University of Basel for tremendous technical and logistical support. Specifically, Dr. Julien Roux, Dominik Viscardi, Stephan Donelli and Stella Stefanovic.

I am very grateful to the members of my PhD advisory committee: Prof. Dr. Fiona Doetsch, Dr. Johannes vom Berg and Prof. Dr. Rainer Glass for taking the time to discuss my projects always very constructively.

Last but not least many thanks to my family for their amazing support ever since and most importantly, dear Lara, thank you for your love, for taking care of so many things and for being the best wife and friend I could have ever wished for.

8 Curriculum Vitae

Personal Details

Surname	Schmassmann
First name(s)	Philip Daniel
Address	Hebelstrasse 20, 4031 Basel
Tel.	+41 612653897
E-Mail	p.schmassmann@unibas.ch

Education

08/2008 – 12/2011 Gymnasium Liestal, Baselland

12/2010 – 05/2011 *Maturarbeit, Department for BioMedical Research, Prenatal Medicine, University of Bern (Prof. Surbek)*

09/2012 – 09/2018 Medical Studies, University of Basel

07/2015 – 12/2015 *Master Thesis, Department of Biomedicine, University of Basel (Prof. Christofori)*

09/2018 Swiss federal examination in medicine, in both Multiple Choice (MC) and Clinical Skills (CS) examinations among the best ten percent.

02/2019 – present MD-PhD Thesis, Brain Tumor Immunotherapy Lab, Department of Biomedicine, University of Basel (Prof. Hutter)

10/2020 *Promotion, Dr. med., University of Basel*

Conferences and Symposia

10/2019 **Swiss Federation of clinical neuro societies (SFCNS) 2019**
Lausanne, Switzerland (oral and poster presentation)

12/2019 **100 years of Microglia – International Symposium**
Lausanne, Switzerland (poster presentation)

02/2020 **Surgical Research Day 2020, University Hospital Basel**
Basel, Switzerland (oral presentation)

11/2021 **Society for Neuro-Oncology (SNO) Annual Scientific Meeting**
Boston, USA (poster presentation)

02/2022	**Surgical Research Day 2022, University Hospital Basel** Basel, Switzerland (oral presentation)
05/2022	**11th Brain Tumor Meeting 2022** Berlin, Germany (oral presentation)
08/2022	**DBM Summer Symposium 2022** Basel, Switzerland (oral presentation)
09/2022	**European Association of Neuro-Oncology (EANO) 2022 meeting** Vienna, Austria (two oral presentations)
09/2022	**Swiss Federation of clinical neuro societies (SFCNS) 2022** Basel, Switzerland (two oral presentations)

Fellowships and Awards

10/2011	First price *BioValley College Award*, University of Basel: CHF 1'500
03/2012	*Basler Maturandenpreis der Novartis:* CHF 2'000
06/2019 – 05/2020	*Personenförderungsstipendium,* Department of Surgery, University Hospital of Basel: 1 year, CHF 23'520
11/2019	Project grant of the *Alumni Medizin Basel*: CHF 20'000
08/2021	*YouClin Thesis Award,* SFCNS: CHF 500
09/2019 – 08/2022	*MD-PhD Fellowship*, SNF MD-PhD program: 3 years, CHF 188'250
09/2022	Award for Best Abstract in Basic Research at the EANO 2022 meeting

Publications

Stefanie Tiede, Nathalie Meyer-Schaller, Ravi Kalathur, Robert Ivanek, Ernesta Fagiani, **Philip Schmassmann**, Patrick Stillhardt, Simon Häfliger, Norbert Kraut, Norbert Schweifer, Irene C. Waizenegger, Ruben Bill and Gerhard Christofori: The FAK-Inhibitor BI853520 exerts anti-tumor effects in breast cancer. **Oncogenesis**. 2018 Sep 20;7(9):73

Manuel Moser, **Philip Schmassmann**, Markus Noger, Martin Baur, Edin Nevzati: Utility of fat suppression MR imaging of osteoporotic vertebral fractures in preventing and predicting subsequent fractures after kyphoplasty**. World Neurosurg**. 2019 Feb 5. pii: S1878-8750(19**)**

Tomas A. Martins*, **Philip Schmassmann*,** Tala Shekarian, Jean-Louis Boulay, Marie-Françoise Ritz, Steven Zanganeh, Johannes Vom Berg and Gregor Hutter: Microglia-centered

Combinatorial Strategies Against Glioblastoma. **Frontiers in Immunology.** 2020 Sep 29;11 *equally contributed

Shekarian, T., Zinner, C. P., Bartoszek, E. M., Duchemin, W., Wachnowicz, A. T., Hogan, S., Etter, M. M., Flammer, J., Paganetti, C., Martins, T. A., **Schmassmann, P**., Zanganeh, S., Le Goff, F., Muraro, M. G., Ritz, M. F., Phillips, D., Bhate, S. S., Barlow, G. L., Nolan, G. P., Schürch, C. M., … Hutter, G: Immunotherapy of glioblastoma explants induces interferon-γ responses and spatial immune cell rearrangements in tumor center, but not periphery. **Science advances**, 2022 8(26).

Philip Schmassmann, Julien Roux, Alicia Buck, Nazanin Tatari, Sabrina Hogan, Jinyu Wang, Sohyon Lee, Berend Snijder, Tomás A. Martins, Marie-Françoise Ritz, Tala Shekarian, Deniz Kaymak, Marta McDaid, Michael Weller, Tobias Weiss, Heinz Läubli and Gregor Hutter: The Siglec-sialic acid-axis is a target for innate immunotherapy of glioblastoma. Submitted

Philip Schmassmann, Julien Roux, Steffen Dettling, Sabrina Hogan, Tala Shekarian, Tomás A. Martins, Marie-Françoise Ritz, Sylvia Herter, Marina Bacac, and Gregor Hutter: Single-cell characterization of human GBM reveals regional differences in tumor-infiltrating leukocyte activation. Submitted